

5-31-2019

# Design and Measurement of a Millimeter-wave 2D Beam Switching Planar Antenna Array

Benjamin Horwath

Follow this and additional works at: [https://scholarcommons.scu.edu/eng\\_phd\\_theses](https://scholarcommons.scu.edu/eng_phd_theses)



Part of the [Electrical and Computer Engineering Commons](#)

---

## Recommended Citation

Horwath, Benjamin, "Design and Measurement of a Millimeter-wave 2D Beam Switching Planar Antenna Array" (2019). *Engineering Ph.D. Theses*. 24.

[https://scholarcommons.scu.edu/eng\\_phd\\_theses/24](https://scholarcommons.scu.edu/eng_phd_theses/24)

This Dissertation is brought to you for free and open access by the Student Scholarship at Scholar Commons. It has been accepted for inclusion in Engineering Ph.D. Theses by an authorized administrator of Scholar Commons. For more information, please contact [rsroggin@scu.edu](mailto:rsroggin@scu.edu).

# Santa Clara University

Department of Electrical Engineering

I HEREBY RECOMMEND THAT THE THESIS PREPARED UNDER MY  
SUPERVISION BY

**Benjamin Horwath**

ENTITLED

**Design and Measurement of a Millimeter-wave 2D Beam Switching Planar Antenna Array**

BE ACCEPTED IN PARTIAL FULFILLMENT OF THE REQUIREMENTS FOR

THE DEGREE OF

**DOCTOR OF PHILOSOPHY IN ELECTRICAL ENGINEERING**

---

Thesis Advisor

Dr. Ramesh Abhari

---

Chair of Department

Dr. Shoba Krishnan

---

Thesis Reader Dr. Tokunbo Ogunfunmi

---

Thesis Reader Dr. Ahmed Amer

---

Thesis Reader Dr. Allen Sweet

---

Thesis Reader Dr. Shoba Krishnan

# Design and Measurement of a Millimeter-wave 2D Beam Switching Planar Antenna Array

By

Benjamin Horwath

Dissertation

Submitted in Partial Fulfillment of the Requirements  
for the Degree of Doctor of Philosophy  
in Electrical Engineering  
in the School of Engineering at  
Santa Clara University, 2019

Santa Clara, California

To my family, Aimée, Marcella, Louisa, and Thea

---

## Acknowledgments

I would like to express my sincere gratitude to Dr. Ramesh Abhari, my advisor, who helped me salvage a sinking project and has provided invaluable support and guidance throughout the years at Santa Clara University. I am grateful to Prof. Tokunbo Ogunfunmi for his classes on adaptive algorithms and DSP hardware – the most direct classroom-to-workplace knowledge I can say I’ve ever received. I also thank Dr. Garret Okamoto for getting me started in the amazing world of wireless communications and antenna arrays.

Measurements at 60 GHz have proven very difficult to come by, so I am extremely grateful for all those that have helped me with experimental evaluations. Shaun Snyder with the Center for Nanostructures has been ever-accommodating and patient while making measurements at Santa Clara University. The Keysight team of Lauren Shapiro, Joel Nelson, and Matt DelMargo kicked off my lab education with two separate rounds of data collection on their great machines. Mark Maloney and Neil Jarvis essentially gave their office at Rohde & Schwarz to Dr. Abhari and I to gather data for an entire afternoon. Finally, thanks to our colleagues at Stanford University, Prof. Amin Arbabian and Dr. Nemat Dolatsha, who helped me out with a tight conference deadline by lending access to their VNA.

I must thank Anne Mahacek at the SCU Maker Lab who offered design and build advice for constructing the two over-the-air measurement systems employed in this work. Also, I thank my colleagues Nivedita Parthasarathy and Ali Khoshniat for our time shared in Dr. Abhari’s research group. It was always a pleasure to see them on campus and know I wasn’t the only one.

To my family, I could never fully express my thanks enough to them. Without their love and support I would never have finished. All three of my amazing daughters can only ever remember me as a PhD student. It's time to change that. And to Aimée, my wife, thank you and I love you.

# Design and Measurement of a Millimeter-wave 2D Beam Switching Planar Antenna Array

Benjamin Horwath

Department of Electrical Engineering  
Santa Clara University  
Santa Clara, California  
2019

## Abstract

A millimeter-wave 2-D beam switching microstrip patch antenna array excited by a 4x4 substrate integrated waveguide (SIW) Modified Butler Matrix is designed and experimentally evaluated in this thesis. A novel architecture is introduced for the Butler Matrix feed network to give designers a choice for phase shifter location to pursue a smaller circuit area. In addition, it enables the designer to control the BM phased outputs for achieving a set of desired 2-D beam directions, e.g.,  $\phi_0=45^\circ$ ,  $135^\circ$ ,  $225^\circ$ , and  $315^\circ$  at  $\theta_0=45^\circ$ , with a passive beam switching network for a given array geometry. Full-wave simulation results show when the so designed 4x4 Butler Matrix feeds a 2x2 planar patch antenna array, 4-quadrant beam switching is achieved.

To meet the goal of providing a low cost small footprint solution, the presented Modified Butler Matrix features straight SIW phase shifter using periodic apertures. The Modified Butler Matrix is fabricated on a single layer Rogers RO4350B substrate, achieving a circuit area of  $222.5 \text{ mm}^2$ , which is a 54% improvement over previously published 60 GHz results. The fully-integrated antenna array system is created by development of a new SIW to planar patch antenna transition

structure which maintains a total antenna frontend area of  $333 \text{ mm}^2$ , just 42% of the area of the next closest SIW 2-D beam switching publication at 60 GHz.

For verification of beam switching via over the air (OTA) measurements at 60 GHz, a bench-top anechoic chamber with proper transmitter and receiver antenna positioners is designed and fabricated using in-house maker laboratory resources. 2-D beam steering is proved in the intended 4 quadrants of radiation space at  $\phi_0=50^\circ$ ,  $140^\circ$ ,  $220^\circ$ , and  $300^\circ$  and  $\theta_0=30\pm 5^\circ$  demonstrating meeting the design specifications with a very good margin. As well, for each switched beam the gain of antenna array was measured to be between 4.8 to 6 dBi at 60 GHz which is within 1dB deviation from the simulated results.

---

# Table of Contents

Chapter 1: Introduction.....	1
1.1: Overview.....	1
1.2: Motivation.....	4
1.3: State of the Art in mm-wave Beam Steering.....	5
1.3.1: 2-D passive beamforming.....	6
1.3.2: Substrate integrated waveguide (SIW).....	8
1.4: Challenges in mm-wave Planar Antenna Array Implementation.....	9
1.4.1: Unwanted radiation, parasitic effects, and EMI.....	9
1.4.2: Challenges of mm-wave measurements.....	11
1.5: Objectives of the Thesis.....	12
1.6: Thesis Contributions.....	14
1.7: Thesis Organization.....	15
Chapter 2: Theory.....	18
2.1: Butler Matrix Operation.....	19
2.2: Applying to 2-D Beam Steering.....	24
2.3: Updating the Conventional Butler Matrix for feeding the Planar Array.....	29
2.3.1: Implementation Considerations for the Phase Shifter.....	36
2.4: Proposed Modified Butler Matrix Architecture.....	38

2.5: 2-D Beam-Steering Limitations.....	42
2.5.1: Updated conventional Butler Matrix architecture.....	42
2.5.2: Proposed Modified Butler Matrix architecture .....	45
2.6: Conclusion .....	48
Chapter 3: Butler Matrix Circuit Design.....	50
3.1: Substrate Integrated Waveguide (SIW).....	50
3.1.1: Transition from Microstrip to SIW .....	57
3.2: Quadrature Coupler Design .....	57
3.3: Crossover Circuit Design.....	60
3.4: Phase Shifter Design.....	61
3.4.1: Phase Shifter Measurements .....	66
3.5: Component Integration into Butler Matrix .....	68
3.6: Conclusion .....	74
Chapter 4: Antenna System Design.....	76
4.1: Slot-fed Microstrip Patch Antenna Design.....	76
4.2: Square Planar Array.....	81
4.3: Planar Array Feed Design.....	84
4.4: Connecting Butler Matrix to the Planar Array.....	89
4.5: Conclusion .....	96
Chapter 5: Experimental Evaluation of the Butler Matrix Design .....	98

5.1: Material Considerations and Impact .....	98
5.2: First Fabricated Prototype.....	99
5.3: Second Fabricated Prototype .....	102
5.4: De-embedded Results .....	111
5.5: Analysis of BM Prototype Performance for Beam-Switching .....	113
5.6: Conclusion .....	116
Chapter 6: Experimental Evaluation of the Full Antenna System.....	118
6.1: Fabricated Full Antenna System Prototype .....	118
6.2: Port Measurements .....	120
6.3: Low-cost OTA Measurement System .....	123
6.4: Antenna Array Pattern Measurements.....	127
6.5: Antenna Gain Measurements.....	129
6.6: Second Test Set-up for OTA Measurements .....	131
6.6.1: Design Modifications .....	131
6.6.2: Pattern Measurements .....	135
6.6.3: Gain Measurements.....	136
6.7: Conclusion .....	137
Chapter 7: Conclusion .....	139
7.1: Summary of Presented Work.....	139
7.2: Next Steps.....	142

7.2.1: System performance and evaluation .....	143
7.2.2: Target illumination range .....	143
7.2.3: Beam scanning .....	144
Appendix I: De-embedding Procedure .....	145

---

## List of Figures

Fig. 1-1: Vehicle-to-vehicle and vehicle-to-infrastructure communications concepts. Adapted from "Millimeter-Wave Vehicular Communication to Support Massive Automotive Sensing," by J. Choi et al, December 2016, IEEE Communications Magazine, pp 163. ....	2
Fig. 1-2: Automotive radar sensing applications. Adapted from "Automotive Radar: A review of signal processing techniques," by S. Patole et al, 2017, IEEE Signal Processing Magazine, vol. 34, no. 2, pp 23.....	3
Fig. 1-3: Diagram of the conventional Butler Matrix and resultant 1-D array factor patterns. Adapted from Antenna Theory and Design by W. L. Stutzman and G. A. Thiele, 2013, 3 <sup>rd</sup> Edition, pp 324.....	7
Fig. 1-4: Diagram of a typical phased array antenna types. ....	7
Fig. 1-5: Three-dimensional view of SIW.....	9
Fig. 1-6: Diagram of a typical rectangular array antenna.....	13
Fig. 1-7: Visualization of the target application. Circles represent ideal beam peak locations for illuminating a planar surface normal to the antenna array.....	13
Fig. 2-1: Diagram of the spherical coordinate system with respect to the Cartesian coordinate system. ....	19
Fig. 2-2: Circuit diagram of the conventional Butler Matrix. ....	20
Fig. 2-3: Diagram of a typical equally-spaced linear array antenna.....	20
Fig. 2-4: Array factor gain, $\phi=0^\circ$ , for an equally-spaced linear array fed by a conventional Butler Matrix.....	22

Fig. 2-5: Visualization of the peak locations for the linear array driven by the standard Butler Matrix.....	24
Fig. 2-6: Diagram of a typical rectangular array antenna.....	25
Fig. 2-7: Array factor gain, $\phi=90^\circ$ , for a square planar array with conventional Butler Matrix outputs.....	27
Fig. 2-8: Array factor gain, $\phi=26.46^\circ$ , for a square planar array with conventional Butler Matrix outputs.....	27
Fig. 2-9: Visualization of the peak locations for the planar array driven by the standard Butler Matrix.....	29
Fig. 2-10: Circuit diagram of the conventional Butler Matrix, with phase shifters left variable to adapt the phased outputs to the array geometry and target specifications.....	30
Fig. 2-11: Array factor gain, $\phi=135^\circ$ , for a square planar array with updated phase shifters in the conventional Butler Matrix architecture. ....	34
Fig. 2-12: Array factor gain, $\phi=45^\circ$ , for a square planar array with updated phase shifters in the conventional Butler Matrix architecture. ....	35
Fig. 2-13: Visualization of the peak locations for the 2x2 square planar array driven by the updated Butler Matrix.....	36
Fig. 2-14: Circuit diagram of the rearranged Butler Matrix, with phase shifters left variable to adapt the phased outputs to the array geometry and target specifications.....	39
Fig. 2-15: Array factor gain, $\phi=45^\circ$ , for a square planar array with updated phase shifters in the Modified Butler Matrix architecture.....	40
Fig. 2-16: Array factor gain, $\phi=135^\circ$ , for a square planar array with updated phase shifters in the Modified Butler Matrix architecture.....	40

Fig. 2-17: Visualization of the peak locations for the 2x2 square planar array driven by the Modified Butler Matrix.....	41
Fig. 2-18: Plot of possible $\phi_{01}$ and $\psi_2$ values versus $\theta_{01}$ for Port 1 excitations to the planar array. ....	43
Fig. 2-19: Plots of $\theta_{0i}$ , $\phi_{0i}$ versus $\psi_2$ for a) Port 1, b) Port 2, c) Port 3, and d) Port 4 excitations. ....	47
Fig. 2-20: Visualizing the target surface beam locations for the planar array excited by the conventional BM with arrows indicating increasing $\psi_2$ from $24.12^\circ$ to $155.88^\circ$ . ....	47
Fig. 3-1: Simple diagram of a section of rectangular waveguide.....	50
Fig. 3-2: Layout of a substrate integrated waveguide (SIW), with top metal layer removed. ..	51
Fig. 3-3: Plot of real and imaginary parts of the propagation constant, $\gamma$ , for the designed SIW width $a=2.5\text{mm}$ in a) RT5880 and b) RO4350B. ....	56
Fig. 3-4: Plot of output phase versus SIW length for RT5880, width $a=2.5\text{mm}$ .....	56
Fig. 3-5: Diagram of transition from microstrip landing to SIW. ....	57
Fig. 3-6: Diagram of the quadrature coupler circuit.....	58
Fig. 3-7: Layout of the SIW quadrature hybrid circuit in HFSS. ....	59
Fig. 3-8: Simulation performance of the SIW quadrature hybrid in HFSS with Port 1 excitation. ....	59
Fig. 3-9: Hybrid coupler simulated field distribution with Port 1 excitation. ....	60
Fig. 3-10: Layout of the SIW crossover circuit in HFSS. ....	61
Fig. 3-11: S-parameter plot for the crossover circuit with Port 1 excitation. ....	62
Fig. 3-12: Crossover simulated field distribution with Port 1 excitation. ....	62
Fig. 3-13: Structure of the SIW Butler Matrix in HFSS, prior to adding phase shift apertures.63	

Fig. 3-14: Layout of the phase shifting slots within the Butler Matrix circuit: just after the crossover circuit in Stages 2 and 4.....	64
Fig. 3-15: Layout of phase shifter comparison board.....	65
Fig. 3-16: Simulated transmission (S21, solid line) and reflection (S11, dash line) parameters for the phase shift comparison of the slot-based phase shifter, the meander phase shifter, and a straight length of SIW.....	66
Fig. 3-17: Measured (a) magnitude and (b) phase of S-parameters for the phase shift comparison prototype after de-embedding. ....	67
Fig. 3-18: Layout structure of the complete Butler Matrix circuit. ....	68
Fig. 3-19: Full layout of the Butler Matrix for evaluation, including input and output lines to enable the use of end launch connectors.....	69
Fig. 3-20: Plot of simulated return loss for all input port excitations of the final Modified Butler Matrix layout.....	71
Fig. 3-21: Plot of simulated insertion loss for a Port 1 excitation of the final Modified Butler Matrix layout.....	71
Fig. 3-22: Plot of the simulated output phases for a Port 1 excitation of the final Modified Butler Matrix layout.....	72
Fig. 3-23: Array factor gain, a) $\phi=45^\circ$ and b) $\phi=135^\circ$ , for a square planar array with simulated output phases from final modified Butler Matrix layout compared to ideal patterns. ....	73
Fig. 3-24: Visualization of the planar surface target being illuminated by the planar array factor excited by the simulated Modified Butler Matrix outputs. ....	74
Fig. 4-1: Side view of the transition to the 2x2 square planar array showing the dielectric stack-up. (Dimensions in mm.) .....	77

Fig. 4-2: Layout of microstrip patch antenna, coupling slot, and matching post illustrating longitudinal orientation with respect to the SIW feed. ....	79
Fig. 4-3: Plot of RL for the optimized patch antenna element of Fig. 4.2.....	79
Fig. 4-4: Plot of normalized E-plane ( $\phi=90^\circ$ ) radiation pattern for the designed microstrip patch antenna. Ideal patch antenna pattern is plotted for comparison.....	80
Fig. 4-5: Plot of normalized H-plane ( $\phi=0^\circ$ ) radiation pattern for the designed microstrip patch antenna. Ideal patch antenna pattern is plotted for comparison.....	80
Fig. 4-6: Simulated 3-D field pattern of a single patch antenna element.....	80
Fig. 4-7: Initial layout of the 4 patch antennas in the square planar array configuration.....	81
Fig. 4-8: 3-D broadside gain pattern for the square planar array. ....	82
Fig. 4-9: 3-D field pattern of the square planar array with simulated Port 1 excitation from the Modified Butler Matrix.....	83
Fig. 4-10: Top view of the transition to the 2x2 square planar array noting feed dimensions and orientation with respect to the reference location of the array.....	85
Fig. 4-11: Reflection and isolation S-parameters of the feed transition from the Butler Matrix to the 2x2 square planar array for a) the initial design and b) the final design.....	86
Fig. 4-12: Plot of $S'_{11}$ (a) magnitude, and (b) phase, corresponding to the transition feed $l_{00}$ for key combinations of searched feed lengths. ....	87
Fig. 4-13: Top view of the transition to the 2x2 square planar array with updated dimensions. ....	88
Fig. 4-14: Top view of layout for the fully-integrated antenna system design. ....	90
Fig. 4-15: Simulated return loss for all ports of the fully-integrated antenna array system.....	91
Fig. 4-16: Simulated isolation for all ports of the fully-integrated antenna array system.....	91

Fig. 4-17: Simulated polar plots of beam patterns resulting from signals applied to ports 1 and 2 of the antenna system prototype, for the $\phi=45^\circ$ cut-plane. ....	92
Fig. 4-18: Simulated polar plots of beam patterns resulting from signals applied to ports 3 and 4 of the antenna system prototype, for the $\phi=135^\circ$ cut-plane. ....	92
Fig. 4-19: 3-D gain patterns for all excitations to the fully-integrated antenna system: a) Port 1, $\theta_{01}=31^\circ$ , $\phi_{01}=212^\circ$ ; b) Port 2, $\theta_{02}=29^\circ$ , $\phi_{02}=41^\circ$ ; c) Port 3, $\theta_{03}=26^\circ$ , $\phi_{03}=314^\circ$ ; and d) Port 4, $\theta_{04}=28^\circ$ , $\phi_{04}=141^\circ$ . ....	93
Fig. 4-20: Plot of simulated gain over frequency for all port excitations of the fully-integrated antenna system. ....	94
Fig. 4-21: Comparison of the array gain field pattern versus the ideal array factor for the Modified Butler Matrix in the a) $\phi=45^\circ$ and b) $\phi=135^\circ$ cut-planes. ....	95
Fig. 4-22: Contour plot of the incident beam patterns on the target planar surface highlighting the 1.5dB power band. ....	96
Fig. 5-1: 1 <sup>st</sup> fabricated Butler Matrix prototype implemented in RT5880. ....	101
Fig. 5-2: Simulated and measured results for a) insertion and return loss, and b) transmission and reflection phases plots between Ports 6 and 1 for 1 <sup>st</sup> Butler Matrix prototype. ....	102
Fig. 5-3: Fabricated 2 <sup>nd</sup> Butler Matrix prototype. ....	104
Fig. 5-4: a) Port 1 and b) Port 2 return loss plot comparing Butler Matrix prototype simulation, measurement, and de-embedded measurement results. ....	105
Fig. 5-5: Plot of insertion loss from a) Port 1 to Port 5, and b) Port 2 to Port 6, comparing Butler Matrix prototype simulation, measurement, and de-embedded measurement results. ....	106
Fig. 5-6: a) Port 1 to Port 2 and b) Port 2 to Port 3 isolation plot comparing Butler Matrix prototype simulation, measurement, and de-embedded measurement results. ....	108

Fig. 5-7: With an input to Port 1, comparison of the phase differential between Ports 5 and 6 of the Butler Matrix prototype for the simulated, measured, and de-embedded results. ....	109
Fig. 5-8: With an input to Port 1, comparison of the phase differential between Ports 5 and 7 of the Butler Matrix prototype for the simulated, measured, and de-embedded results. ....	109
Fig. 5-9: With an input to Port 1, comparison of the phase differential between Ports 5 and 8 of the Butler Matrix prototype for the simulated, measured, and de-embedded results. ....	110
Fig. 5-10: Through-only de-embedding structures used to characterize the connectors, feedlines, and transition sections of the prototypes. The left-hand board is 9.72 mm long and the right-hand is 7.66 mm long.....	111
Fig. 5-11: Measured a) return and insertion loss and b) phase angle of the straight SIW de-embedding test structures.....	112
Fig. 5-12: Array factor gain, a) $\phi=45^\circ$ and b) $\phi=135^\circ$ , for a square planar array with de-embedded measured output phases from fabricated Modified Butler Matrix prototype. ....	114
Fig. 5-13: Visualization of the planar surface target being illuminated by the planar array factor excited by the simulated Modified Butler Matrix outputs.....	115
Fig. 6-1: a) Modified Butler Matrix side and b) antenna side of the fabricated and fully-assembled Antenna System prototype. ....	121
Fig. 6-2: Comparison of return loss for Ports 1 and 4 of the antenna system prototype: simulated (dotted line) and measured results (solid line).....	122
Fig. 6-3: Comparison of return loss for Ports 2 and 3 of the antenna system prototype: simulated (dotted line) and measured results (solid line).....	122
Fig. 6-4: Comparison of isolation results for all neighboring ports of the antenna system prototype: simulated (dotted line) and measured (solid line). ....	123

Fig. 6-5: Beam pattern measurement rig with antenna array prototype and measurement horn antenna.....	125
Fig. 6-6: Diagram of the constructed anechoic chamber for making far field antenna pattern measurements.....	125
Fig. 6-7: Anechoic chamber housing the antenna positioning system in operation without the top cover.....	126
Fig. 6-8: Measured (solid) vs. simulated (dashed) $\theta_{0i}$ cut-plane horizontal beam patterns for all input ports of the antenna system prototype: a) Port 1, $\theta_{01}=35^\circ$ ; b) Port 2, $\theta_{02}=25^\circ$ ; c) Port 3, $\theta_{03}=30^\circ$ ; d) Port 4, $\theta_{04}=30^\circ$ .....	128
Fig. 6-9: Measured (solid) vs. simulated (dashed) $\phi_{0i}$ cut-plane vertical beam patterns for all input ports of the antenna system prototype: a) Port 1, $\phi_{01}=220^\circ$ ; b) Port 2, $\phi_{02}=50^\circ$ ; c) Port 3, $\phi_{03}=300^\circ$ ; d) Port 4, $\phi_{04}=140^\circ$ .....	129
Fig. 6-10: Plots of gain vs frequency for the antenna system prototype. Input Ports 1-4 correspond to graphs (a)-(d), respectively. ....	131
Fig. 6-11: Second beam pattern positioning system with antenna array prototype and standard horn antenna.....	132
Fig. 6-12: 2 <sup>nd</sup> measurement (black, solid) vs. 1 <sup>st</sup> measurement (red, dashed) vs. simulated (blue, dashed) of the $\theta_{01}=30^\circ$ cut-plane horizontal beam pattern for Port 1 of the antenna system prototype. ....	135
Fig. 6-13: 2 <sup>nd</sup> measurement (black, solid) vs. 1 <sup>st</sup> measurement (red, dashed) vs. simulated (blue, dashed) of the $\phi_{01}=220^\circ$ cut-plane horizontal beam pattern for Port 1 of the antenna system prototype. ....	136
Fig. 6-14: Plot of gain vs frequency for input Port 1 to the antenna system prototype.....	137



---

# List of Tables

Table 2-1: PEAK BEAM DIRECTIONS AND SIR COMPARISONS FOR ALL PORT EXCITATIONS FROM STANDARD BUTLER MATRIX APPLIED TO PLANAR ARRAY. ....	28
Table 2-2: PEAK BEAM DIRECTIONS AND SIR COMPARISONS FOR ALL PORT EXCITATIONS FROM UPDATED CONVENTIONAL BUTLER MATRIX APPLIED TO PLANAR ARRAY. ....	35
Table 2-3: COMPARISON OF BEAM STEERING DIRECTIONS FOR ALL REVIEWED BUTLER MATRIX SCENARIOS. ....	41
Table 2-4: POSSIBLE AZIMUTH BEAM ANGLES FOR THE MODIFIED BUTLER MATRIX AND CONVENTIONAL ARCHITECTURE EXTENDED TO 2-D BEAM STEERING. ....	48
Table 3-1: CALCULATED AND SIMULATED SIW PARAMETERS FOR RT5880 AND RO4350B AT WIDTH $a=2.5\text{mm}$ . ....	55
Table 3-2: MODIFIED BUTLER MATRIX OUTPUT MAGNITUDES AND PHASES. ....	70
Table 3-3: PEAK BEAM DIRECTIONS AND SIR COMPARISONS FOR ALL PORT EXCITATIONS FROM THE SIMULATED MODIFIED BUTLER MATRIX APPLIED TO PLANAR ARRAY. ....	74
Table 4-1: SIMULATED PEAK ANTENNA PARAMETERS FOR THE SQUARE PLANAR ARRAY WITH DESIGNED MODIFIED BUTLER MATRIX OUTPUTS. ....	83
Table 4-2: COMPARISON OF ANTENNA, SLOT, AND MATCHING VIA POST DIMENSIONS AND LOCATIONS IN THE PLANAR ARRAY CONFIGURATION. ....	89
Table 4-3: PEAK BEAM DIRECTIONS FOR ALL PORT EXCITATIONS FROM THE SIMULATED FULLY-INTEGRATED ANTENNA SYSTEM. ....	96
Table 5-1: EXPECTED AND MEASURED S-PARAMETER MAGNITUDES OF THE FABRICATED MODIFIED BUTLER MATRIX PROTOTYPE. ....	107

Table 5-2: EXPECTED AND MEASURED DIFFERENTIAL PHASE OUTPUTS WITH RESPECT TO PORT 5 OF THE FABRICATED MODIFIED BUTLER MATRIX PROTOTYPE. ....	110
Table 5-3: PEAK BEAM DIRECTIONS AND SIR COMPARISONS FOR ALL PORT EXCITATIONS FROM THE MEASURED MODIFIED BUTLER MATRIX APPLIED TO A SIMULATED PLANAR ARRAY. ....	115
Table 5-4: COMPARING INTENDED AND RESULTANT BEAM DIRECTIONS FROM SIMULATION AND MEASUREMENT FOR THE MODIFIED BUTLER MATRIX PROTOTYPE PHASED OUTPUTS AT 60 GHZ. ....	116
Table 6-1: COMPARING INTENDED AND RESULTANT BEAM DIRECTIONS FOR THE FULL ANTENNA SYSTEM PROTOTYPE AT 60 GHZ.....	127
Table 7-1: COMPARISON BETWEEN PROPOSED AND REPORTED SIW BUTLER MATRIX FEED NETWORKS. ....	141
TABLE 7-2: COMPARISON BETWEEN PROPOSED AND REPORTED MM-WAVE 2-D ANTENNA ARRAYS. ....	142

---

## Abbreviations

4G	4 <sup>th</sup> -generation cellular
5G	5 <sup>th</sup> -generation cellular
AUT	antenna under test
BM	Butler Matrix
CPW	co-planar waveguide
EMI	electromagnetic interference
HPBW	half power beam width
IL	insertion loss
MIMO	multiple-input, multiple-output
mm-wave	millimeter-wave
MSPA	microstrip patch antenna
OTA	over-the-air
PAN	Personal Area Network
PCB	printed circuit board
RF	radio frequency
RFID	radio frequency identification
RL	return loss
SIW	Substrate Integrated Waveguide
SINR	Signal to Interference + Noise Ratio
SIR	Signal to Interference Ratio
TE	transverse electric (mode)
TM	transverse magnetic (mode)
ULA	uniform linear array
VNA	vector network analyzer

---

# Chapter 1: Introduction

A perspective about the undertaken research work is provided in this chapter. The chapter begins with an overview of emerging millimeter wave (mm-wave) applications for which 2-D beam steering is the essential characteristic of their performance. Following is the discussion on the challenges standing in the way of implementation of mm-wave beam steering antenna frontends and the state-of-the-art published by researchers attempting to solve these challenges. The chapter concludes with a statement of the contributions of the presented work and the organization outline of this thesis.

## 1.1: Overview

Researchers have focused much time and many resources into developing today's highly successful 4th-generation (4G) cellular and Wi-Fi networks that provide users with the ability to consume high definition multimedia services from personal mobile devices at their convenience by taking advantage of the microwave frequency spectrum up to 6 GHz [1]. As users' demands for network ubiquity and new services rise, the need for additional spectrum has become apparent to technology drivers of the telecommunications industry. Many have shifted development focus to the millimeter-wave (mm-wave) frequency range (30-300 GHz) to make use of the uncrowded and larger channel bandwidths. For telecommunication systems, a 5th-generation (5G) mobile standard is being called on to offer much higher data rates to mobile users than the previous 4G systems and be able to handle backhaul services between small cells, both of which require significant increases in achievable network capacity and allocated frequency bands [2].

Recent focus on bringing autonomous vehicles to consumers has strengthened the push for mm-wave innovation as well. The spectrum from 57-64 GHz is allocated for vehicle-to-vehicle and vehicle-to-infrastructure communications [3] as illustrated in Fig. 1-1. The mm-wave band also supports the need for automotive radar and object sensing systems necessary for self-driving cars [4], see Fig. 1-2. In addition, mm-wave short range radar systems are finding application in emerging industrial, medical, and consumer electronic devices that rely on mm-wave sensing of stationary and moving objects. Examples of these new markets include multi-robot and multi-drone systems, vital signs monitoring [5], and gesture sensors like Project Soli developed by Google [6]. All of these new technologies are deployed for use at significantly shorter distances than incumbent systems, typically in the 0.5-30m range as opposed to >100m wireless links of today's conventional systems. This shorter distance will require that these new systems will need not only beam control of the azimuth angle between transmitter and receiver, as is customary today, but the elevation angle as well.

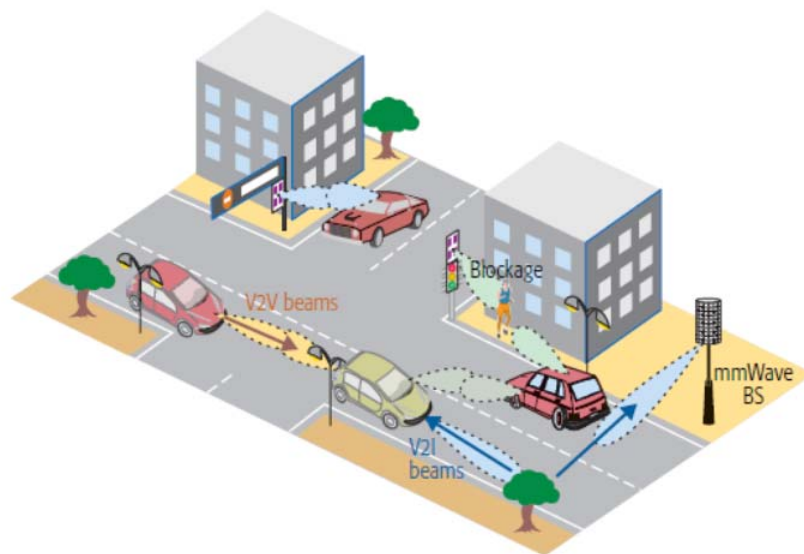


*Fig. 1-1: Vehicle-to-vehicle and vehicle-to-infrastructure communications concepts. Adapted from "Millimeter-Wave Vehicular Communication to Support Massive Automotive Sensing," by J. Choi et al, December 2016, IEEE Communications Magazine, pp 163.*

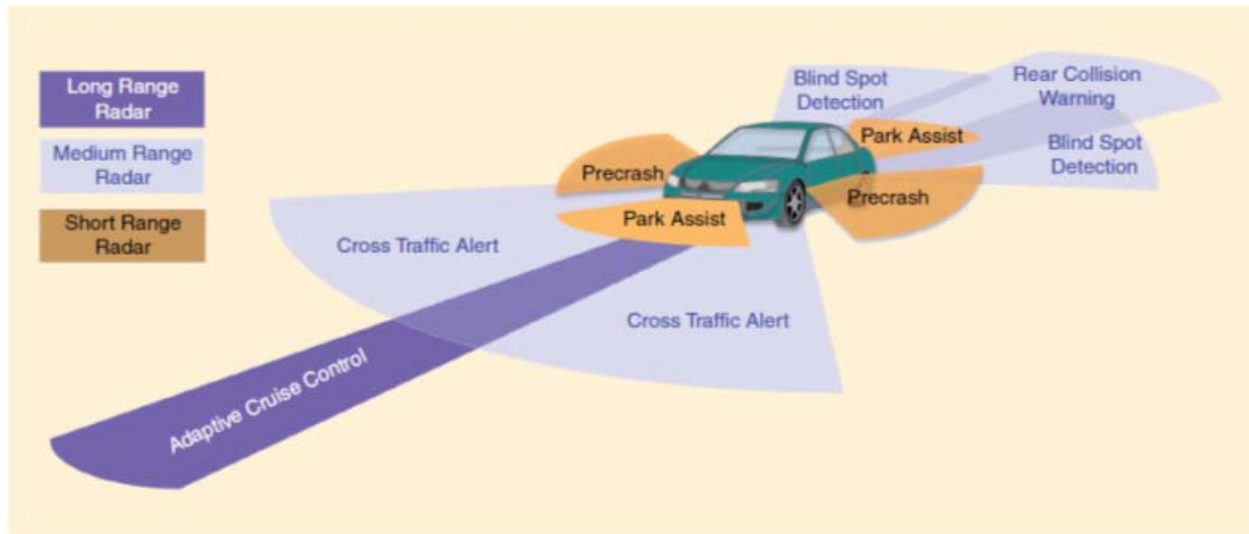


Fig. 1-2: Automotive radar sensing applications. Adapted from "Automotive Radar: A review of signal processing techniques," by S. Patole et al, 2017, *IEEE Signal Processing Magazine*, vol. 34, no. 2, pp 23.

The move to mm-wave technologies has been explored in the past couple of decades yet is still in the primary stages of commercial implementation. The 60 GHz band was considered for creation of Personal Area Networks (PAN) for wireless connection of electronic devices in short range [7]. Also, the use of mm-wave bands for imaging applications and security [8] have all contributed to the development of design and fabrication technologies for these systems and ultimately pushing for lowering the costs for entering commercial application market.

The challenges for deployment of mm-wave wireless systems are significant. First, propagation at mm-wave frequencies is quite sensitive to blockage compared to microwave frequencies [9]. Second, mm-wave electronic systems are prone to fabrication tolerances, unwanted radiation, coupling and reactive loading effects, i.e. parasitic effects, of junctions and discontinuities, which all bring about unprecedented design and measurement challenges and uncertainties.

The small device feature sizes of antennas enabled by moving to the mm-wave spectrum, allow for incorporating many more antennas in the same footprint of a standard radio frequency (RF) client device. This enables engineers to increase the overall radiation gain of their wireless system

designs to compensate for the high mm-wave propagation losses and provide the beam agility needed for dense area coverage, target finding and avoiding intermittent blockages. Nonetheless, the dense RF frontends created for these multi-antenna systems experience higher susceptibility to electromagnetic interference and crosstalk. The physically small feature sizes of layout interconnects and passive components make them more likely to suffer from design and fabrication tolerances as well as creating measurement challenges.

## 1.2: Motivation

Pushing wireless application boundaries means that the next generation systems will require not only the additional spectrum found at mm-wave frequencies, but the parallel advancement of new and more complex design and implementation technologies. These technologies range from two dimensional (2-D) beam scanning, smart antenna arrays and massive multiple-input multiple-output (MIMO) multi-antenna systems [10], [11], [12] to adaptation of bulky microwave structures into compact printed circuit board (PCB) implementation platforms in the form of substrate integrated waveguide (SIW) components [13].

As indicated earlier, increasing the number of antennas in a mm-wave wireless frontend is a must to recover high propagation path losses for improving the available link budget and to enable beam steering. The use of 2-D antenna arrays allows control in the azimuth and elevation angles of the radiation beam, which is essential in 5G, MIMO, radar-based sensors, and all new applications that exploit beam diversity. To date, much emphasis has been placed on using the well-known and less-complicated 1-D antenna array technology to scan radiation beam in a needed direction. Adding a second dimension of beam control can be implemented simply by repeating the 1D array frontend without integrated system design. This tactic is short-sighted, though, as it increases cost, footprint area, unnecessary complexity, and risk of failure, especially at mm-wave

frequencies. More than the typical off-the-shelf components are needed for the successful realization of 2D beam-switching and steering at mm-wave frequencies. Future systems clearly need a savvier agile fully integrated beam control system design and implementation, which is the motivation behind this research work.

### **1.3: State of the Art in mm-wave Beam Steering**

Beamforming techniques have been a critical development focus of antenna engineers for many decades. These well-known methods for weighting and constructively combining the radiation patterns of an array of antenna elements can be categorized in several ways. For example, digital versus analog, or active versus passive beam forming networks [14]. Digital beamforming occurs at the digital baseband level of a Tx/Rx frontend. Analog beamformers have focused on RF phase shifting, applying a vector of weights to an incoming or outgoing stream of signals to generate an array beam in a particular direction for improving gain, avoiding interference, pinpointing a specific location, or a combination of all of the above [15]. While digital techniques have a distinct advantage in the resolution of the generated beam angle, they are often capital intensive and operationally expensive as each computed RF stream requires a full analog mixer and amplifier frontend for each antenna. Analog techniques operate at the less-precise limit of analog components for RF stream weighting and combining but are much less costly and take up much less space since processing occurs very close to the antenna elements themselves.

Active beamformers are defined by whether power is required to control the phasing of antenna input streams. This method provides more precision as well as the potential for dynamic response, allowing antenna array systems to adapt to a changing propagation environment [16]. On the other hand, passive techniques use fixed phase shifters and circuit networks to form switchable beams with the advantage of lower power consumption. Where active beamformers rely on complex

components and algorithms, their passive counterparts are simpler in nature and may require no components at all beyond interconnects.

Further developing of passive beam steering methods could help lower consumer and deployment costs at mm-wave frequencies. The art of passively generating a directed beam pattern from an array of antennas was accelerated with the introduction of Butler Matrix in 1961 [17]. This passive method for generating  $N$  independent beam patterns from  $N$  antenna elements, see in Fig. 1-3, greatly simplified the beamforming circuit by replacing the large number of power dividers ( $N * (N-1)$ ) with a smaller matrix of hybrid couplers ( $N/2 * \log_2 N$ ) [17]. While not the only means for passive beamforming, Butler Matrix has been well-researched, and well-used, and has become the de facto standard for analog beam switching. Unfortunately, the as-is BM misses the mark for applications that require 2-D beam control, i.e. in both elevation and azimuth planes.

Conventional BM implementations have focused on driving uniform linear arrays (ULAs) [16], as seen in Fig. 1-4, but this popular feed network is, by definition, only capable of 1-D beam steering. If the end goal is to achieve 2-D beam steering, an appropriately designed beamforming network is required to feed a planar array (also seen in Fig. 1-4).

### **1.3.1: 2-D passive beamforming**

Few examples exist of 2-D passive beam steering attempts at mm-wave. A simulation study was performed in [18] to present a 3x3 planar array steered by two 2x2 BMs at 29 GHz, achieving four radiation beams. However, the beamforming network was designed with microstrip feeds making implementation at the 60 GHz range and above more problematic in terms of EMI and RF integrity. In [19], a circular array is presented to achieve an axial beam (a controlled beam pattern that is swept 360° around the z-axis) and provides a system to combine phase modes for steering to variable  $\theta_0$ 's and  $\phi_0$ 's, but the design frequency is scaled down significantly at 5 GHz and the array

excitation is via coaxial probe feeds. Neither of these previous works, [18] and [19], presents mm-wave experimental evaluations and only discusses simulated results of antenna array and beamforming network as separate not integrated designs.

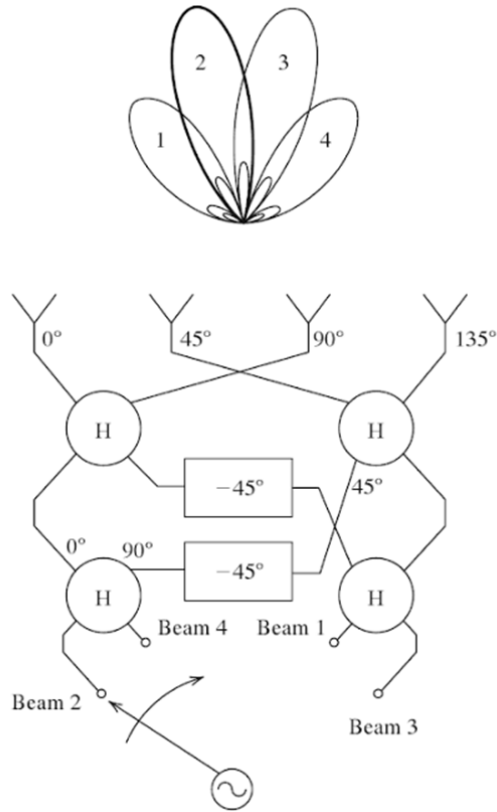


Fig. 1-3: Diagram of the conventional Butler Matrix and resultant 1-D array factor patterns. Adapted from *Antenna Theory and Design* by W. L. Stutzman and G. A. Thiele, 2013, 3<sup>rd</sup> Edition, pp 324.

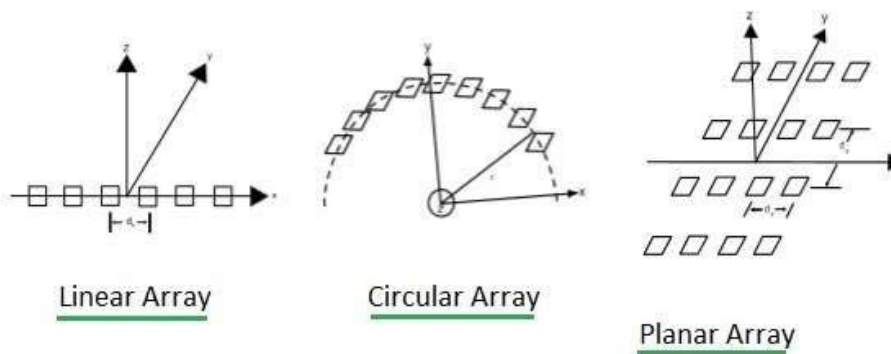
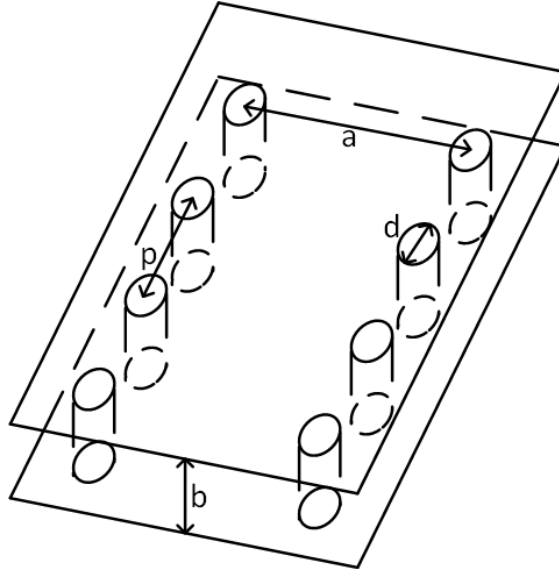


Fig. 1-4: Diagram of a typical phased array antenna types.

More recently, [20] presents simulation of a very large beamforming network consisting of 16 sets of 8x8 BMs to steer an 8x8 planar array of horn antennas fed with WR28 rectangular waveguide, simulating 64 switched beams in 2-D. In [21], [22], and [23] authors present an integrated solution for 2-D beam-switching with a substrate integrated waveguide (SIW) beamforming network at 60GHz. In [21], magneto-electric dipole elements are the radiating elements with aperture coupling from SIWs, but still rigid bulky waveguide feeds are used to connect SIWs to the input feed. The mm-wave designs of [20] and [21], when implemented, occupy a larger than necessary footprint and are prone to unwanted discontinuity effects and RF integrity problems due to longer interconnects and more junctions. A 2x2 planar array of circular patch antennas integrated with a simplified BM at 60GHz is presented in [24] and achieves good results for moving the switched beams from broadside to end-fire patterns, yet the employed microstrip implementation would suffer radiation and integrity issues in the mm-wave range.

### **1.3.2: Substrate integrated waveguide (SIW)**

SIW is a waveguide technology that has been extended from the concept of dielectric-filled bulky metal waveguides often used in microwave and mm-wave communication systems. First patented in 1994 [25], it has been called “laminated waveguide” [26], “post wall waveguide” [27], and “electromagnetic bandgap waveguide” [28], before the name settled to SIW in 2003 [13]. Many design aspects and uses of SIW have been researched, innovated, and optimized [29], [30], [31], [32] from its original design seen in Fig. 1-5. The move to SIW from the more standard microstrip, stripline or coplanar waveguide is essential at higher frequencies, such as the 60 GHz unlicensed spectrum (centered with  $\lambda_0=5\text{mm}$ ), since network lines are squeezed closer to feed tightly-spaced antenna elements. Significant prior work exists on implementing Butler Matrices in substrate integrated waveguide (SIW) technology [33], [34], [35], [36].



*Fig. 1-5: Three-dimensional view of SIW.*

There are noted recent examples of authors attempting to deliver low cost, passive beam-steering with SIW BM implementations, but none offers true 2-D beam agility. From [37] comes a modified BM feed that delivers narrow beams from a 16 GHz linear array for improving small cell network capacity. Another solution uses a novel SIW BM structure to miniaturize the feed network at 12.5 GHz [38] but is not convenient to feed antenna arrays for 2-D scanning. Improving spectrum utilization, [39] introduced a novel BM and array design that achieves multiple beams in 2 separate frequency bands, but the beams are only steerable in the azimuth direction and do not operate in the mm-wave range.

## **1.4: Challenges in mm-wave Planar Antenna Array Implementation**

### **1.4.1: Unwanted radiation, parasitic effects, and EMI**

Beamforming networks operating at mm-wave frequencies suffer from unwanted radiation as the feed lines have comparable dimensions to that of the radiating elements. Connectors, junctions, and transitions, which are discontinuities about the same size as the intentional radiators, also

create parasitic radiated emissions. To address the need for creating compact devices and reduce the effects of discontinuities and parasitic radiators, it is desired to create fully integrated systems, i.e. monolithic integration or 3-D stacked, with the least number of discontinuities and transitions as possible.

In an ultimately assembled mm-wave antenna system, feed network and components are squeezed close together to deliver signals to and from tightly-packed antenna elements. This also results in higher susceptibility to crosstalk and electromagnetic interference (EMI) in comparison to lower frequency systems. Crosstalk in multi-antenna arrangements, such as arrays and MIMO systems, results in coupled antenna input impedance and channel correlation. These in turn degrade the RF integrity of the system which could result in malfunctioning of the system or render it inoperable. For example, crosstalk and coupled input impedances in beam steering antenna arrays could result in scan blindness [14]. In MIMO systems, one of the performance indicators is signal-to-interference-plus-noise ratio (SINR) [15]: crosstalk in the antenna feed network and RF front-end of these systems contributes to the interference component of SINR and thus channel correlation.

Circuit designers need to choose the interconnects and components for implementing mm-wave frontend carefully and devise methods for reducing coupling. Common printed circuit lines such as microstrip and stripline are prone to crosstalk especially in closely integrated systems if no provision for reducing coupling is employed. Coplanar waveguides (CPWs) [40] that are more frequently used in microwave and mm-wave systems could perform better in terms of capacitive crosstalk in comparison to microstrip lines, but are also more prone to substrate coupling via parallel plate mode excitation, especially in multilayer and conductor-backed designs such as Grounded CPW.

Crosstalk and spurious radiation due to the feed network can be eliminated with the use of substrate integrated waveguide (SIW) technology [33], [34], [35], [36], well known for its robust signal isolation capabilities, which allows adjacent channels to share a common wall at the expense of a slightly wider footprint [41], [29]. An innovative approach is needed to implement a full beamforming network in SIW to continue pursuing smaller footprints as well as improving the agility of mm-wave beam-steering systems.

#### **1.4.2: Challenges of mm-wave measurements**

Measurement and verification of radiating mm-wave systems is an ever more challenging task. Not only are feature sizes much smaller than microwave systems which makes design and handling of test structures more difficult, but equipment operating at 60GHz and above is expensive and especially sensitive to noise and interference intercepted at measurement probe tips, junctions and cables and also signal variations due bending of cables.

Complete experimental characterization of mm-wave systems includes conducted port (network) measurements for determining return loss and isolation as well as over the air (OTA) antenna pattern measurements. Conducted port measurements follow an established procedure using vector network analyzers (VNAs) with the needed calibration and de-embedding methods to isolate the performance of the device/component under-test to the extent possible.

Phased array systems need to be assessed for their ability to meet the beam specifications of their intended application. For OTA performance evaluation, radiation patterns are measured in an antenna range or anechoic chamber rated at mm-wave frequencies. Nonetheless, mm-wave test chambers are not widely and readily available at the time or cost desired by the smaller scale companies or on budget developers. Innovative evaluation systems are needed to reduce development costs while still capturing accurate measurement data.

## 1.5: Objectives of the Thesis

Addressing the industry need for low-cost, analog mm-wave 2-D beam steering, this thesis presents a passive 60 GHz antenna system building block consisting of a novel 4x4 Butler Matrix implemented in SIW to direct a 2x2 planar microstrip patch antenna (MSPA) array. The BM beamforming network is chosen because of its simplicity in design and its status as the de facto standard for passive beamforming, and the unexplored possibility of its modification for 2-D beam steering [22].

SIW is the chosen interconnect building block in this thesis that will offer a low-cost, EMI-resistant, compact footprint solution that is backed by a significant amount of research [33], [34], [35], [36], [41]. Having transmission lines in such proximity to one another requires more robust signal isolation strategy to enable a multi-antenna system to deliver its intended performance. SIW interconnects provide such characteristics at the expense of a slightly wider footprint.

For implementing the planar antenna array, the choice of MSPA was directed by the need for a compact application that can be implemented using low cost standard printed circuit board (PCB) fabrication technology. Nonetheless, a new transition structure needs to be developed so that the SIW beamforming network can feed the planar array, diagrammed in Fig. 1-6, directly through aperture-coupling [42]. This allows full integration of feed network and antenna array resulting in a small enough footprint to be implemented on handheld devices as well as at the base station level in the form of a building block subarray.

The project beam switching goal is simple: generate 4 switchable beams with controlled azimuth and elevation angles to illuminate 4 quadrants in the upper radiation space of the planar array. The application goal is visualized on target plane in Fig. 1-7, where circles mark the ideal locations of beam pattern peaks. In this work, the elevation angle is considered to be  $\theta_0=45^\circ$  with four azimuth

directions spaced by multiples of  $90^\circ$  at  $\phi_{01}=45^\circ$ ,  $\phi_{02}=135^\circ$ ,  $\phi_{03}=225^\circ$ , and  $\phi_{04}=315^\circ$ . Such 2-D beam steering capability have real world applications from automotive and short-range radar sensing/mapping to multi-user or multi-device communication systems.

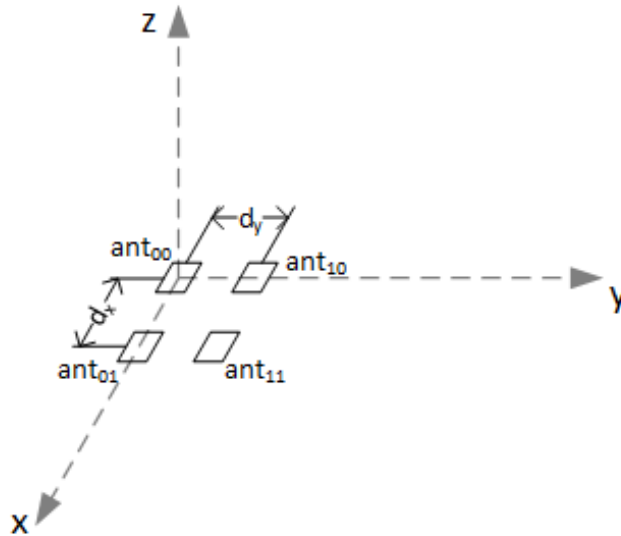


Fig. 1-6: Diagram of a typical rectangular array antenna.

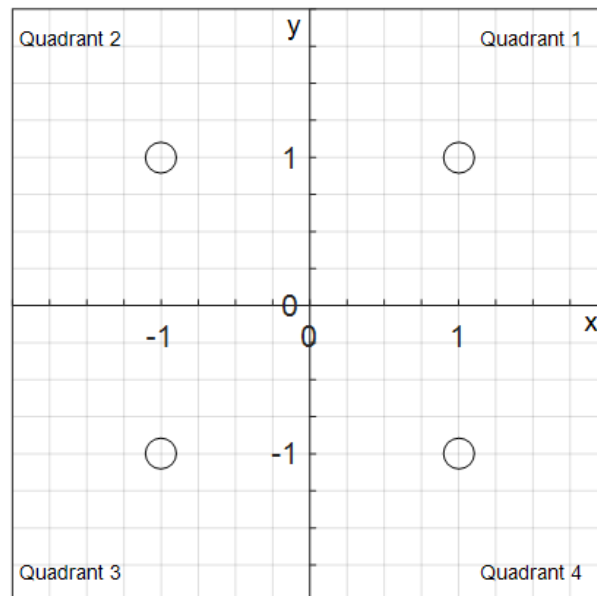


Fig. 1-7: Visualization of the target application. Circles represent ideal beam peak locations for illuminating a planar surface normal to the antenna array.

To meet the application goal of 2-D beam switching to 4 quadrants of a planar surface, the phase blocks and architecture of the conventional BM need to be modified to enable achieving azimuth and elevation angle beam agility.

## **1.6: Thesis Contributions**

A new 4x4 SIW BM for 2-D beam control of a 2x2 planar array at 60 GHz is presented in this thesis. The system features a small footprint, achieved by using periodically-spaced aperture phase shifters in the lower walls of the SIW interconnects to meet the phasing needs of the BM, taking advantage of the large attainable phase delay within a minimal SIW length. Additionally, the transformation of the BM architecture from conventional 1-D operation to full 2-D beam control requires a novel feed design to route the four phase outputs of the 4x4 BM to the inputs of the 2x2 planar MSPA array. All BM network components are designed, optimized and simulated to ensure having a minimal footprint. Then the entire BM network is simulated, fabricated, and evaluated to confirm feasibility. To feed the MSPA in fully integrated system a new transition structure is developed in this thesis that would enable aperture coupling to the 4-patch planar array via SIW feed lines. Two sets of prototypes are fabricated along with the needed test structures for evaluation of phase shifter design and de-embedding the effect of the connectors.

Measurements of the fabricated prototypes are conducted in the mm-wave region to assess antenna performance as well as the system's ability to provide four switchable beams for the target application. Collected data include network parameters for each input port, antenna gain, half power beam width (HPBW), and horizontal and vertical beam patterns in each designed target quadrant. The challenge of finding an OTA measurement lab to evaluate the 3-D beam patterns of the antenna array was solved by designing in-house test set-ups that include a rotating positioning

arm and an enclosure box covered with absorbers. OTA measurements of the fabricated prototype confirmed the 2-D beam agility of the full antenna system.

To summarize, the contributions of this thesis are:

- Development of one of the first fully-integrated SIW Butler Matrix with a 2x2 planar MSPA array for 2-D beam switching at 60GHz. [43]
- Development of new architecture for a 4x4 SIW BM to enable feeding planar patch arrays and beam switching in 4 quadrants of radiation space. [23]
- Innovative use of a periodic aperture phase shifter at mm-wave frequency that enables miniaturization of SIW Butler Matrix. The developed SIW BM footprint not only takes up less space (54%) than previous SIW Butler Matrix designs but also reduces discontinuities and junctions that typically lead to EMI and RF integrity problems at mm-wave frequencies. [22]
- A new transition from SIW to Patch antenna is designed to enable vertical system integration and miniaturization of the overall 2-D antenna array frontend by 42% in comparison to the nearest published SIW implementation. [23]
- Development of a low-cost benchtop OTA measurement system using maker lab resources that includes a positioning system and anechoic chamber for collecting field pattern, for verification of beam switching and determining antenna gain. [43]

## **1.7: Thesis Organization**

The design and evaluation of 4x4 SIW BM and the 2-D beam switching 2x2 planar array is presented in this dissertation as follows. Chapter 2 begins by presenting the case for modifications to the conventional Butler Matrix as the needs for a 2-D beam switching application are not met with the phased outputs meant for 1-D array beam steering. Then, the necessary BM phase block

modifications are described through analysis of the Butler Matrix output and the array factor function for steering an ideal isotropic 2x2 planar array in both azimuth ( $\phi$ ) and elevation ( $\theta$ ) angles. A new architecture for the Butler Matrix is proposed to provide design flexibility depending on how much phase shift is required for a 2-D beam switching application. The chapter concludes with a study of the possible 2-D beam angles and the required phase shifts for a given array geometry.

Chapter 3 addresses the implementation of the Butler Matrix design with a step-by-step analysis of the individual components, which include a hybrid coupler, a crossover circuit, and phase shifters. Since this beamforming network is implemented in SIW, the chapter starts with presenting details of the base SIW interconnect design parameters. Designs for the hybrid coupler and crossover circuits are then presented with simulated results. Due to the critical nature of the phase shifter with respect to meeting the 2-D target application, a prototype of a minimal length phase shifter design first presented by [43], is fabricated and assessed to determine feasibility. Finally, all components are integrated, and simulation results of the full Butler Matrix are presented.

The antenna array is described piece-by-piece in Chapter 4, beginning with a single microstrip patch antenna with a coupled aperture feed. This single element is then extended to a 2x2 planar configuration and the simulated output phases of the Butler Matrix from Chapter 3 are applied to confirm 2-D beam switching capabilities when patch antennas are used. Since this Butler Matrix is adapted to steer the planar array, details are presented to transition from the conventionally 1-D feeds of the Butler Matrix to the 2x2 arrangement of patch antenna elements. Finally, simulation results of the fully-integrated antenna array and Butler Matrix are presented.

Two prototypes were fabricated and assessed for the Butler Matrix design in Chapter 5, differing in their chosen substrate materials and, consequently, their architectures. The performance of the

Butler Matrix in generating appropriate phased outputs is critical to the 2-D beam steering application, so a de-embedding technique to remove the parasitic effects of the input and output interconnect sections (including SIWs, transitions and connectors) is important for analysis of measurement results. A through-only technique is adopted in this work because of its robustness at higher frequencies [44] and SIW de-embedding pass-through sections are prototyped.

After characterization of the modified Butler Matrix feed network, the entire beam switching antenna array prototype is evaluated in Chapter 6. Since the free space wavelength at  $f=60$  GHz is  $\lambda_0=5$  mm and the array's physical aperture area is also small (with a maximum linear dimension of  $D=4.75$  mm), it is feasible to create a bench-top set-up for far field radiation pattern measurement. Fabrication details of an anechoic chamber and antenna positioning system for antenna pattern and gain measurement and verification of beam switching at a minimal cost is discussed in Chapter 6.

This dissertation concludes with a summary in Chapter 7. Additional directions for future efforts are suggested as well as potential improvements to the presented work. An Appendix is included at the end that details the de-embedding procedure used during analysis of measurement results of fabricated prototypes.

---

## Chapter 2: Theory

This chapter presents the theory of operation of the Butler Matrix and quantifies how its phased outputs impact the antenna array factor. First, the standard usage of the BM to generate 1-D beam switching from a linear antenna array is discussed. Next, these standard BM outputs are applied in theory to a planar antenna array. This is followed by elaboration on the changes required to generate the desired 2-D beam switching from the conventional BM. It is shown that a special need arises for a modified BM architecture. Finally, limitations of the BM for 2-D beam switching are analyzed.

Since the focus of application is a planar array of MSPA elements, with directional broadside field patterns pointed in +z-direction (upper half space of the xy-plane), the discussion is only concerned with the +z-direction hemisphere of the spherical coordinate system. That is, referring to the illustration of the spherical coordinate axes in Fig. 2-1, elevation angles  $\theta$  measured down from the z-axis such that  $0^\circ \leq \theta \leq 90^\circ$  and azimuth angles  $\phi$  measured in the xy-plane beginning at the x-axis taking in all angles  $0^\circ \leq \phi \leq 360^\circ$ . When visualizing beam patterns, where a 1-D view is preferable for viewing the  $\theta$  at which peak beam magnitudes occur at a constant value of  $\phi$ , from the range of  $-90^\circ \leq \theta \leq 90^\circ$  is considered.

This theoretical analysis is mostly focused on the goal of the final beam switching system, as stated in Chapter 1, to provide four switchable beam patterns that illuminate four distinct quadrants of a planar surface. In terms of elevation and azimuth angles, this means  $\theta_0=45^\circ$  while  $\phi_{0i}=45^\circ+k*90^\circ$ , where  $k=\{0,1,2,3\}$ .

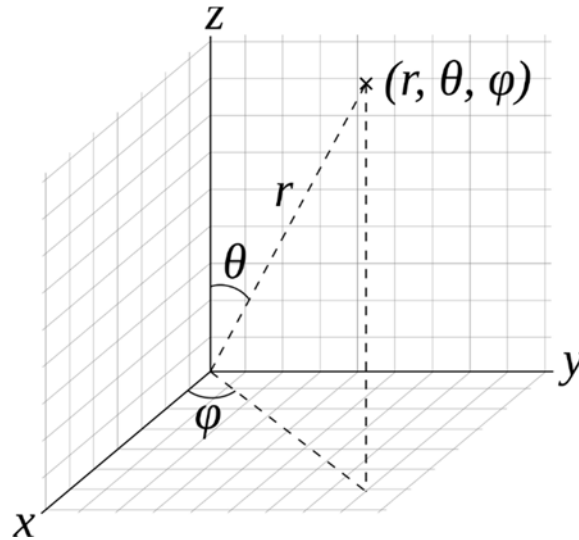


Fig. 2-1: Diagram of the spherical coordinate system with respect to the Cartesian coordinate system.

## 2.1: Butler Matrix Operation

Introduced in Section 1.2.2, the Butler Matrix [17] is a four-input, four-output (4x4) passive beamforming network, seen in Fig. 2-2, that uses hybrid couplers, crossover circuits, and phase shifters to generate four distinct beam patterns from a 4-element linear (1-D) antenna array, seen in Fig. 2-3. In creating beam agile system, the beamforming network creates the proper phase and weight for excitation of antenna array elements ensuring the peak magnitude (due to the constructive interference of the antenna elements) occurs at a desired direction in space (described by the azimuth and elevation angles of the beam) [15]. In beam switching, ideally all the other beams created in excitation of other ports have a null in their pattern (a.k.a orthogonal beams). In the case of the linear antenna array patterns, the beams are switched in just one direction, typically the elevation angle. Only focusing on the factor of the beamforming network, the beam pattern orthogonality can be assessed at the point of array excitation by comparing the phased output vectors of the BM.

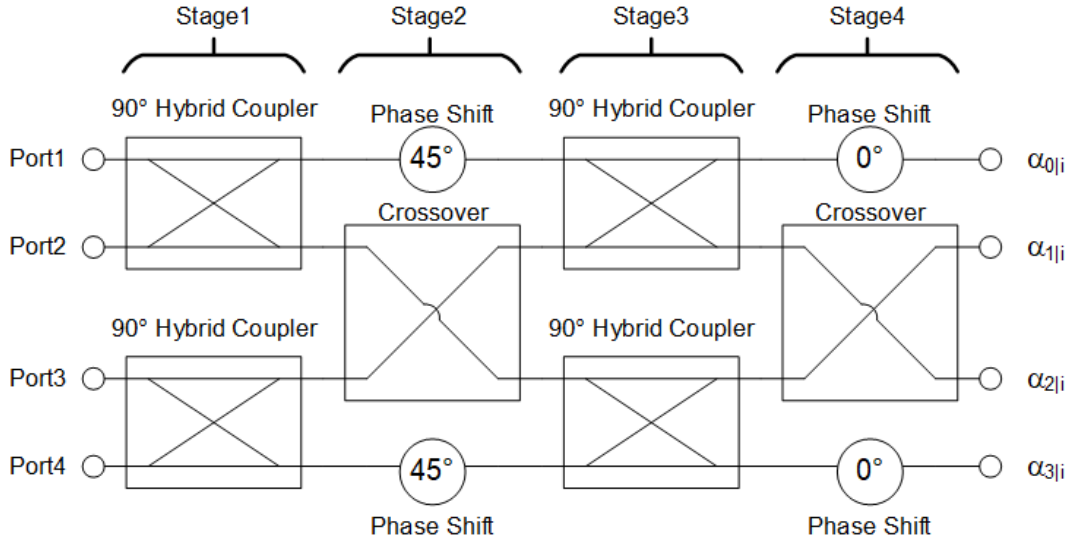


Fig. 2-2: Circuit diagram of the conventional Butler Matrix.

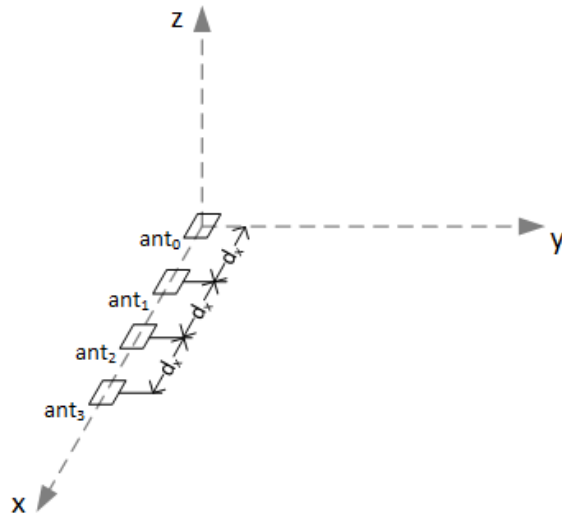


Fig. 2-3: Diagram of a typical equally-spaced linear array antenna.

From Fig. 2-2, the phased output matrix,  $B$ , consisting of each phased output  $e^{j\alpha_n|i}$  corresponding to antenna element  $n$  and input port  $i$ , can be found by inspection to be

$$B = \begin{bmatrix} e^{j\alpha_{0|1}} & e^{j\alpha_{0|2}} & e^{j\alpha_{0|3}} & e^{j\alpha_{0|4}} \\ e^{j\alpha_{1|1}} & e^{j\alpha_{1|2}} & e^{j\alpha_{1|3}} & e^{j\alpha_{1|4}} \\ e^{j\alpha_{2|1}} & e^{j\alpha_{2|2}} & e^{j\alpha_{2|3}} & e^{j\alpha_{2|4}} \\ e^{j\alpha_{3|1}} & e^{j\alpha_{3|2}} & e^{j\alpha_{3|3}} & e^{j\alpha_{3|4}} \end{bmatrix} = \frac{1}{2} \begin{bmatrix} e^{-j\frac{\pi}{4}} & e^{-j\frac{3\pi}{4}} & e^{-j\frac{\pi}{2}} & e^{-j\pi} \\ e^{-j\frac{\pi}{2}} & e^{-j0} & e^{-j\frac{5\pi}{4}} & e^{-j\frac{3\pi}{4}} \\ e^{-j\frac{3\pi}{4}} & e^{-j\frac{5\pi}{4}} & e^{-j0} & e^{-j\frac{\pi}{2}} \\ e^{-j\pi} & e^{-j\frac{\pi}{2}} & e^{-j\frac{3\pi}{4}} & e^{-j\frac{\pi}{4}} \end{bmatrix} \quad (2.1),$$

where phases have been converted to radians. A quick test of the orthogonality of the outputs of the Butler Matrix can be performed by checking whether B is unitary [45], in which the complex transpose  $B^*$  is also the inverse  $B^{-1}$ , or  $BB^*=I$

$$BB^* = \frac{1}{4} \begin{bmatrix} e^{-j\frac{\pi}{4}} & e^{-j\frac{3\pi}{4}} & e^{-j\frac{\pi}{2}} & e^{-j\pi} \\ e^{-j\frac{\pi}{2}} & e^{-j0} & e^{-j\frac{5\pi}{4}} & e^{-j\frac{3\pi}{4}} \\ e^{-j\frac{3\pi}{4}} & e^{-j\frac{5\pi}{4}} & e^{-j0} & e^{-j\frac{\pi}{2}} \\ e^{-j\pi} & e^{-j\frac{\pi}{2}} & e^{-j\frac{3\pi}{4}} & e^{-j\frac{\pi}{4}} \end{bmatrix} \begin{bmatrix} e^{j\frac{\pi}{4}} & e^{j\frac{\pi}{2}} & e^{j\frac{3\pi}{4}} & e^{j\pi} \\ e^{j\frac{3\pi}{4}} & e^{j0} & e^{j\frac{5\pi}{4}} & e^{j\frac{\pi}{2}} \\ e^{j\frac{\pi}{2}} & e^{j\frac{5\pi}{4}} & e^{j0} & e^{j\frac{3\pi}{4}} \\ e^{j\pi} & e^{j\frac{3\pi}{4}} & e^{j\frac{\pi}{2}} & e^{j\frac{\pi}{4}} \end{bmatrix} = \begin{bmatrix} 1 & 0 & 0 & 0 \\ 0 & 1 & 0 & 0 \\ 0 & 0 & 1 & 0 \\ 0 & 0 & 0 & 1 \end{bmatrix}, \quad (2.2)$$

where I is the identity matrix.

For a given input vector,  $\vec{x}$ , that acts as the port selector, the output phase vector,  $\vec{a}$ , from the Butler Matrix is

$$\vec{a} = B\vec{x}. \quad (2.3)$$

For example, if Port 1 is selected, the input vector becomes

$$\vec{x} = \begin{bmatrix} 1 \\ 0 \\ 0 \\ 0 \end{bmatrix}, \quad (2.4)$$

and the output vector is

$$\vec{a} = \frac{1}{2} \begin{bmatrix} e^{-j\frac{\pi}{4}} \\ e^{-j\frac{\pi}{2}} \\ e^{-j\frac{3\pi}{4}} \\ e^{-j\pi} \end{bmatrix} = \begin{bmatrix} e^{j\alpha_{0|1}} \\ e^{j\alpha_{1|1}} \\ e^{j\alpha_{2|1}} \\ e^{j\alpha_{3|1}} \end{bmatrix}. \quad (2.5)$$

This phased output vector, in turn, becomes the input vector to the array. The array factor for a linear array on the x-axis is well-known [14]:

$$A_i(\theta) = \sum_{n=0}^{N-1} e^{j\beta x_n \sin \theta} e^{j\alpha_{n|i}}, \quad (2.6)$$

where  $\beta=2\pi/\lambda_0$  is the free space phase constant at 60 GHz and  $x_n$  are the x coordinates of the array elements. The  $e^{j\beta x_n \sin \theta}$  component of Eqn (2.6) represents the propagation delay pertaining to each element, and the appearance of the  $e^{j\alpha_{n|i}}$  BM output excitations illustrate their direct impact

on the array factor. For the equally-spaced linear array seen in Fig. 2-3, a uniform axial spacing of  $d_x=\lambda_0/2$  between elements exists with element locations given as  $x_n=n \cdot d$ . The element  $\alpha_{0i}$  is therefore considered to be centered at the origin of the array axis and serves as the reference for the array.

Simplifying Eqn (2.6) for the assumed 4-element linear array geometry, the array factor becomes

$$A_i(\theta) = e^{j\alpha_{0i}} + e^{j(\alpha_{1i}+\pi \sin \theta)} + e^{j(\alpha_{2i}+2\pi \sin \theta)} + e^{j(\alpha_{3i}+3\pi \sin \theta)}. \quad (2.7)$$

Applying Port 1's output vector of Eqn (2.5) to Eqn (2.7) yields

$$A_1(\theta) = \frac{1}{2} \left[ e^{-j\frac{\pi}{4}} + e^{j(\pi \sin \theta - \frac{\pi}{2})} + e^{j(2\pi \sin \theta - \frac{3\pi}{4})} + e^{j(3\pi \sin \theta - \pi)} \right]. \quad (2.8)$$

Fig. 2-4 features a plot of the array factor when Port 1 is excited along with the array factors for the excitation of each of the remaining ports of the BM. The concept of beam orthogonality can be seen clearly here: peaks with magnitudes ( $|A_i(\theta_{0i})|^2=4$ ) occur at beam directions  $\theta_{0i}$  where all the other beams experience nulls. A search of  $\theta$  values for the peak magnitude of each  $A_i(\theta)$  returns beam directions of  $\theta_{01}=14.5^\circ$ ,  $\theta_{02}=-48.6^\circ$ ,  $\theta_{03}=48.6^\circ$ , and  $\theta_{04}=-14.5^\circ$ , which can be confirmed in Fig. 2-4.

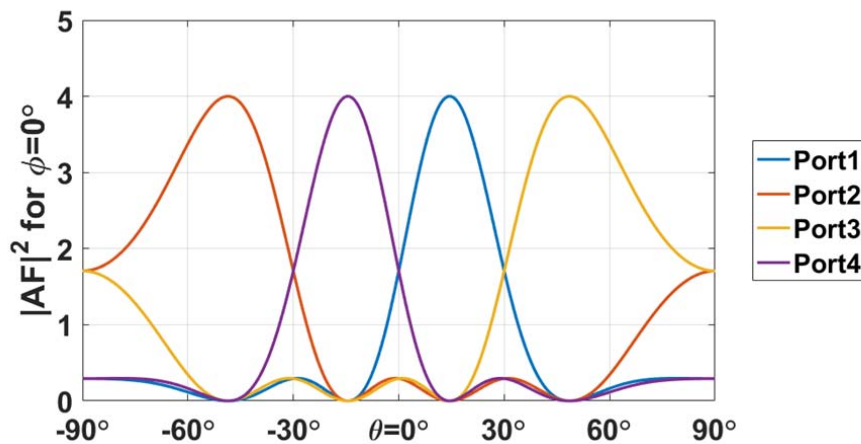


Fig. 2-4: Array factor gain,  $\phi=0^\circ$ , for an equally-spaced linear array fed by a conventional Butler Matrix.

Analytically, the  $A_i(\theta)$  from Eqn (2.6) can be put in matrix form with the BM's phased outputs from Eqn (2.1) as

$$A(\theta) = \frac{1}{2} \begin{bmatrix} e^{-j\frac{\pi}{4}} & e^{-j\frac{3\pi}{4}} & e^{-j\frac{\pi}{2}} & e^{-j\pi} \\ e^{j(\pi \sin(\theta_1) - \frac{\pi}{2})} & e^{j(\pi \sin(\theta_2))} & e^{j(\pi \sin(\theta_3) - \frac{5\pi}{4})} & e^{j(\pi \sin(\theta_4) - \frac{3\pi}{4})} \\ e^{j(2\pi \sin(\theta_1) - \frac{3\pi}{4})} & e^{j(2\pi \sin(\theta_2) - \frac{5\pi}{4})} & e^{j(2\pi \sin(\theta_3))} & e^{j(2\pi \sin(\theta_4) - \frac{\pi}{2})} \\ e^{j(3\pi \sin(\theta_1) - \pi)} & e^{j(3\pi \sin(\theta_2) - \frac{\pi}{2})} & e^{j(3\pi \sin(\theta_3) - \frac{3\pi}{4})} & e^{j(3\pi \sin(\theta_4) - \frac{\pi}{4})} \end{bmatrix}. \quad (2.9)$$

Setting each  $\theta_i$  to the found beam directions  $\theta_{0|i}$  (and switching from radians to degrees), the array factor becomes

$$A(\theta_{0|i}) = \frac{1}{2} \begin{bmatrix} e^{-j45^\circ} & e^{-j135^\circ} & e^{-j90^\circ} & e^{-j180^\circ} \\ e^{-j45^\circ} & e^{-j135^\circ} & e^{-j90^\circ} & e^{-j180^\circ} \\ e^{-j45^\circ} & e^{-j135^\circ} & e^{-j90^\circ} & e^{-j180^\circ} \\ e^{-j45^\circ} & e^{-j135^\circ} & e^{-j90^\circ} & e^{-j180^\circ} \end{bmatrix}, \quad (2.10)$$

From Eqn (2.10), it is easily seen that the peak magnitudes are obtained when radiation from all the elements in the array are in-phase at the observation point.

It can be observed from Fig. 2-4 that at the peak location  $(\theta_{0|i}, \phi_{0|i})$  in each port excitation the array factor (indicating radiated power) of other ports is basically zero. This indicates a large signal to interference plus noise ratio (SINR) [46] when the array is receiving or creation of distinct radiation beams when each port is excited. For example, when Port 1 of the BM in the linear array is activated, the ratio of the resultant array factor to that of the array factors for Ports 2, 3, and 4, at the peak location  $(\theta_{0|1}=14.5^\circ)$  is  $> 50$  dB while large dips ( $< -50$  dB) are seen at the locations of the other patterns' peaks  $(\theta_{0|2}=-48.6^\circ, \theta_{0|3}=48.6^\circ, \text{ and } \theta_{0|4}=-14.5^\circ)$ . This desired behavior is also observed for Port 2, 3, and 4 excitations. Since noise is not part of the scope of this discussion, instead of SINR the term SIR (signal to interference ratio) is used from here on.

Fig. 2-5 illustrates how these beam directions illuminate the target planar surface. The circles in Fig. 2-5 represent beam peak location goals for illuminating the x-axis normal to the antenna array while the star markers plot the actual beam locations for Port 1-4 excitations. For the development

of a 2-D passive beamformer, it is important to next assess how well the standard Butler Matrix output vectors can steer a planar antenna array.

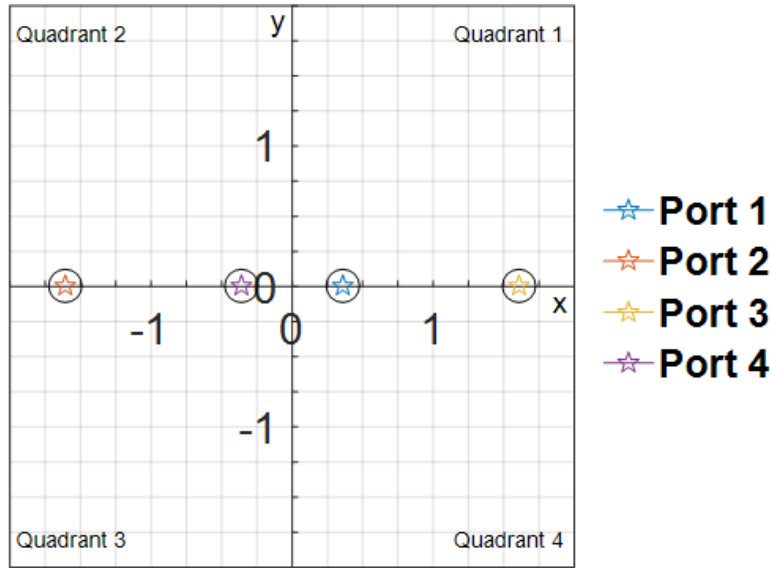


Fig. 2-5: Visualization of the peak locations for the linear array driven by the standard Butler Matrix.

## 2.2: Applying to 2-D Beam Steering

The first test to determine if the Butler Matrix is capable of 2-D beam steering is to apply the standard Butler Matrix outputs from Eqn (2.1) as the steering vector to a planar array, seen in Fig. 2-6, and analyze the resulting beam patterns. The array factor for a planar array is also well-known [14]:

$$A_i(\theta, \phi) = \sum_{n=0}^{N-1} \sum_{m=0}^{M-1} e^{j\beta(x_{mn} \sin \theta \cos \phi + y_{mn} \sin \theta \sin \phi)} e^{j\alpha_{mn}|i} \quad (2.11),$$

where subscripts m and n track antenna elements along the x- and y-axes, respectively. Equation (2.11) reduces down to the linear array factor of Eqn (2.6) when the elements are arranged along the x-axis ( $y_{mn}=0, \phi=0^\circ$ ).

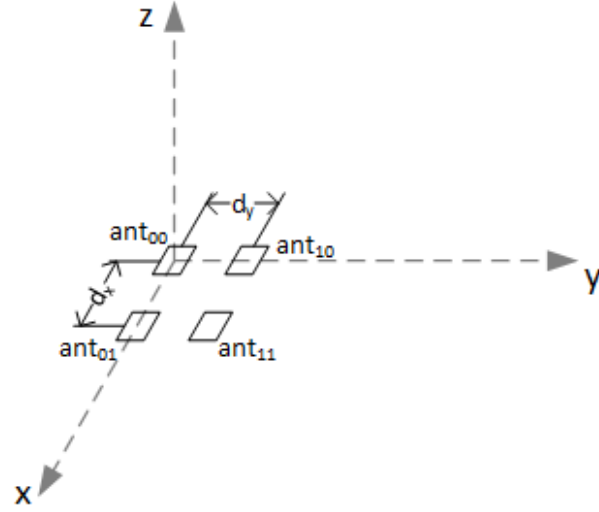


Fig. 2-6: Diagram of a typical rectangular array antenna.

For the 2-D beam scanning application, the planar array seen in Fig. 2-6 is assumed with a uniform axial spacing of  $d=\lambda_0/2$  between elements. Element locations are given as  $x_{mn}=m \cdot d$  and  $y_{mn}=n \cdot d$  for  $m,n=\{0,1\}$ . The element (0,0) is therefore considered to be centered at the origin of the array plane and serves as the reference for the square array.

The elements of the planar array are indexed counter-clockwise in the xy-plane from the reference so that the Butler Matrix outputs, intended for linear array elements  $\{\text{ant}_0, \text{ant}_1, \text{ant}_2, \text{ant}_3\}$ , map respectively to  $\{\text{ant}_{00}, \text{ant}_{10}, \text{ant}_{11}, \text{ant}_{01}\}$ . In terms of the output matrix,  $\{\alpha_{0|i} \rightarrow \alpha_{00|i}, \alpha_{1|i} \rightarrow \alpha_{10|i}, \alpha_{2|i} \rightarrow \alpha_{11|i}, \alpha_{3|i} \rightarrow \alpha_{01|i}\}$ .

Simplifying Eqn (2.11) for the assumed 4-element square array geometry, the array factor becomes

$$A_i(\theta, \phi) = e^{j\alpha_{00|i}} + e^{j(\alpha_{10|i} + \pi \sin \theta \cos \phi)} + e^{j(\alpha_{11|i} + \pi(\sin \theta \cos \phi + \sin \theta \sin \phi))} + e^{j(\alpha_{01|i} + \pi \sin \theta \sin \phi)}. \quad (2.12)$$

The planar array factor will achieve a maximum value at a specific beam direction  $(\phi_{0i}, \theta_{0i})$  when constructive interference of radiation from all antenna elements occurs. Applying the output vector of the standard BM in Port 1 excitation shown in Eqn (2.5) to Eqn (2.12) yields

$$A_1(\theta, \phi) = \frac{1}{2} \left[ e^{-j\frac{\pi}{4}} + e^{j\left(\pi \sin \theta \cos \phi - \frac{\pi}{2}\right)} + e^{j\left(\pi(\sin \theta \cos \phi + \sin \theta \sin \phi) - \frac{3\pi}{4}\right)} + e^{j(\pi \sin \theta \sin \phi - \pi)} \right]. \quad (2.13)$$

With beam angles now specified by two directions,  $\theta_{0i}$  and  $\phi_{0i}$ , it is helpful to view a “cut” of each beam pattern (plotted similarly to Fig. 2-4) but in a plane with one of the angles held constant, called a “cut-plane”. Typically, a cut-plane is chosen where a maximum in the other direction can be easily seen and compared. For instance, the Port 1 planar array factor of Eqn (2.13) is plotted alongside the array factors of the other port excitations in Fig. 2-7 for the cut-plane where the azimuth angle  $\phi_{0|1,4}=90^\circ$ . In this cut-plane, peak beam magnitudes,  $|A_i(\theta_{0i}, \phi_{0i})|^2=3.414$ , occur for Port 1 (blue line) and Port 4 (purple line) excitations at  $\theta_{0|1}=30^\circ$  and  $\theta_{0|4}=-30^\circ$ , respectively. These peak values fall short of the ideal cooperative maximum of 4 elements ( $|A(\theta_0, \phi_0)|^2=4$ ). Additionally, the Port 1 beam peaks at the null location of Ports 3 and 4, but not for Port 2, indicating orthogonality is not achieved for the standard BM excitations.

Fig. 2-8 plots the second cut-plane at  $\phi_{0|2,3}=26.46^\circ$  where peak magnitudes for Port 2 and 3 excitations can be seen for the planar array factor of Eqn (2.12). In this cut-plane, peak beam magnitudes,  $|A_i(\theta_{0i}, \phi_{0i})|^2=3.299$ , occur for Port 2 (orange line) and Port 3 (yellow line) excitations at  $\theta_{0|2}=-90^\circ$  and  $\theta_{0|3}=90^\circ$ , respectively, both of which are end-fire patterns. Again, full orthogonality is not being achieved as each port’s peak value coincides with low magnitudes in the other ports’ beam patterns, but not actual nulls.

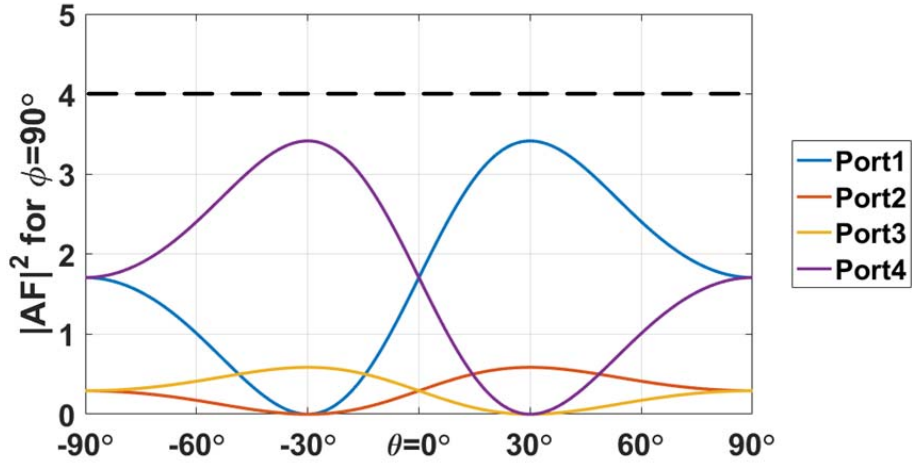


Fig. 2-7: Array factor gain,  $\phi=90^\circ$ , for a square planar array with conventional Butler Matrix outputs.

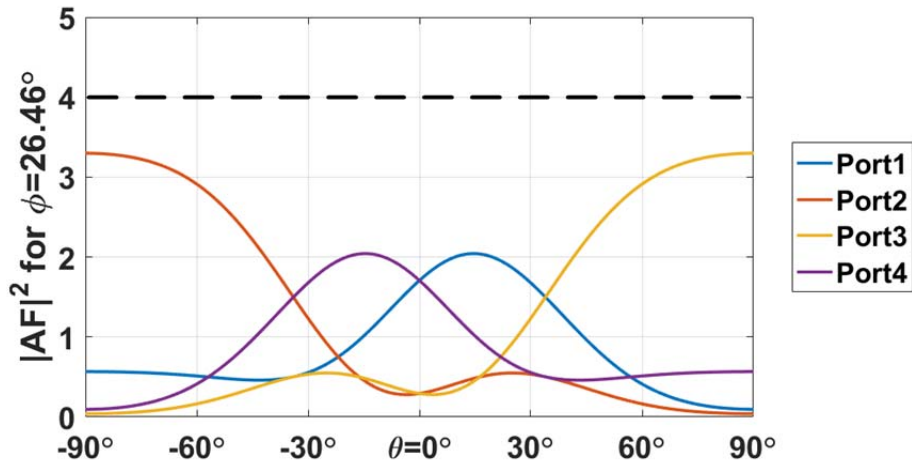


Fig. 2-8: Array factor gain,  $\phi=26.46^\circ$ , for a square planar array with conventional Butler Matrix outputs.

SIR for Port 1 excitation is computed to compare the beam patterns directly. In the  $\phi=90^\circ$  cut-plane, strong peaks ( $> 50$  dB) exist at  $\theta_{0|1}=30^\circ$ ,  $\phi_{0|1}=90^\circ$  when the power ratio is taken between Port 1 and Ports 3 and 4, but not for Port 2. In fact, SIR is flat at 7.66dB for all  $\theta$  when comparing Port 1 to Port 2 in the  $\phi=90^\circ$  cut-plane. In real world application terms, this means that for a radar system receiving with these beam patterns, i.e. reflections from an object located at  $\{\theta_{0|1}=30^\circ, \phi_{0|1}=90^\circ\}$ , it would be detected with the system engaged at Port 1, but not at Port 3 or 4.

Unfortunately, the object would also be sensed on Port 2, with only a 7.66dB power difference, indicating that Port 1 excitation is not strongly unique – even at its own peak beam direction. In fact, neither Port 2 nor Port 3 offer much beam fidelity ( $SIR > 20\text{dB}$ ) at their peak beam locations. SIR comparison for all ports of the standard BM with 1-D phase excitations applied to the planar array is summarize in Table 2-1 for each port’s peak beam direction.

*Table 2-1: PEAK BEAM DIRECTIONS AND SIR COMPARISONS FOR ALL PORT EXCITATIONS FROM STANDARD BUTLER MATRIX APPLIED TO PLANAR ARRAY.*

<b>SIR COMPARISONS</b>					
<b>PORT</b>	<b>PEAK BEAM</b>	<b>PORT 1</b>	<b>PORT 2</b>	<b>PORT 3</b>	<b>PORT 4</b>
<b>1</b>	$\theta_{01}=30^\circ, \phi_{01}=90^\circ$	0dB	7.66dB	64.6dB	56.9dB
<b>2</b>	$\theta_{02}=90^\circ, \phi_{02}=333.54^\circ$	7.65dB	0dB	19.2dB	15.4dB
<b>3</b>	$\theta_{03}=90^\circ, \phi_{03}=26.46^\circ$	15.4dB	19.2dB	0dB	7.65dB
<b>4</b>	$\theta_{04}=30^\circ, \phi_{04}=270^\circ$	56.9dB	64.6dB	7.66dB	0dB

Finally, Fig. 2-9 maps the peak beam locations for all ports in terms of the target application. It can be seen that only Port 1 and 4 excitations actually illuminate a surface in broadside along the y-axis, while Port 2 and 3 beams are pointed parallel to the target surface and cannot be seen in Fig. 2-9 since they are end-fire patterns from the array. The lack of orthogonality for the resultant 2-D beam patterns and inability to illuminate the 4 quadrants of the target surface indicates that the standard Butler Matrix phased outputs are meant for linear arrays and cannot be directly applied to the chosen planar array configuration. Modifications are necessary to achieve fully orthogonal 2-D beam patterns using a conventional BM architecture.

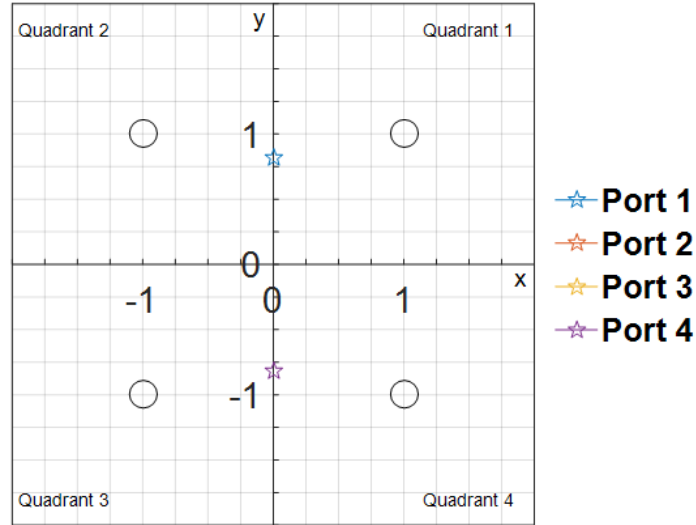


Fig. 2-9: Visualization of the peak locations for the planar array driven by the standard Butler Matrix.

### 2.3: Updating the Conventional Butler Matrix for feeding the Planar Array

Embarking to determine what changes are necessary to drive a planar array with the Butler Matrix, it is important to further analyze how the circuit generates its phased outputs. Referring to the diagram of the conventional Butler Matrix architecture given in Fig. 2-10, the phase shift values of Stages 2 and 4 have been replaced with variables  $\psi_1$  and  $\psi_2$ , respectively. Upon inspection, the outputs for the Butler Matrix become

$$\begin{aligned}
 B &= \begin{bmatrix} e^{j\alpha_{00|1}} & e^{j\alpha_{00|2}} & e^{j\alpha_{00|3}} & e^{j\alpha_{00|4}} \\ e^{j\alpha_{10|1}} & e^{j\alpha_{10|2}} & e^{j\alpha_{10|3}} & e^{j\alpha_{10|4}} \\ e^{j\alpha_{11|1}} & e^{j\alpha_{11|2}} & e^{j\alpha_{11|3}} & e^{j\alpha_{11|4}} \\ e^{j\alpha_{01|1}} & e^{j\alpha_{01|2}} & e^{j\alpha_{01|3}} & e^{j\alpha_{01|4}} \end{bmatrix} \\
 &= \frac{1}{2} \begin{bmatrix} e^{-j(\psi_1+\psi_2)} & e^{-j(\psi_1+\psi_2+\frac{\pi}{2})} & e^{-j(\psi_2+\frac{\pi}{2})} & e^{-j(\psi_2+\pi)} \\ e^{-j\frac{\pi}{2}} & e^{-j0} & e^{-j(\psi_1+\pi)} & e^{-j(\psi_1+\frac{\pi}{2})} \\ e^{-j(\psi_1+\frac{\pi}{2})} & e^{-j(\psi_1+\pi)} & e^{-j0} & e^{-j\frac{\pi}{2}} \\ e^{-j(\psi_2+\pi)} & e^{-j(\psi_2+\frac{\pi}{2})} & e^{-j(\psi_1+\psi_2+\frac{\pi}{2})} & e^{-j(\psi_1+\psi_2)} \end{bmatrix}, \quad (2.14)
 \end{aligned}$$

and the output vector when engaging Port 1 is

$$\vec{a} = \frac{1}{2} \begin{bmatrix} e^{-j(\psi_1+\psi_2)} \\ e^{-j\frac{\pi}{2}} \\ e^{-j(\psi_1+\frac{\pi}{2})} \\ e^{-j(\psi_2+\pi)} \end{bmatrix}. \quad (2.15)$$

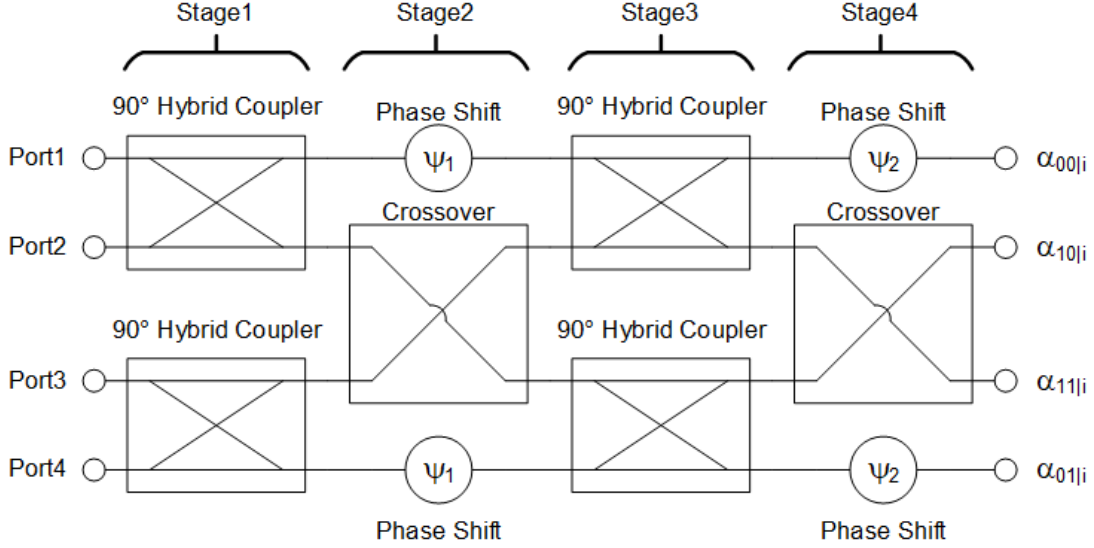


Fig. 2-10: Circuit diagram of the conventional Butler Matrix, with phase shifters left variable to adapt the phased outputs to the array geometry and target specifications.

When Eqn (2.15) is applied to Eqn (2.12), the 2x2 square planar array factor for Port 1 becomes

$$A_1(\theta, \phi) = \frac{1}{2} [e^{j(-\psi_1-\psi_2)} + e^{j(\pi \sin \theta \cos \phi - \frac{\pi}{2})} + e^{j(\pi \sin \theta (\cos \phi + \sin \phi) - \psi_1 - \frac{\pi}{2})} + e^{j(\pi \sin \theta \sin \phi - \psi_2 - \pi)}]. \quad (2.16)$$

As demonstrated earlier for the linear array driven by the standard Butler Matrix, maximal constructive interference of the array elements will occur at  $\{\theta_{01}, \phi_{01}\}$  when the phase components of all terms in Eqn (2.16) are aligned, or

$$\psi_1 + \psi_2 = \frac{\pi}{2} - \pi \sin \theta_{01} \cos \phi_{01}, \quad (2.17)$$

$$= \psi_1 + \frac{\pi}{2} - \pi \sin \theta_{01} (\cos \phi_{01} + \sin \phi_{01}), \quad (2.18)$$

$$= \psi_2 + \pi - \pi \sin \theta_{01} \sin \phi_{01}. \quad (2.19)$$

Rearranging Eqns (2.17) and (2.19), the relationships between BM output phases and beam direction are simplified:

$$\pi \sin \theta_{0|1} \cos \phi_{0|1} = \frac{\pi}{2} - \psi_1 - \psi_2, \quad (2.20)$$

$$\pi \sin \theta_{0|1} \sin \phi_{0|1} = \pi - \psi_1, \quad (2.21)$$

and when substituted back into Eqn (2.18) obtain

$$\psi_1 + \psi_2 = \psi_1 + \frac{\pi}{2} - \pi + \psi_1 - \frac{\pi}{2} + \psi_1 \xrightarrow{\text{yields}} 2\psi_1 = \pi. \quad (2.22)$$

Equation (2.22) indicates the phase shift line with  $\psi_1$  must have a  $|\pi/2|$  phase shift with respect to the outputs of the corresponding crossover in Stage 2 of the Butler Matrix. Applying each of the output vectors for Ports 2-4 from Eqn (2.14) to Eqn (2.12) results in:

$$\begin{aligned} \text{Port 2: } A_2(\theta, \phi) &= \frac{1}{2} [e^{j(-\psi_1 - \psi_2 - \frac{\pi}{2})} + e^{j(\pi \sin \theta \cos \phi)} \\ &+ e^{j(\pi(\sin \theta \cos \phi + \sin \theta \sin \phi) - \psi_1 - \pi)} + e^{j(\pi \sin \theta \sin \phi - \psi_2 - \frac{\pi}{2})}], \end{aligned} \quad (2.23)$$

$$\pi \sin \theta_{0|2} \cos \phi_{0|2} = -\frac{\pi}{2} - \psi_1 - \psi_2, \quad (2.24)$$

$$\pi \sin \theta_{0|2} \sin \phi_{0|2} = -\psi_1, \quad (2.25)$$

$$\psi_1 + \psi_2 + \frac{\pi}{2} = \psi_1 + \pi + \frac{\pi}{2} + \psi_1 + \psi_2 + \psi_1 \xrightarrow{\text{yields}} 2\psi_1 = -\pi, \quad (2.26)$$

$$\begin{aligned} \text{Port 3: } A_3(\theta, \phi) &= \frac{1}{2} [e^{j(-\psi_2 - \frac{\pi}{2})} + e^{j(\pi \sin \theta \cos \phi - \psi_1 - \pi)} \\ &+ e^{j(\pi(\sin \theta \cos \phi + \sin \theta \sin \phi))} + e^{j(\pi \sin \theta \sin \phi - \psi_1 - \psi_2 - \frac{\pi}{2})}], \end{aligned} \quad (2.27)$$

$$\pi \sin \theta_{0|3} \cos \phi_{0|3} = \frac{\pi}{2} + \psi_1 - \psi_2, \quad (2.28)$$

$$\pi \sin \theta_{0|3} \sin \phi_{0|3} = \psi_1, \quad (2.29)$$

$$\psi_2 + \frac{\pi}{2} = -\frac{\pi}{2} - \psi_1 + \psi_2 - \psi_1 \xrightarrow{\text{yields}} 2\psi_1 = -\pi, \quad (2.30)$$

$$\begin{aligned} \text{Port 4: } A_4(\theta, \phi) &= \frac{1}{2} [e^{j(-\psi_2 - \pi)} + e^{j(\pi \sin \theta \cos \phi - \psi_1 - \frac{\pi}{2})} \\ &+ e^{j(\pi(\sin \theta \cos \phi + \sin \theta \sin \phi) - \frac{\pi}{2})} + e^{j(\pi \sin \theta \sin \phi - \psi_1 - \psi_2)}], \end{aligned} \quad (2.31)$$

$$\pi \sin \theta_{0|4} \cos \phi_{0|4} = -\frac{\pi}{2} + \psi_1 - \psi_2, \quad (2.32)$$

$$\pi \sin \theta_{0|4} \sin \phi_{0|4} = \psi_1 - \pi , \quad (2.33)$$

$$\psi_2 + \pi = \frac{\pi}{2} + \frac{\pi}{2} - \psi_1 + \psi_2 - \psi_1 + \pi \xrightarrow{\text{yields}} 2\psi_1 = \pi , \quad (2.34)$$

which all confirm the same magnitude requirement for  $\psi_1$ . This condition for  $\psi_1$  holds no matter what the desired beam direction ( $\phi_{0|i}$ ,  $\theta_{0|i}$ ) is or which port is engaged: to apply this modified Butler Matrix to a square planar array,  $|\psi_1|$  must be  $\pi/2$ .

The relationships expressed in (2.22), (2.26), (2.30), and (2.34) are peculiar in that the required value of  $\psi_1$  changes sign: as if the phase shift must lag ( $+\pi/2$ ) for Ports 1 and 4, and lead ( $-\pi/2$ ) for Ports 2 and 3. The true requirement from these equations is that the added phase differential between elements  $\text{ant}_{00}$  and  $\text{ant}_{11}$  to be equal to  $\pm\pi$  for Port 1 and 2 excitations. Similarly, elements  $\text{ant}_{10}$  and  $\text{ant}_{01}$  must have a  $\pm\pi$  added phase differential for Port 3 and 4 excitations. This ambiguity in phase requirement means the choice of a leading or lagging phase shift is up to the designer, as long as  $|\psi_1|=\pi/2$ .

For the Butler Matrix architecture of Fig. 2-10, a more conventional lagging phase shift with respect to a pass-through path is chosen, so  $\psi_1=+\pi/2$ . It should be noted here that the value of the variable  $\psi_1$  is positive, though the actual phase shift is negative given the sign convention established in Eqn (2.14). This selection of  $\psi_1$  can then update the Port 1 excitation relationships, Eqns (2.20) and (2.21), for a Port 1 input:

$$\pi \sin \theta_{0|1} \cos \phi_{0|1} = -\psi_2 , \quad (2.35)$$

$$\pi \sin \theta_{0|1} \sin \phi_{0|1} = \frac{\pi}{2} . \quad (2.36)$$

With two equations and three unknowns ( $\phi_{0|1}$ ,  $\theta_{0|1}$ ,  $\psi_2$ ), the designer again must make a decision on an aspect of the beam steering system. For the application of illuminating 4 quadrants of a

planar surface facing broadside to the array,  $\theta_{0i}$  is chosen to be a constant  $45^\circ$  for all port inputs.

Equations (2.35) and (2.36) become

$$\cos \phi_{0|1} = -\psi_2 \frac{\sqrt{2}}{\pi}, \quad (2.37)$$

$$\sin \phi_{0|1} = \frac{\pi \sqrt{2}}{2 \pi} = \frac{1}{\sqrt{2}}. \quad (2.38)$$

Solving Eqn (2.38),  $\phi_{0|1}$  must be either  $45^\circ$  or  $135^\circ$ . Substituting these possibilities into Eqn (2.37) results in two familiar options for  $\psi_2$ : either  $+\pi/2$  or  $-\pi/2$ . Continuing the use of the conventional lagging phase shift of  $\psi_2=+\pi/2$ , the design settles on  $\phi_{0|1}=135^\circ$ . Solving equations (2.24), (2.25), (2.28), (2.29), (2.32), and (2.33) with the chosen  $\psi_2$  and  $\theta_{0i}$  yields  $\phi_{0|2}=315^\circ$ ,  $\phi_{0|3}=45^\circ$ , and  $\phi_{0|4}=225^\circ$ , which are all centered in adjacent quadrants of the application target.

The updated phased output matrix from the Butler Matrix becomes

$$B = \frac{1}{2} \begin{bmatrix} e^{-j\pi} & e^{-j\frac{3\pi}{2}} & e^{-j\pi} & e^{-j\frac{3\pi}{2}} \\ e^{-j\frac{\pi}{2}} & e^{-j0} & e^{-j\frac{3\pi}{2}} & e^{-j\pi} \\ e^{-j\pi} & e^{-j\frac{3\pi}{2}} & e^{-j0} & e^{-j\frac{\pi}{2}} \\ e^{-j\frac{3\pi}{2}} & e^{-j\pi} & e^{-j\frac{3\pi}{2}} & e^{-j\pi} \end{bmatrix}, \quad (2.39)$$

which can be confirmed for orthogonality

$$\begin{aligned} BB^* &= \frac{1}{4} \begin{bmatrix} e^{-j\pi} & e^{-j\frac{3\pi}{2}} & e^{-j\pi} & e^{-j\frac{3\pi}{2}} \\ e^{-j\frac{\pi}{2}} & e^{-j0} & e^{-j\frac{3\pi}{2}} & e^{-j\pi} \\ e^{-j\pi} & e^{-j\frac{3\pi}{2}} & e^{-j0} & e^{-j\frac{\pi}{2}} \\ e^{-j\frac{3\pi}{2}} & e^{-j\pi} & e^{-j\frac{3\pi}{2}} & e^{-j\pi} \end{bmatrix} \begin{bmatrix} e^{j\pi} & e^{j\frac{\pi}{2}} & e^{j\pi} & e^{j\frac{3\pi}{2}} \\ e^{j\frac{3\pi}{2}} & e^{j0} & e^{j\frac{3\pi}{2}} & e^{j\pi} \\ e^{j\pi} & e^{j\frac{3\pi}{2}} & e^{j0} & e^{j\frac{3\pi}{2}} \\ e^{j\frac{3\pi}{2}} & e^{j\pi} & e^{j\frac{\pi}{2}} & e^{j\pi} \end{bmatrix} \\ &= \begin{bmatrix} 1 & 0 & 0 & 0 \\ 0 & 1 & 0 & 0 \\ 0 & 0 & 1 & 0 \\ 0 & 0 & 0 & 1 \end{bmatrix}. \end{aligned} \quad (2.40)$$

Additionally, the Port 1 square planar array factor equation of (2.20) becomes

$$A_1(\theta, \phi) = \frac{1}{2} [e^{-j\pi} + e^{j(\pi \sin \theta \cos \phi - \frac{\pi}{2})}]$$

$$+e^{j(\pi(\sin \theta \cos \phi + \sin \theta \sin \phi) - \pi)} + e^{j(\pi \sin \theta \sin \phi - \frac{3\pi}{2})}]. \quad (2.41)$$

Array factor plots for all port excitations of the Butler Matrix from Eqn (2.39) applied to Eqn (2.12) are shown in Fig. 2-11 and Fig. 2-12 at two different  $\phi$ -cut-planes,  $\phi_{0|1,2}=135^\circ$  and  $\phi_{0|3,4}=45^\circ$ , respectively. From these two graphs, it can be seen that each port's peak value,  $|A_i(\theta_{0|i}, \phi_{0|i})|^2=4.0$ , coincides with a null in all three other ports' beam patterns. This orthogonality condition illustrates that the updated phase shifts ( $\psi_1=\psi_2=\pi/2$ ) applied to the conventional Butler Matrix architecture successfully steers the chosen 2x2 square planar array configuration and achieves the targeted 2-D beam patterns of the application.

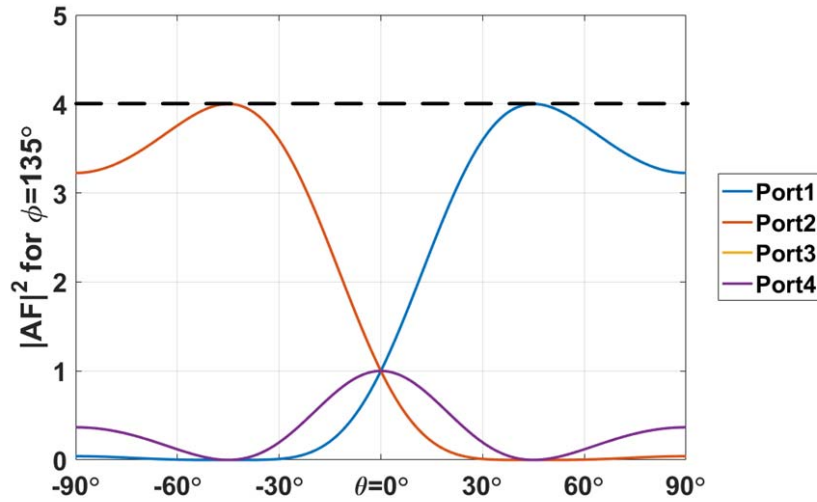


Fig. 2-11: Array factor gain,  $\phi=135^\circ$ , for a square planar array with updated phase shifters in the conventional Butler Matrix architecture.

Additionally, a check of SIR for Port 1 to the other ports in the  $\phi=135^\circ$  cut-plane finds a strong peak (162 dB) at  $\theta_{0|1}=45^\circ$ ,  $\phi_{0|1}=135^\circ$  and large valleys (-162 dB) at  $\theta_{0|1}=-45^\circ$ . Comparing Port 3 excitation in the  $\phi=45^\circ$  cut-plane to other ports shows similar attributes, with large SIR (162 dB) at  $\theta=45^\circ$  and deep valleys (-162 dB) at  $\theta=-45^\circ$ .

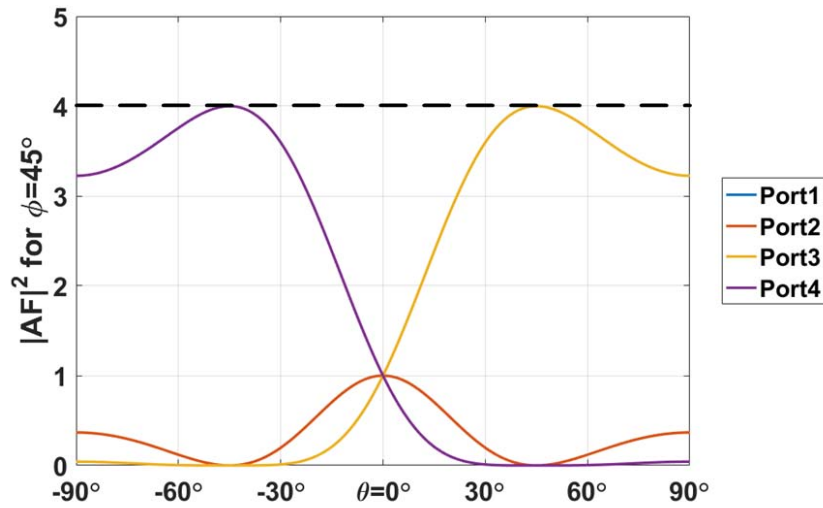


Fig. 2-12: Array factor gain,  $\phi=45^\circ$ , for a square planar array with updated phase shifters in the conventional Butler Matrix architecture.

Table 2-2 summarizes the peak beam locations and SIR comparison for this updated conventional Butler Matrix architecture and shows that each beam pattern is unique.

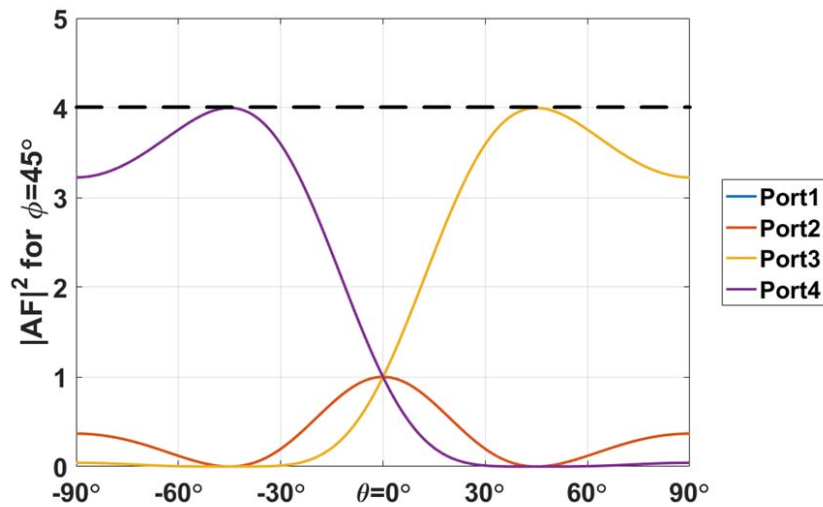


Fig. 2-12: Array factor gain,  $\phi=45^\circ$ , for a square planar array with updated phase shifters in the conventional Butler Matrix architecture.

Table 2-2: PEAK BEAM DIRECTIONS AND SIR COMPARISONS FOR ALL PORT EXCITATIONS FROM UPDATED CONVENTIONAL BUTLER MATRIX APPLIED TO PLANAR ARRAY.

---



---

**SIR COMPARISONS**

---

PORT	PEAK BEAM	PORT 1	PORT 2	PORT 3	PORT 4
1	$\theta_{01}=45^\circ, \phi_{01}=135^\circ$	0dB	162dB	162dB	162dB
2	$\theta_{02}=45^\circ, \phi_{02}=315^\circ$	162dB	0dB	162dB	162dB
3	$\theta_{03}=45^\circ, \phi_{03}=45^\circ$	162dB	162dB	0dB	162dB
4	$\theta_{04}=45^\circ, \phi_{04}=225^\circ$	162dB	162dB	162dB	0dB

Finally, the peak beam locations for all ports can be checked in terms of the target application. Fig. 2-13 plots the beam pointing directions on the grid representing the planar target surface. Each beam precisely matches its corresponding goal location, confirming the updated phase shifts for the conventional Butler Matrix architecture extend the beam switching capabilities from 1-D to 2-D beam control.

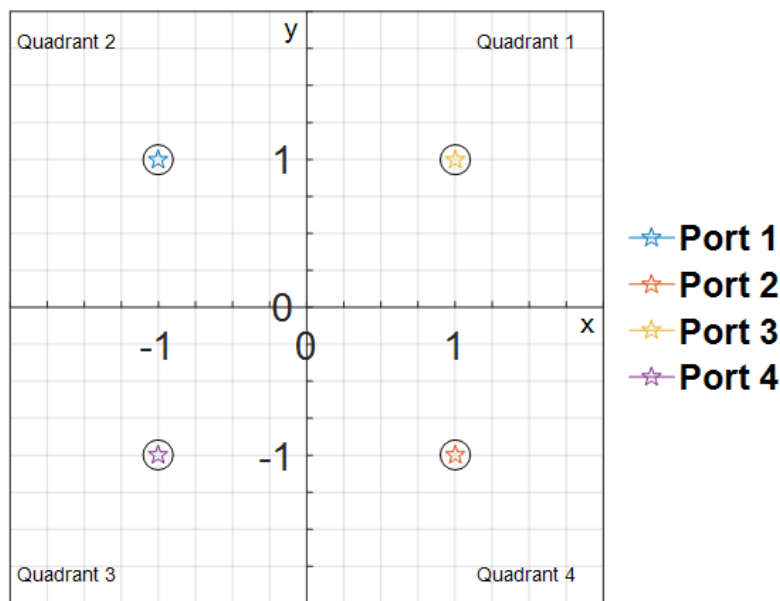


Fig. 2-13: Visualization of the peak locations for the 2x2 square planar array driven by the updated Butler Matrix.

### 2.3.1: Implementation Considerations for the Phase Shifter

Beyond theory, it is important to consider the other project goal: to provide passive 2-D beam switching capability for the mm-wave spectrum in a minimal footprint desired in a fully integrated

system. A significant design consideration has become apparent in this chapter's analytical presentation. Returning to the Butler Matrix architecture of Fig. 2-10, the phase shift values,  $\psi_1$  and  $\psi_2$ , represent the differential phase between the output of the crossover circuits and the output of the outer SIW interconnects prior to Stages 2 and 4, respectively. So, the concept of "leading" or "lagging" phase shift can be interpreted by the designer in one of two ways. First, from the point of view of phase shifter, adding a phase delay to a signal causes it to "lag" an unimpeded signal, whereas removing phase delay at that location would cause it to "lead." Adding phase delay is a well-known and well-used technique and can be accomplished as simply as by extending the length of the interconnect media, i.e. a meander line. Other techniques for introducing phase delay, specifically focused on SIW technology, have been presented with excellent results [36], [43]. Creating phase leads is another design premise, where researchers have been exploring the use of metamaterials [47].

An alternative interpretation of a phase "lag" or "lead" could be with respect to the location of the phase shifter. If the phase differential is marked between the output of the crossover circuit and the outer SIW interconnect, then placing the phase shifter at the output of the crossover changes the impact of the phase shift. Additional phase delay at the crossover section of the stage would make the appearance of the phase of the outer SIW interconnect "lead." This may be preferable to the SIW circuit designer if a minimal footprint phase shifter is available. These considerations will be explored in more detail in Chapter 3.

For now, since using a conventional phase delay is typically easier for implementation, a rule of thumb is handy for deciding on whether a location change – which changes the architecture of the Butler Matrix – is necessary for the phase shifter. If the condition exists such that  $\psi_i$ , the phase differential between with SIW interconnect and the output of the crossover circuit, can either lead

or lag, then the choice of phase shifter location depends on how much inherent phase delay the crossover circuit has. If the crossover circuit has less phase delay than  $|\psi_i|$ , then the phase shifter should follow the crossover, and a modified Butler Matrix architecture is needed. If not, the phase shifter should be located in the SIW pass-through in parallel with the crossover in Stages 2 and 4, as it is in the conventional Butler Matrix architecture.

For example, given the presented  $|\psi_i|=\pi/2$  necessary for the target application, if the crossover circuit causes a smaller  $\pi/4$  phase delay with respect to a straight SIW of the same length, a  $\pi/4$  phase shifter could be place serially to yield the total  $\pi/2$  phase differential. In this case,  $\psi_i$  would “lead”: the outputs of the crossover circuit would be  $\pi/2$  radians behind the outputs of the SIW interconnects. It is prudent to confirm that this change in architecture is still operationally sufficient, which is addressed in Section 2.4.:

## 2.4: Proposed Modified Butler Matrix Architecture

If the phase shifter is to be relocated to the outputs of the crossover circuit, a new Butler Matrix architecture becomes apparent (as seen in Fig. 2-14) and its beamforming capabilities must be confirmed. Applying the calculated phase shifts,  $\psi_1=\psi_2=+\pi/2$ , from Section 2.3.; this Modified Butler Matrix has a new phased output matrix

$$B = \begin{bmatrix} e^{j\alpha_{00|1}} & e^{j\alpha_{00|2}} & e^{j\alpha_{00|3}} & e^{j\alpha_{00|4}} \\ e^{j\alpha_{10|1}} & e^{j\alpha_{10|2}} & e^{j\alpha_{10|3}} & e^{j\alpha_{10|4}} \\ e^{j\alpha_{11|1}} & e^{j\alpha_{11|2}} & e^{j\alpha_{11|3}} & e^{j\alpha_{11|4}} \\ e^{j\alpha_{01|1}} & e^{j\alpha_{01|2}} & e^{j\alpha_{01|3}} & e^{j\alpha_{01|4}} \end{bmatrix} = \frac{1}{2} \begin{bmatrix} e^{-j0} & e^{-j\frac{\pi}{2}} & e^{-j\pi} & e^{-j\frac{3\pi}{2}} \\ e^{-j\frac{3\pi}{2}} & e^{-j\pi} & e^{-j\frac{3\pi}{2}} & e^{-j\pi} \\ e^{-j\pi} & e^{-j\frac{3\pi}{2}} & e^{-j\pi} & e^{-j\frac{3\pi}{2}} \\ e^{-j\frac{3\pi}{2}} & e^{-j\pi} & e^{-j\frac{\pi}{2}} & e^{-j0} \end{bmatrix}. \quad (2.42)$$

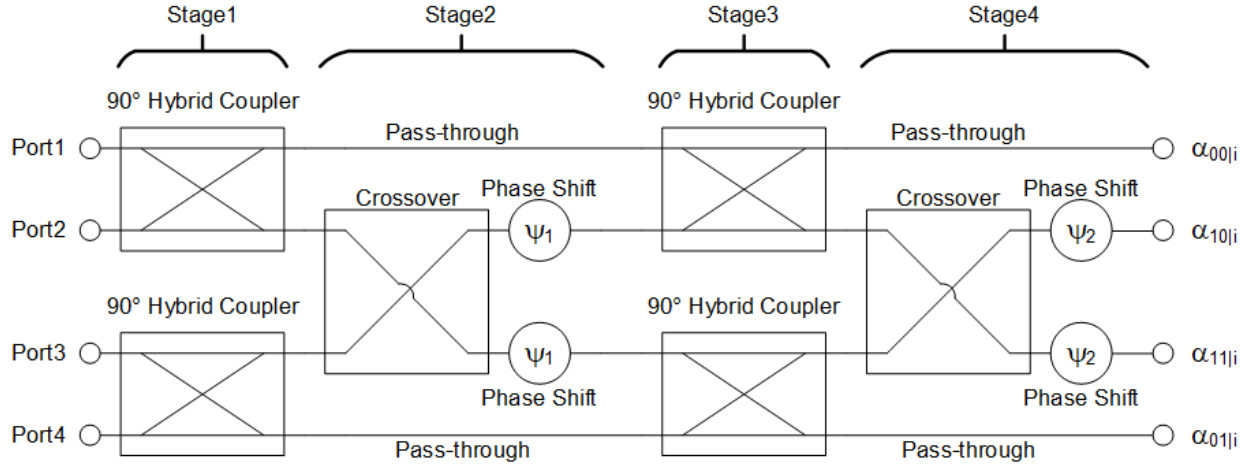


Fig. 2-14: Circuit diagram of the rearranged Butler Matrix, with phase shifters left variable to adapt the phased outputs to the array geometry and target specifications.

When Eqn (2.42) is applied to Eqn (2.12), the same array beam patterns arise with  $\theta_{0i}=45^\circ$ , only the targeted quadrants of the test application (azimuth angles) are circularly shifted. For example, an input applied to Port 1 results in a  $\phi_{01}=225^\circ$  steering direction, which was reported in Section 2.3: as the direction for a Port 4 input. Additionally, the new direction for Port 2 is  $\phi_{02}=45^\circ$ , for Port 3 is  $\phi_{03}=315^\circ$ , and for Port 4 is  $\phi_{04}=135^\circ$ , corresponding to Port 3, Port 2, and Port 1, respectively, as reported in Section 2.3. The Modified Butler Matrix architecture behaves exactly like the conventional architecture of Fig. 2-10, only Ports 1 and 4, and Ports 2 and 3, are swapped. The rearrangement of the array beam patterns is easily seen in Fig. 2-15 and Fig. 2-16 below, and confirms peak magnitudes of  $|A_i(\theta_{0i}, \phi_{0i})|^2=4.0$  and the orthogonality of the array patterns at each beam direction for the Modified Butler Matrix architecture.

A review of SIR for Port 1 excitation from the Modified Butler Matrix further indicates identical performance with the updated conventional BM for the planar array presented in the previous section. Fig. 2-17 illustrates the locations of beam illumination for all ports on the target planar surface are still falling precisely at the goal beam directions. Fig. 2-17 is also useful for visualizing the beam direction swaps between Ports 1 and 4, and Ports 2 and 3, when compared with the

corresponding plot for the updated conventional BM in Fig. 2-13. A summary of each Butler Matrix scenario covered in this chapter and the associated array factor beam peaks is presented in Table 2-3.

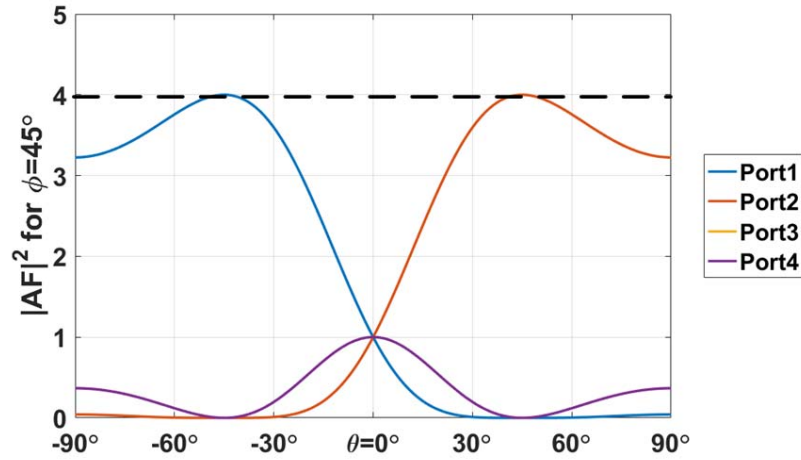


Fig. 2-15: Array factor gain,  $\phi=45^\circ$ , for a square planar array with updated phase shifters in the Modified Butler Matrix architecture.

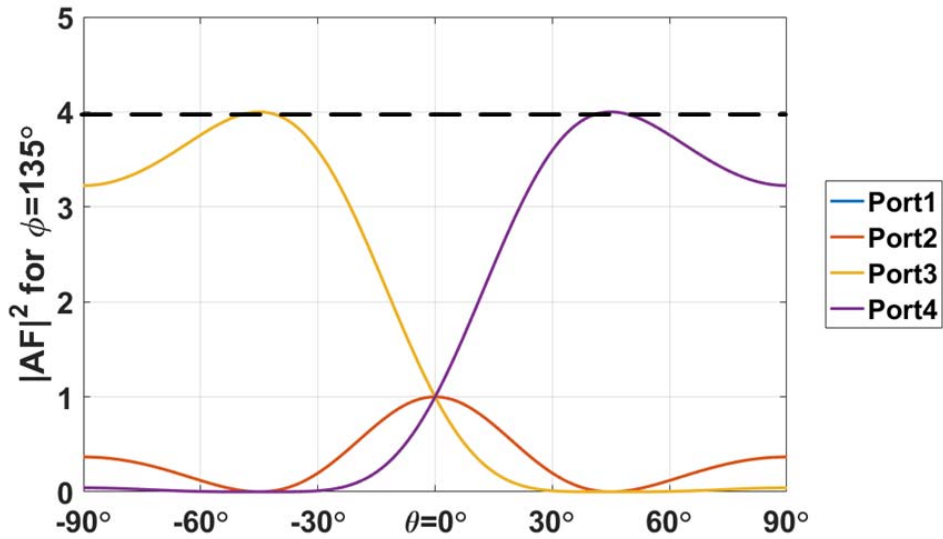


Fig. 2-16: Array factor gain,  $\phi=135^\circ$ , for a square planar array with updated phase shifters in the Modified Butler Matrix architecture.

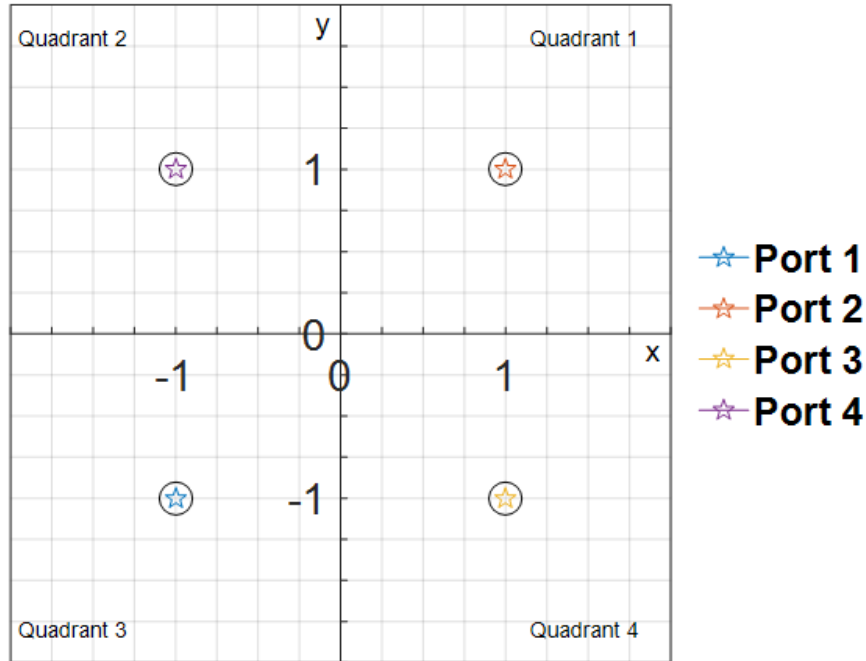


Fig. 2-17: Visualization of the peak locations for the 2x2 square planar array driven by the Modified Butler Matrix.

Table 2-3: COMPARISON OF BEAM STEERING DIRECTIONS FOR ALL REVIEWED BUTLER MATRIX SCENARIOS.

Port	Standard BM with linear array	Standard BM with planar array	Updated conventional BM with planar array	Modified BM with planar array
1	$\theta_{01}=14.5^\circ$	$\theta_{01}=30^\circ$ , $\phi_{01}=90^\circ$	$\theta_{01}=45^\circ$ , $\phi_{01}=135^\circ$	$\theta_{01}=45^\circ$ , $\phi_{01}=225^\circ$
2	$\theta_{02}=-48.6^\circ$	$\theta_{02}=90^\circ$ , $\phi_{02}=333.54^\circ$	$\theta_{02}=45^\circ$ , $\phi_{02}=315^\circ$	$\theta_{02}=45^\circ$ , $\phi_{02}=45^\circ$
3	$\theta_{03}=48.6^\circ$	$\theta_{03}=90^\circ$ , $\phi_{03}=26.46^\circ$	$\theta_{03}=45^\circ$ , $\phi_{03}=45^\circ$	$\theta_{03}=45^\circ$ , $\phi_{03}=315^\circ$
4	$\theta_{04}=-14.5^\circ$	$\theta_{04}=30^\circ$ , $\phi_{04}=270^\circ$	$\theta_{04}=45^\circ$ , $\phi_{04}=225^\circ$	$\theta_{04}=45^\circ$ , $\phi_{04}=135^\circ$

## 2.5: 2-D Beam-Steering Limitations

### 2.5.1: Updated conventional Butler Matrix architecture

Returning to the proposed phase shifter changes for the conventional Butler Matrix architecture discussed in Section 2.3, a choice is presented for the designer to solve a set of two equations, (2.35) and (2.36), with three unknowns. This scenario is ripe for exploration: quantifying the relationship between the three unknowns will allow the engineer pick one as a control variable to direct the other two parameters. In terms of the target applications needs,  $\theta_{0i}=45^\circ$  was fixed by the specification for all inputs and the  $\phi_{0i}$ 's and  $\psi_2$  were solved for. Here, for investigating the 2-D beam-steering capabilities of the 2x2 square planar array, a different approach begins with finding a range of acceptable values for the  $\theta_{0i}$ 's,  $\phi_{0i}$ 's, and  $\psi_2$  and the realistic bounds on restricting  $\theta_{0i}$ , such that  $0^\circ \leq \theta_{0i} \leq 90^\circ$ , since the array beam patterns fall off rapidly as the ground plane is encountered at the horizon ( $\theta=90^\circ$ ) for the planar of MSPA elements. Equation (2.16) is updated to reflect the array factor for a Port 1 excitation with a  $\psi_1=+\pi/2$  phase differential

$$A_1(\theta, \phi) = \frac{1}{2} [e^{j(-\psi_2 - \frac{\pi}{2})} + e^{j(\pi \sin \theta \cos \phi - \frac{\pi}{2})} + e^{j(\pi \sin \theta (\cos \phi + \sin \phi) - \pi)} + e^{j(\pi \sin \theta \sin \phi - \psi_2 - \pi)}]. \quad (2.43)$$

For this multivariate problem, multiple maxima can be found by quantifying the relationship between the unknowns. From Section 2.3, Eqn (2.36) can be rearranged to get a relationship between the elevation angle  $\theta_{01}$  and corresponding azimuth  $\phi_{01}$

$$\sin \phi_{01} = \frac{1}{2 \sin \theta_{01}} \text{ or } \phi_{01} = \sin^{-1} \frac{1}{2 \sin \theta_{01}}. \quad (2.44)$$

Observing the denominator of Eqn (2.44) leads to the first constraint:  $|\sin \theta_{01}|$  must be  $>0.5$  for the resulting  $\phi_{01}$  to be real, therefore

$$\frac{1}{2} \leq \sin \theta_{0|1} \leq 1 \xrightarrow{\text{yields}} \frac{\pi}{6} \leq \theta_{0|1} \leq \frac{\pi}{2} \quad (2.45)$$

and the possible values for azimuth  $\phi_{0|1}$  are

$$\frac{1}{2} \leq \sin \varphi_{0|1} \leq 1 \xrightarrow{\text{yields}} \frac{\pi}{6} \leq \varphi_{0|1} \leq \frac{5\pi}{6}. \quad (2.46)$$

Next, Eqn (2.35) is slightly rearranged to solve for the Stage 4 phase differential

$$\psi_2 = -\pi \sin \theta_{0|1} \cos \varphi_{0|1}, \quad (2.47)$$

as a function of  $\theta_{0|1}$  and  $\phi_{0|1}$ . Another constraint becomes apparent from Eqn (2.47): because the term  $\sin \theta_{0|1}$  will be positive and it is desired to have a lagging phase shift ( $\psi_2 \geq 0$ ),  $\cos \varphi_{0|1}$  must be  $\leq 0$  such that

$$-1 \leq \cos \varphi_{0|1} \leq 0 \xrightarrow{\text{yields}} \frac{\pi}{2} \leq \varphi_{0|1} \leq \frac{5\pi}{6} \quad (2.48)$$

Using the constraints of Eqns (2.45) and (2.48) in Eqn (2.47) finds a range for possible  $\psi_2$ :

$$0 \leq \psi_2 \leq \frac{\sqrt{3}}{2} \pi \text{ or } 0^\circ \leq \psi_2 \leq 155.88^\circ. \quad (2.49)$$

Fig. 2-18 features the possible values of  $\theta_{0|1}$ ,  $\phi_{0|1}$ , and  $\psi_2$  based on this analysis.

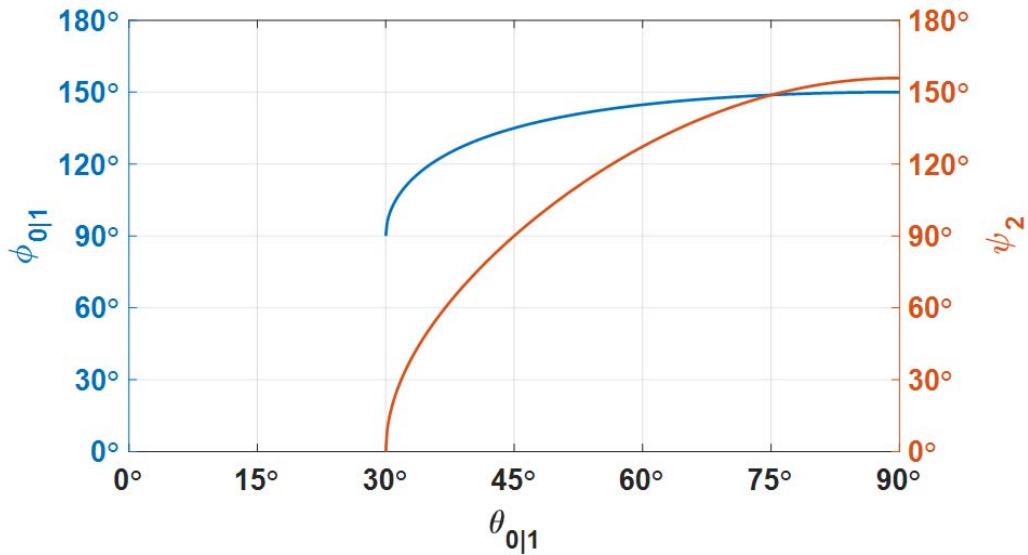


Fig. 2-18: Plot of possible  $\phi_{0|1}$  and  $\psi_2$  values versus  $\theta_{0|1}$  for Port 1 excitations to the planar array.

Repeating this procedure for Port 2 excitation helps narrow down the Stage 4 phase shift range. Recalling the relationship for  $\theta_{0|2}$ ,  $\phi_{0|2}$ , and  $\psi_2$  from Eqns (2.24) and (2.25), updating for the solved value of  $\psi_1$ , and rearranging yields

$$\sin \phi_{0|2} = \frac{-1}{2 \sin \theta_{0|2}} \text{ and} \quad (2.50)$$

$$\psi_2 = \pi - \pi \sin \theta_{0|2} \cos \phi_{0|2}. \quad (2.51)$$

In this case, the range of  $\theta_{0|2}$  is comparable to that for Port 1 excitation,  $\frac{\pi}{6} \leq \theta_{0|2} \leq \frac{\pi}{2}$ , but the possible values for azimuth  $\phi_{0|2}$  are located in the 4<sup>th</sup> quadrant of the unit circle,  $\frac{3\pi}{2} \leq \phi_{0|2} \leq \frac{11\pi}{6}$ .

Using these constraints in Eqn (2.51) finds a different range for possible  $\psi_2$ :

$$\frac{2-\sqrt{3}}{2}\pi \leq \psi_2 \leq \pi \text{ or } 24.12^\circ \leq \psi_2 \leq 180^\circ. \quad (2.52)$$

Combining the constrained ranges for  $\psi_2$  from Eqns (2.49) and (2.52) yields the final possible range

$$\frac{2-\sqrt{3}}{2}\pi \leq \psi_2 \leq \frac{\sqrt{3}}{2}\pi \text{ or } 24.12^\circ \leq \psi_2 \leq 155.88^\circ. \quad (2.53)$$

Continued analysis for Port 3 and 4 excitations does not further narrow the possible choices for  $\psi_2$ . Applying the  $\psi_2$  range of Eqn (2.53) to Eqns (2.47) and (2.51), as well as to the relationships for Port 3, Eqns (2.28) and (2.29), and Port 4, Eqns (2.32) and (2.33), updates the possible values for all  $\phi_{0|i}$ :  $105^\circ \leq \phi_{0|1} \leq 150^\circ$ ,  $285^\circ \leq \phi_{0|2} \leq 330^\circ$ ,  $30^\circ \leq \phi_{0|3} \leq 75^\circ$ , and  $210^\circ \leq \phi_{0|4} \leq 255^\circ$ , while  $\theta_{0|i}$  becomes  $31.14^\circ \leq \theta_{0|i} \leq 90^\circ$  for all conventional BM excitations.

The relationships between the presented design variables are captured in Fig. 2-19 where  $\theta_{0|i}$  and  $\phi_{0|i}$  are plotted as a function of  $\psi_2$ . These ranges are correlated to each other, meaning that a selection of a value for one variable “locks down” the values of the other variables. In the case of the target application beam directions, seen previously in Fig. 2-11 and Fig. 2-12, selecting

$\theta_{01}=45^\circ$  pinned  $\psi_2$  to  $90^\circ$ , forcing the other  $\theta_{0i}$ 's to  $45^\circ$  and the azimuth angles became  $\phi_{01}=135^\circ$ ,  $\phi_{02}=315^\circ$ ,  $\phi_{03}=45^\circ$ , and  $\phi_{04}=225^\circ$ . Fig. 2-20 illustrates the impact to beam location when varying the Stage 4 phase shift: arrows indicate how  $\theta_{0i}$  and  $\phi_{0i}$  change with increasing  $\psi_2$  within the range  $24.12^\circ \leq \psi_2 \leq 155.88^\circ$ .

### 2.5.2: Proposed Modified Butler Matrix architecture

The above ranges for the values of  $\theta_{0i}$ ,  $\phi_{0i}$ , and  $\psi_2$  are confirmed for the Modified Butler Matrix architecture as well, following the behavior swap for the ports as presented in Section 2.4. The range of possible  $\theta_{0i}$  values is identical,  $31.14^\circ \leq \theta_{0i} \leq 90^\circ$ , as is the range of effective  $\psi_2$  values,  $24.12^\circ \leq \psi_2 \leq 155.88^\circ$ .

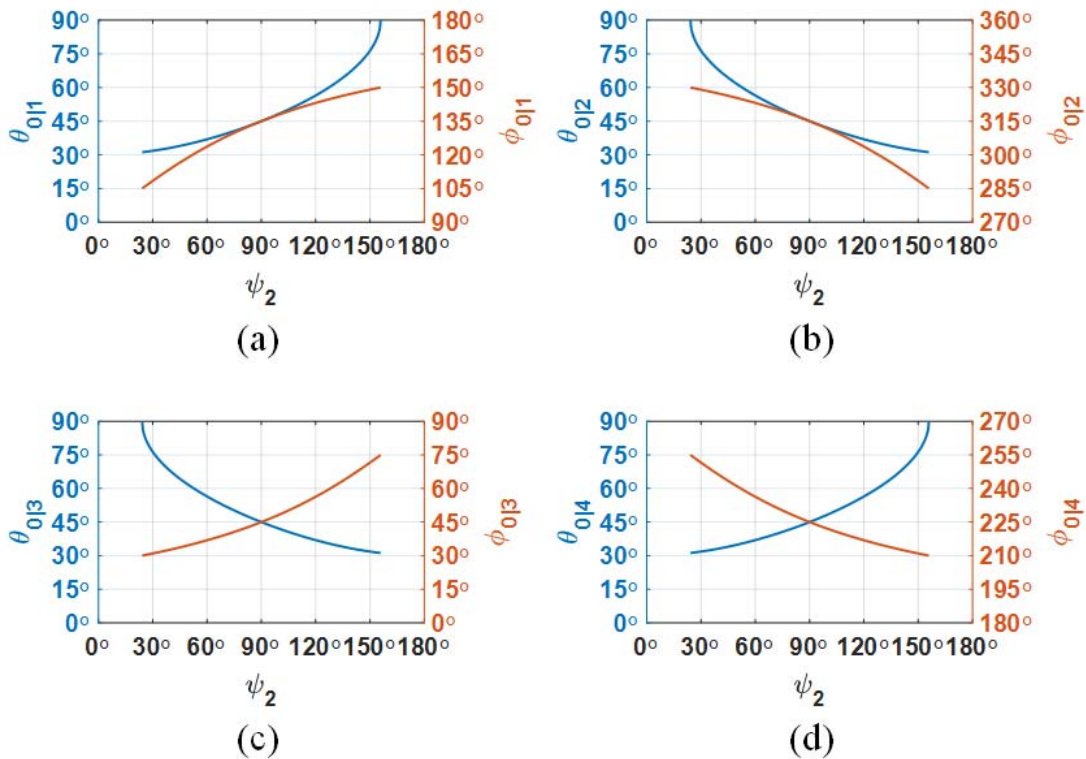


Fig. 2-19: Plots of  $\theta_{0i}$ ,  $\phi_{0i}$  versus  $\psi_2$  for a) Port 1, b) Port 2, c) Port 3, and d) Port 4 excitations.

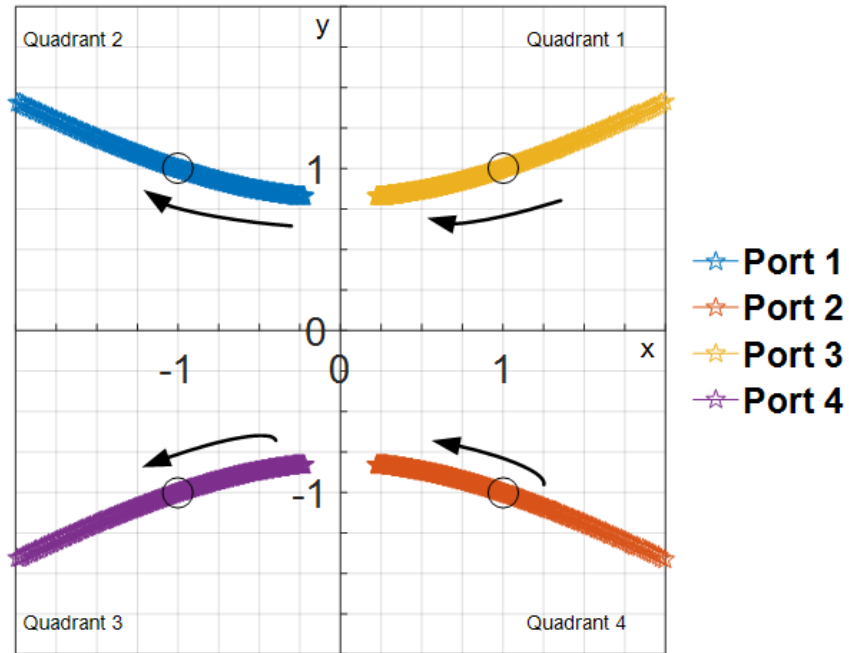


Fig. 2-20: Visualizing the target surface beam locations for the planar array excited by the conventional BM with arrows indicating increasing  $\psi_2$  from  $24.12^\circ$  to  $155.88^\circ$ .

Table 2-4 compares the azimuth angle possibilities for the 2-D beam switching capability of the Modified BM architecture to those of the conventional BM.

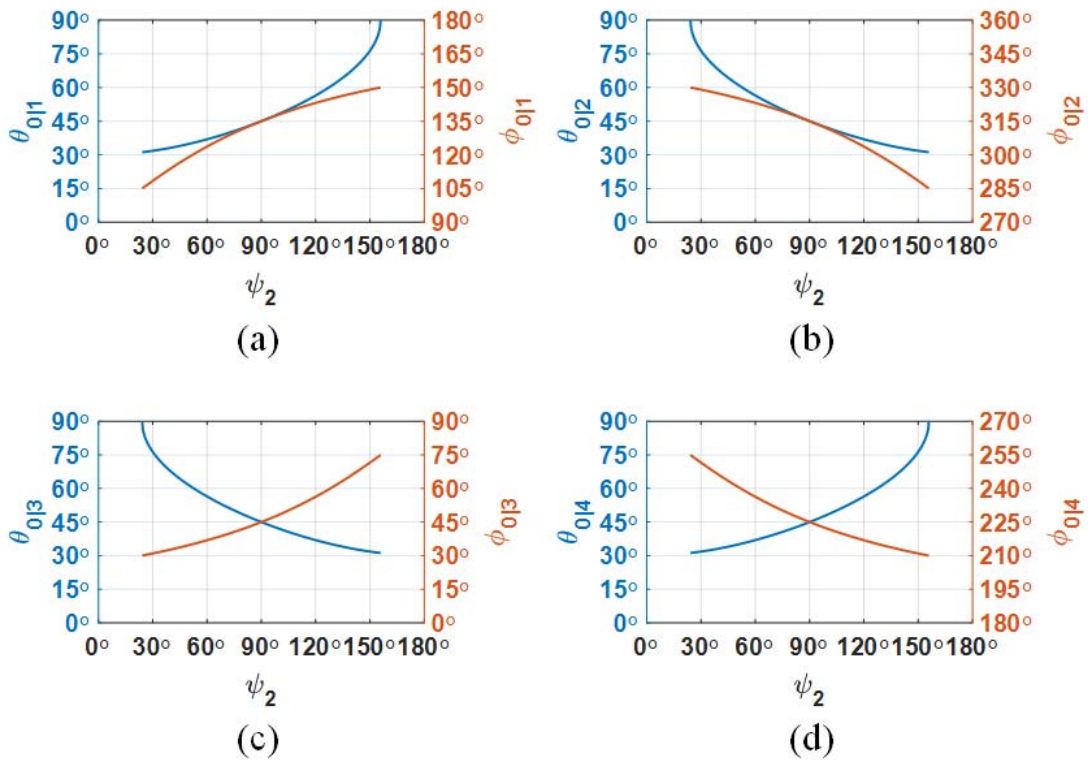


Fig. 2-19: Plots of  $\theta_{0ji}$ ,  $\phi_{0ji}$  versus  $\psi_2$  for a) Port 1, b) Port 2, c) Port 3, and d) Port 4 excitations.

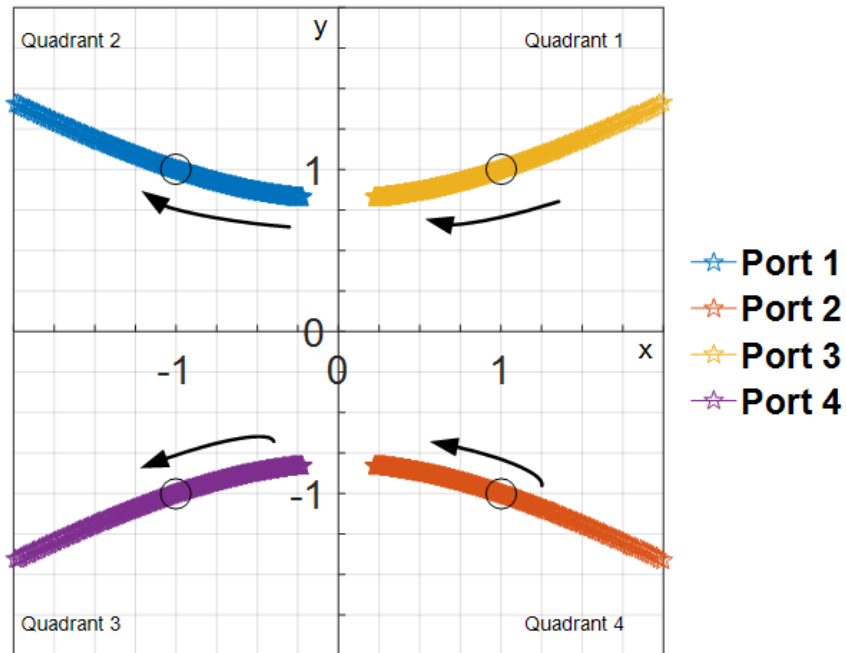


Fig. 2-20: Visualizing the target surface beam locations for the planar array excited by the conventional BM with arrows indicating increasing  $\psi_2$  from  $24.12^\circ$  to  $155.88^\circ$ .

*Table 2-4: POSSIBLE AZIMUTH BEAM ANGLES FOR THE MODIFIED BUTLER MATRIX AND CONVENTIONAL ARCHITECTURE EXTENDED TO 2-D BEAM STEERING.*

Port Excitation	Conventional BM Architecture	Modified BM Architecture
<b>1</b>	$105^\circ \leq \phi_{0 1} \leq 150^\circ$	$210^\circ \leq \phi_{0 1} \leq 255^\circ$
<b>2</b>	$285^\circ \leq \phi_{0 2} \leq 330^\circ$	$30^\circ \leq \phi_{0 2} \leq 75^\circ$
<b>3</b>	$30^\circ \leq \phi_{0 3} \leq 75^\circ$	$285^\circ \leq \phi_{0 3} \leq 330^\circ$
<b>4</b>	$210^\circ \leq \phi_{0 4} \leq 255^\circ$	$105^\circ \leq \phi_{0 4} \leq 150^\circ$

## 2.6: Conclusion

Employing the Butler Matrix as the feed network of a planar 2x2 antenna array to generate 2-D beam patterns at select directions was investigated in this chapter. It was found that without any changes, the standard Butler Matrix does not optimally steer a planar array because the output excitations do not fully cooperate to provide full constructive interference amongst the antenna elements. When the conventional architecture is updated with new phase shift values of  $\psi_{1i}=+90^\circ$  and  $\psi_{2i}=+90^\circ$  at Stages 2 and 4, respectively, the target application goals are met with four theoretical orthogonal beams pointing at  $\phi_{0|1}=135^\circ$ ,  $\phi_{0|2}=315^\circ$ ,  $\phi_{0|3}=45^\circ$ , and  $\phi_{0|4}=225^\circ$  with  $\theta_{0i}=45^\circ$  for all input ports.

Because a choice of using a leading or lagging phase shift was possible for the phase shifters due to the calculated value of  $\psi_{1,2}=\pm\pi/2$ , a new architecture for the Butler Matrix was proposed. This architecture allows the phase shifter to directly follow the crossover circuit in Stages 2 and 4. This option offers the designer an alternative that could allow a smaller phase shift to be implemented, potentially reducing losses and discontinuities. It was confirmed there is no operational impact to using the modified architecture: the new Modified Butler Matrix provides identical 2-D beam patterns as the conventional Butler extended to 2-D operation, only differing in the index of the port numbers.

Finally, the ranges of beam direction angles and phase shift values was investigated to provide a glimpse of the limitations to 2-D beam switching with the studied Butler Matrix architectures, i.e updated conventional and newly proposed. When either BM is used, the 2x2 square planar array topology can achieve beams with  $\theta_0$  values ranging from  $31.14^\circ \leq \theta_{0|i} \leq 90^\circ$ , and correlated  $\phi_0$  values of  $105^\circ \leq \phi_{0|1} \leq 150^\circ$ ,  $285^\circ \leq \phi_{0|2} \leq 330^\circ$ ,  $30^\circ \leq \phi_{0|3} \leq 75^\circ$ , and  $210^\circ \leq \phi_{0|4} \leq 255^\circ$  for the conventional BM and  $210^\circ \leq \phi_{0|1} \leq 255^\circ$ ,  $30^\circ \leq \phi_{0|2} \leq 75^\circ$ ,  $285^\circ \leq \phi_{0|3} \leq 330^\circ$ , and  $105^\circ \leq \phi_{0|4} \leq 150^\circ$  for the Modified BM. Improving the range of possible  $\theta_{0|i}$ 's and  $\phi_{0|i}$ 's may be possible by using a different array geometry than that presented here. The difference can be seen by comparing Eqn (2.11) with the simplified Eqn (2.12) that serves as the basis for the planar array beam direction and phase shift calculations. With the theoretical changes specified through this chapter's analytical discussion, focus now shifts to implementing the updated Butler Matrix design in SIW technology.

---

## Chapter 3: Butler Matrix Circuit Design

Each component of the Butler Matrix feed network driving the planar patch array, i.e. quadrature coupler, crossover, and phase shifters, is presented and discussed in this chapter. The development of an SIW Butler Matrix starts with first designing the SIW interconnect followed by design considerations from [33] to calculate the layout dimensions for the quadrature coupler and crossover sections, respectively stages 1 and 3, and 2 and 4 from Fig. 2-14.

### 3.1: Substrate Integrated Waveguide (SIW)

To meet the integration and noise immunity needs of a millimeter wave design, SIW is the chosen interconnect medium. The technology operates in a similar fashion to a standard rectangular waveguide filled with a dielectric, seen in Fig. 3-1. SIW is constructed in a single PCB layer, with top and bottom metal layers acting as upper and lower conductor walls and via fences that act as the side walls, as seen in Fig. 3-2.

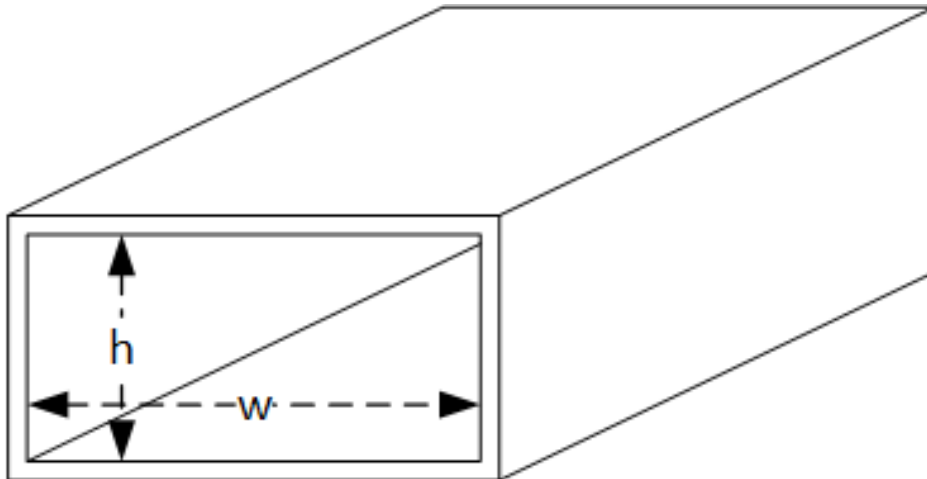


*Fig. 3-1: Simple diagram of a section of rectangular waveguide.*

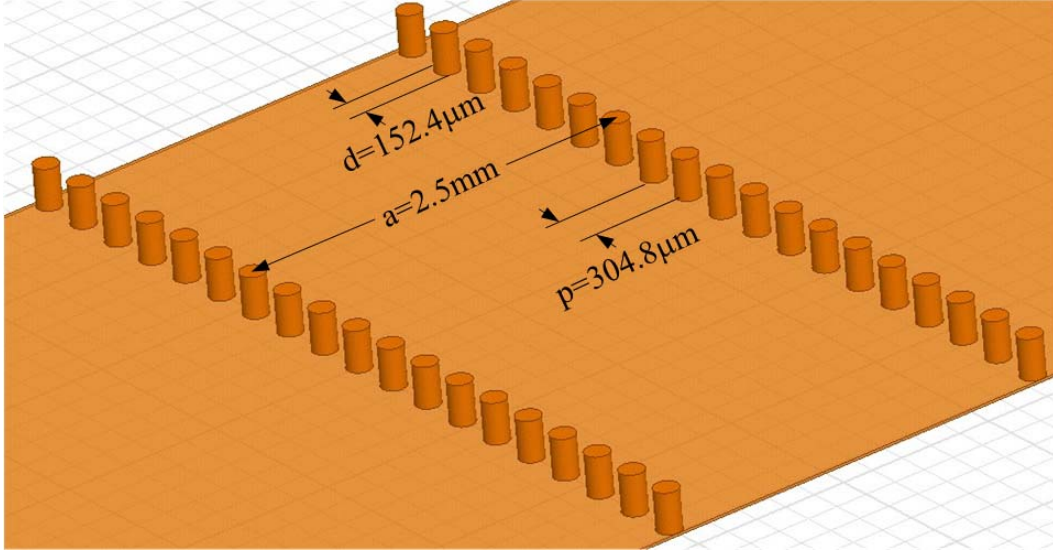


Fig. 3-2: Layout of a substrate integrated waveguide (SIW), with top metal layer removed.

To start, rectangular waveguides have been historically designed so that the intended operating range is 125% to 189% of the guide's cutoff frequency,  $f_c$ , to avoid near cut off dispersion. Cut off frequency,  $f_c$ , is defined as the frequency where waves propagate in a waveguide and the phase constant

$$\beta = k \sqrt{1 - \left(\frac{f_c}{f}\right)^2}, \quad (3.1)$$

becomes nonzero. In the above equation,  $k$  is the wavenumber ( $k=2\pi/\lambda$ ).

Related to the cutoff frequency is the cutoff wavenumber,  $k_c$ , defined by

$$k_c = \frac{2\pi f_c}{c_0}, \quad (3.2)$$

with the speed of light,  $c_0=299,792,458$  m/s. In a waveguide, there could be multiple propagating modes depending on the frequency range of operation, and each mode has a cutoff frequency determined from the waveguide's cross-section dimensions. For an air-filled rectangular waveguide, the general relation for cutoff wavenumber calculated from the guide dimensions is

$$k_c = \sqrt{\left(\frac{m\pi}{w}\right)^2 + \left(\frac{n\pi}{h}\right)^2}, \quad (3.3)$$

where  $m$  is the number of half-wave lengths fitting across the width of the waveguide and  $n$  is the number of half-wave lengths fitting across the height. Since the width is larger than the height in rectangular waveguide, the starting propagating mode has a half wavelength fitting in the width of the waveguide.

There are two groups of propagating modes defined based on existence of the E or H field vector along the longitudinal direction of a waveguide, i.e. TE (transverse electric) and TM (transverse magnetic). TE modes have no longitudinal E-field component while TM modes have no longitudinal H-field component, so only the cross-sectional dimensions of the waveguide,  $w$  and  $h$  of Eqn (3.3), determine the existence of these modes. Further, since SIW has discontinuous side walls created by vias fences, it cannot support TM modes and only TE modes can exist [30].

Therefore, the dominant propagating mode in an SIW is  $TE_{mn}=TE_{10}$  mode ( $m=1, n=0$ ), simplifying Eqn (3.3) to

$$k_c = \frac{\pi}{w}, \quad (3.4)$$

which then leads to the cutoff frequency,  $f_c$ , after equating with Eqn (3.2)

$$f_c = \frac{c_0}{2w}. \quad (3.5)$$

To find the equivalent width,  $w_d$ , of a dielectric filled waveguide, the dielectric constant,  $\epsilon_r$ , needs to be included [31] according to

$$f_c = \frac{c_0}{2w\sqrt{\epsilon_r}} \quad (3.6)$$

and

$$w_d = \frac{w}{\sqrt{\epsilon_r}}. \quad (3.7)$$

For an SIW, given the side walls are implemented as a row of periodically-spaced vias, the equations for an ideal rigid waveguide need to be adjusted slightly. Much work [30], [31] has been

focused on finding effective dimensions of an SIW. An empirical equation is presented in [30] that takes into account the SIW width,  $a$ , as well as via diameter,  $d$ , and spacing,  $p$ , to find the effective width,  $w_{eff}$ , of the SIW:

$$w_{eff} = a - 1.08 \frac{d^2}{p} + 0.1 \frac{d^2}{a} \quad (3.8).$$

Beyond the search for an appropriate width, many authors have published design rules to ensure leakage losses and degradation of propagation characteristics due to dispersion are minimized. Typically, these rules insist the ratio of via spacing to diameter be less than 2.0, or  $\frac{p}{d} < 2.0$ , and the SIW width be at least 5 times the via diameter, or  $\frac{d}{a} < \frac{1}{5}$ . According to [30], if the SIW width is at least 8 times the diameter of the vias, or  $\frac{d}{a} < \frac{1}{8}$ , the spacing-to-diameter constraint can be relaxed to 2.5, or  $\frac{p}{d} < 2.5$ .

To design an SIW for a particular operating frequency,  $f_{op}$ , the designer must

- 1) Find a suitable cutoff frequency,  $f_c$ , such that  $f_{op}$  is 125% to 189% greater,
- 2) For a chosen dielectric material, calculate the width of an equivalent dielectric filled waveguide,  $w_d$ , from Eqn (3.7).
- 3) With guidance from a manufacturer on capabilities for via diameter,  $d$ , and spacing,  $p$ , in their fabrication process, solve for the SIW width,  $a$ , by setting the effective width,  $w_{eff}$ , from (3.8) to the calculated equivalent width,  $w_d$ .

Two Rogers copper laminate materials of thickness  $h=0.254\text{mm}$  were investigated for implementing the antenna array and its feed system: RT5880 ( $\epsilon_r=2.20$ ,  $\tan \delta=0.0009$  @ 10 GHz, 0.5oz copper with thickness  $t=17.5\mu\text{m}$ ) and RO4350B laminate ( $\epsilon_r=3.66$ ,  $\tan \delta=0.0037$  @ 10 GHz, 1oz copper with thickness  $t=35\mu\text{m}$ ). Additionally, a local PCB fabricator was interviewed to find a feasible combination of via diameter and spacing of  $d=6\text{mil}=152.4\mu\text{m}$  and  $p=12\text{mil}=304.8\mu\text{m}$ ,

respectively, which helpfully meets the design rule of  $\frac{p}{d} < 2.5$ . For RT5880, via diameter and spacing remain the same and the above SIW design procedure yields a wall width  $a=2.5$  mm that should achieve  $f_c=41.8$  GHz for the  $TE_{10}$  mode, which makes operating at  $f_{op}=60$  GHz feasible (143% of  $f_c$ ). A check of the cutoff frequencies for other TE modes yields  $f_c=400$  GHz for  $TE_{11}$ ,  $f_c=83.6$  GHz for  $TE_{20}$ , and  $f_c=125$  GHz for  $TE_{30}$ .

The higher dielectric constant,  $\epsilon_r$ , of RO4350B drives the SIW cutoff frequency lower for an equivalent width, with a calculated  $f_c=32.4$  GHz for the  $TE_{10}$  mode with an SIW width of  $a=2.5$ mm, which is still within standard waveguide design rules at 60 GHz (185% of  $f_c$ ). The next closest mode is  $TE_{20}$ , which has a cutoff frequency of  $f_c=64.8$  GHz for  $a=2.5$ mm. It is possible the  $TE_{20}$  mode could introduce coupling effects at the higher end of the 60 GHz band, but since the operating bandwidth of the antenna system will be evaluated from 58 to 62 GHz, it is expected that the impact will be minimal. Due to circuit planning and spacing constraints between antenna elements (conveniently  $\lambda_0/2=2.5$ mm), it was decided to stay with the SIW width  $a=2.5$ mm instead of searching for a smaller width that would yield an operating frequency  $f_{op}$  closer to 150% of  $f_c$ .

After finding a practical width, an engineer should calculate guide wavelength,  $\lambda_g$ , for designing interconnects and components in SIW. This is the distance between two equal phase planes along the waveguide, and calculated [32] as

$$\lambda_g = \frac{2\pi}{\sqrt{\left(\frac{\epsilon_r(2\pi f_{op})^2}{c_0^2}\right) - \left(\frac{\pi}{a}\right)^2}} \quad (3.9).$$

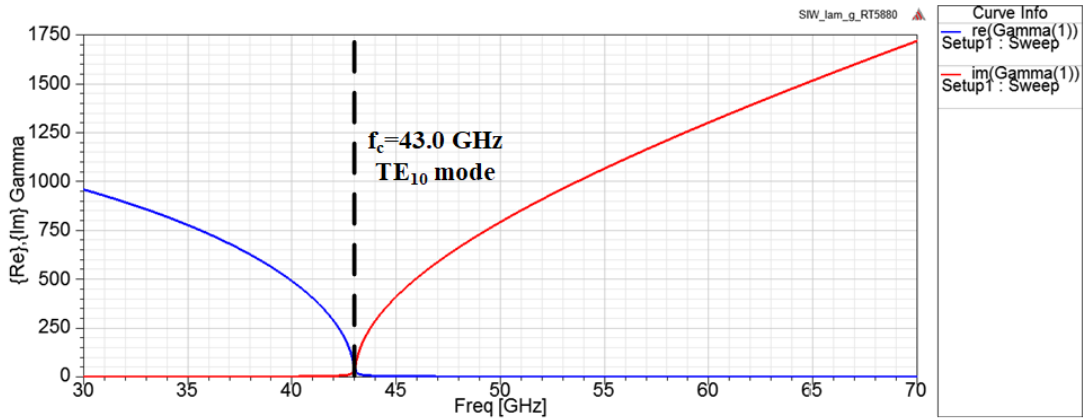
The SIW guided wavelength for RT5880 was calculated to be  $\lambda_g=4.56$ mm while RO4350B evaluated to  $\lambda_g=3.06$ mm. Table 3-1 summarizes calculated and simulated SIW design variables at  $a=2.5$ mm for both RT5880 and RO4350B.

*Table 3-1: CALCULATED AND SIMULATED SIW PARAMETERS FOR RT5880 AND RO4350B AT WIDTH a=2.5mm.*

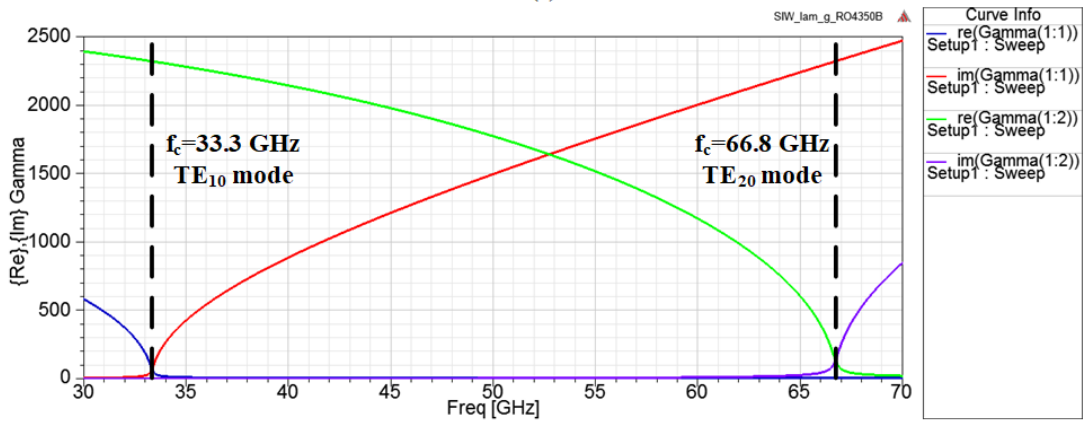
Material	$\epsilon_r$	$\tan \delta$	Calculated		Simulated		
			$f_c$ [GHz]	$\lambda_g$ [mm]	$f_c$ [GHz]	$\lambda_g$ [mm]	Insertion Loss [dB/ $\lambda_g$ ]
RT5880	2.20	0.0009	41.8	4.56	43.0	4.84	0.12
RO4350B	3.66	0.0037	32.4	3.06	33.3	3.15	0.20

HFSS simulations were used to model SIW to find  $f_c$  and  $\lambda_g$  for both materials. The cutoff frequency is found by plotting the propagation constant of the simulated guide versus frequency and finding the point at which the phase constant is zero. To pinpoint this zero-crossing frequency from a propagation constant plot, the point at which the real and imaginary parts are equal is found. Fig. 3-3a features the plot for RT5880 and confirms  $f_c=43.0$  GHz for the TE<sub>10</sub> mode. Additionally, various lengths can be simulated in HFSS to evaluate the output phase and confirm a guide wavelength. For RT5880, a parametric sweep in HFSS captured output phase for SIW lengths ranging from 4.45 to 4.85mm. Phase values are plotted in Fig. 3-4 and a guide wavelength of  $\lambda_g=4.84$ mm is confirmed. The insertion loss for a full guide wavelength in RT5880 is 0.12 dB. For RO4350B, HFSS simulations yield  $f_c=33.3$  GHz for the TE<sub>10</sub> mode and  $f_c=66.8$  GHz for the TE<sub>20</sub> mode, both of which can be seen in Fig. 3-3b, and  $\lambda_g=3.15$ mm from an SIW width  $a=2.5$ mm with an insertion loss of 0.20 dB. Simulated values are summarized in Table 3-1.

For reasons that will be discussed in Chapter 5:, the primary substrate material for evaluation became RO4350B. Given this, the remaining components of the Butler Matrix will focus on design procedure and simulation results with only RO4350B.



(a)



(b)

Fig. 3-3: Plot of real and imaginary parts of the propagation constant,  $\gamma$ , for the designed SIW width  $a=2.5\text{mm}$  in a) RT5880 and b) RO4350B.

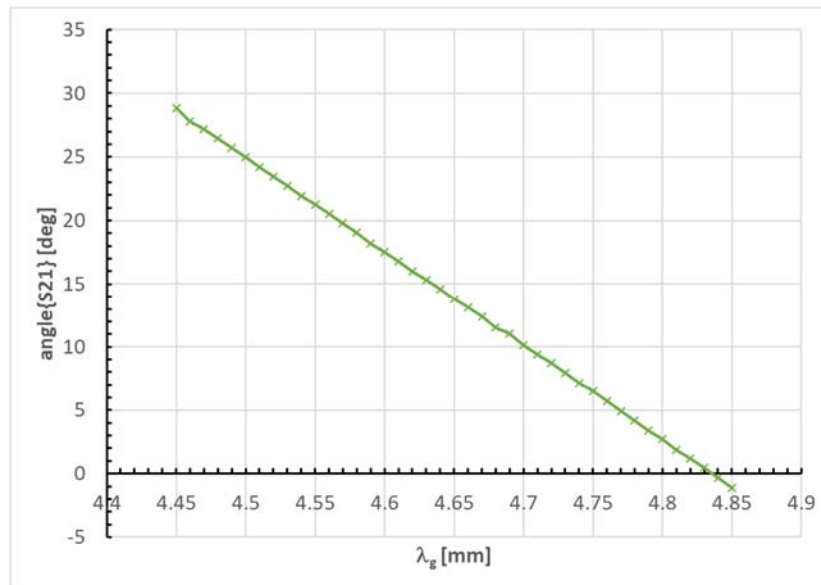


Fig. 3-4: Plot of output phase versus SIW length for RT5880, width  $a=2.5\text{mm}$ .

### 3.1.1: Transition from Microstrip to SIW

Since most board connectors are designed for microstrip or coplanar waveguide landings, it is important to have an interface that provides the transition from microstrip to SIW: with four inputs and four outputs to the 4x4 Butler Matrix, a total of eight 1.85 mm female end-launch connectors will need to be used on a fabricated prototype. This transitional structure comprises of a short taper from the board edge, a microstrip line, and then a longer taper to nearly the width of the SIW [48]. Starting at the edge of the board, this transition consists of a taper from connector landing to a microstrip width of 0.881 mm, a straight microstrip section of length 2.865mm, then a second taper to 1.781mm for the transition to SIW. The transition and all dimensions, which were first determined by calculations from [48] then optimized for return (24.21 dB) and insertion (0.62 dB) losses via full-wave simulations, are depicted in Fig. 3-5. This transition is used for a phase shifter test board, the Butler Matrix prototype, and the final antenna array system board.

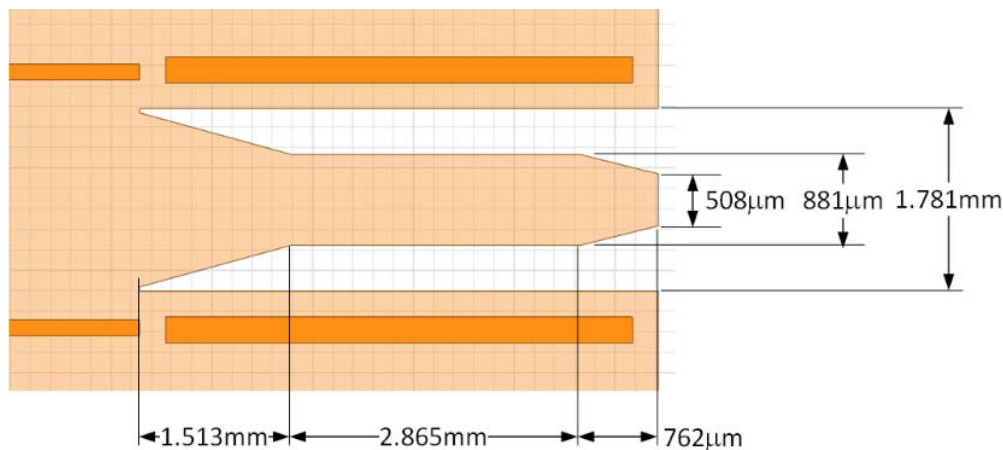


Fig. 3-5: Diagram of transition from microstrip landing to SIW.

### 3.2: Quadrature Coupler Design

The quadrature coupler (also known as a 90° hybrid coupler) is needed in four separate locations for the Butler Matrix circuit: twice in Stage 1 (of Fig. 2-14) and twice again in Stage 3. This circuit, illustrated in Fig. 3-6, is a special version of a 4-port directional coupler that has two goals: 1) an

equal power split from the inputs to the outputs (i.e. insertion loss = 3 dB for  $S_{21}$ ,  $S_{31}$ ,  $S_{24}$ , and  $S_{34}$ ), and 2) demonstrating the  $90^\circ$  phase difference on the outputs,  $\angle S_{31} - \angle S_{21}$  and  $\angle S_{24} - \angle S_{34}$ . As the Butler Matrix is a reciprocal device, it is expected that the quadrature coupler achieves comparable performance when used in reverse (i.e. apply inputs to ports 2 and 3).

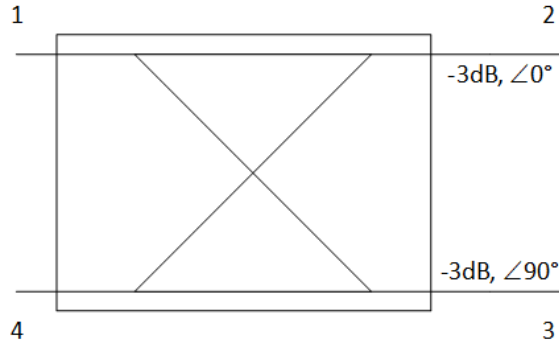


Fig. 3-6: Diagram of the quadrature coupler circuit.

Fig. 3-7 illustrates the general layout of the quadrature hybrid in SIW, where blue walls (solid thick lines) indicate the via fences that make up the SIW side walls. Empirical equations from [33] were used to find baseline dimensions of the quadrature coupler:

$$w_{hyb} = \frac{\pi}{k} \sqrt{\frac{4(3n+1)(n+1)}{4n+1}} \quad (3.10)$$

$$l_{hyb} = \frac{\pi}{k} \sqrt{\frac{(3n+1)(n+1)}{3}} \quad (3.11),$$

where  $k$  is the wavenumber ( $k = \frac{2\pi\sqrt{\epsilon_r}}{\lambda_c}$ ) for propagation in dielectric and  $n$  is a positive integer.

The design procedure begins with evaluation at incrementing values of  $n$  to find the dimensions that best fit the designer's needs (i.e circuit area). Choosing  $n=1$  leads to the smallest width  $w_{hyb}=3.30$  mm and length  $l_{hyb}=2.13$  mm with RO4350B, then the dimensions were optimized in HFSS to reduce and balance the insertion loss between ports and realize the  $90^\circ$  phase differentials. The resulting final values were  $w_{hyb}=3.65$  mm and  $l_{hyb}=2.51$  mm, and simulation results are plotted in Fig. 3-8 for a Port 1 excitation. Simulations show good performance at 60 GHz, with  $22.15 \pm 0.55$

dB return loss for input Ports 1 and 4 (reference line AA'),  $3.30 \pm 0.28$  dB insertion loss to Ports 2 and 3 (reference line BB') from the inputs, and a phase differential of  $89.6 \pm 0.1^\circ$  when comparing  $\angle S_{31} - \angle S_{21}$  and  $\angle S_{34} - \angle S_{24}$ . Reference [33] demonstrated similar simulation performance, reporting  $\sim 3.3$  dB insertion loss to Ports 2 and 4, return loss of  $-18$  dB, and  $\sim 90^\circ$  phase differential at the outputs. The simulated field distribution for the hybrid coupler shown in Fig. 3-9 for a Port 1 excitation illustrates the field movement through the SIW circuit.

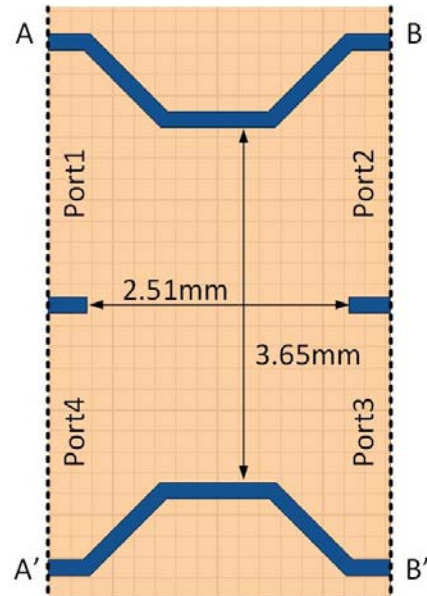


Fig. 3-7: Layout of the SIW quadrature hybrid circuit in HFSS.

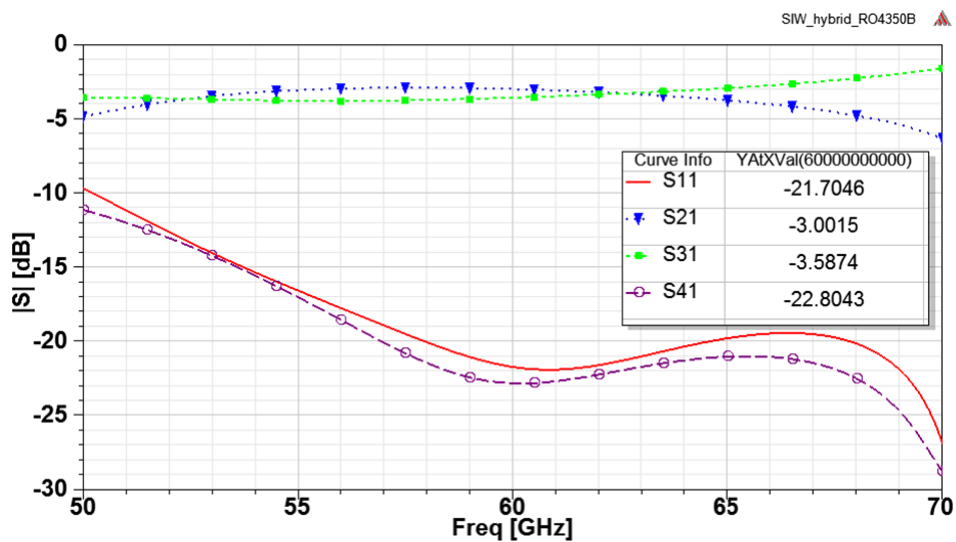


Fig. 3-8: Simulation performance of the SIW quadrature hybrid in HFSS with Port 1 excitation.

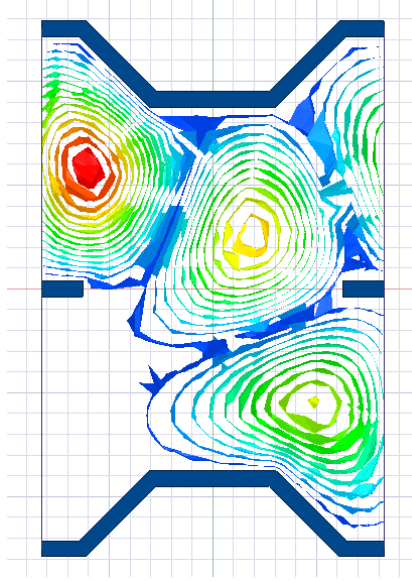


Fig. 3-9: Hybrid coupler simulated field distribution with Port 1 excitation.

### 3.3: Crossover Circuit Design

For the crossover circuit seen in Stages 2 and 4 of Fig. 2-14, another design approach could be taken because phase shift apertures in the upper SIW wall [43] would be used for the phase shifters, instead of meandered lines as used in [33]. Fig. 3-10 illustrates the layout and ports of the crossover in SIW. Operationally, the crossover is a simple circuit in which the paths of signals applied to input ports 1 and 4 (reference line BB') in Fig. 3-10 traverse one another as they pass through to Ports 3 and 2, respectively, (reference line CC') and must work reciprocally.

Care should be taken by the designer to minimize insertion loss and ensure the phase differential between outputs is zero. The dimensions of the crossover, again following design equations from [33], can be calculated from

$$w_{crs} = \frac{\pi}{k} \sqrt{\frac{(6n+1)(2n+3)}{8n}} \quad (3.12)$$

$$l_{crs} = \frac{\pi}{k} \sqrt{\frac{(6n+1)(2n+3)}{12}} \quad (3.13).$$

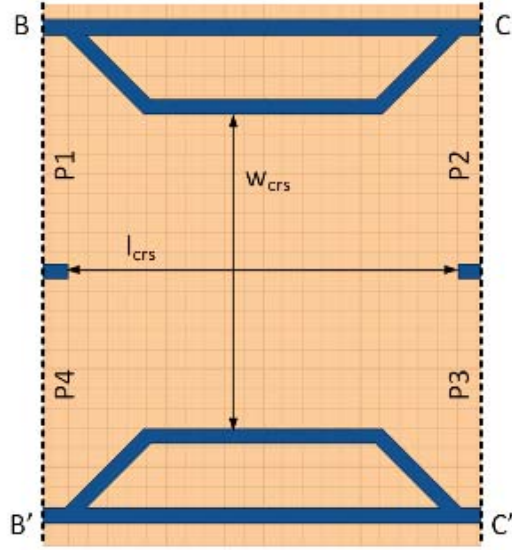


Fig. 3-10: Layout of the SIW crossover circuit in HFSS.

Initially computed with  $n=1$ , the width  $w_{crs}=3.19$  mm and length  $l_{crs}=3.69$  mm are optimized with HFSS to  $w_{crs}=3.23$  mm and  $l_{crs}=3.94$  mm. Crossover circuit simulations predict good performance at 60 GHz for both forward (BB' to CC') and reverse operation, with  $16.5\pm 0.1$  dB return loss for inputs at BB' ( $S_{11}$ ,  $S_{22}$ ), 0.49 dB insertion loss to the intended crossover outputs at CC' ( $S_{31}$ ,  $S_{24}$ ),  $29.3\pm 6.2$  dB isolation ( $S_{41}$ ,  $S_{21}$ ,  $S_{14}$ ,  $S_{34}$ ), and a phase differential of  $0.03^\circ$  between the crossover paths ( $\angle S_{31}-\angle S_{24}$ ). Simulation results from [33] are comparable:  $\sim 0.5$  dB insertion loss,  $21.5\pm 1.5$  dB isolation, and 40 dB return loss. For a Port 1 excitation, simulated S-parameters are plotted in Fig. 3-11 and the simulated field distribution is depicted in Fig. 3-12.

### 3.4: Phase Shifter Design

With the hybrid coupler and crossover designed, the overall structure of the SIW Butler Matrix takes shape, as seen in Fig. 3-13, but the crossover stages need a phase shifter to ensure the outputs achieve the intended phase differentials,  $\psi_{1,2}$ . As mentioned in 0, a total phase differential of  $90^\circ$  is needed at both Stage 2 and 4 to generate four orthogonal 2-D beams from the Butler Matrix. The simulated crossover outputs show a phase lag of  $50.8^\circ$  with respect to the outer pass-through

channels (seen in Fig. 3-10) and, according to the design rules presented in Section 2.3.1., a  $39.2^\circ$  phase shifter needs to follow the crossover circuit. This choice of phase shifter location means the Modified Butler Matrix architecture presented in Section 2.4 is needed.

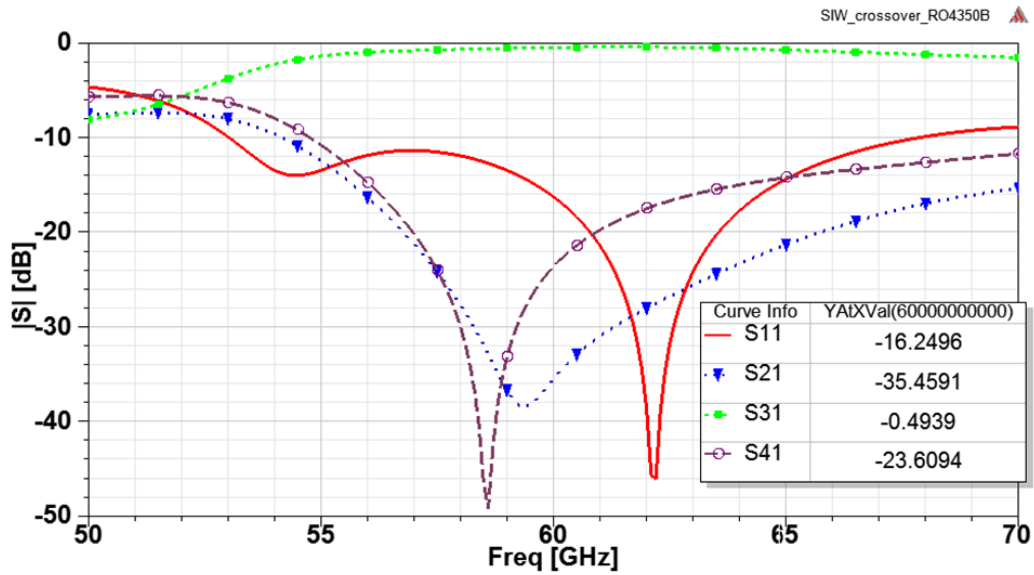


Fig. 3-11: S-parameter plot for the crossover circuit with Port 1 excitation.

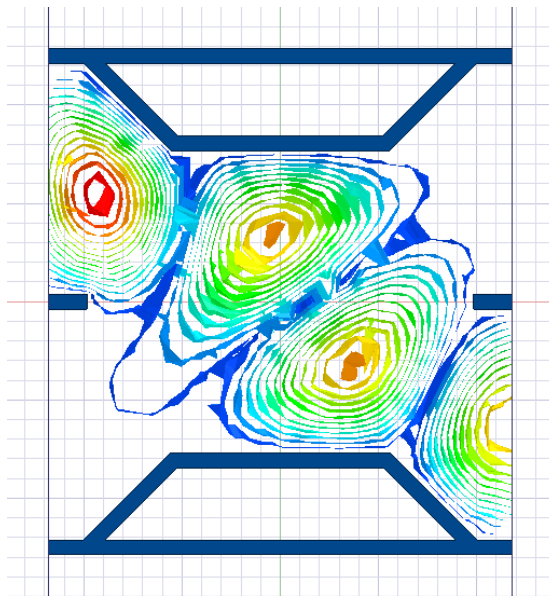


Fig. 3-12: Crossover simulated field distribution with Port 1 excitation.

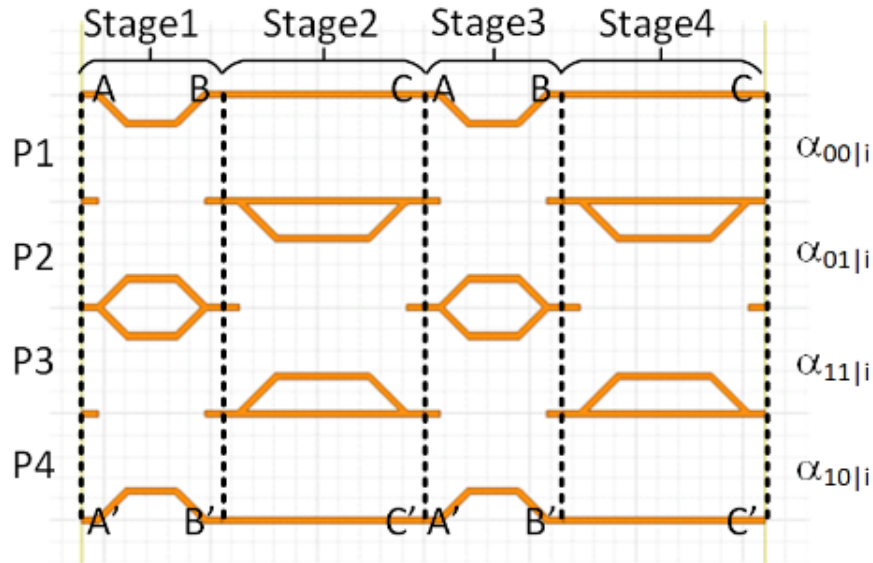
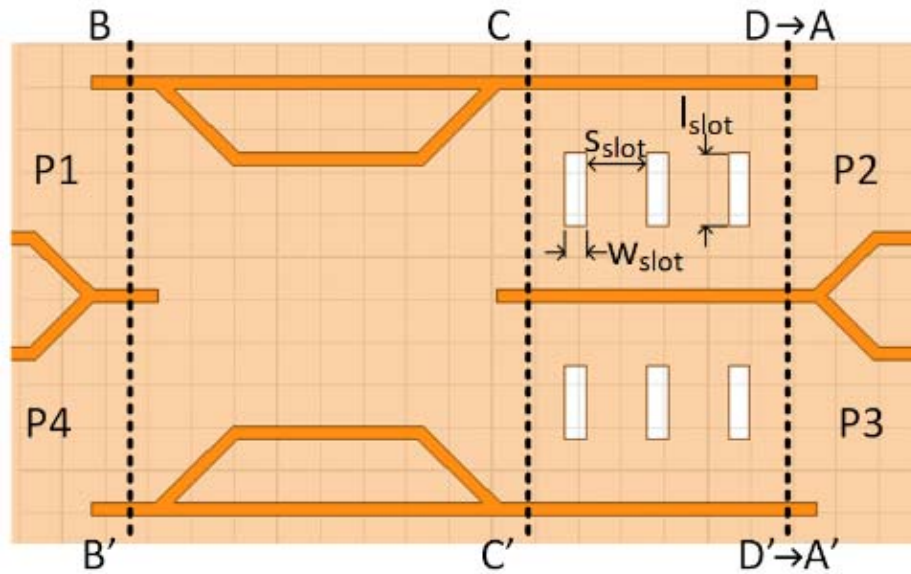


Fig. 3-13: Structure of the SIW Butler Matrix in HFSS, prior to adding phase shift apertures.

PCB designers will typically rely on a meandered line as a phase shifter in their circuit designs, an option that costs layout area as the fixed delay line must deviate away and then come back to the center line of the incoming transmission line. Designers working with substrate integrated waveguide (SIW) interconnects are no different, having to sacrifice the size of the circuit footprint to achieve the right amount of phase shift. Researchers have thus focused on developing straight SIW phase shifters to shrink design area while maintaining the favorable performance of SIW for mm-wave circuits.

According to [43], apertures in the top or bottom wall of an SIW, as seen in Fig. 3-14, change the phase constant of the waveguide channel. The change offers an additional phase lag with respect to an SIW with no slot. Parametric layout simulations show each slot yields a phase shift of 8 to 24° when changing the area of slot from 0.081mm<sup>2</sup> to 0.484mm<sup>2</sup>. In general, increasing the spacing and area of the rectangular slots had a direct relationship with the magnitude of the phase shift and return loss, and inversely correlated to the insertion loss. The radiation loss (calculated as  $\text{RadLoss} = 1 - |S_{11}|^2 - |S_{21}|^2$ ) was observed as measure of adverse impact on performance when increasing the higher number of slots. Also, the total area occupied by the phase shifter, which

includes all the apertures and the spacing in between, is another measure in evaluating footprint miniaturization versus performance.



*Fig. 3-14: Layout of the phase shifting slots within the Butler Matrix circuit: just after the crossover circuit in Stages 2 and 4.*

A parametric search of slot dimensions and count was conducted to choose a structure to achieve the desired phase shift. It was found that three apertures, 0.25mm x 0.9mm slots spaced 0.7mm apart, would be sufficient to achieve the phase differential within the range 24° to 42°, the final value depending on several outside factors such as the input impedance to the phase shifter and total length of the SIW sections before and after the slots (basically matching at the input and output ports). When simulated in series with the crossover circuit, the phase values slightly change due to the loading of cascaded sections. Therefore, a full-wave optimization tool was used to tune the dimensions of each aperture to 0.248mm x 0.866mm with 0.704mm spacing to meet the total Stage 2 and 4 phase differential goal of 90° - implying a total added phase delay of 39.2°. To compare the performance of this phase shifter, two other structures, a meandered SIW and a baseline straight SIW (as shown in Fig. 3-15) are simulated using HFSS.

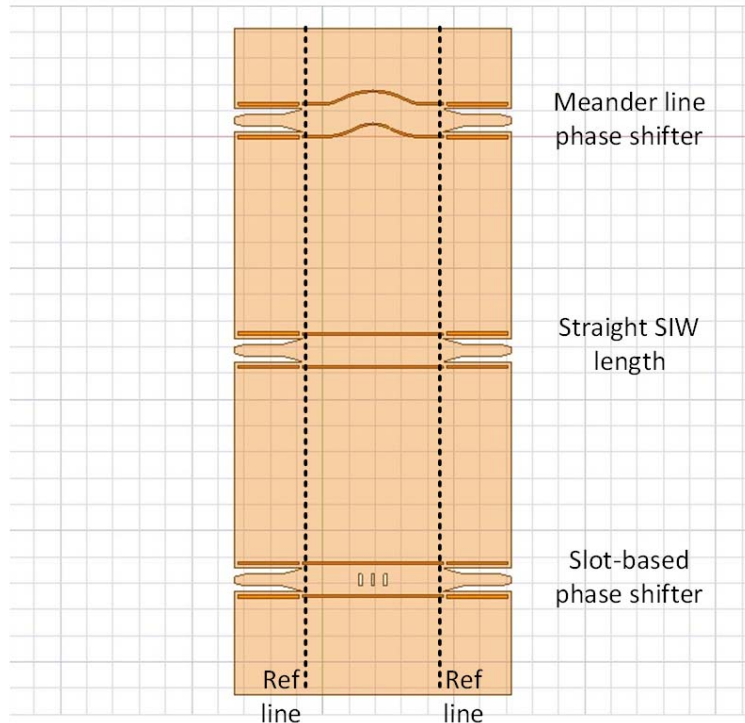


*Fig. 3-15: Layout of phase shifter comparison board.*

Since the periodic aperture phase shifter, meandered line phase shifter, and baseline straight SIW sub-circuits will be fabricated and measured, each require a microstrip-to-SIW transition (see Fig. 3-5) at the input and output. The slot-based phase shifter topology yielded favorable insertion loss (IL) of 1.76 dB and return loss (RL) of 29.1 dB at 60 GHz. The expected phase differential with respect to a straight SIW is  $31.6^\circ$ , showing the impact of the cascaded sections when placed in series with the crossover. Simulation results also show that at 60 GHz the insertion loss of meandered SIW and the baseline straight SIW are 1.72 and 1.70 dB, respectively, while the return loss is 27.2 and 21.4 dB, respectively. The meander phase shifter achieves a  $31.8^\circ$  phase differential with respect to the straight SIW. Simulation results for insertion loss and return loss are plotted in Fig. 3-16.

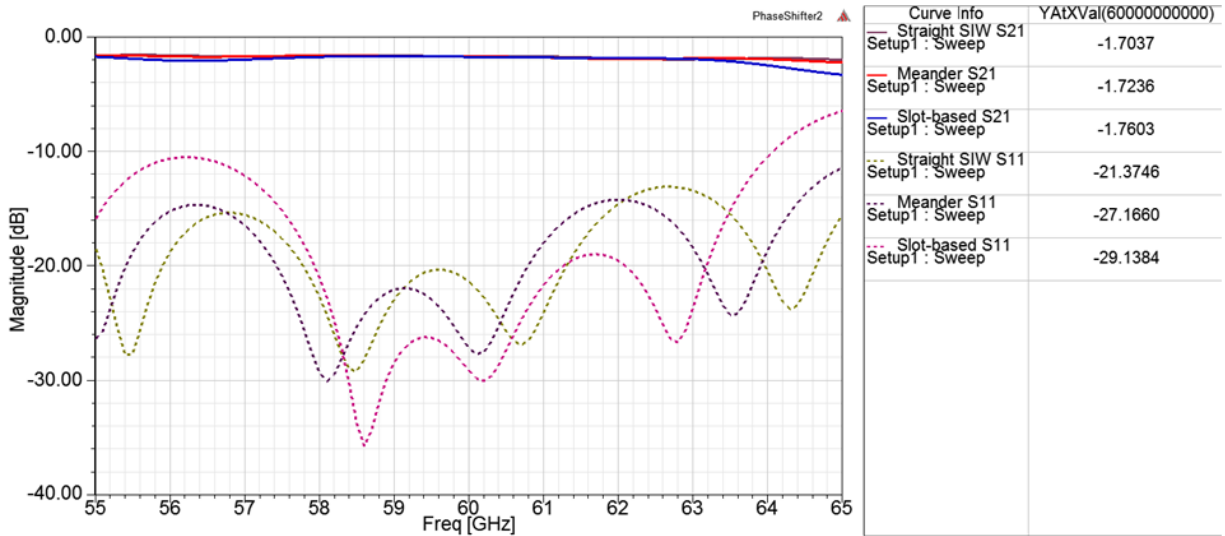


Fig. 3-16: Simulated transmission ( $S_{21}$ , solid line) and reflection ( $S_{11}$ , dash line) parameters for the phase shift comparison of the slot-based phase shifter, the meander phase shifter, and a straight length of SIW.

A separate simulation was run without the microstrip-to-SIW transitions (see the reference line of Fig. 3-15), yielding insertion loss of 0.47 dB, 0.49 dB, and 0.53 dB for the straight SIW, meander line, and the slot-based phase shifter, respectively. When this insertion loss is considered, the RadLoss of the periodic aperture phase shifter is calculated to be 18.9dB.

Finally, the periodic aperture phase shifter was integrated with the crossover circuit, as in Fig. 3-14, where a total Stage phase shift of  $85.8^\circ$  and IL of 0.79 dB were simulated with HFSS. For reference, the accompanying SIW pass-throughs in Stages 2 and 4 each have an IL of 0.49 dB.

### 3.4.1: Phase Shifter Measurements

To evaluate the feasibility of using the slot-based phase shifter, a phase shift evaluation board was fabricated with the three structure layout shown in Fig. 3-15 using the chosen Rogers RO4350B laminate. For both input and output ports of this test board, 1.85mm female end-launch connectors were used. To remove the added effects of the connectors, microstrip-to-SIW transition structures, and the extra  $\lambda_g/2$  SIW feedlines of the phase shifter test prototype, a de-embedding

technique in needed. A through-only de-embedding technique based on [44] is chosen for evaluating the fabricated prototype measurements and is detailed in Chapter 5 and Appendix I. Scattering parameters for each of the three structures are measured, de-embedded, and plotted in Fig. 3-17. The meandered line showed the highest IL (seen in Fig. 3-17a) of 2.62dB at 60 GHz while the straight SIW and slot-based phase shifter both measured around 1.85dB. The meander phase shifter achieved a phase differential (seen in Fig. 3-17b) of  $46.4^\circ$  with respect to the straight SIW, while the periodic aperture phase shifter had a  $20.3^\circ$  phase differential. The discrepancy between the simulated and measured results is most likely due to variability in the contacts between the prototype board and end launch connectors. Nonetheless, the measurements confirm achieving phase shift by using transverse periodic apertures without sacrificing additional board (or chip) real estate.

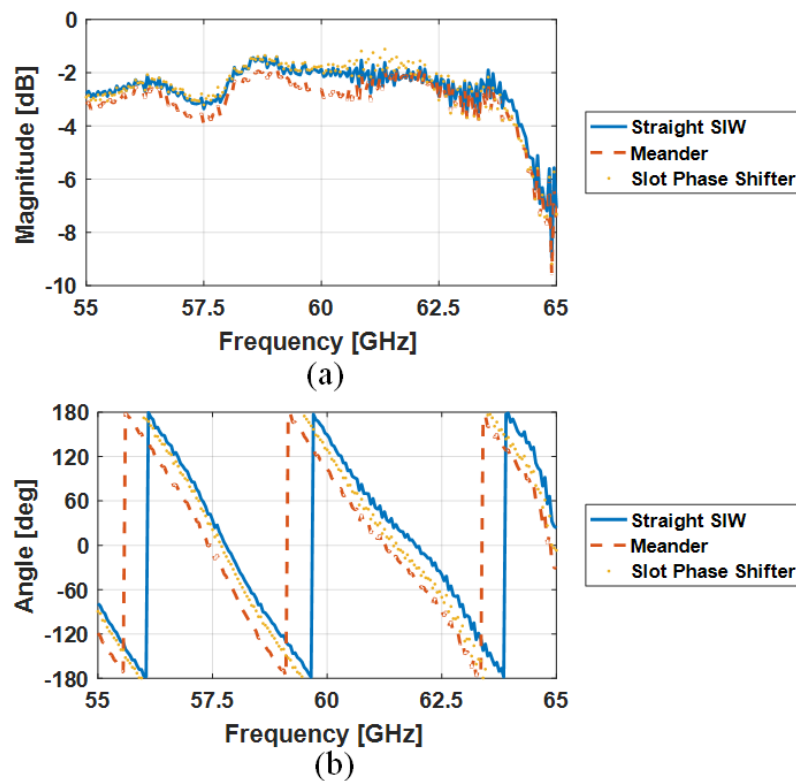


Fig. 3-17: Measured (a) magnitude and (b) phase of S-parameters for the phase shift comparison prototype after de-embedding.

### 3.5: Component Integration into Butler Matrix

Ultimately, all components of the proposed modified Butler Matrix architecture are integrated following the diagram of Fig. 2-14 and the complete subsystem layout is presented in Fig. 3-18. The so designed Butler Matrix measured 21.92mm long by 10.15mm wide, a reduction in circuit area of 53.9% over the fabricated prototype presented by [33]. Given Stages 1 and 3 each have an IL of  $3.30 \pm 0.28$  dB and Stages 2 and 4 have an IL of  $0.64 \pm 0.15$  dB, the total expected IL of the Butler Matrix feed network is  $7.88 \pm 0.86$  dB.

To fabricate a prototype for verification of the BM design, microstrip-to-SIW transitions spaced to accommodate end-launch connectors were added to the layout. Since the connectors were each 5 times as wide as the designed SIW channel, feed lines to and from the inputs and outputs of the BM were extended and bent to provide enough separation between connectors. The result, seen in Fig. 3-19, is the final layout used for prototype board fabrication that measured 65.97 mm by 45.76 mm. The impact to IL cannot be overlooked in Fig. 3-19, though, as these prototyping SIW feeds are each 19.5 mm long ( $5.7\lambda_g$ ) and have 1.14 dB of insertion loss each. Accompanied by the microstrip-to-SIW transition presented in Section 3.1.1., each input or output feed introduces an IL of 1.76 dB bringing the total budgeted IL for each input to  $11.4 \pm 0.86$  dB.

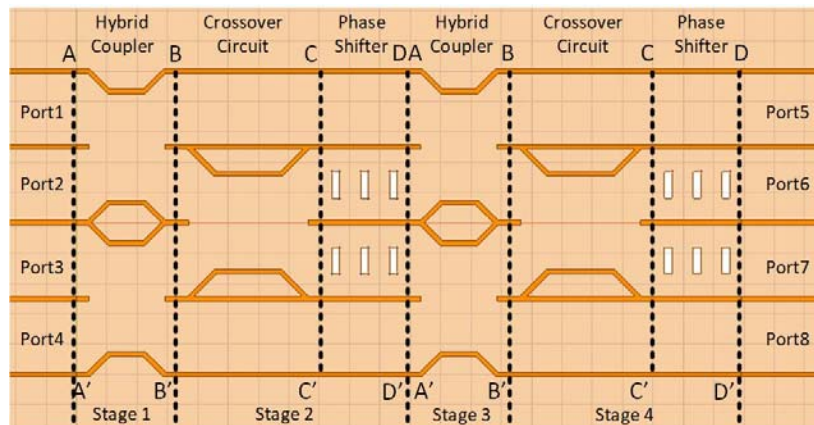
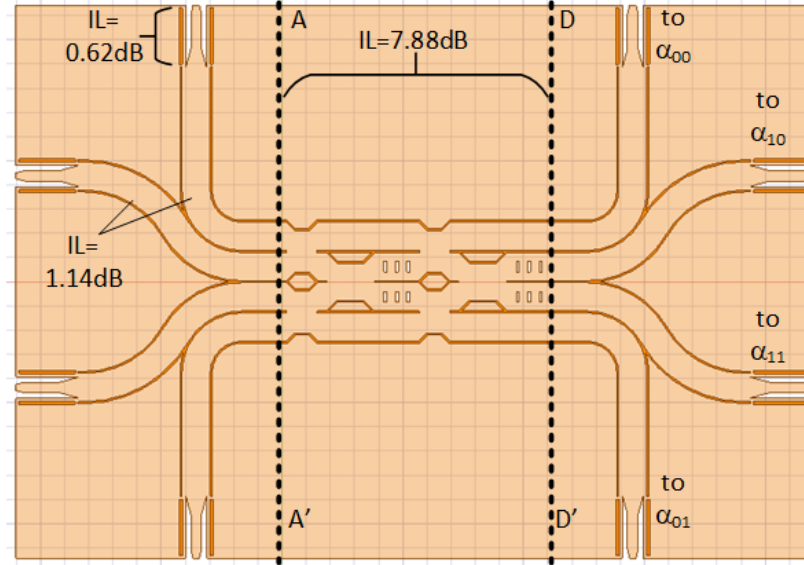


Fig. 3-18: Layout structure of the complete Butler Matrix circuit.



*Fig. 3-19: Full layout of the Butler Matrix for evaluation, including input and output lines to enable the use of end launch connectors.*

Full-wave simulations are conducted for the final Butler Matrix layout and the 4x4 S-parameter matrix is generated. The simulated magnitudes and phases at the output ports of the SIW beamforming network at 60 GHz are shown in Table 3-2. The table sections indicate the excited port with all the other ports terminated to match impedance and compare simulated results with theoretical values. Simulated return loss for all input excitations is plotted in Fig. 3-20, while insertion loss and output phases for a Port 1 excitation are shown in Fig. 3-21 and Fig. 3-22, respectively.

It can be seen that a minimum of  $-2.39^\circ$  phase deviation (for input Port 1, output Port 8) and a maximum of 27.9% deviation ( $25.1^\circ$  difference from the ideal output phase value of  $90^\circ$  for input Port 3 to output Port 6) are obtained in comparison to the theoretical values. The output magnitudes drop by a maximum of 5.9 dB (beyond the 6dB loss from hybrid couplers in Stages 1 and 3) as expected due to the addition of microstrip transition sections and the extra SIW sections needed for connecting to the input and output end-launch connectors. Simulation results presented in [33] and [36] both reported an insertion loss of 2.5-2.7 dB (again beyond the 6 dB loss from two hybrid

couplers), but neither used end-launch connectors so there was no additional SIW sections for routing or any microstrip-to-SIW transitions. As well, the simulated phase results from [36] indicated maximum phase deviation of  $41^\circ$  at 60 GHz which is much higher than what is achieved here.

*Table 3-2: MODIFIED BUTLER MATRIX OUTPUT MAGNITUDES AND PHASES.*

Output	Ideal Magnitude	Simulated Magnitude	Ideal Phase	Simulated Phase	%Dev Simulated Phase
Input: Port 1					
<i>Port5</i>	-6.0dB	-11.2dB	$0^\circ$	$-2.69^\circ$	-
<i>Port6</i>	-6.0dB	-11.5dB	$90^\circ$	$84.63^\circ$	6.0%
<i>Port7</i>	-6.0dB	-11.8dB	$180^\circ$	$166.18^\circ$	7.7%
<i>Port8</i>	-6.0dB	-11.3dB	$90^\circ$	$92.39^\circ$	-2.7%
Input: Port 2					
<i>Port5</i>	-6.0dB	-11.6dB	$-90^\circ$	$-109.19^\circ$	-21.3%
<i>Port6</i>	-6.0dB	-11.9dB	$180^\circ$	$160.53^\circ$	10.8%
<i>Port7</i>	-6.0dB	-10.8dB	$90^\circ$	$64.93^\circ$	27.9%
<i>Port8</i>	-6.0dB	-11.6dB	$180^\circ$	$170.29^\circ$	5.4%
Input: Port 3					
<i>Port5</i>	-6.0dB	-11.6dB	$180^\circ$	$172.98^\circ$	3.9%
<i>Port6</i>	-6.0dB	-10.8dB	$90^\circ$	$64.91^\circ$	27.9%
<i>Port7</i>	-6.0dB	-11.9dB	$180^\circ$	$163.03^\circ$	9.4%
<i>Port8</i>	-6.0dB	-11.4dB	$-90^\circ$	$-110.76^\circ$	23.1%
Input: Port 4					
<i>Port5</i>	-6.0dB	-11.3dB	$90^\circ$	$95.08^\circ$	-5.6%
<i>Port6</i>	-6.0dB	-11.8dB	$180^\circ$	$164.19^\circ$	8.8%
<i>Port7</i>	-6.0dB	-11.6dB	$90^\circ$	$86.33^\circ$	4.1%
<i>Port8</i>	-6.0dB	-11.1dB	$0^\circ$	$-3.37^\circ$	-

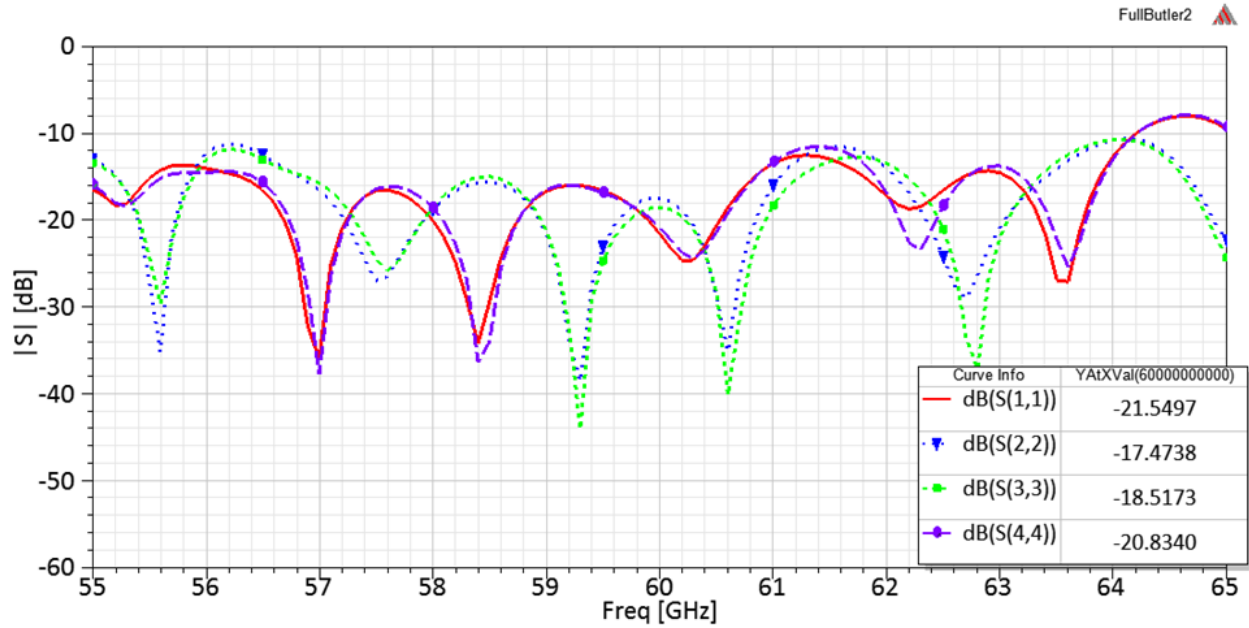


Fig. 3-20: Plot of simulated return loss for all input port excitations of the final Modified Butler Matrix layout.

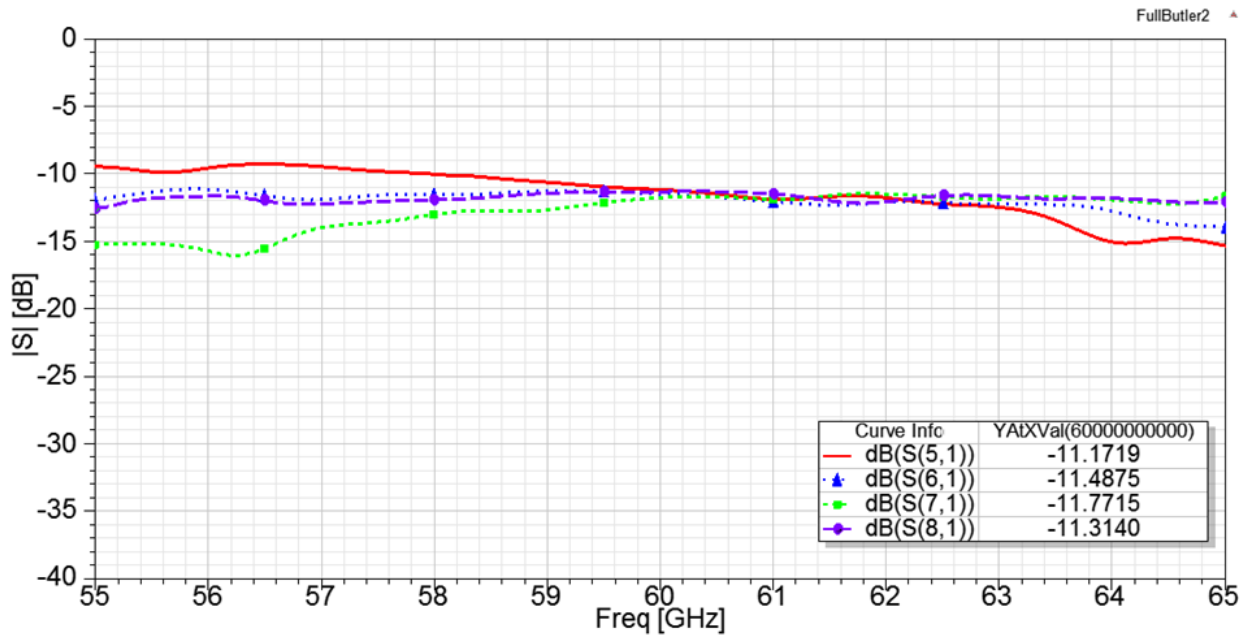


Fig. 3-21: Plot of simulated insertion loss for a Port 1 excitation of the final Modified Butler Matrix layout.

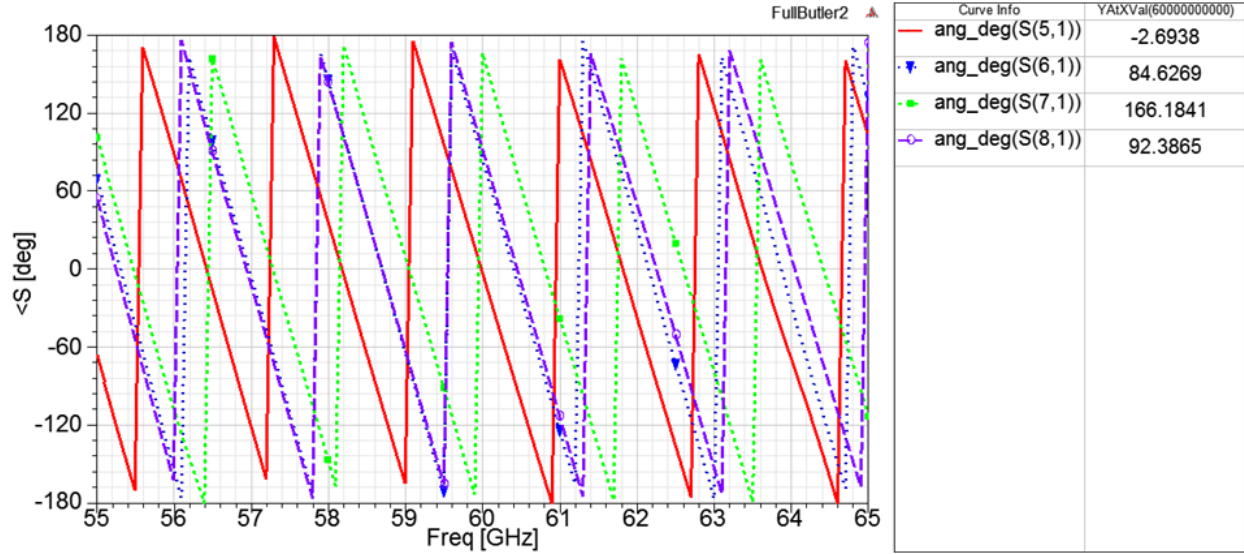


Fig. 3-22: Plot of the simulated output phases for a Port 1 excitation of the final Modified Butler Matrix layout.

Updating the Butler Matrix output phase matrix to reflect the simulated results

$$B = \frac{1}{2} \begin{bmatrix} e^{-j2.69^\circ} & e^{-j109.19^\circ} & e^{j172.98^\circ} & e^{j95.08^\circ} \\ e^{j84.63^\circ} & e^{j160.53^\circ} & e^{j64.91^\circ} & e^{j164.19^\circ} \\ e^{j166.18^\circ} & e^{j64.93^\circ} & e^{j163.03^\circ} & e^{j86.33^\circ} \\ e^{j92.39^\circ} & e^{j170.29^\circ} & e^{-j110.76^\circ} & e^{-j3.37^\circ} \end{bmatrix} \quad (3.14)$$

allows a check for orthogonality

$BB^*$

$$= \frac{1}{4} \begin{bmatrix} e^{-j2.69^\circ} & e^{-j109.19^\circ} & e^{j172.98^\circ} & e^{j95.08^\circ} \\ e^{j84.63^\circ} & e^{j160.53^\circ} & e^{j64.91^\circ} & e^{j164.19^\circ} \\ e^{j166.18^\circ} & e^{j64.93^\circ} & e^{j163.03^\circ} & e^{j86.33^\circ} \\ e^{j92.39^\circ} & e^{j170.29^\circ} & e^{-j110.76^\circ} & e^{-j3.37^\circ} \end{bmatrix} \begin{bmatrix} e^{j2.69^\circ} & e^{-j84.63^\circ} & e^{-j166.18^\circ} & e^{-j92.39^\circ} \\ e^{j109.19^\circ} & e^{-j160.53^\circ} & e^{-j64.93^\circ} & e^{-j170.29^\circ} \\ e^{-j172.98^\circ} & e^{-j64.91^\circ} & e^{-j163.03^\circ} & e^{j110.76^\circ} \\ e^{-j95.08^\circ} & e^{-j164.19^\circ} & e^{-j86.33^\circ} & e^{j3.37^\circ} \end{bmatrix}$$

$$= \begin{bmatrix} 1.000 \angle 0^\circ & 0.023 \angle 11.2^\circ & 0.007 \angle 95.1^\circ & 0.040 \angle 3.0^\circ \\ 0.023 \angle 348.8^\circ & 1.000 \angle 0^\circ & 0.030 \angle 357^\circ & 1.000 \angle 0^\circ \\ 0.007 \angle 264.9^\circ & 0.030 \angle 3.0^\circ & 1.000 \angle 0^\circ & 0.023 \angle 357.9^\circ \\ 0.040 \angle 357.0^\circ & 0.005 \angle 84.0^\circ & 0.023 \angle 2.1^\circ & 1.000 \angle 0^\circ \end{bmatrix} \quad (3.15)$$

It can be seen that the generated output phase vectors from the Modified Butler Matrix do not create an ideal unitary matrix. Yet, inspecting the resultant array factor beam patterns in Fig. 3-23 shows they are very similar to those for the ideal Modified Butler Matrix architecture (dotted line plots). Fig. 3-23a and Fig. 3-23b also show that peak magnitudes are nearly ideal

$(|A_i(\theta_{0i}, \phi_{0i})|^2 = 3.97 \pm 0.01)$  and are located very close to nulls in the beam patterns of the other port excitations.

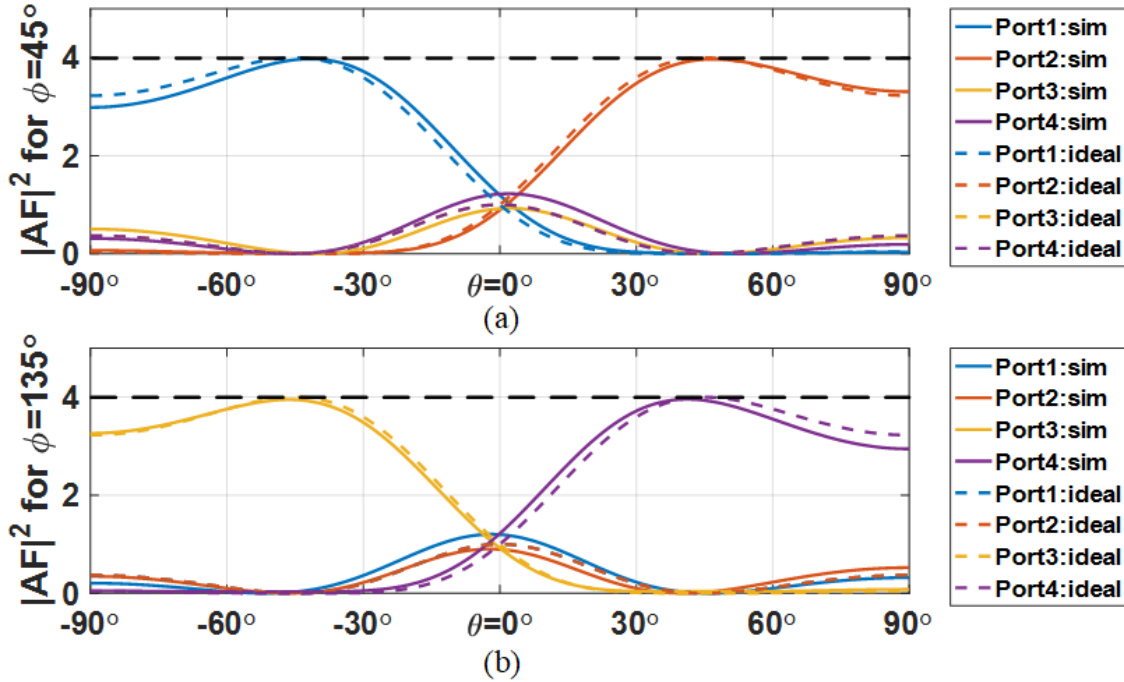


Fig. 3-23: Array factor gain, a)  $\phi=45^\circ$  and b)  $\phi=135^\circ$ , for a square planar array with simulated output phases from final modified Butler Matrix layout compared to ideal patterns.

Applying the measured output phases from the simulated Butler Matrix layout to the planar array factor yields the peak beams slightly askew from the target application: for Port 1 excitation,  $|A_1(\theta_{01}, \phi_{01})|^2 = 3.99$ ,  $\theta_{01} = 41.58^\circ$ ,  $\phi_{01} = 227.70^\circ$ ; for Port 2,  $|A_2(\theta_{02}, \phi_{02})|^2 = 3.98$ ,  $\theta_{02} = 46.98^\circ$ ,  $\phi_{02} = 41.94^\circ$ ; for Port 3,  $|A_3(\theta_{03}, \phi_{03})|^2 = 3.96$ ,  $\theta_{03} = 46.44^\circ$ ,  $\phi_{03} = 318.06^\circ$ ; and for Port 4,  $|A_4(\theta_{04}, \phi_{04})|^2 = 3.97$ ,  $\theta_{04} = 41.22^\circ$ ,  $\phi_{04} = 131.94^\circ$ . These peak beam locations are visualized for the planar target surface in Fig. 3-24, where each port excitation drives the beam to each of the intended quadrants. Further validation of the phased output results can be seen in SIR comparison in Table 3-3, where each beam has a significant power advantage ( $> 20\text{dB}$ ) over the other beams for its own quadrant. It is expected that this final Butler Matrix layout is capable of meeting the goals of 2-D beam steering when fully-integrated with the planar antenna array in Chapter 4.

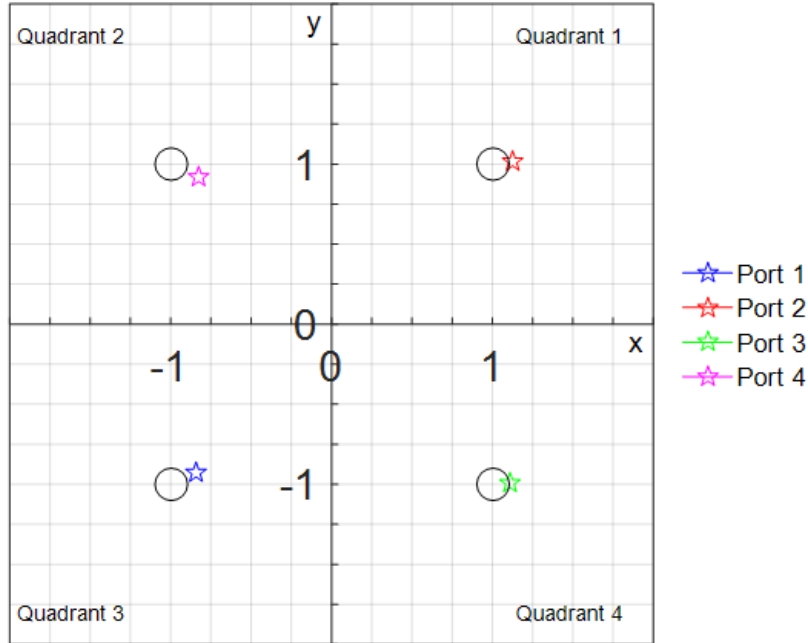


Fig. 3-24: Visualization of the planar surface target being illuminated by the planar array factor excited by the simulated Modified Butler Matrix outputs.

Table 3-3: PEAK BEAM DIRECTIONS AND SIR COMPARISONS FOR ALL PORT EXCITATIONS FROM THE SIMULATED MODIFIED BUTLER MATRIX APPLIED TO PLANAR ARRAY.

SIR COMPARISONS					
PORT	PEAK BEAM	PORT 1	PORT 2	PORT 3	PORT 4
1	$\theta_{01}=41.58^\circ, \phi_{01}=227.70^\circ$	0dB	23.6dB	33.4dB	30.3dB
2	$\theta_{02}=46.98^\circ, \phi_{02}=41.94^\circ$	24.4dB	0dB	27.5dB	32.6dB
3	$\theta_{03}=46.44^\circ, \phi_{03}=318.06^\circ$	33.0dB	27.6dB	0dB	20.9dB
4	$\theta_{04}=41.22^\circ, \phi_{04}=131.94^\circ$	30.8dB	31.9dB	20.4dB	0dB

### 3.6: Conclusion

The implementation of the Butler Matrix was explored, beginning with the base SIW interconnect dimensions and proceeding through sub-circuit designs of the hybrid coupler, crossover, and phase shifter. A minimal length, periodic aperture phase shifter was utilized in series with the crossover circuit, taking advantage of the proposed Modified Butler Matrix

architecture presented in Section 2.4: Measurements of the slot-based phase shifter demonstrated acceptable performance compared to a meandered line phase shifter, taking up much less board real estate. Using the transverse periodic phase shifter in Stages 2 and 4 of the Modified Butler Matrix architecture also allowed a smaller footprint design for the full BM layout, saving nearly 54% of the area presented in [33].

Full-wave simulations of the SIW Butler Matrix showed that output magnitudes can drop up to 5.9dB beyond the expected 6dB loss from two hybrid couplers due to the microstrip-to-SIW transitions (0.62 dB IL per transition) and extended feed lines (1.14 dB IL per feed) necessary for implementing end-launch connectors on the fabricated prototype. Additionally, up to 27.9% deviation can be seen between calculated and simulated output phases. Despite this, the output excitations to the 2x2 square planar array are nearly orthogonal, and experimental evaluations should confirm four distinct beam patterns pointed close to the previously calculated beam directions for the modified Butler Matrix architecture:  $\phi_{01}=225^\circ$ ,  $\phi_{02}=45^\circ$ ,  $\phi_{03}=315^\circ$ , and  $\phi_{04}=135^\circ$  for  $\theta_{0i}=45^\circ$ .

---

## Chapter 4: Antenna System Design

In this chapter, the design focus shifts to the antenna elements, beginning with a single MSPA that is fed from underneath through aperture coupling by an SIW interconnect. This becomes the building block for the 2x2 square planar array. After optimizing performance as an array, a wrap-around interconnect network must be developed to bring four parallel SIW output channels from the SIW Butler Matrix to feed four elements. This new SIW to planar array transition is proposed in this for the first time and enables creation of a fully-integrated planar antenna system with the modified Butler Matrix proposed in Chapter 3.

### 4.1: Slot-fed Microstrip Patch Antenna Design

Microstrip patch antennas are well-known [14] as a low-cost, low-profile printed antenna element. Consisting of a metallic patch on top of a dielectric substrate with a ground plane on the bottom, microstrip patch antennas had historically been edge fed by a microstrip transmission line or probe fed with a coaxial transmission line. This is until 1985, when [40] presented a contactless means to couple a transmission line to a patch on a parallel substrate through an opening in the ground plane. Aperture-coupling has gone on to be considered the best means for transitioning from an SIW, with an inherent ground plane as its top wall, to a microstrip patch antenna while avoiding loss- and discontinuity-prone junctions.

To begin design, the simulation environment must now take into account a multilayer substrate to allow for vertical coupling between the end of an SIW line and the patch element. An identical Rogers RO4350B substrate layer is selected for the antenna layer ( $t_{\text{sub}}=0.254\text{mm}$ ,  $\epsilon_r=3.66$ ,  $\tan \delta=0.0037$  @ 10 GHz, 1oz copper with thickness  $t_{\text{copper}}=35\mu\text{m}$ ) as was used for the SIW feed

network, but requires a bonding layer to adhere to the upper copper wall of the SIW. Rogers RO4450B ( $t_{\text{bond}}=0.2032\text{mm}$ ,  $\epsilon_r=3.54$ ,  $\tan \delta=0.004$ ) is chosen to bond the two RO4350B substrates together. Fig. 4-1 illustrates the PCB stack-up containing the SIW layer adhered to the antenna layer.

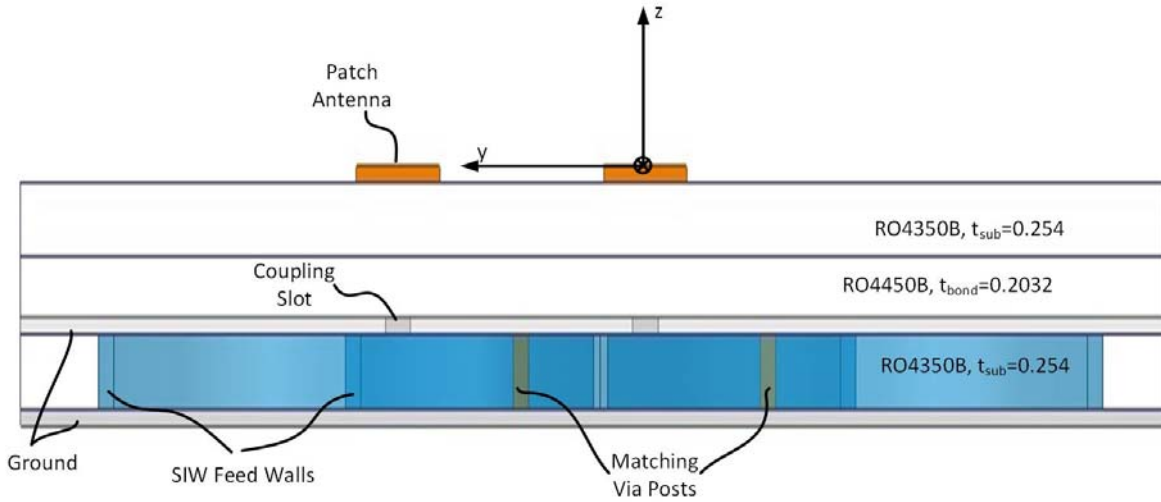


Fig. 4-1: Side view of the transition to the  $2 \times 2$  square planar array showing the dielectric stack-up. (Dimensions in mm.)

Well-known design equations from [14] were used to calculate the microstrip patch antenna width

$$w_{\text{ant}} = \frac{\lambda}{2} \left[ \frac{\epsilon_r + 1}{2} \right]^{-1/2} \quad (4.1),$$

which is calculated at resonance, and the patch length

$$l_{\text{ant}} = 0.5 \frac{\lambda}{\sqrt{\epsilon_r}} - 2\Delta L \quad (4.2),$$

where

$$\Delta L = 0.412 \frac{(\epsilon_{re} + 0.3) \left( \frac{w_{\text{ant}}}{t_{\text{sub}}} + 0.264 \right)}{(\epsilon_{re} - 0.258) \left( \frac{w_{\text{ant}}}{t_{\text{sub}}} + 0.8 \right)} \quad (4.3),$$

and

$$\epsilon_{re} = \frac{\epsilon_r + 1}{2} + \frac{\epsilon_r - 1}{2} \left( 1 + \frac{10t_{sub}}{w_{ant}} \right)^{-0.5} \quad (4.4).$$

Using an equivalent dielectric constant of  $\epsilon_r=3.61$  (to account for the stacked dielectric constants and thicknesses), the initial calculated dimensions are  $w_{ant}=1.646\text{mm}$  and  $l_{ant}=0.917\text{mm}$ .

A longitudinal orientation with matching post was chosen for the coupling slot at the end of each SIW feed. As shown in [42], this slot topology allows for a shorter distance ( $\sim\lambda_g/4$ ) from the back wall to the center of the coupling aperture than a transverse configuration. Given the chosen SIW parameters presented in Section 3.1.; this smaller spacing ensures that when put in the planar array configuration, the patch antenna elements may be placed with a separation  $\leq \lambda_0/2$ . The authors of [42] expressed the need for a great deal of dimension optimization using an EM solver tool to combine the resonance frequencies of the patch and the slot, but gave guidelines for selecting initial parameters.

To begin, the suggested starting slot dimensions are a length of  $l_{slot}=0.5\lambda_g=1.575\text{mm}$  and width  $w_{slot}=0.1\lambda_g=0.315\text{mm}$ . The aperture is centered below the midline of the patch and a matching post via (with diameter  $d=152.4\mu\text{m}$ , same as SIW wall vias) is placed on the same centerline on the opposite side of the SIW. Fig. 4-2 provides a clear illustration of the orientation of the patch, slot, and matching post with respect to the SIW line. The centerline is initially set  $P_x=\lambda_g/4=0.788\text{mm}$  from the back wall. The matching via also begins  $P_y=\lambda_g/4=0.788\text{mm}$  from the side wall, and the patch and slot center point are tethered at a distance  $P_{slot}=\lambda_g/2=1.575\text{mm}$ .

The HFSS optimization tool was used to search for the best combination of dimensions and locations to ensure resonance at 60 GHz, reduce return loss, and maximize broadside ( $\theta=0^\circ$ ) gain. The patch dimensions changed to  $W_{ant}=1.12\text{mm}$ ,  $L_{ant}=0.771\text{mm}$ , the slot to  $L_{slot}=1.51\text{mm}$ ,  $W_{slot}=0.287\text{mm}$ , post located at  $P_x=0.935\text{mm}$ ,  $P_y=0.866\text{mm}$ , and pulled the slot and patch closer

to the post  $P_{\text{slot}}=1.21\text{mm}$ . Most striking was the 32% reduction in the width of the patch antenna, but a similar shift was seen in [42] for the longitudinal orientation. The results were a return loss of 14.81dB at 60 GHz with a 10dB bandwidth of 15.46 GHz (plotted in Fig. 4-3), a peak realized gain of 5.88dB, a radiation efficiency of 95%, a half power beam width (HPBW) of  $113^\circ$ , and front-to-back ratio of 12.5dB. Fig. 4-4 and Fig. 4-5 plot the normalized simulated 60 GHz E-plane and H-plane field patterns, respectively, for the element with comparison to an ideal microstrip patch antenna pattern [14], and Fig. 4-6 visualizes the simulated 3-D field pattern at 60 GHz.

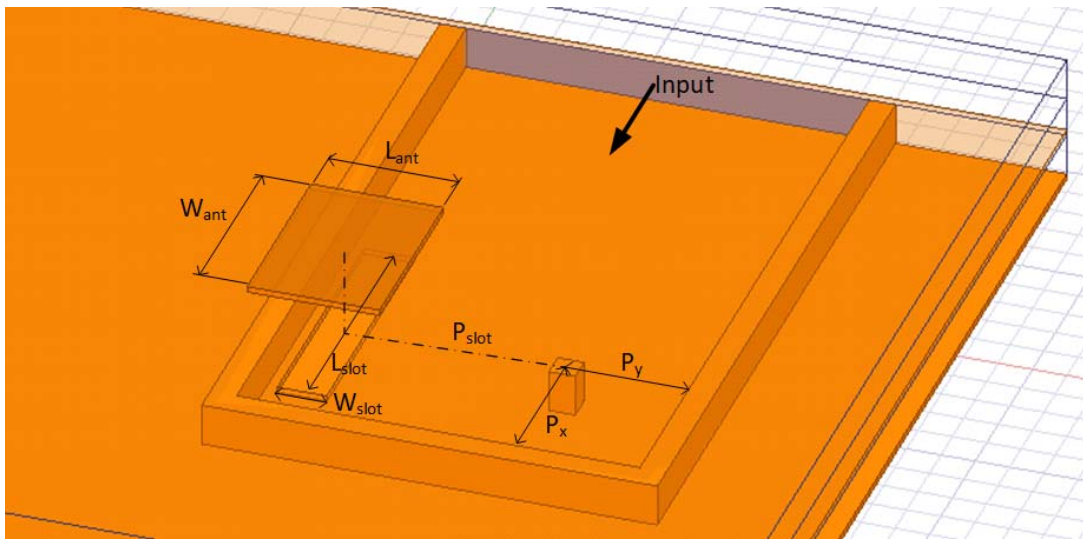


Fig. 4-2: Layout of microstrip patch antenna, coupling slot, and matching post illustrating longitudinal orientation with respect to the SIW feed.

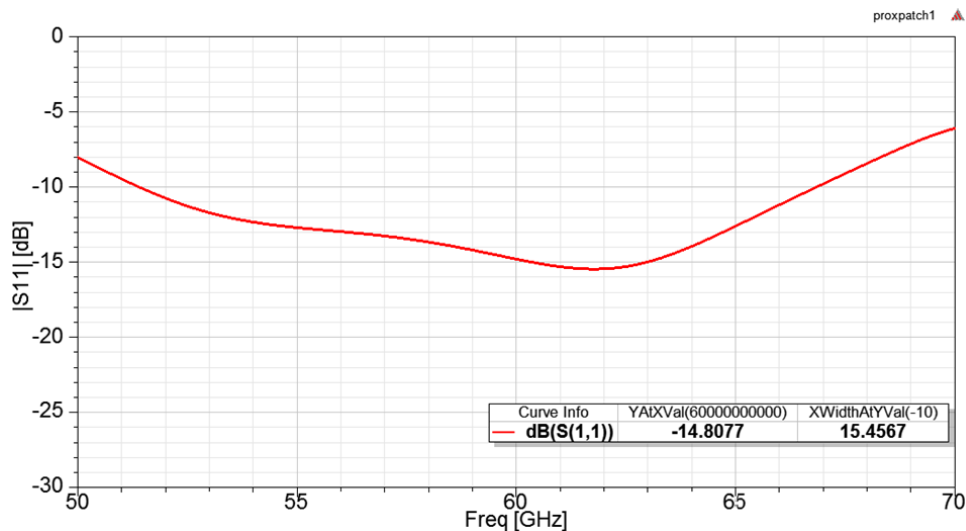


Fig. 4-3: Plot of RL for the optimized patch antenna element of Fig. 4.2.

### E-plane Antenna Pattern, $\phi = 90^\circ$

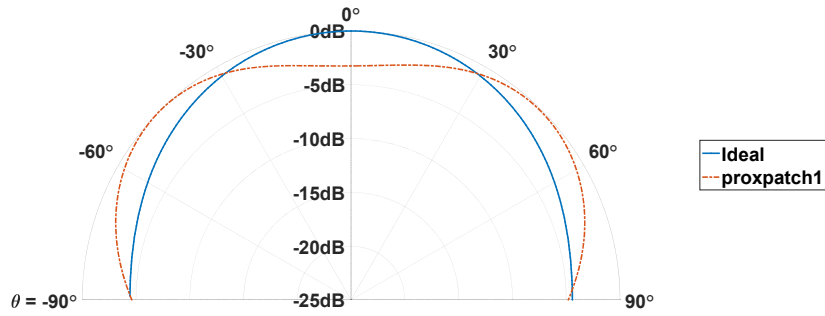


Fig. 4-4: Plot of normalized E-plane ( $\phi=90^\circ$ ) radiation pattern for the designed microstrip patch antenna. Ideal patch antenna pattern is plotted for comparison.

### H-plane Antenna Pattern, $\phi = 0^\circ$

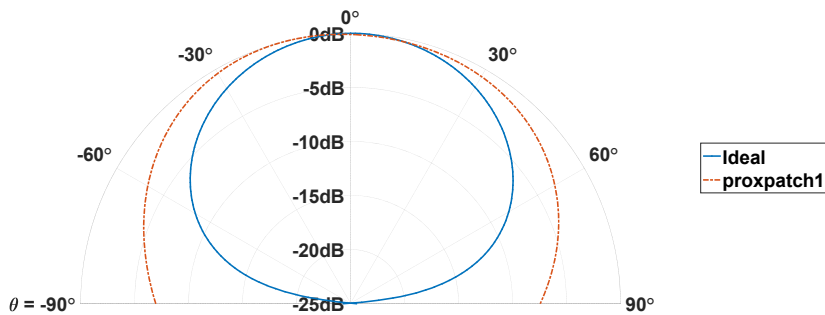


Fig. 4-5: Plot of normalized H-plane ( $\phi=0^\circ$ ) radiation pattern for the designed microstrip patch antenna. Ideal patch antenna pattern is plotted for comparison.

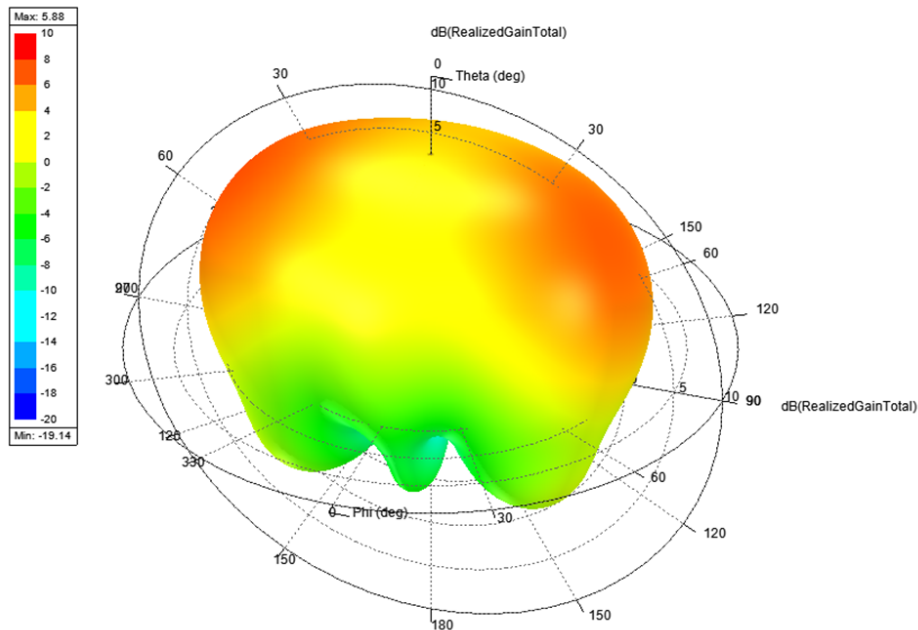
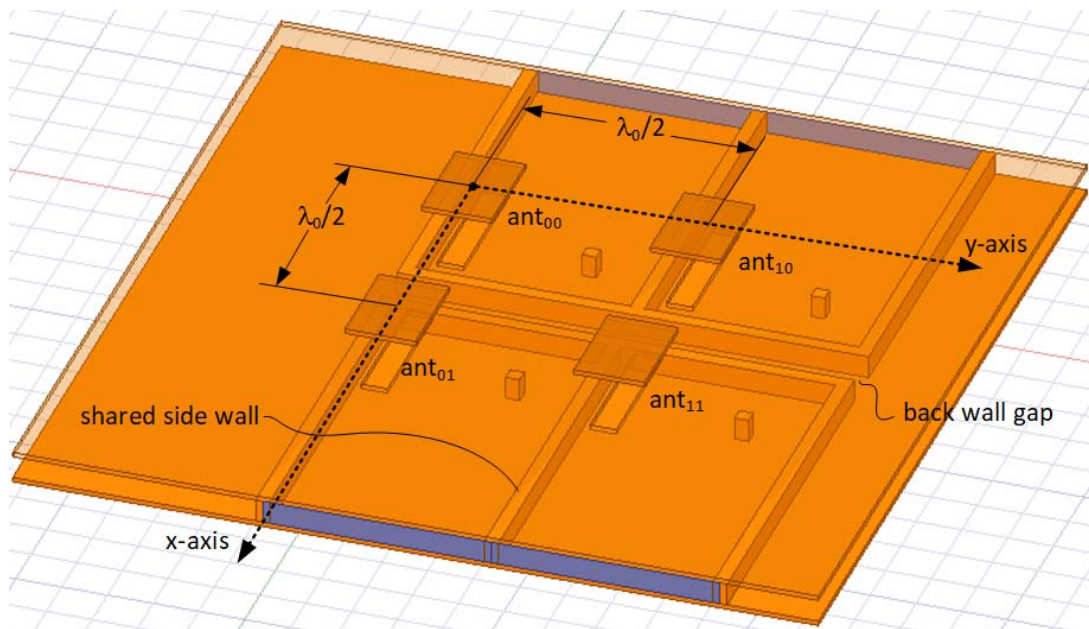


Fig. 4-6: Simulated 3-D field pattern of a single patch antenna element.

## 4.2: Square Planar Array

The microstrip patches get placed in a planar array configuration, with equidistant  $\lambda_0/2$  spacing for each node along the x- and y-axes, as previously described in Chapters 1 and 2. To achieve equal  $\lambda_0/2$  axial spacing between elements but to maintain the same orientation with respect to the feed approach, the four feed/element subsystems are first grouped into pairs that each share an SIW feed wall, antennas  $ant_{00}/ant_{10}$  and  $ant_{01}/ant_{11}$  in Fig. 4-7, to take advantage of the SIW line width  $a=2.5\text{mm}=\lambda_0/2$  for y-axis spacing. Then, the SIW back walls of each pair is separated to achieve x-axis  $\lambda_0/2$  spacing: given the center point of each antenna, slot, and matching post is  $P_x=0.935\text{mm}$  from the back wall, and the wall via diameters are  $d=152.4\mu\text{m}$ , the gap between back walls is  $0.325\text{mm}$ .



*Fig. 4-7: Initial layout of the 4 patch antennas in the square planar array configuration.*

First simulated results from this combination with no phased inputs resulted in a broadside pattern featuring 11.1dB realized gain, 15.6dB return loss for all ports at 60 GHz with a 10dB bandwidth of 15.3 GHz, 97% radiation efficiency, and  $52^\circ$  HPBW. Using pattern multiplication

of the single element with the ideal square planar array factor from Eqn (2.6) with no  $\alpha_i$ 's, an 11.2dB broadside realized gain and 15.1dB return loss should be expected, so these results confirm the initial array design is feasible. Fig. 4-8 depicts the 3-D broadside gain pattern of the square planar array.

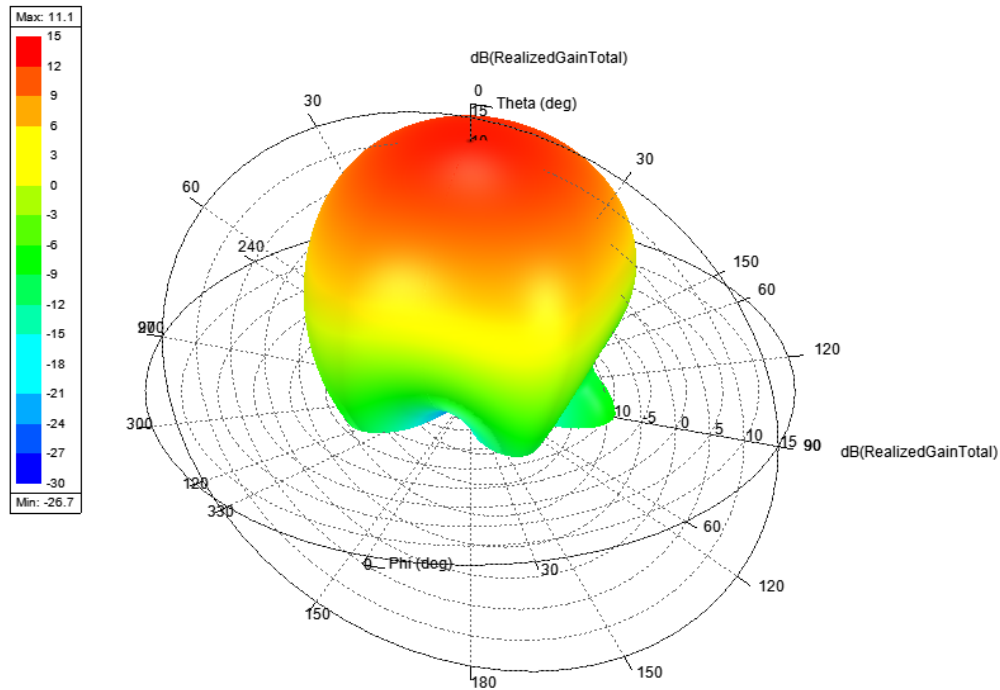


Fig. 4-8: 3-D broadside gain pattern for the square planar array.

Second, the expected phased outputs from the Butler Matrix are set as sources to the array to evaluate beam performance directed away from broadside ( $\theta \neq 0^\circ$ ). Port 1 Butler Matrix output phases from Eqn (3.14),  $\{\alpha_{00|1} = -2.69^\circ, \alpha_{10|1} = 84.63^\circ, \alpha_{11|1} = 166.18^\circ, \alpha_{01|1} = 92.39^\circ\}$ , were applied as the input sources of the planar array. The peak gain of 9.09dB, seen in the 3-D field pattern of Fig. 4-9, has a HPBW=68° and occurred at  $\theta_{0|1} = 36^\circ, \phi_{0|1} = 231^\circ$ , compared with a goal of  $\theta_{0|1} = 45^\circ, \phi_{0|1} = 225^\circ$ . Table 4-1 summarizes the simulated antenna performance corresponding to the designed modified Butler Matrix outputs. Generally, the gain is lower by 2dB and HPBW increases

by 13-16°, which is consistent with reported expectations when moving the beam away from the broadside projection.

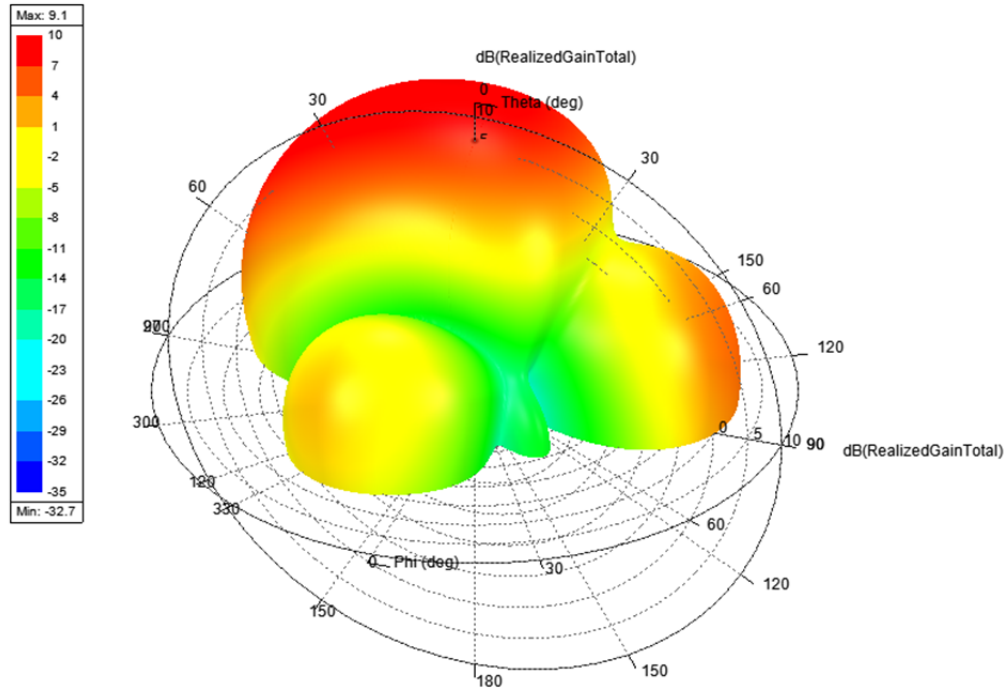


Fig. 4-9: 3-D field pattern of the square planar array with simulated Port 1 excitation from the Modified Butler Matrix.

Table 4-1: SIMULATED PEAK ANTENNA PARAMETERS FOR THE SQUARE PLANAR ARRAY WITH DESIGNED MODIFIED BUTLER MATRIX OUTPUTS.

Input Port $i$	Expected $\theta_{0i}, \phi_{0i}$	Simulated $\theta_{0i}, \phi_{0i}$	Gain	HPBW
1	45°, 225°	36°, 231°	9.08dB	68°
2	45°, 45°	39°, 47°	9.06dB	65°
3	45°, 315°	38°, 313°	9.03dB	65°
4	45°, 135°	36°, 129°	9.09dB	68°

### 4.3: Planar Array Feed Design

The last design step for the array is to create a transition from the adjacent BM outputs (Ports 5-8 in Fig. 3-18) all on one side to the 2x2 planar array (antennas  $ant_{00}/ant_{10}$  and  $ant_{01}/ant_{11}$  in Fig. 4-7). The planar array configuration requires some feeds to be longer than others given the parallel output SIW lines from the Butler Matrix circuit. To implement the design, the inner output lines (Ports 6-7 from Fig. 3-18) are fed directly to elements  $ant_{01}$  and  $ant_{11}$  while the feeds to  $ant_{00}$  and  $ant_{10}$  are wrapped around to the other side of the array while sustaining the SIW width and to maintain the relative orientation of the array elements. The wraparound feed design can be seen in Fig. 4-10. To ensure these outer feeds do not disturb the designed phase differentials from the BM, the extended length of each guide, i.e., labeled as  $l_{00}$  and  $l_{01}$  starting from the dashed reference line  $EE'$  in Fig. 4-10, should be close to a multiple of  $\lambda_g$ . The path for measuring these extended lengths is the longitudinal symmetry line in the mid-width of each SIW to the center marking line going through each coupling aperture and its adjacent via post. Based on the physical array dimensions, the initial design guess for  $l_{00}$  and  $l_{10}$  was  $3\lambda_g$ .

The HFSS optimization tool was used to initially tune the lengths of the feed lines to provide the desired phases to the corresponding coupling apertures. The inner SIW feeds are  $0.797\lambda_g$  from the reference line  $DD'$  (see Fig. 4-10) to the shared back wall. Feeds to the corresponding back walls of  $\alpha_{00i}$  and  $\alpha_{01i}$  are  $3.837\lambda_g$ , extending just beyond the initial guess to compensate for the turns around the array. This additional length is accounted for in design simulations, with all four elements confirmed to be in phase with respect to the  $DD'$  reference line.

Once the feed lines were confirmed to be in phase, initial simulated S parameters for the antenna subsystem yielded reflections of about -16dB and isolation between ports to be -16 to -30dB. The return loss and isolation results with respect to Port 1', in this case the feed line to antenna element

ant<sub>00</sub>, are plotted in Fig. 4-11a. Broadside realized gain ( $\alpha_i=0^\circ$ ) was simulated to be 10.5dB at 60 GHz. A final parameter search and optimization routine was needed to improve the reflection and isolation results while keeping feed lines in phase and maintaining antenna broadside gain.

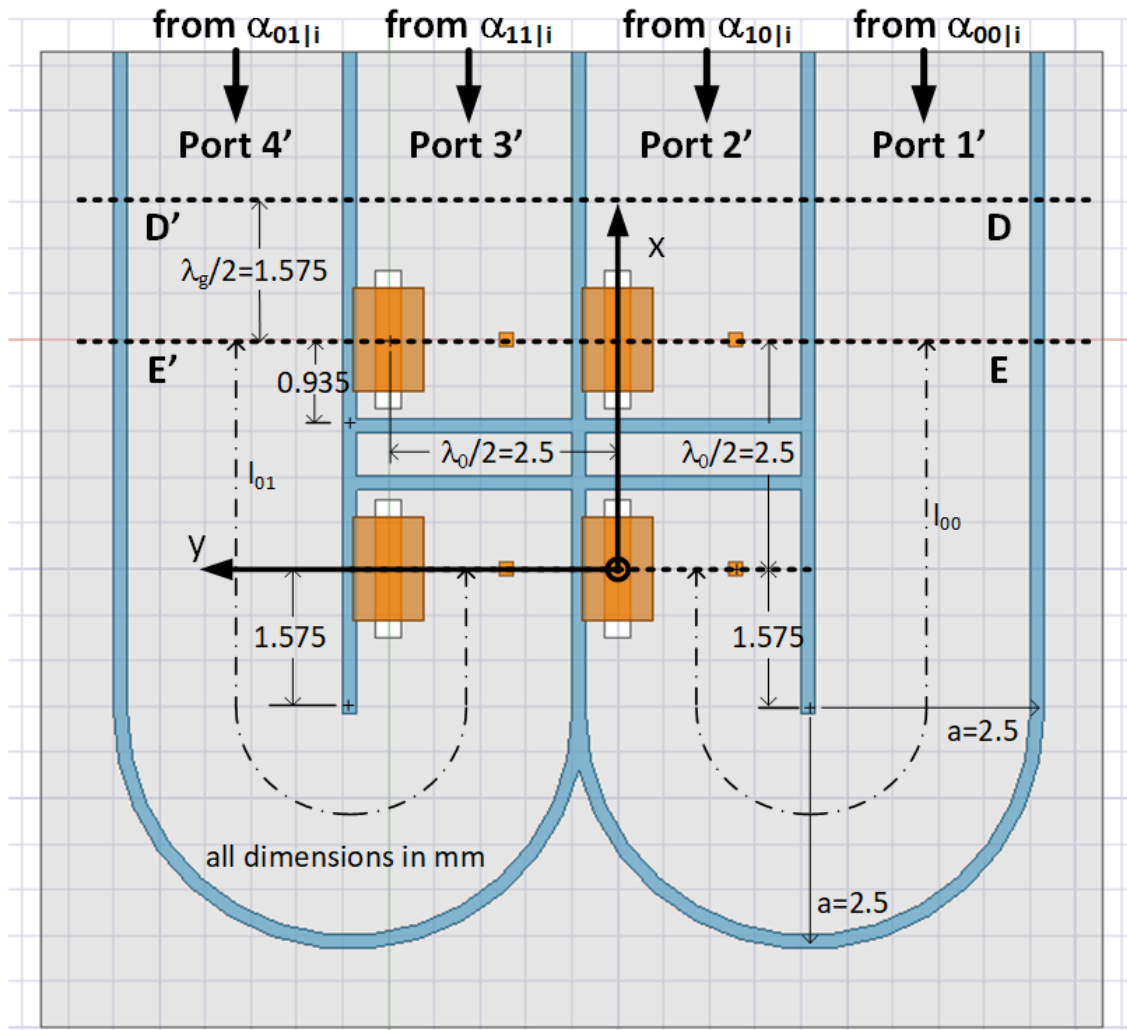


Fig. 4-10: Top view of the transition to the 2x2 square planar array noting feed dimensions and orientation with respect to the reference location of the array.

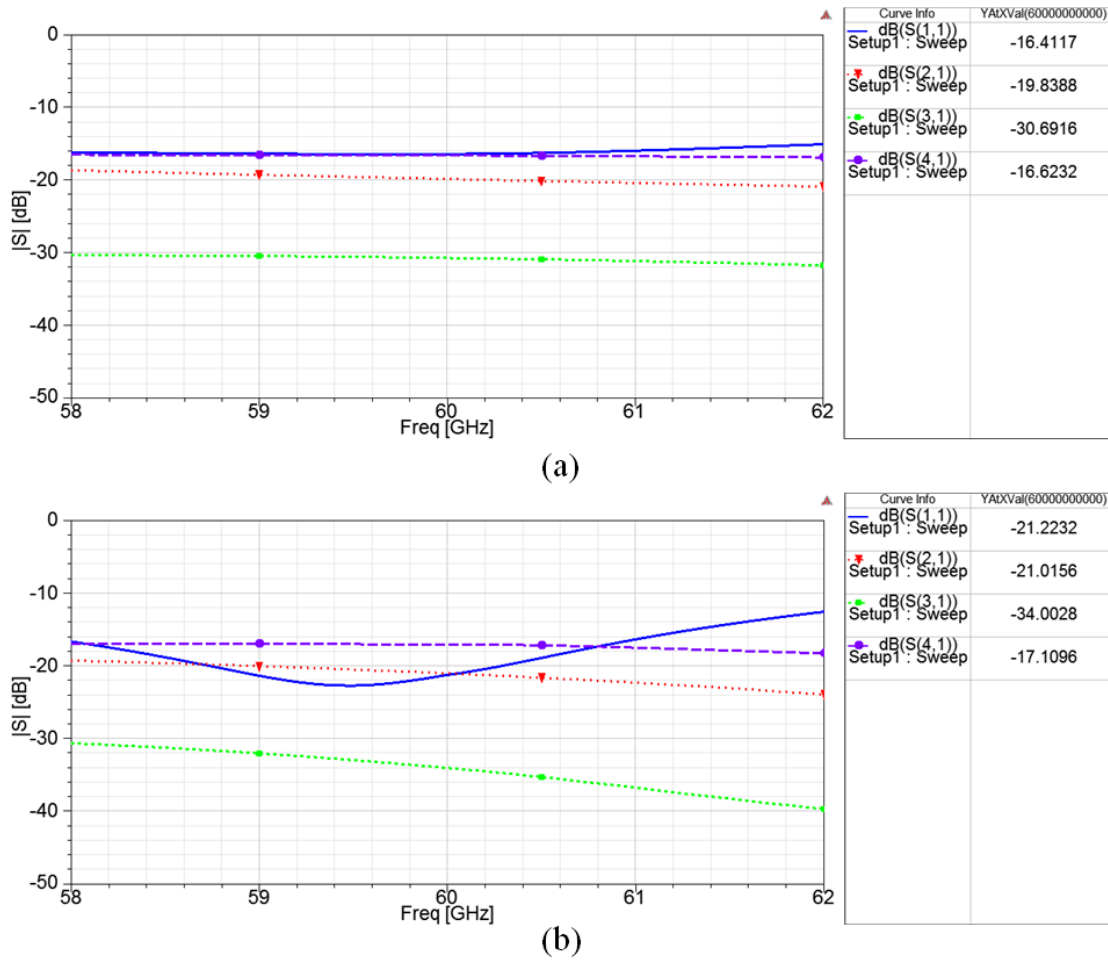


Fig. 4-11: Reflection and isolation S-parameters of the feed transition from the Butler Matrix to the 2x2 square planar array for a) the initial design and b) the final design.

The HFSS parametric search tool was used to evaluate variations in the return loss for each feed at the reference line EE' when  $l_{00}$  and  $l_{01}$  were concurrently swept from  $2.96\lambda_g$  to  $3.04\lambda_g$ . Fig. 4-12 plots the magnitude and phase for  $S'_{11}$  (reflections on Port 1', corresponding to feed  $l_{00}$ ) as a sample, since this is the case with the most sensitivity to the feed length. In general, the impact on the return loss was minimal over all variations. From simulations it was observed that typically  $S'_{11}$  (Fig. 4-12a) and  $S'_{44}$  (reflections on Port 4', the feed to  $ant_{01}$ ) were 0.3-0.5dB more than the return loss corresponding to inner feeds for  $ant_{10}$  and  $ant_{11}$  elements, which is expected given the extended length. Fig. 4-12b plots the  $S'_{11}$  phase seen on the  $l_{00}$  feed for 3 different lengths. Phase

variations of  $-13^\circ$  and  $+16^\circ$  compared to  $\lambda_g/2$  can be seen at 60 GHz when the extremes of the search lengths are reached  $l_{00}=2.96\lambda_g$ ,  $l_{01}=3.04\lambda_g$ . The best performing combination occurred at  $l_{00}=2.99\lambda_g$ ,  $l_{01}=2.97\lambda_g$ .

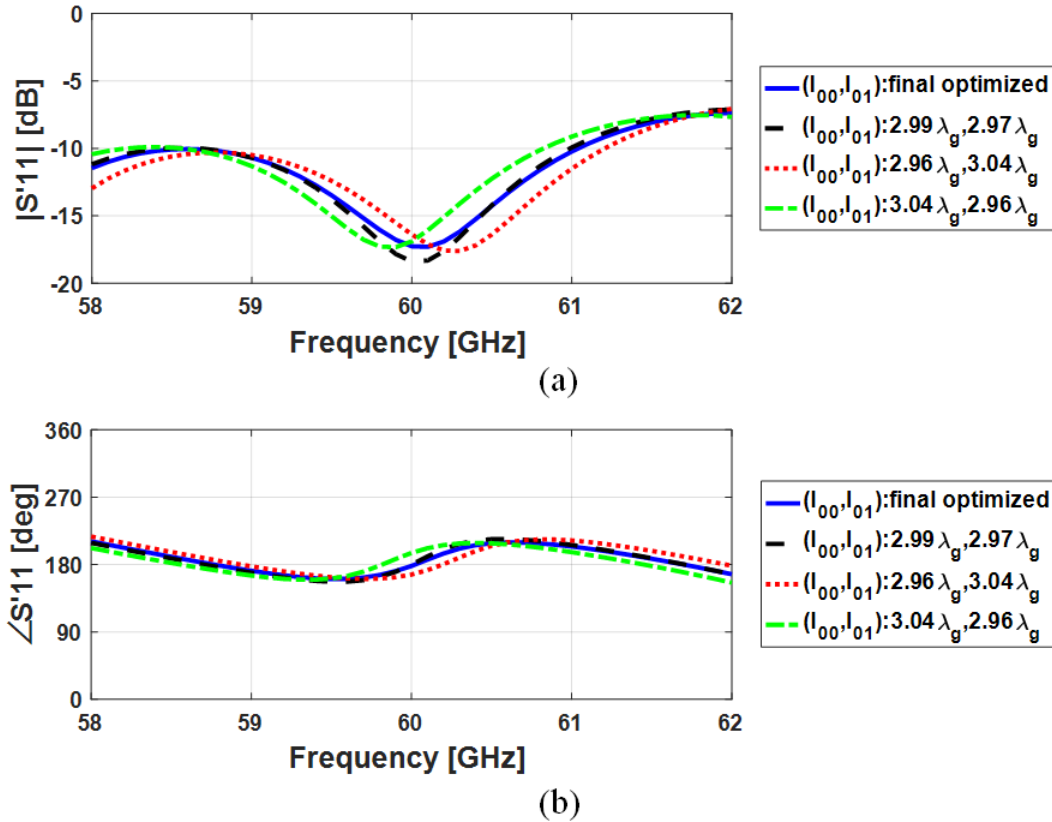


Fig. 4-12: Plot of  $S'_{11}$  (a) magnitude, and (b) phase, corresponding to the transition feed  $l_{00}$  for key combinations of searched feed lengths.

The final HFSS optimization step used the antenna size and location, slot dimensions and location, grounding via post location, and the feed line lengths as constrained tuning variables. Interestingly, several changes helped improve the reflection parameter and isolation between ports to  $-21\text{dB}$  and  $-17$  to  $-34\text{dB}$ , respectively, as seen in Fig. 4-11b. Even the broadside gain saw a modest improvement to  $10.8\text{dB}$ . Most notably, the patch dimensions increased to  $W_{\text{ant}}=1.21\text{mm}$  and  $L_{\text{ant}}=0.842\text{mm}$  while the distance from the back SIW wall to the patch center (also the center of the via post and slot) lengthened to  $1.184\text{mm}$ . Extending the distance to the back wall had an

interesting effect: the gap between back feed walls has disappeared and now SIW feeds share both side and back walls, making implementation of the via walls much simpler and reduces the fabrication cost. Final dimensions for  $l_{00}$  and  $l_{10}$  were found for the fully-integrated antenna system (solid blue curves in Fig. 4-12), yielding values of  $2.993\lambda_g$  and  $2.976\lambda_g$ , respectively, which are very close to the best performing search combination (dashed black curve in Fig. 4-12).

The new dimensions are updated in Fig. 4-13 and Table 4-2 summarizes all the dimension changes from the single MSPA element to the planar array with full feed lines. Now that all components have been designed, the pieces must be assembled together into the full beam-switching system.

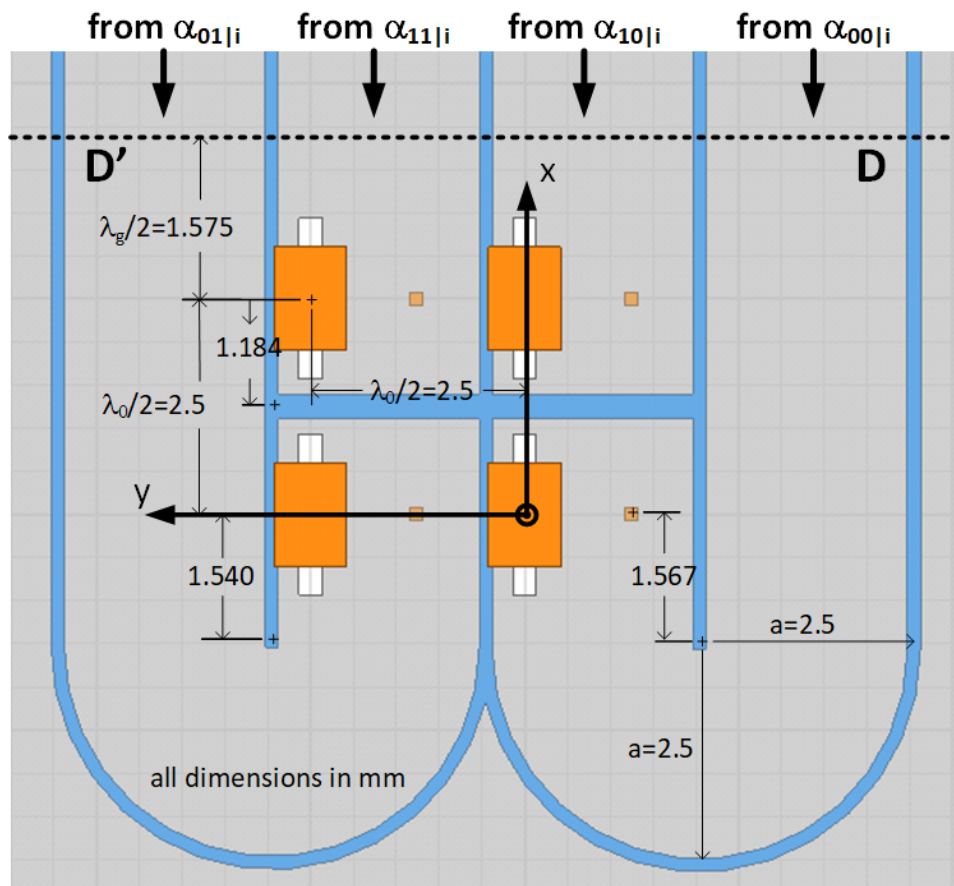


Fig. 4-13: Top view of the transition to the 2x2 square planar array with updated dimensions.

*Table 4-2: COMPARISON OF ANTENNA, SLOT, AND MATCHING VIA POST DIMENSIONS AND LOCATIONS IN THE PLANAR ARRAY CONFIGURATION.*

<b>Dimension</b>	<b>Single MSPA</b>	<b>Planar Array with Transitional Feed Lines</b>
<b><math>W_{ant}</math></b>	1.119mm	1.206mm
<b><math>L_{ant}</math></b>	0.771mm	0.842mm
<b><math>W_{slot}</math></b>	0.286mm	0.268mm
<b><math>L_{slot}</math></b>	1.510mm	1.865mm
<b><math>P_x</math> (dist to back wall)</b>	0.935mm	1.184mm
<b><math>P_y</math> (from post to side wall)</b>	0.866mm	0.882mm
<b><math>P_{slot}</math> (from patch, slot to post)</b>	1.211mm	1.166mm
<b>Feed length (from DD' to back wall)</b>	2.510mm	2.759mm (ant <sub>10</sub> , ant <sub>11</sub> ) 12.188mm (ant <sub>00</sub> ) 12.135mm (ant <sub>01</sub> )

#### **4.4: Connecting Butler Matrix to the Planar Array**

Finally, the Butler Matrix (design from Chapter 3) and antenna subsystems will be integrated to yield the final system build. Previous design steps for the planar antenna array have already taken the physical dimensions of the Butler Matrix circuit into account with regards to the adjacent output SIW feeds and how they become the input feeds to the antenna elements. The process of connecting the Butler Matrix to the array, though, is not a simple matter of cut-and-paste within the CAD layout tool. Additional dielectric layers must be introduced to the Butler Matrix circuit since the planar array is a multi-layer circuit with the antenna elements on the topmost metal layer (see Fig. 4-1). These layers (the antenna dielectric as well as a bonding substrate) on top of the Butler Matrix mean the phase shifters must be moved to the bottom SIW wall so that they are open to free space and not covered by the dielectric layers. It is critical, though, to confirm that there is no performance degradation from the union of the two circuits: reflections can be introduced from

an impedance mismatch not seen during simulations of the subsystems or from the rearrangement and introduction of many more potential discontinuities.

The layout of the joined subsystems can be seen in Fig. 4-14 and intuitively it seems that new coupling impedance will be minimal since the circuits have similar connections (the SIW lines were designed with a constant width  $a=2.5$  mm) and neither subsystem has metallic structures that impinges on the other. The full antenna prototype was simulated with HFSS. Return loss at 60 GHz for each port ranged from 17.5 to 25.2dB at 60 GHz, seen in Fig. 4-15, and isolation between ports ranges from 23.1 to 43.1dB, seen in Fig. 4-16, both matching well with the simulated performance of the Modified Butler Matrix. Given the feed lengths for the transition to the array elements presented in Section 4.3.; it is expected that the insertion loss for the integrated BM feed network and antenna array to be  $7.98\pm 0.86$  dB to elements  $ant_{10}$  and  $ant_{11}$ , and  $8.58\pm 0.86$  dB to elements  $ant_{00}$  and  $ant_{01}$ .

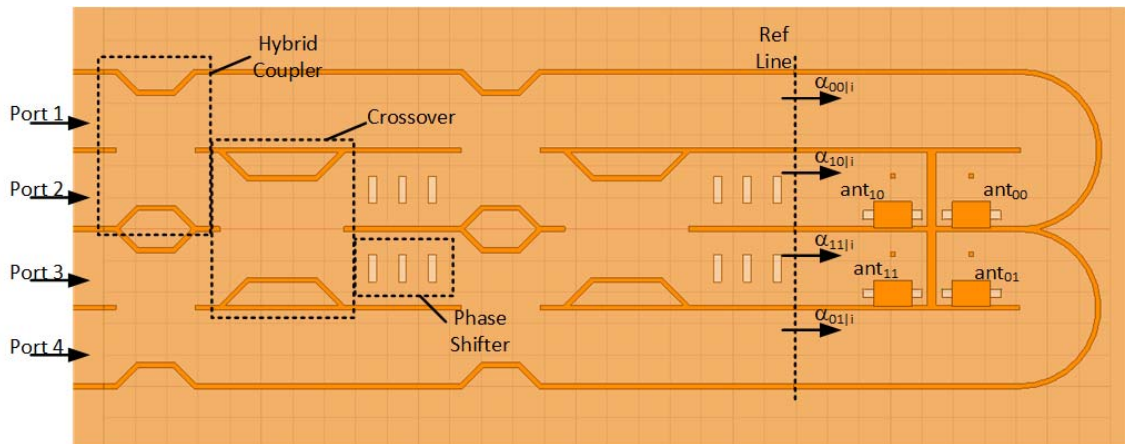


Fig. 4-14: Top view of layout for the fully-integrated antenna system design.

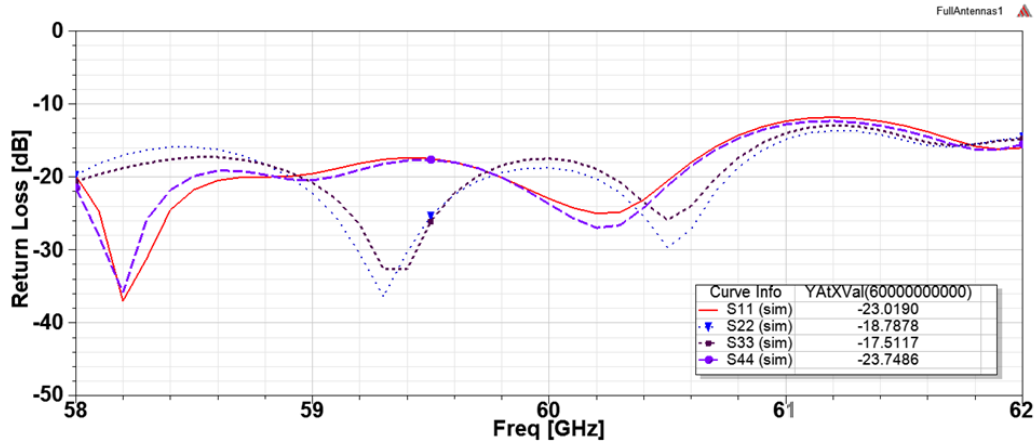


Fig. 4-15: Simulated return loss for all ports of the fully-integrated antenna array system.

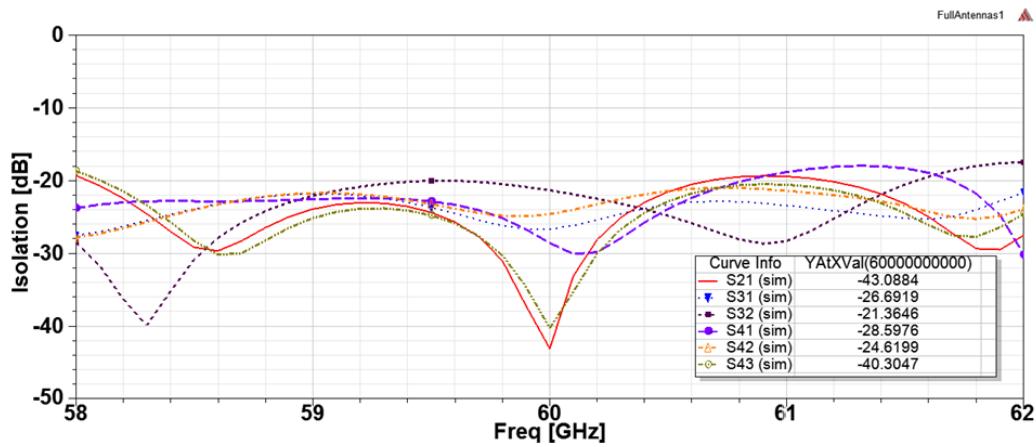


Fig. 4-16: Simulated isolation for all ports of the fully-integrated antenna array system.

Now that the two components are finally combined, the ultimate design goal of the project can be simulated to confirm the beam-switching capability of the antenna system with input microstrip-to-SIW transitions and feed lines. A virtual switch can be implemented by enabling the input ports one by one within HFSS. Polar plots of the  $\phi=45^\circ$  and  $\phi=135^\circ$  cut-planes are shown in Fig. 4-17 and Fig. 4-18, respectively, and demonstrate how each pattern cooperates with its complement pattern in  $\phi$ -direction – where one pattern peaks, the other has a null. The 3-D radiation patterns for each corresponding port are plotted in Fig. 4-19 to show how the beam pattern switches based on the applied input.

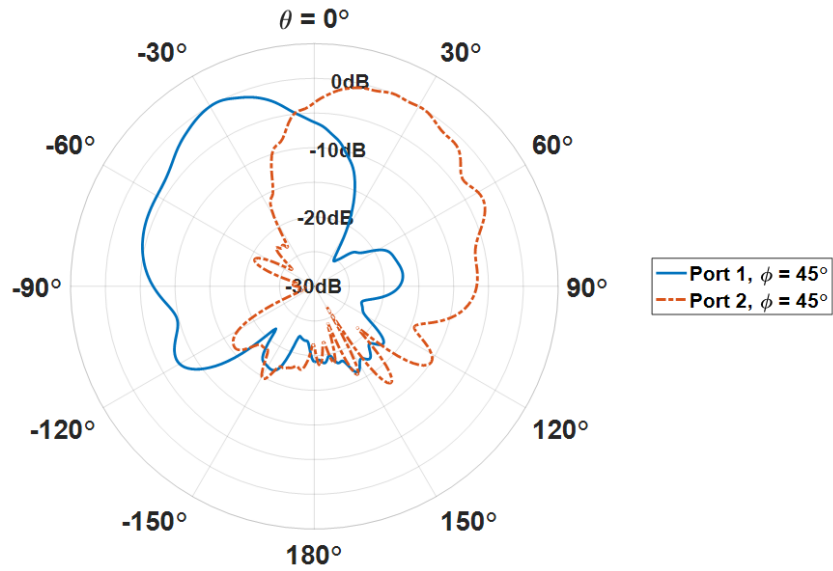


Fig. 4-17: Simulated polar plots of beam patterns resulting from signals applied to ports 1 and 2 of the antenna system prototype, for the  $\phi=45^\circ$  cut-plane.

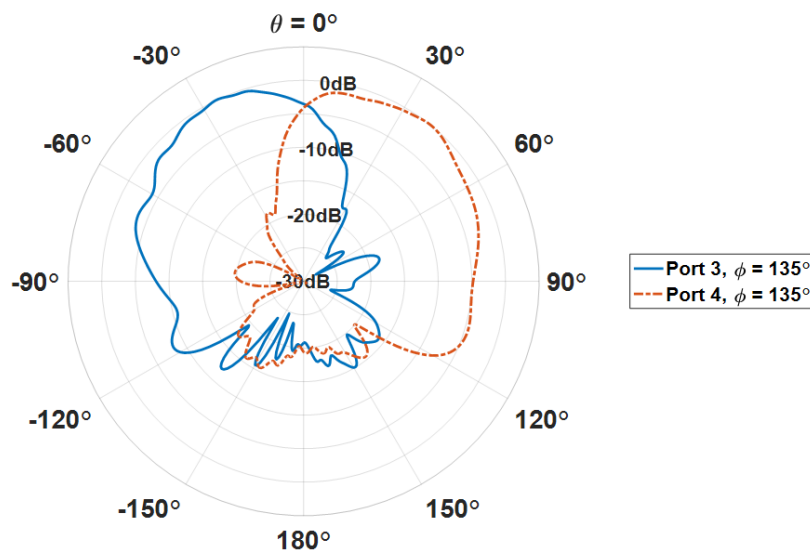


Fig. 4-18: Simulated polar plots of beam patterns resulting from signals applied to ports 3 and 4 of the antenna system prototype, for the  $\phi=135^\circ$  cut-plane.

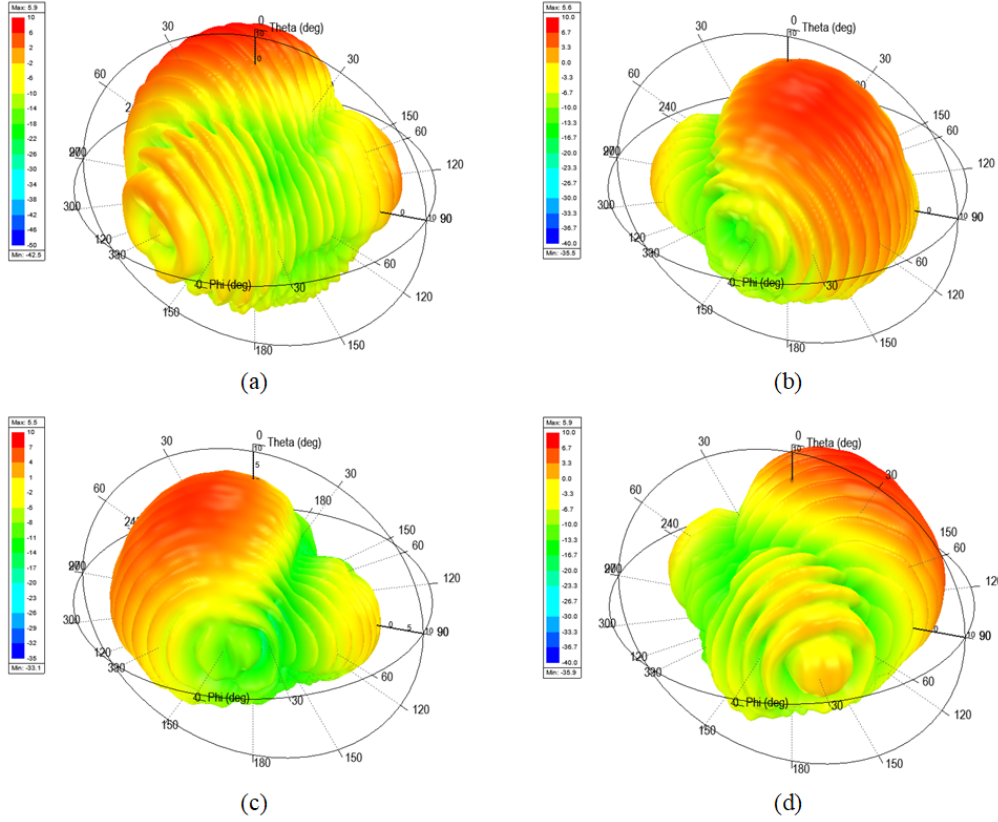
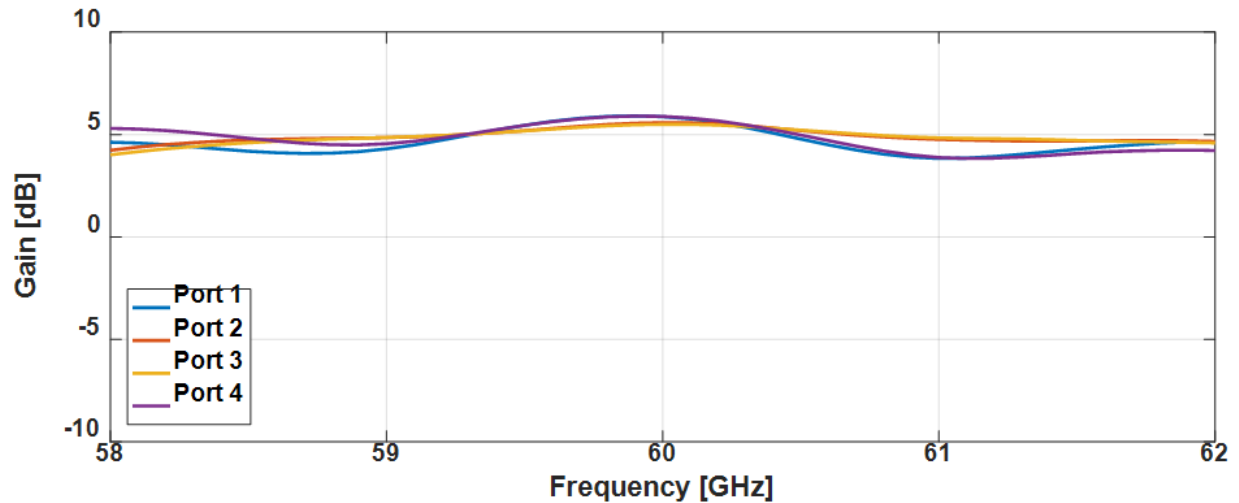


Fig. 4-19: 3-D gain patterns for all excitations to the fully-integrated antenna system: a) Port 1,  $\theta_{01}=31^\circ$ ,  $\phi_{01}=212^\circ$ ; b) Port 2,  $\theta_{02}=29^\circ$ ,  $\phi_{02}=41^\circ$ ; c) Port 3,  $\theta_{03}=26^\circ$ ,  $\phi_{03}=314^\circ$ ; and d) Port 4,  $\theta_{04}=28^\circ$ ,  $\phi_{04}=141^\circ$ .

The full-wave radiated field simulations confirmed the antenna system should perform as expected for the target 4 quadrant illumination, yielding switched patterns with beam angles of  $\{\theta_{01}=31^\circ$  and  $\phi_{01}=212^\circ$ ;  $\theta_{02}=29^\circ$  and  $\phi_{02}=41^\circ$ ;  $\theta_{03}=26^\circ$  and  $\phi_{03}=314^\circ$ ;  $\theta_{04}=28^\circ$  and  $\phi_{04}=141^\circ\}$ . Realized gain at the peak beam location ranged from 5.50-5.89 dB at 60 GHz and gain over frequency from 58 to 62 GHz (plotted in Fig. 4-20) is relatively flat averaging 5 dB with  $\pm 0.9$  dB variation. This lower gain is expected given the 7.98 to 8.58 dB IL for the array feed network and additional 1.76 dB IL per input microstrip transition and feed line. These losses prevent the full input power to the excitation port from reaching the elements themselves. The beams have a HPBW of  $36 \pm 2^\circ$  in the vertical ( $\phi = \phi_{0i}$ ) cut-plane and  $82 \pm 2^\circ$  in the horizontal ( $\theta = \theta_{0i}$ ) cut-plane.



*Fig. 4-20: Plot of simulated gain over frequency for all port excitations of the fully-integrated antenna system.*

The simulated beam patterns are compared with the ideal Modified Butler Matrix array factor patterns from Chapter 2 in Fig. 4-21, where it can be seen that the peak beam elevation angles have moved closer to broadside by  $14^\circ$  to  $19^\circ$ . This behavior is expected from the implementation of MSPA elements and their inherently directional field patterns, whereas the ideal array factor assumes omnidirectional point sources for elements. In the case where the antenna system is used as both transmitter and receiver, the SIR for each port excitation ranges from 5.8 to 24.8 dB.

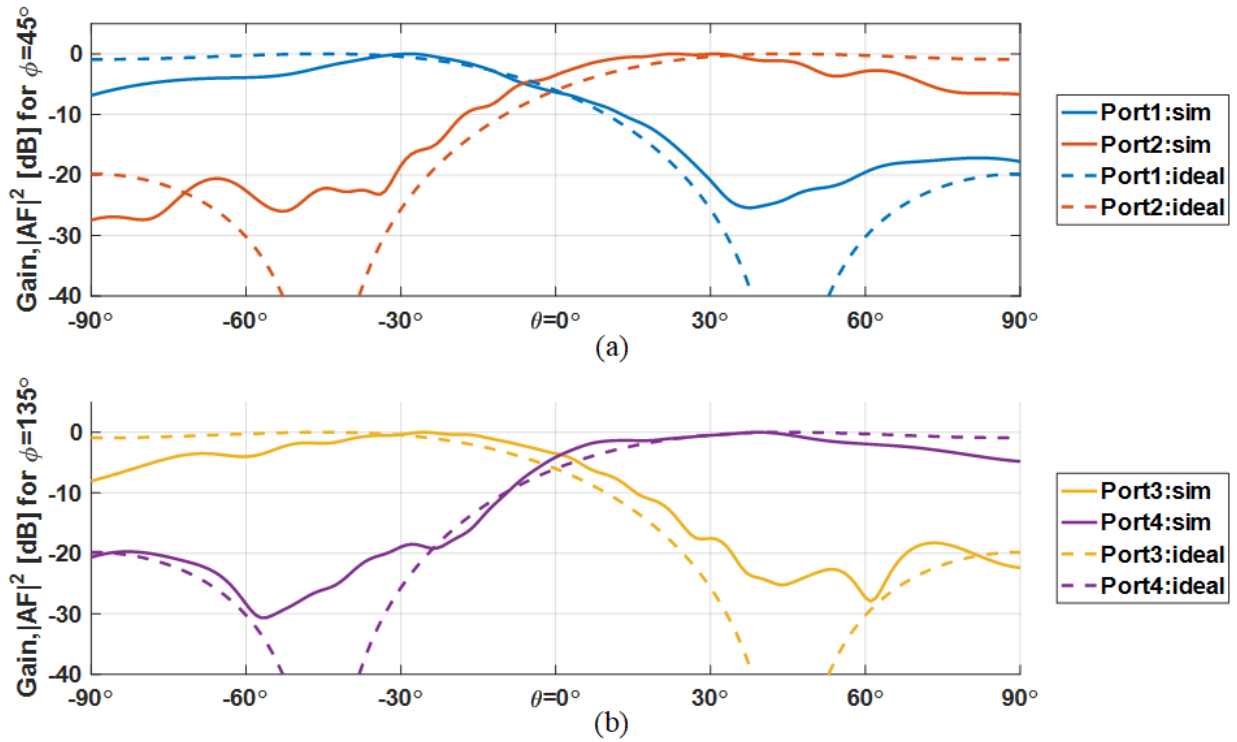


Fig. 4-21: Comparison of the array gain field pattern versus the ideal array factor for the Modified Butler Matrix in the a)  $\phi=45^\circ$  and b)  $\phi=135^\circ$  cut-planes.

Table 4-3 captures the steering direction for each beam and compares to the ideal and designed goals reported in previous chapters. With simulated beams that will distinctly meet the needs of the target application, the work moves to experimental evaluation. It should be mentioned here that the radiators are patch antennas that are not by nature narrow beam radiators. The ripples in the element radiation pattern that happen due to slight mismatches create drops in the pattern for the fully integrated system as well. A good measure to assess beam directions would be the 1.5 dB power band which yield the target beam contours as shown in Fig. 4-22.

Table 4-3: PEAK BEAM DIRECTIONS FOR ALL PORT EXCITATIONS FROM THE SIMULATED FULLY-INTEGRATED ANTENNA SYSTEM.

	IDEAL MODIFIED BUTLER MATRIX THEORY	SIMULATED MODIFIED BM WITH IDEAL AF	SIMULATED FULLY-INTEGRATED ANTENNA ARRAY
PORT	PEAK BEAM	PEAK BEAM	PEAK BEAM
1	$\theta_{01}=45^\circ, \phi_{01}=225^\circ$	$\theta_{01}=41.58^\circ, \phi_{01}=227.70^\circ$	$\theta_{01}=31^\circ, \phi_{01}=212^\circ$
2	$\theta_{02}=45^\circ, \phi_{02}=45^\circ$	$\theta_{02}=46.98^\circ, \phi_{02}=41.94^\circ$	$\theta_{02}=29^\circ, \phi_{02}=41^\circ$
3	$\theta_{03}=45^\circ, \phi_{03}=315^\circ$	$\theta_{03}=46.44^\circ, \phi_{03}=318.06^\circ$	$\theta_{03}=26^\circ, \phi_{03}=314^\circ$
4	$\theta_{04}=45^\circ, \phi_{04}=135^\circ$	$\theta_{04}=41.22^\circ, \phi_{04}=131.94^\circ$	$\theta_{04}=28^\circ, \phi_{04}=141^\circ$

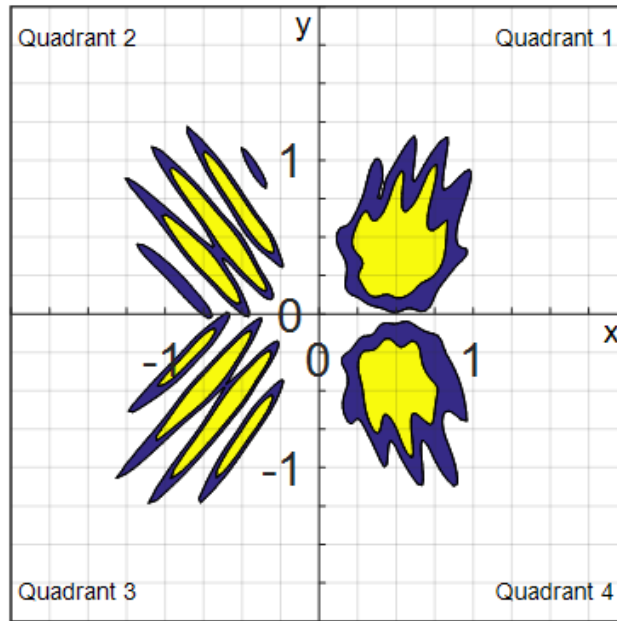


Fig. 4-22: Contour plot of the incident beam patterns on the target planar surface highlighting the 1.5dB power band.

## 4.5: Conclusion

The beam switching system was developed from a single MSPA element with aperture coupling from an SIW feed all the way to the fully-integrated 2x2 square planar antenna array with the Modified Butler Matrix feed network. The single designed element achieves a simulated gain of

5.9dB at 60 GHz, in line with conventionally expected 5-7dB gain for MSPAs. Implementation as a 2x2 square planar array with  $\lambda_0/2$  spacing was straightforward, demonstrating a clear single broadside beam with 11.1dB gain at 60 GHz when no phasing is used. Designing the interconnect between the Modified Butler Matrix and the planar array was a more complex endeavor, requiring two direct feed lines to the forward side of the array and two that wrap around the array to feed elements on the backside of the array. Two HFSS optimization routines were needed to ensure the performance of the antenna array, with a simulated gain of 10.8dB, reflections of -21dB, and isolation between ports of -17 to -34dB at 60 GHz.

When the antenna system is fully-integrated with the Modified Butler Matrix, peak beam locations are seen to move closer to broadside. This is due to the use of simulated MSPA elements instead of the ideal point sources assumed by the theoretical planar array factor equations. Still, illumination is confirmed in the four quadrants of the target surface application achieving peak gain values are 5.50-5.89 dB at 60 GHz. This lower gain is expected because of IL inherent to the BM design and additional losses introduced by the microstrip-to-SIW transitions and feed structures necessary for prototyping the antenna system design.

---

## Chapter 5: Experimental Evaluation of the Butler Matrix Design

The updates and modifications needed for a Butler Matrix to enable 2-D beam switching, as presented in Chapter 2, are implemented in two different materials for experimental evaluations. The first fabricated prototype is the conventional Butler Matrix architecture with updated phase shifters while the second prototype features the Modified Butler Matrix. Measured results are presented in their raw form as well as after de-embedding to analyze the effectiveness of the design for steering a 2x2 square planar array.

### 5.1: Material Considerations and Impact

The choice of substrate material for implementation of microwave and mm-wave systems brings about various cost and performance trade-offs. Choosing a low dielectric constant RF substrate, for instance, often helps lower losses but would increase wavelength dependent feature sizes and could be more expensive to use due to the extra fabrication processing steps that might be required. In the case of the mm-wave Butler Matrix, the material selection is even more critical due to the high frequency operation and the importance of obtaining balanced power division and the intended output phases for driving the planar array.

As an example, the first iteration of the presented work had assumed an industry standard prototyping material (Rogers RT/duroid 5880, aka RT5880) as its basis for simulations since it has a loss tangent ( $\tan \delta=0.0009$ ) with dielectric constant ( $\epsilon_r=2.20$ ) and is commonly used in high-frequency applications. The design called for the conventional Butler Matrix architecture (Fig. 2-10) since the natural phase delay of the crossover circuit ( $98.94^\circ$ ) with respect to the pass-

through was over the required phase shift needed for 2-D beam-steering ( $90^\circ$ ). A phase shifter was designed to compensate for  $8.94^\circ$  in the SIW pass-through and the total BM circuit was 20.81mm long by 10.01mm wide, a 56.8% circuit area savings over the design presented in [33].

When a second design was needed due to fabrication considerations (for multi-layer and fully integrated system implementation) that steered away from using RT5880 and switched to Rogers RO4350B ( $\epsilon_r=3.66$  and  $\tan \delta=0.0037$ ), the impact was significant enough to warrant a switch to the Modified Butler Matrix architecture (as seen in Fig. 2-14). The 2<sup>nd</sup> designed crossover circuit had a much smaller phase delay ( $50.8^\circ$ ), and so a phase shift of  $39.2^\circ$  was needed serially to achieve the  $90^\circ$  phase differential. This second iteration led to a total BM circuit footprint of 21.92mm long by 10.15mm wide, which is slightly (5.3%) longer than the first design, but the fabrication cost dropped from \$188 per board for RT5880 to \$21 per board for RO4350B. This Modified Butler Matrix still offers a 53.9% smaller circuit footprint over the 1-D beam switching Butler Matrix from [33].

## 5.2: First Fabricated Prototype

The first attempt in implementing the Butler Matrix prototype used Rogers RT/duroid 5880 ( $\epsilon_r=2.20$ ,  $\tan \delta=0.0009$  @ 10 GHz) with thickness  $t=0.254\text{mm}$  during simulation work. This dielectric had 0.5oz electrodeposited copper (thickness  $t=18\mu\text{m}$ ) on its top and bottom surfaces, which would be the upper and lower walls of the SIW lines. Input/output SIW feedlines that provide the interface between BM ports and the relatively bulky mm-wave connector required some meandering to ensure enough separation between the connector bases yet identical electrical lengths from the connector landing to the corresponding input or output of the Butler Matrix architecture. The final dimensions of the first Butler Matrix board with feed lines were 72.7mm

long by 46.2mm wide and 0.290mm thick, which is 3.5 times longer and 4.6 times wider than the BM circuit itself.

A local board fabrication house was chosen for prototype fabrication. They require Gerber files for production runs which include separate artwork files for each metallic layer as well as individual instruction files that annotate the coordinates of each drilling spot for a given hole type. To begin the Gerber file generation process, the HFSS simulation layout was exported to DXF file format and imported into AutoCAD. In AutoCAD, evenly-spaced vias can be drawn for the side walls of the SIW lines and drawing layers could be organized appropriately. The physical upper and lower metallic layers must have their own digital drawing layers and the via drilling sites must be noted on those layers and be accompanied by a specific drilling file. Specifically, layer 1 contained microstrip-to-SIW transitions for adding connectors, the via locations, and the apertures for the phase shifters while layer 2 just repeats the locations of the vias.

After these drawing layers are compiled in AutoCAD, the multi-layer DWG file is exported into Keysight's ADS to confirm manufacturability and generate the official Gerber files. In total, this prototype board design requires 5 different files to fully specify the fabrication job. These files are uploaded to the online the verification tool of the board fabrication vendor to check for design errors such as feature spacing, drill size, and geometric tolerances. The cost to create small quantities of this prototype board was relatively higher (\$188 per board) compared to common FR4 board fabrication due to extreme processing steps needed to work with RT5880. Since there are many holes to be drilled and plated with copper for the via walls of the SIW, the manufacturer must do a plasma wash to remove the excess substrate material. According to the board fabrication vendor input, the RT5880 dielectric substrate is PTFE, also known as Teflon, which scatters a lot in drilling and requires such plasma wash step.

Upon receiving the finished boards, 1.85mm edge mount connectors were soldered onto the input and output lines of the board. There was some difficulty finding suitable connectors as most lower cost connectors are designed to fit a 1.575mm thick PCB while the prototype board was only 0.290mm thick. A piece of vinyl ( $\epsilon_r=3.5-4.5$ ) approximately 1mm thick was used as a shim to keep the connectors upright and the pins aligned to the microstrip input/output traces. Fig. 5-1 shows the completely assembled first Butler Matrix prototype board.

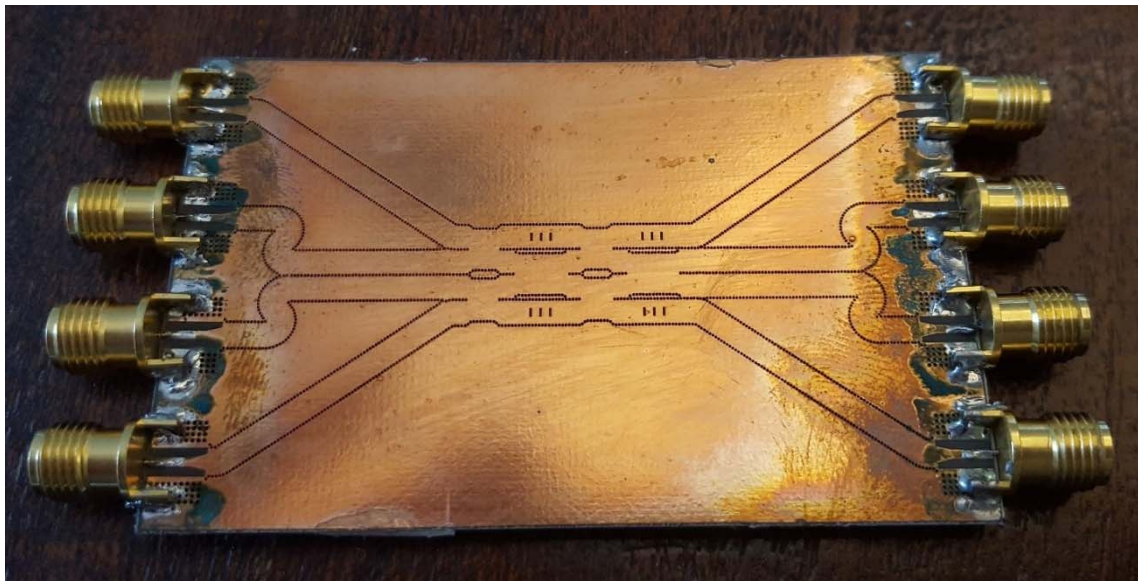


*Fig. 5-1: 1<sup>st</sup> fabricated Butler Matrix prototype implemented in RT5880.*

Scattering parameter measurements of the first Butler Matrix prototype were performed with a Keysight N5227A Network Analyzer. S-parameters were captured by connecting the VNA to 4 prototype connectors one at a time while terminating the other ports to  $50\ \Omega$  standards. S-parameter performance was generally very poor, measuring insertion loss at least 20dB greater than simulation results and wild swings in phase differentials over all ports. Measurement results are compared for a Port 1 to Port 6 connection in Fig. 5-2. These performance issues are believed to be due to nonideal and insufficient contact between the edge mount connectors and the microstrip traces, as well as the instability of these junctions while connected to the cables in measurements.

It was determined that a better connector solution and more robust integration method would be needed for the subsequent design iterations.

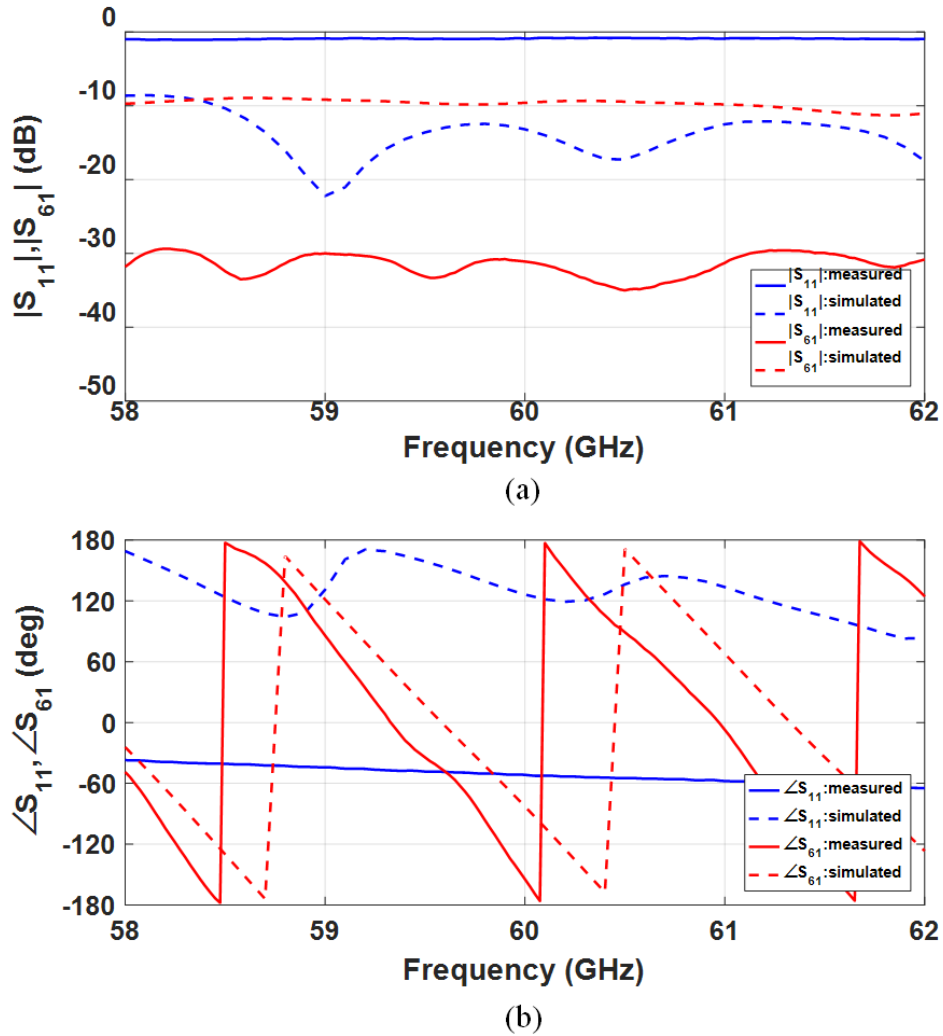


Fig. 5-2: Simulated and measured results for a) insertion and return loss, and b) transmission and reflection phases plots between Ports 6 and 1 for 1<sup>st</sup> Butler Matrix prototype.

### 5.3: Second Fabricated Prototype

There were several reasons to move away from using Rogers RT5880 for mm-wave prototyping, but the chief motivation was not directly-related to the Butler Matrix: the fabrication vendor was not able to bond a 2<sup>nd</sup> board to the PTFE material in RT5880, yet this capability is critical to the chosen stacked feed-antenna integration approach. This meant the alignment between the coupling

apertures at the antenna transition of the layer 2 (bottom board) and the antenna elements on layer 4 (upper board) could not be guaranteed since the boards had to be mounted by hand and somehow held in place with scotch tape. The other reason was avoiding the plasma wash processing cost.

Hence, a 2<sup>nd</sup> Butler Matrix design was prototyped on a 0.254 mm thick Rogers RO4350B laminate ( $\epsilon_r=3.66$ ,  $\tan \delta=0.0037$  @ 10 GHz) with 35 $\mu\text{m}$  thick electrodeposited copper on each side. With 4 inputs and 4 outputs, a total of eight 1.85mm female end-launch connectors are needed as seen in Fig. 5-3. These more expensive connectors are bolted onto the board and can tighten to a wide range of board heights, ensuring a much more stable hold to the prototype during testing. Each connector requires a microstrip landing and an accompanying microstrip-to-SIW transition structure. Finally, the prototype required equal lengths of SIW lines to route incoming and outgoing signals to and from the BM circuit. Since the connector bases are relatively wide and did not fit comfortably side-by-side on two sides of the board, additional SIW bends were added to route 4 of the BM ports to the two empty sides of the board while maintaining the same phase delay as the other 4 ports.

For board fabrication, the same fabrication house as the first prototype was used. Due to the multilayer fabrication, an additional drilling layer was required to account for the post holes needed for the new connectors. The Gerber file package now needed 7 separate files to fully detail the fabrication layout. The cost impact of moving to the RO4350B material was immediately seen: the 2<sup>nd</sup> BM prototype cost just \$21 per board, a reduction of 89%. Even the cost of a multilayer RO4350B board, such as the fabricated prototype of the full antenna system presented in Chapter 6, was significantly less at \$48 per board. However, the overall cost of more stable end-launch connectors was higher. Assembling the new prototype was a simple process of placing the connectors at the corresponding input and output lines, inserting screws, and tightening down to

get a firm placement on the board. The connector manufacturer specified that soldering the pins to the microstrip traces was optional, and this was confirmed with a negligible return loss difference measured on a test board with and without soldered connections.

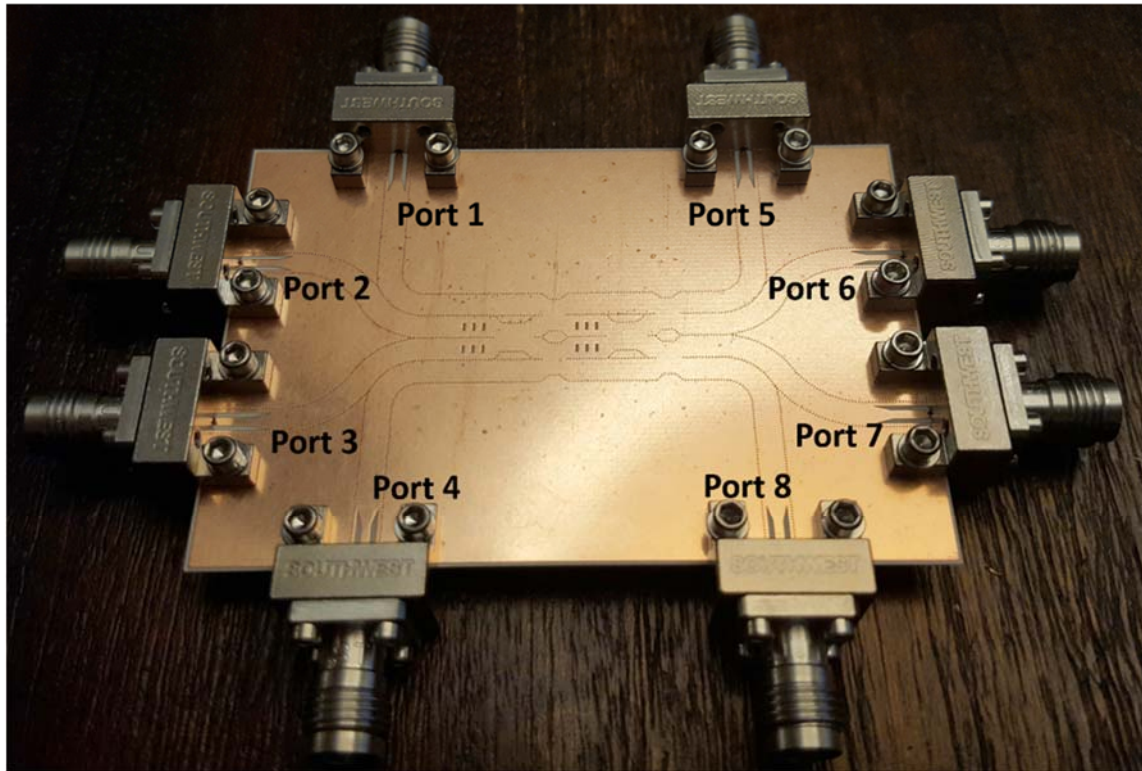
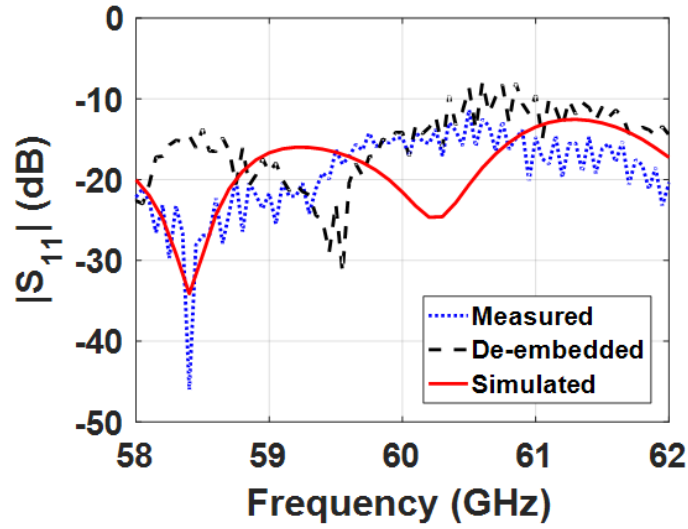
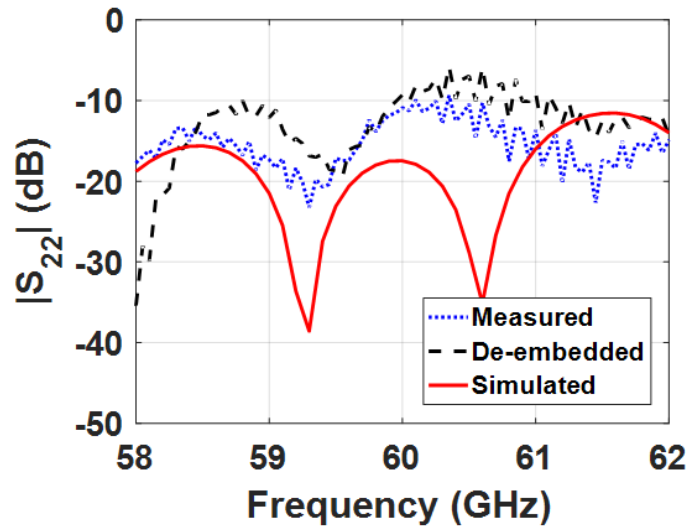


*Fig. 5-3: Fabricated 2<sup>nd</sup> Butler Matrix prototype.*

Scattering parameter measurements of the Butler Matrix prototype were performed with a 4-port Rohde & Schwarz ZVA67 Vector Network Analyzer. S-parameters were captured by connecting the VNA to 4 of the prototype connectors one at a time while terminating the other ports to 50  $\Omega$  standards. The reflection coefficient for input Ports 1 to 4 are measured at 60 GHz showing values that are 7-9 dB higher than the simulated results, but still below -10 dB for all input ports. The  $S_{11}$  and  $S_{22}$  plots are shown in Fig. 5-4a and Fig. 5-4b, respectively. Plots of  $S_{33}$  and  $S_{44}$  are not included for brevity, since  $S_{11}$  and  $S_{44}$ , and  $S_{22}$  and  $S_{33}$ , have similar signatures as expected due to the symmetry of the Butler Matrix prototype.



(a)

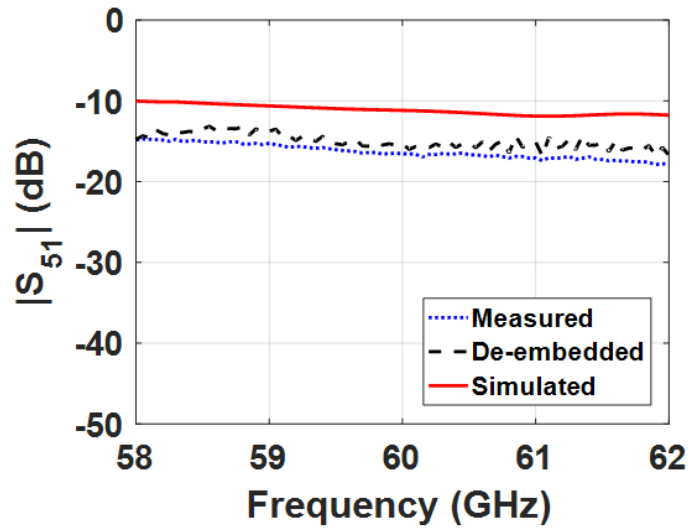


(b)

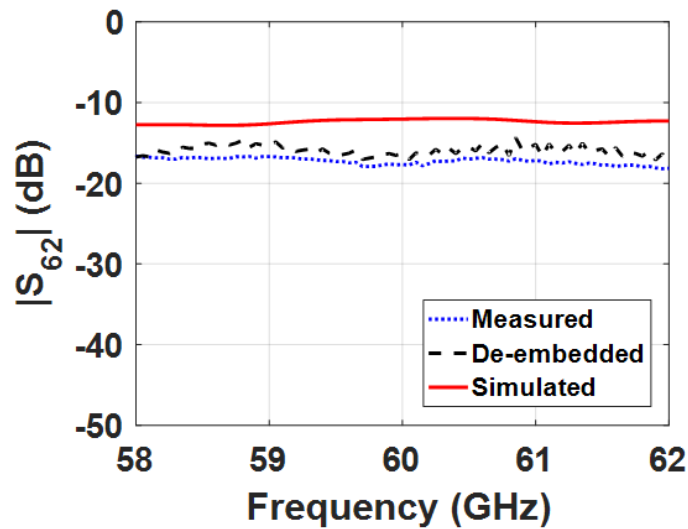
Fig. 5-4: a) Port 1 and b) Port 2 return loss plot comparing Butler Matrix prototype simulation, measurement, and de-embedded measurement results.

Insertion loss (IL) in signal transmission from Port 1 to Port 5, and from Port 2 to Port 6, are plotted in Fig. 5-5a and Fig. 5-5b, respectively. Due to the similarities in measured IL results to the other ports, only  $S_{51}$  and  $S_{62}$  are shown here for brevity. On average, simulation results expected an IL of 11.5dB while measurements revealed an average IL of 17.3dB. The difference between the IL values from measurements and simulations at 60 GHz when each input port was individually excited ranged between 3.1-6.3dB. This deviation from simulated results is attributed to variability

in the contacts between the prototype board and end-launch connectors and tolerances due to a relatively low-cost fabrication process. Measured magnitude results are summarized for all ports in Table 5-1.



(a)



(b)

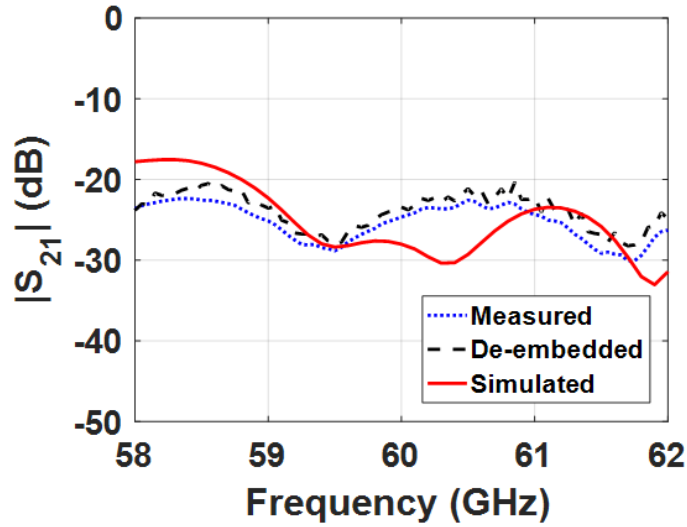
Fig. 5-5: Plot of insertion loss from a) Port 1 to Port 5, and b) Port 2 to Port 6, comparing Butler Matrix prototype simulation, measurement, and de-embedded measurement results.

*Table 5-1: EXPECTED AND MEASURED S-PARAMETER MAGNITUDES OF THE FABRICATED MODIFIED BUTLER MATRIX PROTOTYPE.*

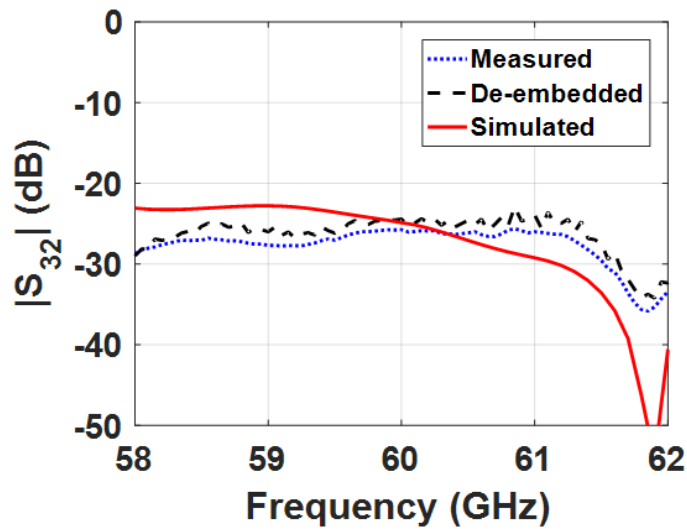
Output	Ideal Magnitude	Simulated Magnitude	Measured Magnitude	De-embedded Magnitude
Input: Port 1				
<i>Port5</i>	-6.0dB	-11.2dB	-16.5dB	-15.3dB
<i>Port6</i>	-6.0dB	-11.5dB	-15.9dB	-14.6dB
<i>Port7</i>	-6.0dB	-11.8dB	-19.2dB	-18.0dB
<i>Port8</i>	-6.0dB	-11.3dB	-16.5dB	-15.2dB
Input: Port 2				
<i>Port5</i>	-6.0dB	-11.6dB	-16.7dB	-15.4dB
<i>Port6</i>	-6.0dB	-11.9dB	-17.7dB	-16.3dB
<i>Port7</i>	-6.0dB	-10.8dB	-17.6dB	-16.3dB
<i>Port8</i>	-6.0dB	-11.6dB	-19.0dB	-17.6dB
Input: Port 3				
<i>Port5</i>	-6.0dB	-11.6dB	-19.1dB	-17.9dB
<i>Port6</i>	-6.0dB	-10.8dB	-16.4dB	-15.1dB
<i>Port7</i>	-6.0dB	-11.9dB	-18.1dB	-16.8dB
<i>Port8</i>	-6.0dB	-11.4dB	-16.1dB	-14.7dB
Input: Port 4				
<i>Port5</i>	-6.0dB	-11.3dB	-16.7dB	-15.5dB
<i>Port6</i>	-6.0dB	-11.8dB	-18.6dB	-17.3dB
<i>Port7</i>	-6.0dB	-11.6dB	-16.3dB	-15.0dB
<i>Port8</i>	-6.0dB	-11.1dB	-16.2dB	-14.9dB

Port-to-port isolation between inputs to the Modified Butler Matrix is plotted in Fig. 5-6a and Fig. 5-6b, which demonstrate better than -24dB performance at 60 GHz for Port1 to Port 2 and Port 2 to Port 3, respectively. Plots of  $S_{31}$ ,  $S_{41}$ ,  $S_{42}$ , and  $S_{43}$  are not included for brevity, since non-adjacent ports (Port 1 to Port 3, Port 1 to Port 4, and Port 2 to Port 4) typically showed better isolation performance and the symmetry of the Butler Matrix prototype yields an  $S_{43}$  plot similar to  $S_{21}$ . It should be noted that isolation data was captured with a two-port VNA and only four termination loads available, meaning two of the BM prototype ports had to be left open during measurements. In general, all collected isolation information shows a good fit between simulation,

measured, and de-embedded results, confirmed with multiple measurements performed with various combinations of port termination.



(a)



(b)

Fig. 5-6: a) Port 1 to Port 2 and b) Port 2 to Port 3 isolation plot comparing Butler Matrix prototype simulation, measurement, and de-embedded measurement results

Ultimately, the BM provides the phased outputs to feed a beam switching antenna array. For this reason, the difference in the phase of the signals at the output Ports 6, 7, and 8 with respect to the reference port at the top end (Port 5) is obtained. Fig. 5-7, Fig. 5-8, and Fig. 5-9 show the phase

differentials between output Ports 5-8 when Port 1 is excited and  $S_{51}$  phase at Port 5 is considered the reference zero. Experimental and simulation results at 60 GHz deviated the least ( $1.2^\circ$ ) for the phase differential between  $\angle S_{71} - \angle S_{51}$  and the most ( $34.3^\circ$ ) for the difference between  $\angle S_{61} - \angle S_{51}$ . Summarized differential phase results with respect to  $\angle S_{51}$  for all input ports can be found in Table 5-2.

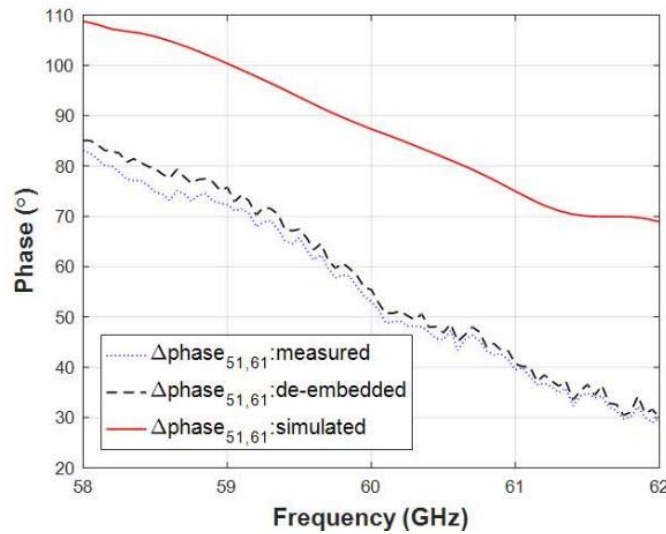


Fig. 5-7: With an input to Port 1, comparison of the phase differential between Ports 5 and 6 of the Butler Matrix prototype for the simulated, measured, and de-embedded results.

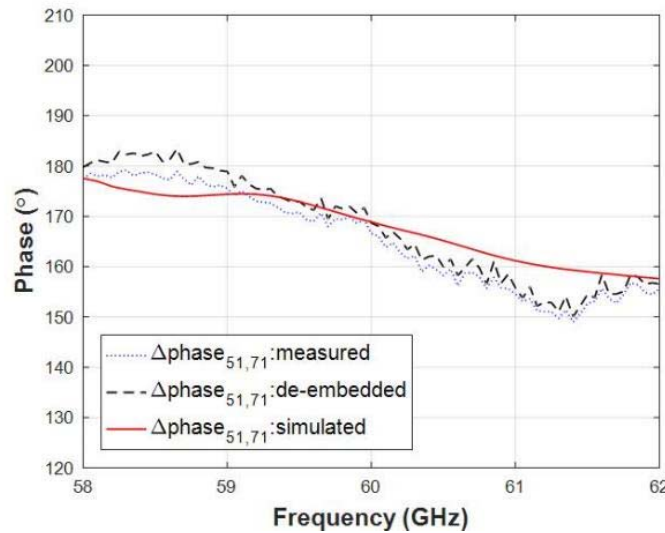


Fig. 5-8: With an input to Port 1, comparison of the phase differential between Ports 5 and 7 of the Butler Matrix prototype for the simulated, measured, and de-embedded results.

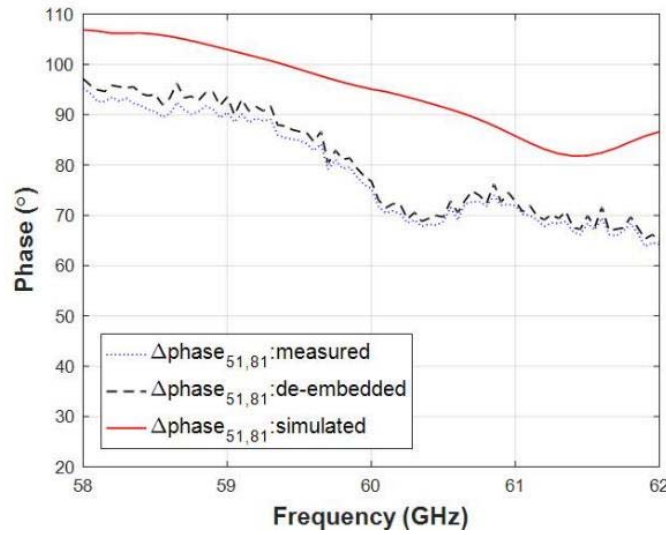


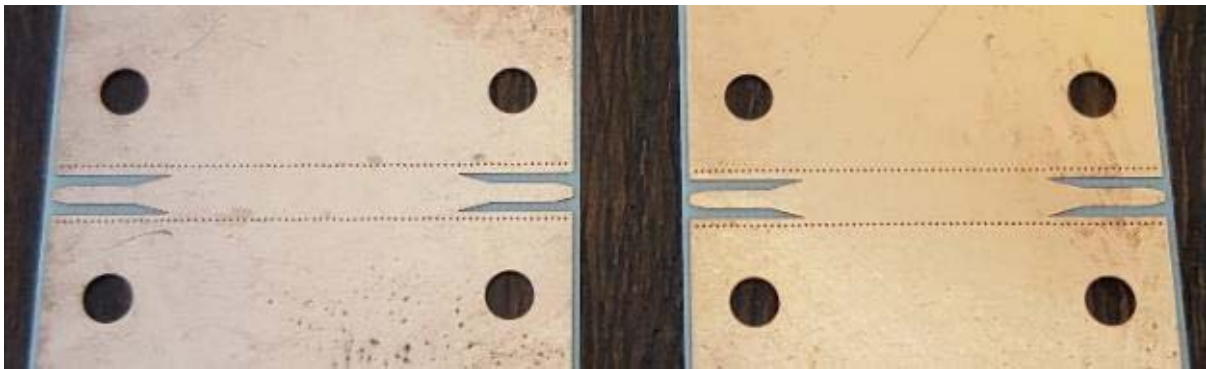
Fig. 5-9: With an input to Port 1, comparison of the phase differential between Ports 5 and 8 of the Butler Matrix prototype for the simulated, measured, and de-embedded results.

Table 5-2: EXPECTED AND MEASURED DIFFERENTIAL PHASE OUTPUTS WITH RESPECT TO PORT 5 OF THE FABRICATED MODIFIED BUTLER MATRIX PROTOTYPE.

Output	Specified $\Delta\text{Phase}$	Simulated $\Delta\text{Phase}$	Measured $\Delta\text{Phase}$	De-embedded $\Delta\text{Phase}$
Input: Port 1				
Port6	90°	87.32°	53.03°	55.40°
Port7	180°	167.88°	166.61°	168.68°
Port8	90°	95.08°	72.74°	76.75°
Input: Port 2				
Port6	-90°	-90.28°	-125.09°	-123.33°
Port7	180°	174.12°	159.56°	161.49°
Port8	-90°	-80.52°	-104.51°	-103.22°
Input: Port 3				
Port6	-90°	-108.07°	-84.24°	-82.09°
Port7	0°	-9.95°	-5.96°	-3.82°
Port8	90°	76.26°	124.89°	126.18°
Input: Port 4				
Port6	90°	69.10°	93.94°	95.89°
Port7	0°	-8.75°	-10.10°	-8.03°
Port8	-90°	-98.46°	-54.38°	-53.19°

## 5.4: De-embedded Results

The connectors, microstrip-to-SIW transition structures and the extra feedlines of the modified Butler Matrix prototype introduce discontinuities and parasitic effects in measurements which are not all present in the simulated design. So, it is important to have a de-embedding technique to remove their effects from the measurement data. All the input and output ports have identical connectors, and transition structures and the length of extra SIW feed lines was  $\lambda_g/2$  for all ports. Through-only de-embedding technique is a well-known method for extracting the S-parameter response of a device-under-test from the overall measured results that contain extra effects of connectors, junctions and extended feed lines. For this method, two test structures that feature identical connectors, transitions, and  $\lambda_g/2$  feeds for both input and output, shown in Fig. 5-10, are fabricated. The straight sections of SIW for the two structures is the only physical difference: the left-side board of Fig. 5-10 is 9.72mm long ( $3.09 \lambda_g$ ) while the right-hand board is 7.66mm ( $2.43 \lambda_g$ ). The s-parameters of these structures are measured, shown in Fig. 5-11, and following the steps detailed in Appendix I, S-parameters of the prototyped BM can be extracted.



*Fig. 5-10: Through-only de-embedding structures used to characterize the connectors, feedlines, and transition sections of the prototypes. The left-hand board is 9.72 mm long and the right-hand is 7.66 mm long.*

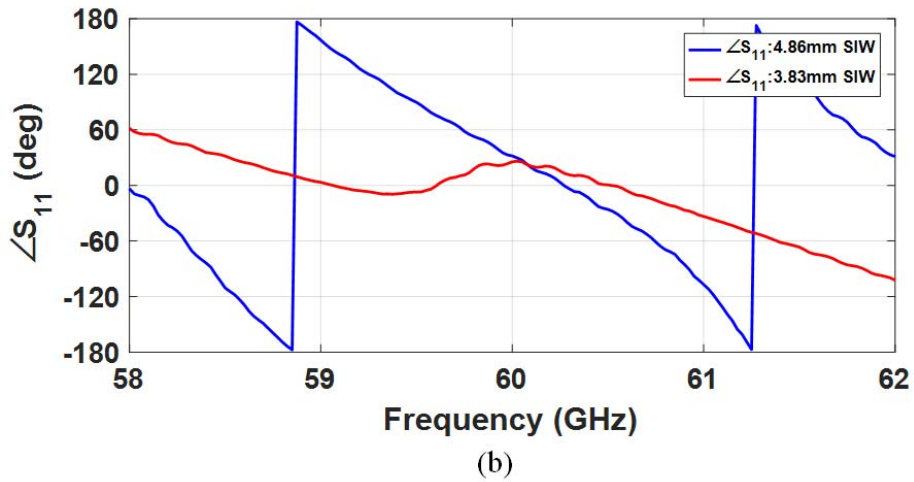
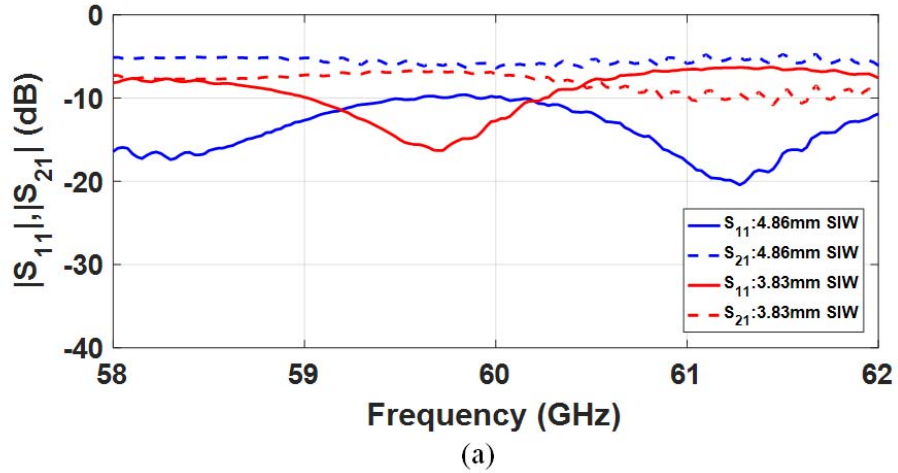


Fig. 5-11: Measured a) return and insertion loss and b) phase angle of the straight SIW de-embedding test structures.

After removing the effects of connectors, transition sections and feed lines from the measured Butler Matrix scattering parameters, IL results typically improved by up to 1.4 dB and ranging from 14.6 to 18.0 dB at 60 GHz, with the greatest output magnitude imbalance of 3.34dB seen at Port 1. The impact of the de-embedding procedure can be seen in Fig. 5-5 which shows the characteristic IL improvement of about 1.3 dB from Port 1 to Port 5. Also, in the reflection coefficient plots shown in Fig. 5-4a and Fig. 5-4b, much more pronounced peaks and dips are observed. De-embedded magnitude results for all ports are included in Table 5-1.

## 5.5: Analysis of BM Prototype Performance for Beam-Switching

To evaluate the performance of the modified Butler Matrix prototype in achieving the desired phased outputs, the phases of Ports 6-8 were compared to the reference Port 5 for each given input. The results of this analysis are plotted with input Port 1 measurement and simulation results in Fig. 5-7, Fig. 5-8, and Fig. 5-9, and summarized for all ports in Table 5-2. De-embedded phase differentials typically varied from the ideal specified phase by  $+8^\circ$  to  $-18^\circ$  at 60 GHz, though some anomalies due to manufacturing defects created deviations of up to  $36^\circ$ . Some of the discrepancies can also be attributed to the deviation of simulated phase results from theoretical values, where the average phase drift was up to  $25^\circ$  from expected values. For comparison, Port 1 and 2 excitations reported in [33] showed output phases deviating from ideal values by  $+11^\circ$  to  $-17^\circ$  at 60 GHz.

When the de-embedded phase outputs from the fifth column of Table 5-2 are applied to an ideal 2x2 planar array, slight shifts in beam angles away from the target specifications can be expected, as seen in Section 3.5.: Beginning with the Butler Matrix phased output matrix

$$B = \frac{1}{2} \begin{bmatrix} e^{j0^\circ} & e^{j0^\circ} & e^{j0^\circ} & e^{j0^\circ} \\ e^{j55.40^\circ} & e^{-j123.33^\circ} & e^{-j82.09^\circ} & e^{j95.89^\circ} \\ e^{j168.68^\circ} & e^{j161.49^\circ} & e^{-j3.82^\circ} & e^{-j8.03^\circ} \\ e^{j76.75^\circ} & e^{-j103.22^\circ} & e^{j126.18^\circ} & e^{-j53.19^\circ} \end{bmatrix}, \quad (5.1)$$

the measured outputs can be checked for orthogonality:

$$BB^* = \frac{1}{4} \begin{bmatrix} e^{j0^\circ} & e^{j0^\circ} & e^{j0^\circ} & e^{j0^\circ} \\ e^{j55.40^\circ} & e^{-j123.33^\circ} & e^{-j82.09^\circ} & e^{j95.89^\circ} \\ e^{j168.68^\circ} & e^{j161.49^\circ} & e^{-j3.82^\circ} & e^{-j8.03^\circ} \\ e^{j76.75^\circ} & e^{-j103.22^\circ} & e^{j126.18^\circ} & e^{-j53.19^\circ} \end{bmatrix} \begin{bmatrix} e^{j0^\circ} & e^{-j55.40^\circ} & e^{-j168.68^\circ} & e^{-j76.75^\circ} \\ e^{j0^\circ} & e^{j123.33^\circ} & e^{-j161.49^\circ} & e^{j103.22^\circ} \\ e^{j0^\circ} & e^{j82.09^\circ} & e^{j3.82^\circ} & e^{-j126.18^\circ} \\ e^{j0^\circ} & e^{-j95.89^\circ} & e^{j8.03^\circ} & e^{j53.19^\circ} \end{bmatrix} \\ = \begin{bmatrix} 1.000 \angle 0^\circ & 0.014 \angle 8.7^\circ & 0.078 \angle 280.9^\circ & 0.003 \angle 325.5^\circ \\ 0.014 \angle 351.3^\circ & 1.000 \angle 0^\circ & 0.045 \angle 167.3^\circ & 0.077 \angle 64.8^\circ \\ 0.078 \angle 79.1^\circ & 0.045 \angle 192.7^\circ & 1.000 \angle 0^\circ & 0.021 \angle 220.0^\circ \\ 0.003 \angle 34.5^\circ & 0.077 \angle 295.2^\circ & 0.021 \angle 140.0^\circ & 1.000 \angle 0^\circ \end{bmatrix}. \quad (5.2)$$

This matrix shows that the generated output phase vectors from the Modified Butler Matrix demonstrate slightly stronger deviation from the desired unitary matrix for  $BB^*$  compared to that

of simulation results from Section 3.5.: Despite this, the simulated beam patterns based on these output phases with the originally calculated cut-planes ( $\phi=45^\circ$  and  $135^\circ$ ) shown in Fig. 5-12 are very similar to those shown for the ideal modified Butler Matrix architecture in Fig. 2-15 and Fig. 2-16. Fig. 5-12a and Fig. 5-12b also show that peak magnitudes are only slightly less than ideal values ( $|A_i(\theta_{0i},\phi_{0i})|^2=3.87\pm 0.07$ ) and are located very close to beam pattern nulls from the other port excitations.

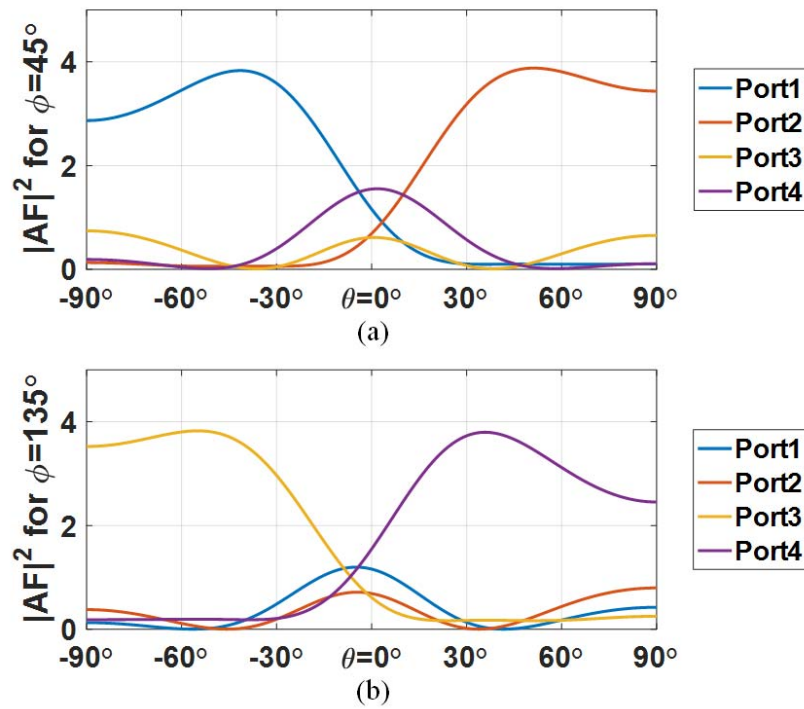


Fig. 5-12: Array factor gain, a)  $\phi=45^\circ$  and b)  $\phi=135^\circ$ , for a square planar array with de-embedded measured output phases from fabricated Modified Butler Matrix prototype.

Applying the measured output phases from the fabricated Butler Matrix prototype to the planar array factor yield peak beams slightly askew from the target application: for Port 1 excitation,  $|A_1(\theta_{01},\phi_{01})|^2=3.90$ ,  $\theta_{01}=41.94^\circ$ ,  $\phi_{01}=232.20^\circ$ ; for Port 2,  $|A_2(\theta_{02},\phi_{02})|^2=3.94$ ,  $\theta_{02}=51.66^\circ$ ,  $\phi_{02}=39.24^\circ$ ; for Port 3,  $|A_3(\theta_{03},\phi_{03})|^2=3.83$ ,  $\theta_{03}=54.90^\circ$ ,  $\phi_{03}=316.08^\circ$ ; and for Port 4,  $|A_4(\theta_{04},\phi_{04})|^2=3.81$ ,  $\theta_{04}=35.82^\circ$ ,  $\phi_{04}=131.94^\circ$ . These simulated peak beam locations are visualized

for the planar target surface in Fig. 5-13, where each measured port excitation drives the beam to each of the intended quadrants. Further validation of the phased output results can be seen in SIR comparison in Table 5-3, where each beam has a good power advantage (> 13dB, up to 39.7dB) over the other beams for its own quadrant.

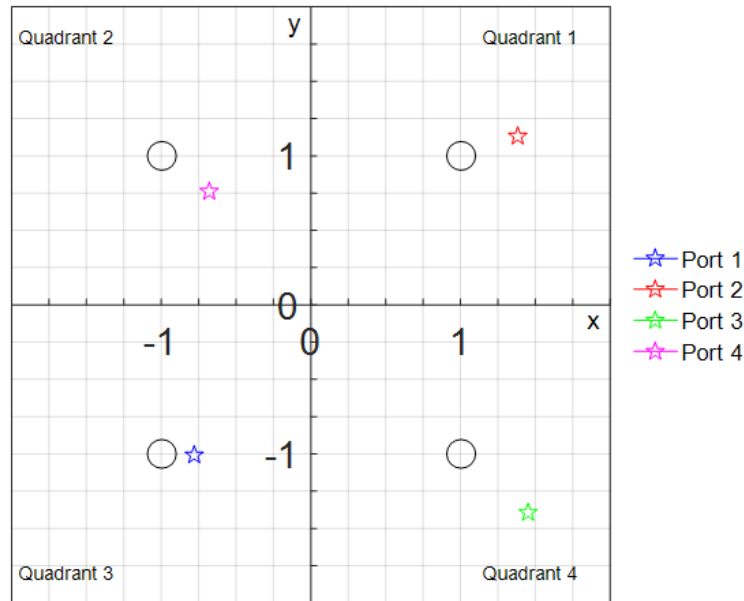


Fig. 5-13: Visualization of the planar surface target being illuminated by the planar array factor excited by the simulated Modified Butler Matrix outputs.

Table 5-3: PEAK BEAM DIRECTIONS AND SIR COMPARISONS FOR ALL PORT EXCITATIONS FROM THE MEASURED MODIFIED BUTLER MATRIX APPLIED TO A SIMULATED PLANAR ARRAY.

<b>SIR COMPARISONS</b>					
<b>PORT</b>	<b>PEAK BEAM</b>	<b>PORT 1</b>	<b>PORT 2</b>	<b>PORT 3</b>	<b>PORT 4</b>
<b>1</b>	$\theta_{01}=41.94^\circ, \phi_{01}=232.20^\circ$	0dB	18.2dB	37.5dB	25.1dB
<b>2</b>	$\theta_{02}=51.66^\circ, \phi_{02}=39.24^\circ$	15.9dB	0dB	20.1dB	33.7dB
<b>3</b>	$\theta_{03}=54.90^\circ, \phi_{03}=316.08^\circ$	39.7dB	20.0dB	0dB	13.0dB
<b>4</b>	$\theta_{04}=35.82^\circ, \phi_{04}=131.94^\circ$	24.6dB	38.4dB	13.4dB	0dB

Table 5-4 summarizes the comparison between the intended theoretical beam directions, and expected values after simulation and de-embedding the S-parameters of the BM. Reference [33]

demonstrated similar impact to the target 1-D beam angles when applying the measured output results. It is still expected that this Modified Butler Matrix can meet the project goals of 2-D beam switching, which will be evaluated with the full antenna system in the next chapter.

*Table 5-4: COMPARING INTENDED AND RESULTANT BEAM DIRECTIONS FROM SIMULATION AND MEASUREMENT FOR THE MODIFIED BUTLER MATRIX PROTOTYPE PHASED OUTPUTS AT 60 GHZ.*

Input $i$	Specified		Simulation-based		Measurement-based	
	$\theta_{0i}$	$\phi_{0i}$	$\theta_{0i} (\Delta\theta)$	$\phi_{0i} (\Delta\phi)$	$\theta_{0i} (\Delta\theta)$	$\phi_{0i} (\Delta\phi)$
1	45°	225°	41.58° (-3.42°)	227.70° (2.70°)	41.94° (-3.06°)	232.20° (7.20°)
2	45°	45°	46.98° (1.98°)	41.94° (-3.06°)	51.66° (6.66°)	39.24° (-5.76°)
3	45°	315°	46.44° (1.44°)	318.06° (3.06°)	54.90° (9.90°)	316.08° (1.08°)
4	45°	135°	41.22° (-3.78°)	131.94° (-3.06°)	35.82° (-9.18°)	131.94° (-3.06°)

## 5.6: Conclusion

To evaluate the effectiveness of the Butler Matrix design changes to enable 2-D beam switching, prototypes were fabricated and evaluated. A first device was manufactured in Rogers RT5880 that illustrated the use of the conventional Butler Matrix architecture with minimal-length periodic aperture phase shifters, achieving a 56.8% circuit area improvement over [33] but yielded poor measurement results due to inadequate connectors. The move to a more suitable substrate for multilayer fabrication, Rogers RO4350B, with sturdier connectors for a second prototype resulted in a slightly larger layout, but with much less expensive manufacturing cost (\$21 vs \$188 per board). With the second prototype, the proposed Modified Butler Matrix architecture was employed since the phase delay of the designed crossover circuit in RO4350B had a smaller phase delay (51.8°) than the required phase differential ( $\psi_{1,2}=90^\circ$ ).

Measurement results showed some deviations from simulated insertion loss (3.1-6.3dB higher), return loss (7-9 dB lower), and phase differentials (askew by 1.2-34.3°). A de-embedding

procedure was used to remove discontinuities and parasitic effects from the measurements, which made some marginal gains in all three categories. Despite this, the measured results still perform well when applied to the planar array factor of Eqn (2.12), achieving four distinct beam directions that differ from the target elevation angle  $\theta_{0i}$  by  $3^\circ$  to  $9.9^\circ$ , and from the azimuth angles  $\phi_{0i}$  by  $1^\circ$  to  $7.2^\circ$ . The next step is to evaluate the fully-integrated antenna array system with measurements of a fabricated prototype.

---

## Chapter 6: Experimental Evaluation of the Full Antenna System

Phased array systems need to be evaluated for their ability to meet the beam specifications of their intended application. These experimental characterizations include conducted port (network) measurements for determining return loss and isolation as well as over the air (OTA) antenna pattern measurements. Millimeter-wave bands present considerable challenges in the experimental evaluation of antennas and their RF front-end components. This is due to the fact that the feature sizes of the devices and interconnects are at the mm scale, thus, resulting in a variety of unintentional radiators and interference sources that impact the integrity of OTA and port measurements.

The considered beam switching 2x2 square planar array designed in Chapter 4 provides a specific beam angle for each input excitation by using the Modified Butler Matrix feed network. Some modifications to Butler Matrix were needed to provide the desired phased outputs to steer the radiated beam in one of the 4 quadrants of the space illuminated by the planar array. In this chapter, the fully-integrated antenna array prototype is evaluated to assess its scattering parameter and OTA radiation performance. Conducted port measurements follow the established procedure of using vector network analyzers (VNAs) with the needed calibration.

### 6.1: Fabricated Full Antenna System Prototype

There are a few crucial steps to design and fabricate a prototype of the full system for testing. Staying consistent with the 2<sup>nd</sup> Butler Matrix prototype from Chapter 5 and the assumed substrates from simulations in Chapter 4, the previously mentioned Rogers materials are used here again:

Rogers RO4350B ( $\epsilon_r=3.66$ ,  $\tan \delta=0.0037$  @ 10 GHz) with thickness  $t=0.254\text{mm}$  for the primary dielectric substrate (lower feed network layers and upper antenna array layer) with 1oz electrodeposited copper (thickness  $t=35\mu\text{m}$ ) plus Rogers RO4450B ( $\epsilon_r=3.52$ ,  $t=0.203\text{mm}$ ) for bonding. The first design stage of creating input feedlines to provide a connector interface to the circuit is straightforward because this process can borrow from the previous Butler Matrix prototype. In fact, since the input to the full antenna system is still the input to the Butler Matrix, the prototype layout is a cut-and-paste job with a final simulation step to confirm no irregularities are introduced. The final dimensions of the full antenna system board are 57.9mm long by 46.3mm wide and 0.781mm thick.

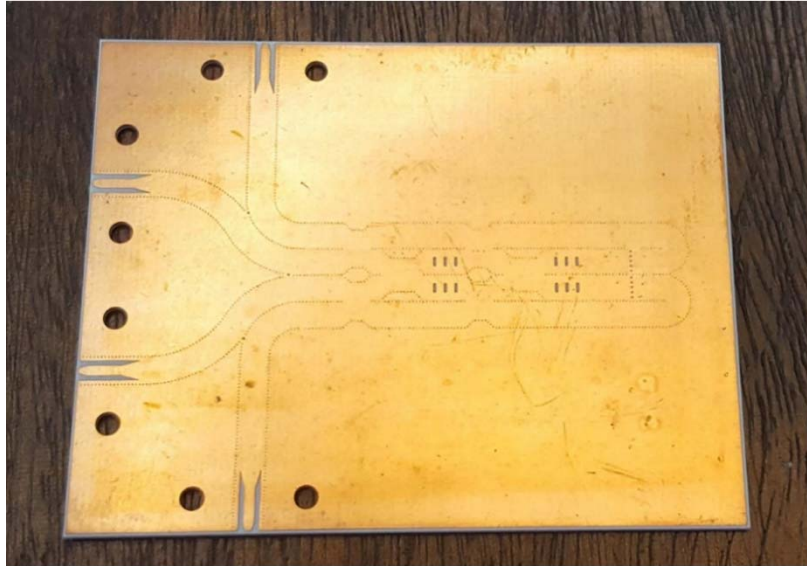
A more challenging step is to confirm the manufacturing steps necessary to have the board fabricated and ready for connector assembly. As mentioned in Chapter 5, the fabrication vendor requires separate artwork files for each metallic layer as well as individual instruction files that annotate the coordinates of each drilling spot for a given hole type. To generate the Gerber files a similar tool flow was employed. First, the HFSS layout was exported to DXF file format and imported into AutoCAD. This serves an additional purpose beyond drawing evenly-spaced vias and organizing drawing layers as reported in the Chapter 5 section on prototyping: each metallic feature needs to be placed the correct drawing layer and there are now 2 different categories of drilling. Specifically for the antenna prototype, layer 1 contains the four antenna elements of the planar array, layer 2 is an empty intermediate between the bonding layer and the antenna substrate that must still be accounted for, layer 3 is the upper wall of the Butler Matrix feed network and must mark via locations as well as slots for coupling between the end of the SIW lines and the antenna elements, and layer 4 is the bottom wall of the SIW lines that has slots for each of the Butler Matrix phase shifters, transitions from microstrip feeds to SIW, and via locations.

Additionally, there must be a layout and drilling file for the vias connecting layers 3 and 4 to form the SIW walls and another set for the supporting screw holes from layer 1 to 4 that are used to attach connectors.

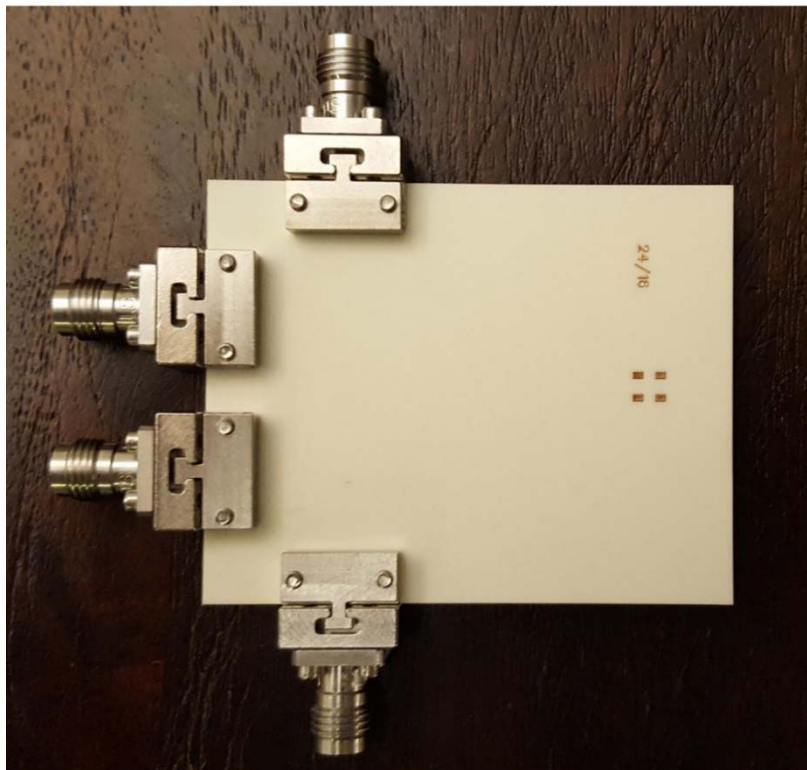
After these drawing layers are compiled in AutoCAD, the multi-layer DWG file is exported into Keysight's ADS to confirm manufacturability and generate official Gerber files. In total, this multilayer board design requires 9 different files to fully specify the fabrication job. These files are uploaded to an online verification tool from the local fabricator to check for design errors such as feature spacing, drill size, and geometric tolerances. The cost to create this board increased from \$21 to \$48 per unit for a similar footprint due to the added complexity of multilayer fabrication. According to the local manufacturer, the fabrication process started with cutting the features of two 2-layer boards (layers 1/2 and 3/4), drilling and then plating the vias for the SIW feed board (layers 3/4), using an x-ray machine to align and bond the two board together, and then drilling the final through-holes required for the connectors. Fig. 6-1 shows the completely assembled prototype of the full beam-switching antenna array system.

## **6.2: Port Measurements**

Return loss at all 4 ports of the full antenna system prototype was evaluated using an Anritsu VNA. These measurements are compared to simulation data as presented in Fig. 6-2 and Fig. 6-3 for Ports 1,4 and Ports 2,3, respectively. In general, the peaks and valleys expected from simulation results are seen in the measured plots, but with a shift toward the higher frequencies. Nonetheless, very good reflection coefficient profile ( $< -15$  dB) is measured across the 58-62 GHz band indicating excellent matching at 60 GHz for all the excitation ports.



(a)



(b)

*Fig. 6-1: a) Modified Butler Matrix side and b) antenna side of the fabricated and fully-assembled Antenna System prototype.*

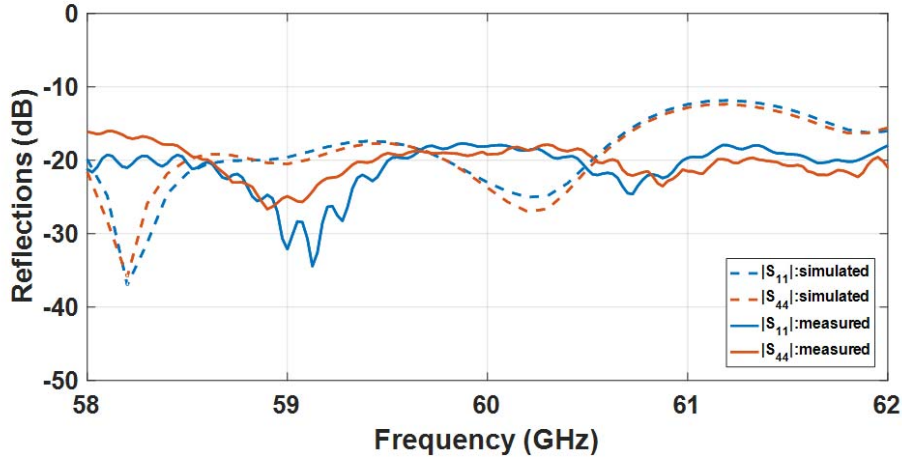


Fig. 6-2: Comparison of return loss for Ports 1 and 4 of the antenna system prototype: simulated (dotted line) and measured results (solid line).

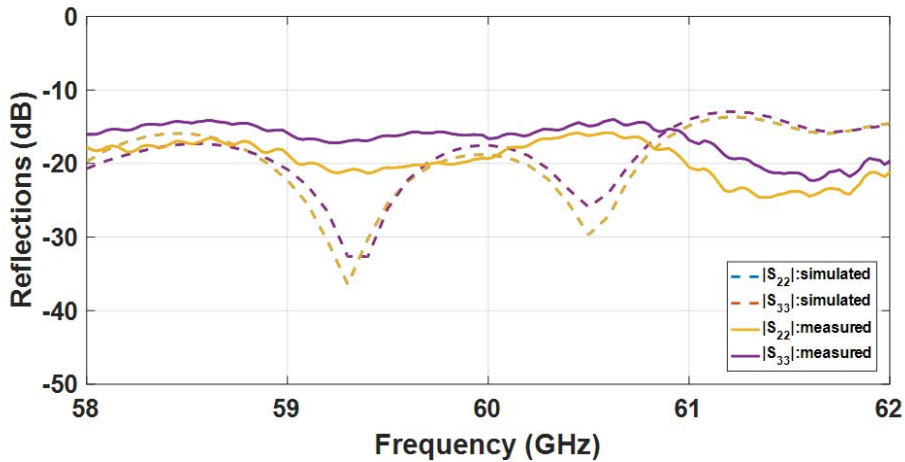


Fig. 6-3: Comparison of return loss for Ports 2 and 3 of the antenna system prototype: simulated (dotted line) and measured results (solid line).

Port isolation is plotted for all neighboring ports in Fig. 6-4, contrasting simulated with measured results. VNA measurements show excellent isolation (<-28 dB) between all input ports, outperforming simulations by 10dB on average. This improved performance indicates there is less leakage than simulations expected from one port to another, which could be due to better impedance matching than expected or a mismatch in the circuit (poor return loss, for example) that could be preventing a leakage issue because power is being diverted elsewhere. Port isolation plot peaks and valleys appear to be 0.6-0.8 GHz lower in frequency than their simulated counterparts.

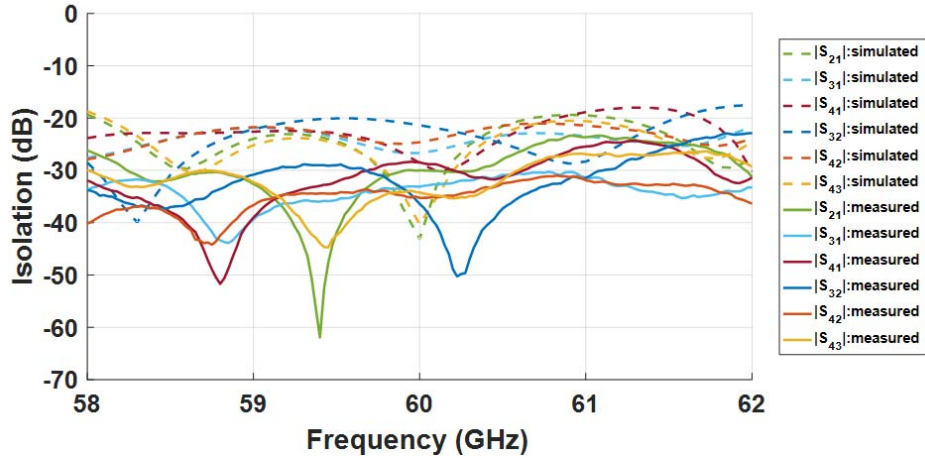


Fig. 6-4: Comparison of isolation results for all neighboring ports of the antenna system prototype: simulated (dotted line) and measured (solid line).

### 6.3: Low-cost OTA Measurement System

For OTA performance evaluation, radiation patterns are measured in an antenna range or anechoic chamber rated at mm-wave frequencies. At the time of this work, a working and cost-effective mm-wave test chamber was not available for the project. To discuss the experimental evaluation of the planar antenna array here, the test fixtures and set ups uniquely designed and built for this purpose need to be described. Since the free space wavelength at  $f=60$  GHz is  $\lambda_0=5$  mm and the array's physical aperture area is also small (with a maximum linear dimension of  $D=4.75$  mm), it is feasible to create a bench-top set-up for far field radiation pattern measurement which is undertaken in this project.

Given the small distance to be considered in the far field, the antenna measurement can easily be made indoors on a table but requires an anechoic chamber to reduce reflections from the surroundings. The distance between probe antenna and AUT should be large enough to ensure far field region measurement at all points. For this antenna system, the Fraunhofer distance is  $r_{ff} > 2D^2/\lambda_0=9.03$  mm, where  $D=4.75$  mm is the largest dimension of the array. Therefore, a separation of 9.3 cm was chosen for constructing a positioning system due to fabrication convenience. The

bench-top anechoic chamber for OTA measurements should enclose the reference antenna (or probe antenna), AUT, and a controllable positioning system for holding these two antennas.

Seen in Fig. 6-5, the positioning rig consists of an AUT holding platform that fits into a base with graduated notches for accurately rotating the prototype by  $5^\circ$  increments in  $\phi$  direction, from  $0^\circ \leq \phi \leq 360^\circ$ . A pyramidal horn antenna (50-75 GHz operating range, 15 dBi gain) is held above the AUT by a slot-and-peg system between two arms anchored at the edge of the base. The arms maintain a consistent radius of 9.3 cm above the center of the AUT platform and the pegs can be adjusted in  $5^\circ$  increments along the arm radius,  $0^\circ \leq \theta \leq 90^\circ$ . The arms and base of the positioning system are made from laser cut acrylic ( $\epsilon_r=2.7-4.5$ ) while the AUT platform and pegs were fabricated via 3D printer with acrylonitrile butadiene styrene (ABS,  $\epsilon_r=2.4-4.1$ ).

A box, shown in Fig. 6-6, with measurement of 30.5 cm per side is created and its top inside wall and four side walls are lined with an absorbing material [49] to serve as an anechoic chamber. The absorber linings are foam sheets with a thickness of 6.35 mm ( $1.27 \lambda_0$ ) and rated to reduce reflections by more than 20 dB at frequencies from 40-110 GHz. To cover the floor of the chamber where the cables are routed to the horn antenna and AUT, a sheet of absorber foam was modified to create an opening for AUT as well as the positioner arm. Finally, a half circle of absorbing foam was used to cover the connectors on the AUT circuit board to further reduce reflections in the chamber. Fig. 6-7 shows a photo of the developed in-house anechoic chamber in operation without the top cover. It should be mentioned that the effectiveness of the absorber foam was also assessed using our test rig: when an absorber sheet was placed between AUT and the horn probe antenna a drop of 15-20 dB across the frequency sweep was observed.

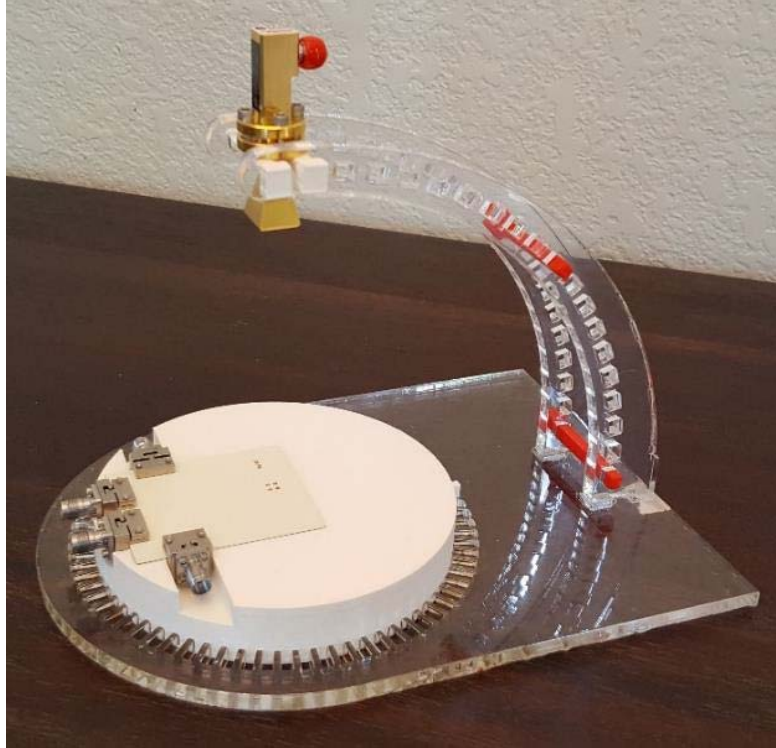


Fig. 6-5: Beam pattern measurement rig with antenna array prototype and measurement horn antenna.

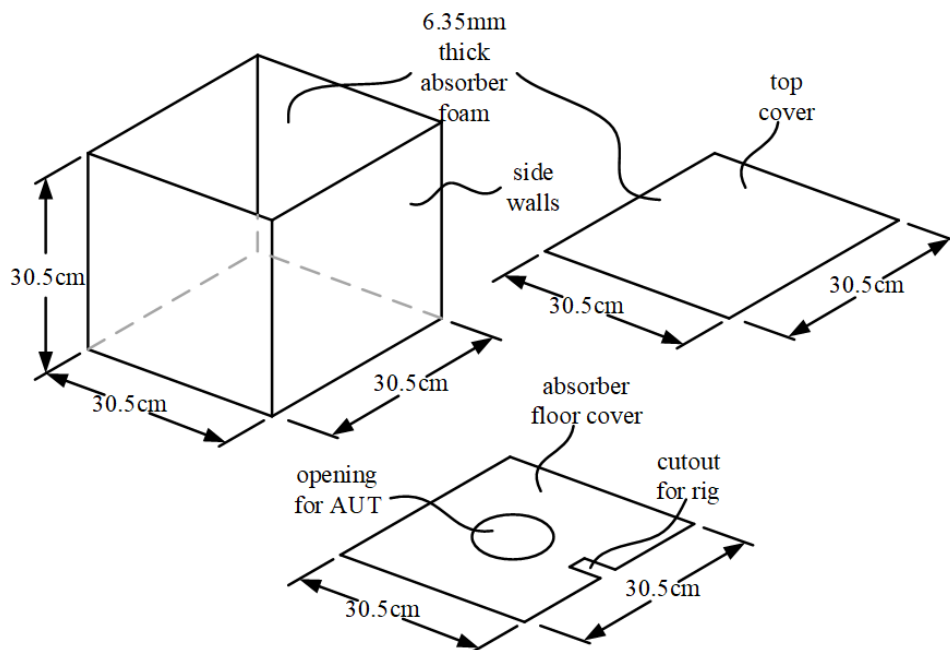
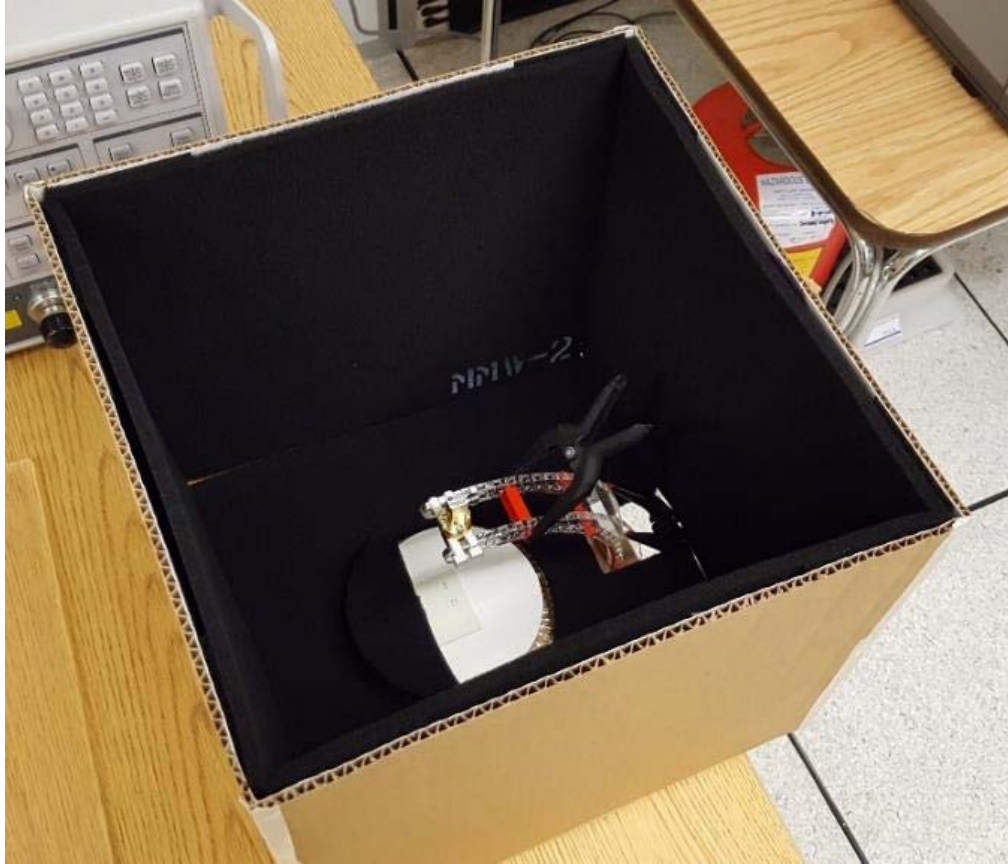


Fig. 6-6: Diagram of the constructed anechoic chamber for making far field antenna pattern measurements.



*Fig. 6-7: Anechoic chamber housing the antenna positioning system in operation without the top cover.*

To confirm the performance of the antenna range, a series of transmission ( $S_{21}$ ) measurements were made from 55 to 65 GHz to compare results when using the anechoic chamber versus no chamber, covering the connectors and cables with absorber material or not, and presence or removing the top cover. It was determined that the presence or removal of the absorbers influences the results as expected. For instance, covering just the connectors with absorber foam (no chamber walls) resulted in reducing the probed field by 1.4 dB at 60 GHz. Laying absorber foam over both the cables and connectors reduced this value further by 1.0 dB at 60 GHz. No significant difference was seen when operating the anechoic chamber with or without the top cover.

## 6.4: Antenna Array Pattern Measurements

Relative gain pattern is obtained from  $|S_{21}|$  measurements at 60 GHz for each port with the first positioning system. By moving the horn antenna along the arm at the allocated  $5^\circ$  increments of  $\theta$  and rotating the base at the  $5^\circ$  intervals along  $\phi$  for each excitation port, achieving the main beam angles at their expected quadrants, with  $\{\theta_{0|1}=35^\circ$  and  $\phi_{0|1}=220^\circ$ ;  $\theta_{0|2}=25^\circ$  and  $\phi_{0|2}=50^\circ$ ;  $\theta_{0|3}=30^\circ$  and  $\phi_{0|3}=300^\circ$ ;  $\theta_{0|4}=30^\circ$  and  $\phi_{0|4}=140^\circ\}$  was confirmed. These results are tabulated alongside the simulated results in Table 6-1. Fig. 6-8(a-d) shows the  $\theta_{0|i}$  cut-plane plots of the normalized relative horizontal gain patterns when each of the input ports to the antenna system is excited one at a time, while Fig. 6-9(a-d) shows the  $\phi_{0|i}$  cut-plane plots for the vertical patterns.

*Table 6-1: COMPARING INTENDED AND RESULTANT BEAM DIRECTIONS FOR THE FULL ANTENNA SYSTEM PROTOTYPE AT 60 GHZ.*

Input i	SIMULATED		MEASURED	
	$\phi_0$	$\theta_0$	$\phi_0$	$\theta_0$
1	212°	31°	220°	35°
2	41°	29°	50°	25°
3	314°	26°	300°	30°
4	141°	28°	140°	30°

Procedurally, finding the best 2-D pattern cut-planes for each port excitation began with a localized search around the intended  $\{\theta_{0|i}, \phi_{0|i}\}$ . First, the radiation peak at  $\theta_{0|i}$  was detected by changing the horn antenna location at each quadrant and then fine tuning the search by rotating the AUT platform by  $\pm 15^\circ$  in  $5^\circ$  increments. Next, the horizontal pattern was collected with the horn antenna at the found  $\theta_{0|i}$  elevation and by incrementally rotating the AUT platform  $5^\circ$  for a full  $360^\circ$   $\phi$  sweep and confirming the peak at  $\phi_{0|i}$ . Finally, with the platform azimuth angle set at  $\phi_{0|i}$ ,

the vertical pattern was gathered by rotating the horn antenna in  $5^\circ$  steps allocated on acrylic arms to collect  $-90^\circ \leq \theta \leq 90^\circ$ . For this pattern measurement the holding arms of the horn antenna were rotated by  $180^\circ$  to capture  $-90^\circ < \theta < 0^\circ$  measurements. This also provided a final confirmation of the peak at  $\theta_{0i}$ . In cases where the final  $\{\theta_{0i}, \phi_{0i}\}$  for measured peak gain values did not match well with the initial search (i.e.  $>5^\circ$  discrepancy), another iteration was performed to collect horizontal and vertical pattern cut-planes.

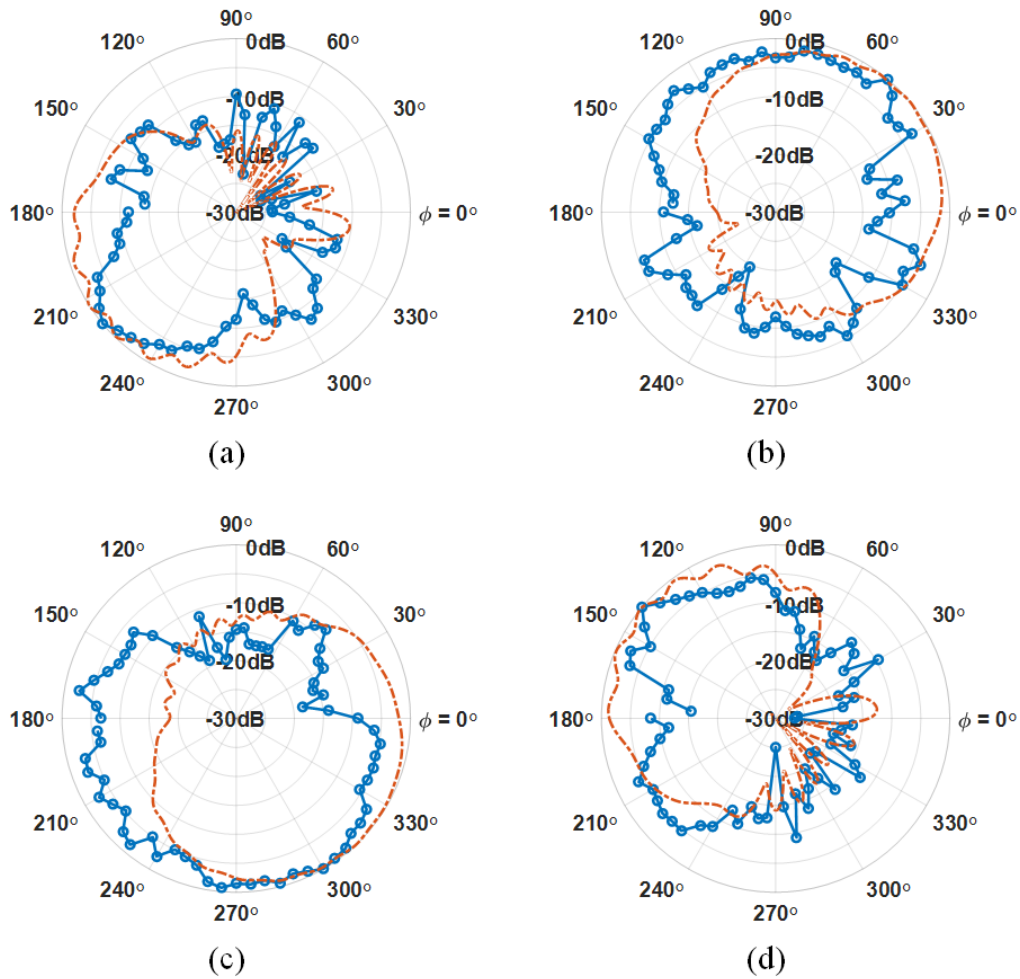


Fig. 6-8: Measured (solid) vs. simulated (dashed)  $\theta_{0i}$  cut-plane horizontal beam patterns for all input ports of the antenna system prototype: a) Port 1,  $\theta_{01}=35^\circ$ ; b) Port 2,  $\theta_{02}=25^\circ$ ; c) Port 3,  $\theta_{03}=30^\circ$ ; d) Port 4,  $\theta_{04}=30^\circ$ .

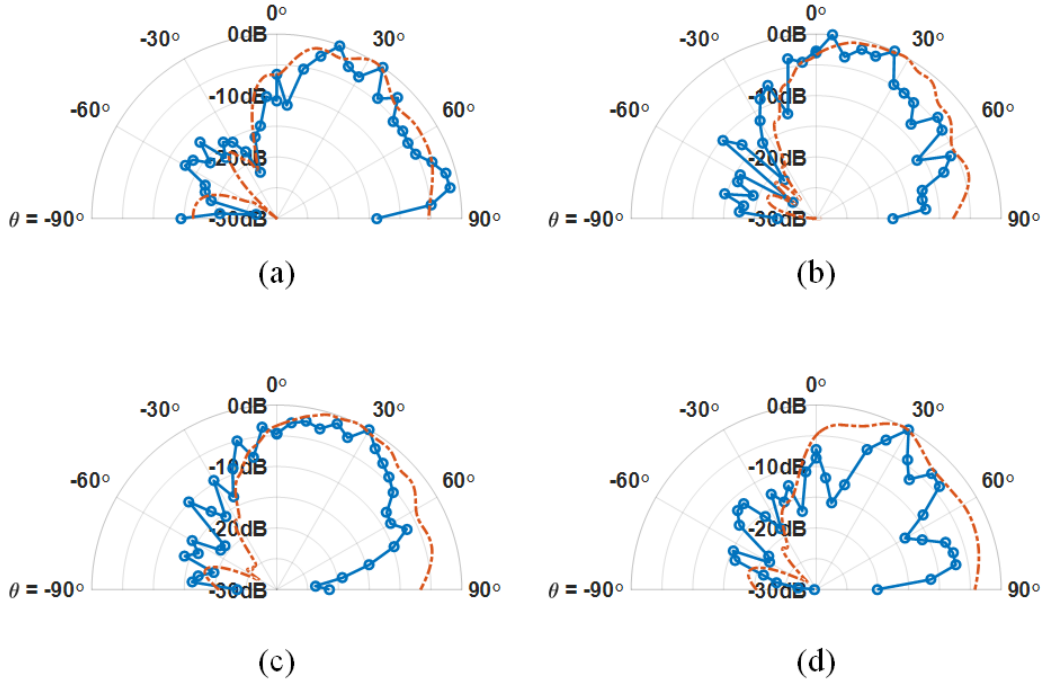


Fig. 6-9: Measured (solid) vs. simulated (dashed)  $\phi_{0i}$  cut-plane vertical beam patterns for all input ports of the antenna system prototype: a) Port 1,  $\phi_{01}=220^\circ$ ; b) Port 2,  $\phi_{02}=50^\circ$ ; c) Port 3,  $\phi_{03}=300^\circ$ ; d) Port 4,  $\phi_{04}=140^\circ$ .

Some variation can be seen in the pattern plots as the measurement setup required significant physical manipulation of cables, horn antenna, AUT, and the rig while incrementing through the varying values of  $\phi$  and  $\theta$ . Despite some magnitude variations, there is a strong resemblance between the simulated and measured patterns, and it can be concluded that the Butler Matrix system is achieving the goal of beam steering to four distinct quadrants in radiation space.

## 6.5: Antenna Gain Measurements

To assess gain performance over frequency, network parameters were collected from 58 to 62 GHz at the  $\theta_0$  and  $\phi_0$  corresponding to the four peak beam patterns. Following the Friis transmission formula, the received power  $P_R$  is

$$P_R = \frac{P_T G_T G_R \lambda^2}{(4\pi R)^2}, \quad (6.1)$$

where  $P_T$  is the transmitted power,  $G_T$  is the transmitter gain,  $G_R$  is the receiver gain,  $\lambda$  is free space wavelength, and  $R$  is the distance between transmitter and receiver. For the two port VNA measurement setup used to gather radiation pattern data, the collected  $S_{12}$  network parameter is the ratio of the power transmitted by the horn antenna to the power received at the AUT, or

$$|S_{12}|^2 = \frac{P_R}{P_T}. \quad (6.2)$$

Rearranging Eqn (6.4) and substituting in Eqn (6.5),

$$G_R = \frac{P_R(4\pi R)^2}{P_T G_T \lambda^2} = \frac{|S_{12}|^2 (4\pi R)^2}{G_T \lambda^2}, \quad (6.3)$$

which shows that the gain of the AUT can be found from the VNA measurements as well as knowledge of the horn antenna gain and the fixed chamber distance between horn antenna and AUT,  $R=9.3$  cm, for the first positioning system. It is the result of Eqn (6.3) that gets scaled down by the correction factor,  $k_G$ , for measurements in this portion of the near field zone. The value of  $k_G$  will be determined in the next subsection when information from the second positioning system is presented.

Fig. 6-10 plots the antenna gain derived from Eqn (6.3) versus frequency for each of the four input ports and compares to simulation results. The designed antenna system achieved 4.82-5.99 dB gain at 60 GHz for each input in HFSS, varying +1.0 to -8 dB at other frequencies in the 58-62 GHz range. A good correlation is seen between the simulated work and the gain calculated at 60 GHz, which was 1.0 dB lower for Port 1 (4.82 dB) in Fig. 6-10a, 0.5 dB lower for Port 2 (4.98 dB) in Fig. 6-10b, and comparable for Ports 3 (5.89 dB) and 4 (5.99 dB) in Fig. 6-10c and Fig. 6-10d, respectively.

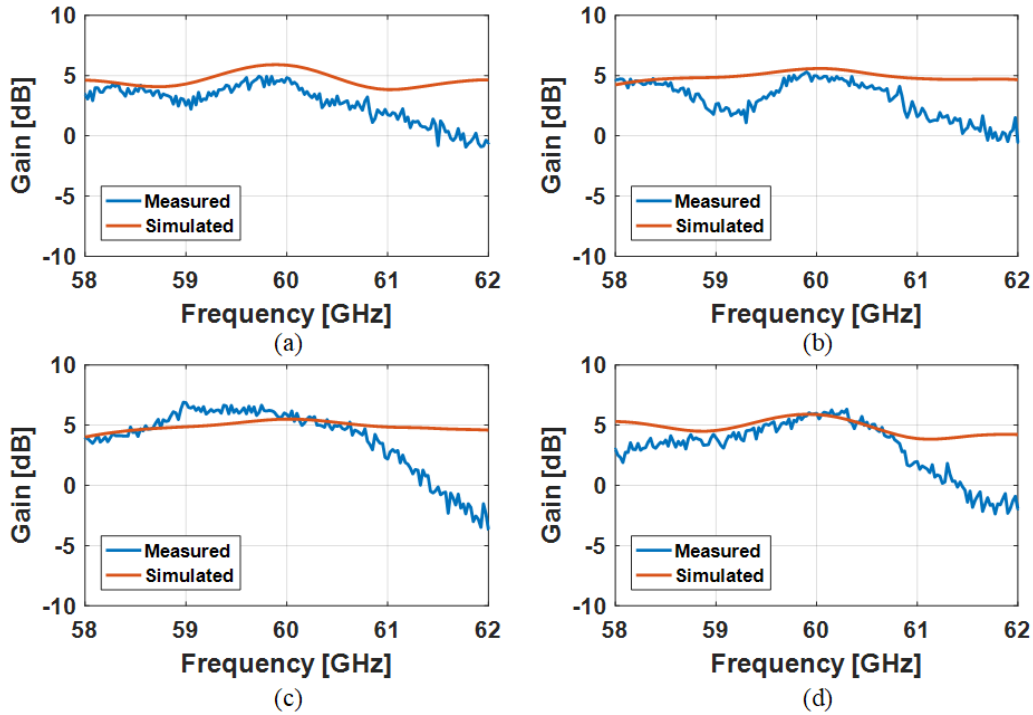


Fig. 6-10: Plots of gain vs frequency for the antenna system prototype. Input Ports 1-4 correspond to graphs (a)-(d), respectively.

## 6.6: Second Test Set-up for OTA Measurements

### 6.6.1: Design Modifications

The manual measurement of an OTA pattern is a lengthy process requiring careful point by point field measurements, but with the obvious benefit of making the expensive mm-wave measurement possible in-house using maker lab resources. The first set up can be modified to improve the process of OTA measurements by increasing the radius and length of the holder arm. Thus, a second positioning system was designed and fabricated with the same materials as shown in Fig. 6-5 for another round of OTA measurements.

In this new design, the radial arm is replaced with an arch with integrated rails for smoother movement of the horn antenna when changing  $\theta$  observation angles from  $-90^\circ \leq \theta \leq 90^\circ$ . The horn antenna will be held at a constant distance  $R=17.1$  cm with the boresight pointing directly at the

AUT. The platform for holding the AUT is kept the same except for a slight modification: the notch system for setting  $\phi$  increments from  $0^\circ \leq \phi \leq 360^\circ$  is replaced with a pin system. Both  $\theta$  and  $\phi$  have fixed  $5^\circ$  increments as in the first positioning system.

To accommodate the larger system, the front and back walls and ceiling of the anechoic chamber are extended to 61 cm in length while maintaining the 30.5 cm height/width. Side walls retain the 30.5 cm square dimensions. Floor absorber material was extended to the 61 cm length, but still provides the ability to adapt to moving cables from the VNA. The fabricated system, seen in Fig. 6-11 does not show the new anechoic chamber specifically made for this positioning system. The second set of measurements obtained with the new set up are used to confirm the beam pattern and gain calculations from the first round of data collection, both of which will be discussed in the following sections.

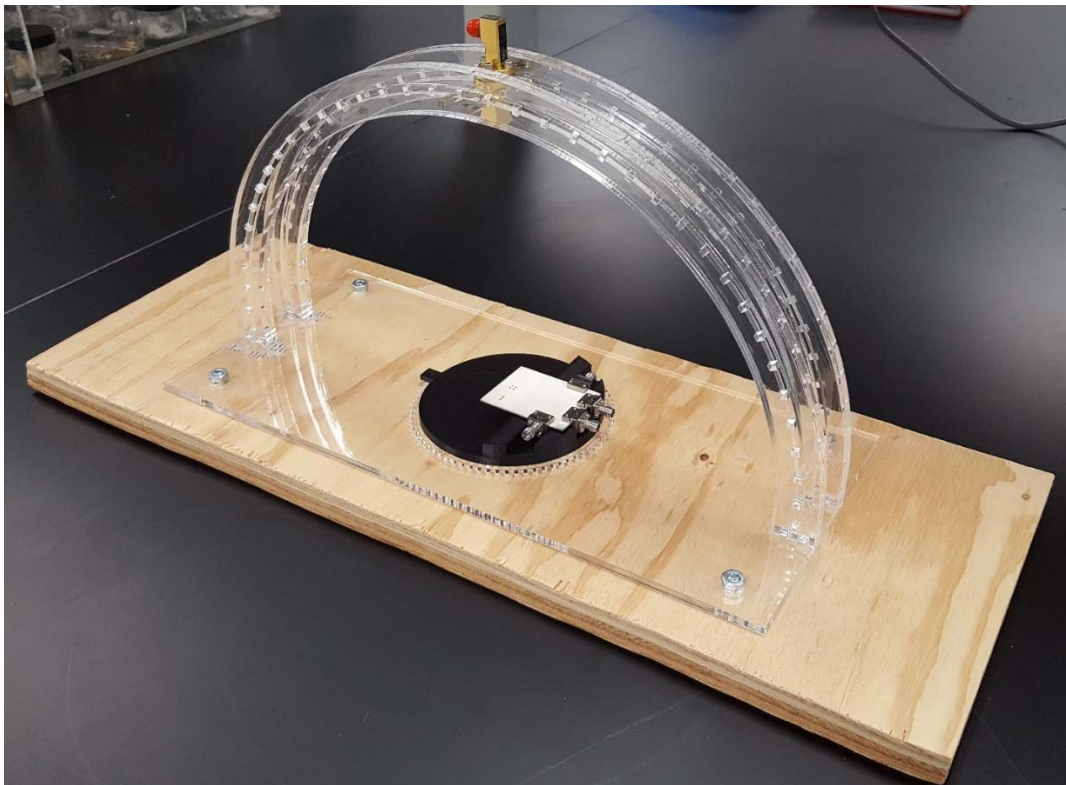


*Fig. 6-11: Second beam pattern positioning system with antenna array prototype and standard horn antenna.*

The radius of the positioner arm in the new set up is also increased to ensure far field measurement. The completed first positioning system considered the far field distance requirements based on the largest dimension of antenna under test (AUT)  $D=4.75$  mm for the convenience of fabrication of the set-up and compactness of the bench top chamber. Nonetheless, the reference horn antenna's dimensions must be considered as well for determining the radiative far field range and to reduce the approximation errors in ignoring the reactive field components. The aperture of the horn measures 15 mm by 12 mm. Since the  $TE_{10}$  mode is the mode of operation of the horn antenna from  $r_{ff} > 2D^2/\lambda_0 = 2(15)^2/5 = 9.00$  cm, which complies with the far field range requirement for  $TE_{10}$  mode in the first set up. However, if the excitation of higher order modes is considered, a computed diagonal length of 19.21 mm yields the far field range, a.k.a. Fraunhofer distance, as  $r_{ff} > 2D^2/\lambda_0 = 14.76$ . The first positioning system was designed to hold the horn antenna's boresight at a constant radial distance of  $R=9.3$  cm from the AUT, so in the far field range for  $D=15$  mm but not for  $D=19.21$  mm.

A literature search turned up no conclusive information on which dimension is most appropriate for determining a safe distance to ensure measurements in the far field range of a horn antenna. Therefore, the fields of a fundamental magnetic dipole radiator are considered as a first order estimation herein. From [14], the total electric and magnetic fields at a point  $(r, \theta, \phi)$  from an ideal magnetic dipole source are

$$\mathbf{E} = -\frac{I^m \Delta z}{4\pi} j\beta \left[ \frac{1}{r} + \frac{1}{j\beta r^2} \right] e^{-j\beta r} \sin \theta \hat{\boldsymbol{\phi}}, \text{ and} \quad (6.4)$$

$$\mathbf{H} = \frac{I^m \Delta z}{4\pi} j\omega \epsilon \left[ \frac{1}{r} + \frac{1}{j\beta r^2} - \frac{1}{\beta^2 r^3} \right] e^{-j\beta r} \sin \theta \hat{\boldsymbol{\theta}} + \frac{I^m \Delta z}{2\pi} j\omega \epsilon \left[ \frac{1}{j\beta r^2} - \frac{1}{\beta^2 r^3} \right] e^{-j\beta r} \cos \theta \hat{\mathbf{r}}, \quad (6.5)$$

where both transverse and radial components are present. To obtain far field representations, a large  $r$  is assumed so that  $\beta r \gg 1$  and the field equations reduces to

$$\mathbf{E} = -\frac{I^m \Delta z}{4\pi} j\beta \frac{e^{-j\beta r}}{r} \sin \theta \hat{\boldsymbol{\phi}} \text{ and} \quad (6.6)$$

$$\mathbf{H} = \frac{I^m \Delta z}{4\pi} j\omega \varepsilon \frac{e^{-j\beta r}}{r} \sin \theta \hat{\boldsymbol{\theta}}. \quad (6.7)$$

The near field region is also categorized based on  $\beta r$  assumptions. The reactive near field is said to occur where  $\beta r \ll 1$  and the reduced electric field equation becomes

$$\mathbf{E} = -\frac{I^m \Delta z}{4\pi} \frac{e^{-j\beta r}}{r^2} \sin \theta \hat{\boldsymbol{\phi}}. \quad (6.8)$$

$$\mathbf{H} = -j\omega \varepsilon \frac{I \Delta z}{4\pi \beta^2} \frac{e^{-j\beta r}}{r^3} \sin \theta \hat{\boldsymbol{\theta}} - j\omega \varepsilon \frac{I \Delta z}{2\pi \beta^2} \frac{e^{-j\beta r}}{r^3} \cos \theta \hat{\boldsymbol{r}}. \quad (6.9)$$

With the first positioning system radial arm at a constant  $R=9.3$  cm,  $\beta r$  is equal to 116.9, therefore  $\gg 1$ . According to [14], the ratio of reactive to radiated power density is  $1/(\beta r)^3$ , which in this case is  $1.6 \times 10^6$  (62 dB) greater. Still, equations (6.4) - (6.9) deal with the ideal magnetic dipole and not an aperture antenna like the horn standard used for measurements.

The near field of horn antennas was numerically and experimentally evaluated in [50], which concluded that close to the horn antenna, the phase front radiating from the horn is 1.25 times more curved than a sphere. The field structure in the experimentally evaluated near field region showed phase front distortions very close to the antenna ( $r < \lambda$ ) and then, as the observation distance stretched away from the antenna, perturbations tend to occur away from boresight outside of the  $\theta > 20^\circ$  cone. Only a slight magnitude difference, ranging from 5-10% was seen at the antenna's boresight as  $r$  approaches  $r_{ff}$ , disappearing when  $r=r_{ff}$ . In terms of evaluating the effects on the measurement results from the first set up with  $R=9.3$ cm, it can be stated that since the horn is always held in boresight with respect to AUT, the deviation from far field values should be minimal but can be considered as a gain correction factor,  $k_G$ , which is very close to 1.

## 6.6.2: Pattern Measurements

The procedure to find the peak beam azimuth and elevation angles remained the same with the second positioning system. Measurements were repeated to collect data for Port 1 excitation, confirming a peak beam location of  $\{\theta_{01}=30^\circ, \phi_{01}=220^\circ\}$ , which matched closely with the first measurements. The  $\theta_{01}=30^\circ$  cut-plane beam pattern is featured in Fig. 6-12 plotted along with the first measurement and simulated results. Similar variability was seen for data collected at varying  $\phi$ 's, but the peak clearly occurs in the  $\phi=5\pi/4$ , i.e. the 3rd quadrant.

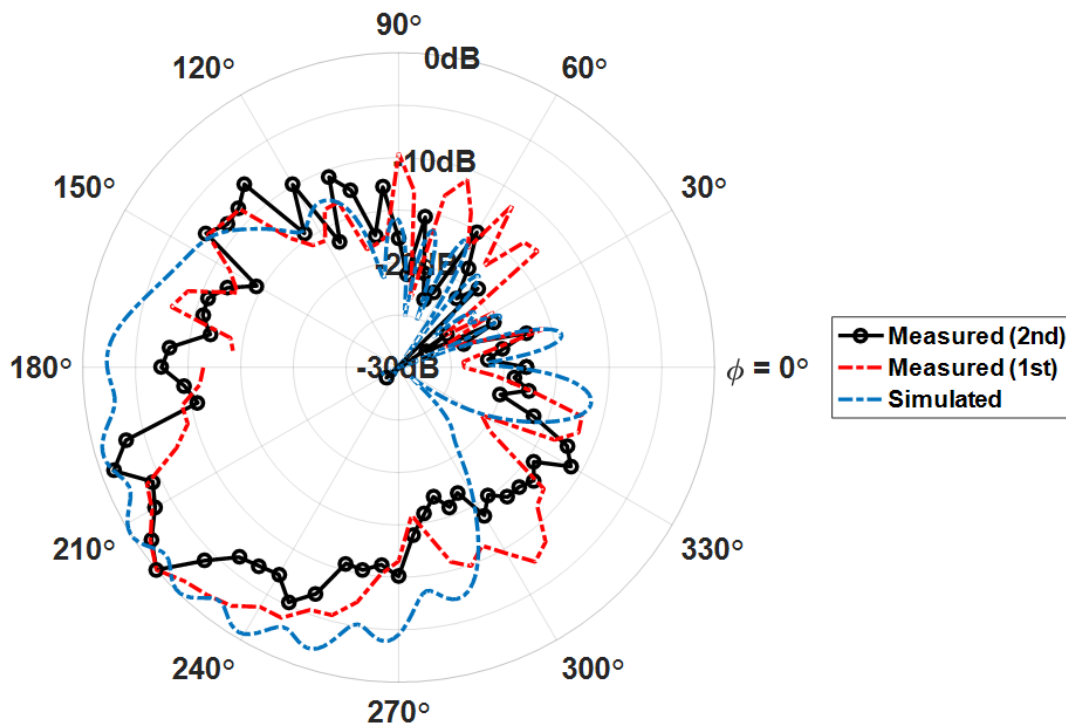


Fig. 6-12: 2<sup>nd</sup> measurement (black, solid) vs. 1<sup>st</sup> measurement (red, dashed) vs. simulated (blue, dashed) of the  $\theta_{01}=30^\circ$  cut-plane horizontal beam pattern for Port 1 of the antenna system prototype.

Fig. 6-13 shows the  $\phi_{01}=220^\circ$  cut-plane, or vertical, pattern with the first measurement and simulated results. Here, more variability can be seen as  $\theta$  is swept from  $-90^\circ$  to  $+90^\circ$  by shifting the position of the horn antenna. The sharp valleys in the pattern typically appear whenever the

entire positioning system must be moved to accommodate the cable attached to the horn antenna. The first collected pattern appears to capture the main lobe better than the second data set, suggesting the first positioning system, with less restriction for cable movement, is better for collecting data while varying the elevation angle. It does not appear that the radial distance between the AUT and horn antenna caused a discernible difference between peak beam pattern measurement sets.

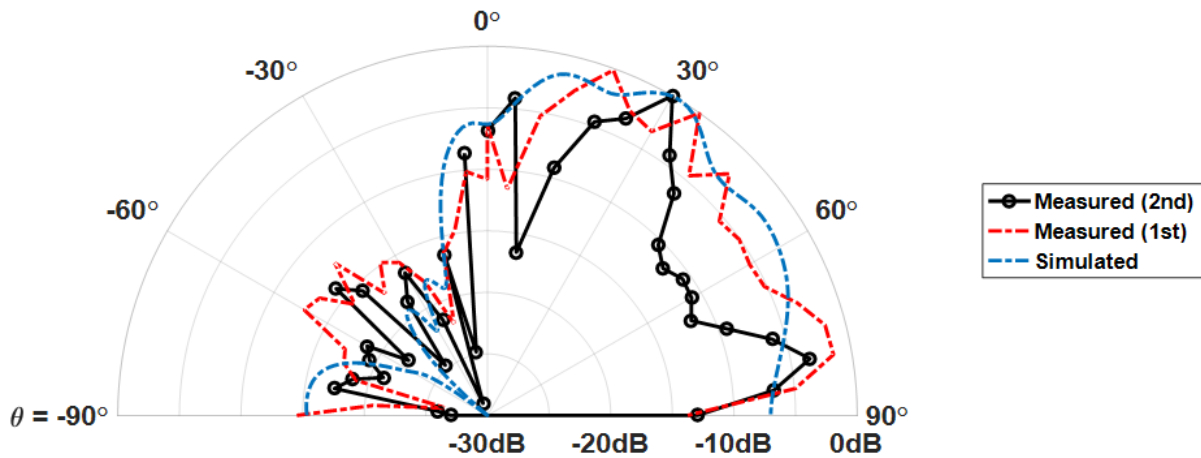


Fig. 6-13: 2<sup>nd</sup> measurement (black, solid) vs. 1<sup>st</sup> measurement (red, dashed) vs. simulated (blue, dashed) of the  $\phi_{0|1}=220^\circ$  cut-plane horizontal beam pattern for Port 1 of the antenna system prototype.

### 6.6.3: Gain Measurements

Antenna gain was calculated as presented above with network parameters collected for Port 1 excitation at the peak beam location,  $\{\theta_{0|1}=30^\circ, \phi_{0|1}=220^\circ\}$ , with the second positioning system. The only parameter that changes in Eqn (6.3) is the value of  $R=17.1$  cm for the new measurement rig. Fig. 6-14 captures gain as a function of frequency for Port 1 of the antenna system. The plot is similar to Fig. 6-10a, with a slightly lower gain of 4.52 dB at 60 GHz and steeper roll-off at 62 GHz. With this new calculated gain, the correction factor  $k_G$  can be estimated by comparing the first and second measurement results:

$$k_G = \frac{G_R@(R=9.3cm)}{G_R@(R=17.1cm)} = \frac{3.03}{2.83} = 1.07. \quad (6.10)$$

Applying  $k_G$  to the remaining port data collected with the first positioning systems yields gains of 4.69 dB, 5.60 dB, and 5.70 dB for Ports 2-4, respectively.

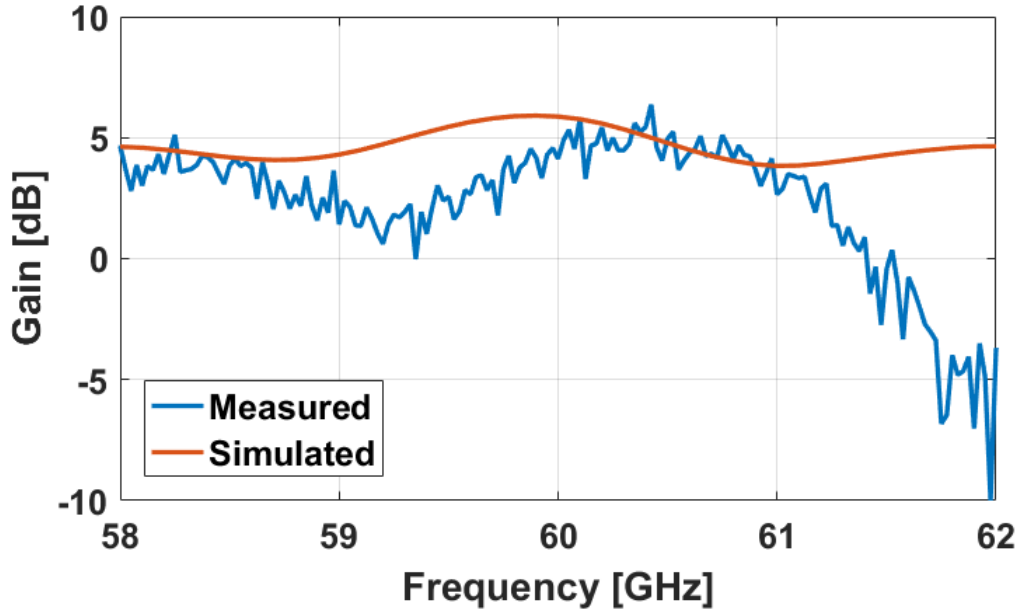


Fig. 6-14: Plot of gain vs frequency for input Port 1 to the antenna system prototype.

## 6.7: Conclusion

The fully-integrated antenna system was fabricated on a multi-layer PCB with Rogers RO4350B substrates for the SIW feed network and the antenna layers, with a bonding layer of RO4450B holding them together. Experimental evaluations showed good port reflection ( $< -15$  dB) and isolation ( $< -28$  dB) performance from measured scattering parameters. To collect OTA pattern and gain information, a bench-top positioning system and anechoic chamber was constructed to make in-house measurements. There is some ambiguity as to whether the first measuring system was positioned in the far field region of the standard horn antenna used for measurements, so a second positioning system was created showing the quick prototyping capability of this bench-top design.

The captured OTA information confirmed peak beam locations for each input port of  $\{\theta_{01}=35^\circ$  and  $\phi_{01}=220^\circ$ ;  $\theta_{02}=25^\circ$  and  $\phi_{02}=50^\circ$ ;  $\theta_{03}=30^\circ$  and  $\phi_{03}=300^\circ$ ;  $\theta_{04}=30^\circ$  and  $\phi_{04}=140^\circ\}$ , meeting the target application goal of illuminating the four quadrants of a surface parallel to the antenna array. Gain was calculated at 4.82 dB, 4.98 dB, 5.89 dB, and 5.99 dB for Ports 1-4 at 60 GHz with the first positioning system. Port 1 measurements were replicated with the second positioning system to re-confirm at peak beam location of  $\{\theta_{01}=30^\circ, \phi_{01}=220^\circ\}$  and get a new gain value of 4.52 dB at 60 GHz. This second data point allows an estimate of the gain correction factor,  $k_G=1.07$ , for the data collected with the first measurements.

---

## Chapter 7: Conclusion

### 7.1: Summary of Presented Work

The presented body of work began with the idea of creating a low-cost two-dimensional beam switching system to answer the needs of the millimeter-wave communications and radar-based industries. A passive Butler Matrix beamforming network integrated with a planar microstrip patch antenna array on just two substrate layers through SIW interconnect technology provides the needed low-power small-footprint 2D beam steering solution. This thesis has documented the unique characteristics of this work, showing that no other work exists that has demonstrated a two-layer SIW Butler Matrix able to drive a 2x2 planar array of MSPA elements to produce four distinct beam patterns with control in both elevation and azimuth angles.

The process began in Chapter 2 with a theoretical approach to determine the necessary changes to the standard Butler Matrix to transform its capabilities from 1-D to 2-D beam switching. That investigation highlighted that where the 1-D system has a single solution for orthogonal beamforming, the proposed 2-D updates to the BM enable many beam illumination solution sets. With an application goal to illuminate four quadrants of the upper half radiation space of the antenna array, a design goal was established to use  $90^\circ$  phase differentials at Stages 2 and 4 in either the conventional BM architecture or a Modified BM architecture, a choice that allows the designer to select the best phase shifter location to minimize the circuit footprint. With such a change, the antenna system will generate four switchable beams at an elevation angle of  $\theta_{0i}=45^\circ$  and  $\phi_{0i}=\{225^\circ, 45^\circ, 315^\circ, 135^\circ\}$  for input excitations to Ports  $i=1, 2, 3,$  and  $4,$  respectively.

Chapters 3 and 5 present the design and experimental evaluation of the Butler Matrix, respectively. Stepping from the design of a simple SIW interconnect to the integration of the hybrid couplers, crossovers, and phase shifters, Chapter 3 illustrates the case well where Modified Butler Matrix should be used instead of the conventional BM architecture to reduce the feed network footprint. The end result is a design area that is 54% smaller than the standard SIW BM presented in [33], with measurement results presented in Chapter 5 that confirm Modified Butler Matrix will be able to deliver four distinct beams pointed to  $\{\theta_{01}=41.94^\circ, \phi_{01}=232.20^\circ; \theta_{02}=51.66^\circ, \phi_{02}=39.24^\circ; \theta_{03}=54.90^\circ, \phi_{03}=316.08^\circ; \theta_{04}=35.82^\circ, \phi_{04}=131.94^\circ\}$ . While simulations demonstrate 10.8 to 11.9 dB insertion loss for all input ports of the BM, much of the excess loss is attributed to interface structures such as the microstrip-to-SIW transitions and the feed lines extended to accommodate large end launch connectors. Table 7-1 captures how the presented Modified Butler Matrix design compares to state-of-the-art publications in the SIW Butler Matrix field. It can be observed that the presented work is not only the first 2-D SIW-based BM at 60 GHz but does so while matching the smallest reported area for a 60 GHz BM circuit.

Moving to the antenna design in Chapter 4, the aperture-coupled MSPA elements were straightforward to layout and simulate. Most of the design discussion focused on proposing a novel transition from the Modified Butler Matrix outputs to feed the planar array, where two of the elements required wrap-around routing to the opposite side of the array while maintaining equal phasing with respect to the direct inputs. Simulated results showed the antenna system gain dropped from 10.8 dB for a broadside beam to 5.50-5.89 dB at 60 GHz, which can be credited to IL from the input structures as well as scan loss from steering the beam away from the array broadside. Once the BM feed network and 2x2 square planar array were integrated, a prototype was fabricated for experimental evaluation in Chapter 6.

Table 7-1: COMPARISON BETWEEN PROPOSED AND REPORTED SIW BUTLER MATRIX FEED NETWORKS.

Ref.	Phase Shifter Type	Beam Steering	F <sub>op</sub>	Layers	Feed	Circuit Area
[33]	Meander	1-D	60 GHz	1	GSG Probe	482.4 mm <sup>2</sup>
[34]	Meander	1-D	77 GHz	1	Waveguide	897.8 mm <sup>2</sup>
[35]	Shrunken width SIW	1-D	9.5 GHz	2	GSG Probe	1870 mm <sup>2</sup>
[36]	Expanded width SIW	1-D	60 GHz	1	Wave Port [simulated]	222.8 mm <sup>2</sup>
[37]	Meander	1-D	16 GHz	1	Coax	19250 mm <sup>2</sup> (4x8 BM)
[38]	Meander	1-D	12.5 GHz	2	Microstrip	3015 mm <sup>2</sup>
This Work	Periodic Aperture	2-D	60 GHz	1	Microstrip	222.5 mm <sup>2</sup>

A typical procedure was used to capture scattering parameters for the system, but a bench-top OTA measurement setup had to be created when an antenna measurement lab could not be found to assess the 60 GHz design. The OTA system consisted of a positioning system to hold the AUT and a standard horn antenna at proper azimuth and elevation angles increments while anechoic chamber walls, floor, and ceiling covered with absorber foam kept out unwanted noise and interference from the surrounding lab environment. The low-cost measurement platform confirmed the antenna system generated peak beam locations at  $\{\theta_{0|1}=35^\circ, \phi_{0|1}=220^\circ; \theta_{0|2}=25^\circ, \phi_{0|2}=50^\circ; \theta_{0|3}=30^\circ, \phi_{0|3}=300^\circ; \theta_{0|4}=30^\circ, \phi_{0|4}=140^\circ\}$ , meeting the application goal of 4 target quadrants, and the antenna gain of  $5.4 \pm 0.6$  dB at 60 GHz for each input excitation. Table 7-2 compares the presented work to other publications in the mm-wave 2-D antenna array space. The area reported in column 5 is the sum of all layout areas for all layers. It can be observed that the presented work is the most compact SIW-fed 60GHz 2-D beam switching solution while providing four quadrant target surface illumination.

TABLE 7-2: COMPARISON BETWEEN PROPOSED AND REPORTED MM-WAVE 2-D ANTENNA ARRAYS.

Ref.	Antenna Type	Array Size (area)	$F_{op}$	Layers (area)	Interconnect (Feed)	Beam Directions
[18]	MSPA	3x3 (96.67mm <sup>2</sup> )	29 GHz	1 (912mm <sup>2</sup> )	Microstrip (Microstrip)	$\theta_{0,sim}=20^\circ$ $\phi_{0,sim}=\$ 0°,90°,180°,270°
[19]	Slot	N (circular)	mm-wave (5 GHz)	2 (varies)	Cylindrical Waveguide Cavity (Coax)	$\theta_{0,sim}=\text{varies}$ $\phi_{0,sim}=\text{sweep}$ 0-360°
[20]	Horn	8x8 (10,609mm <sup>2</sup> )	29 GHz	8 (volume: 6.26e6 mm <sup>3</sup> )	Waveguide (Waveguide)	64 beams 8 $\theta$ -steps, 8 $\phi$ -steps
[21]	Cavity-backed ME dipole	2x2 (64mm <sup>2</sup> )	60 GHz	3 (783mm <sup>2</sup> )	SIW (Waveguide)	$\theta_{0,meas}=\sim 20^\circ$ $\phi_{0,sim}=\$ 45°,135°,225°,315°
[24]	MSPA (circular)	2x2 (13.4mm <sup>2</sup> )	60 GHz	2 (132mm <sup>2</sup> )	Microstrip (Microstrip)	$\theta_{0,sim}=90^\circ$ $\phi_{0,sim}=\$ 45°,135°,225°,315°
This Work	MSPA	2x2 (12.39mm <sup>2</sup> )	60 GHz	2 (333mm <sup>2</sup> )	SIW (Microstrip)	$\theta_{0,meas}=30\pm 5^\circ$ $\phi_{0,meas}=\$ 50°,140°,220°,300°

## 7.2: Next Steps

In general, beam steering projects tend to get pushed to greater numbers of antenna, better resolution, larger bandwidth, narrower beam width, smaller footprint, or lower cost – and these factors are not mutually exclusive. While there are many avenues for furthering the presented discussion, three particular directions have stood out that this thesis work could follow next for improvement: system performance and evaluation, target illumination range, and beam scanning. Each of these areas will be discussed separately below.

### **7.2.1: System performance and evaluation**

While the presented work was successful in meeting the application goal of illuminating the four quadrants of a planar surface target, a few system performance metrics could use some improvement. Specifically, connectors seemed to introduce a good deal of insertion loss (see Fig. 5-5) that made verifying the performance of the Modified Butler Matrix feed network challenging while antenna gain (see Fig. 6-10) for the fully-integrated system was lower than what would have been expected for a 2x2 planar array of MSPA elements. Another design iteration, beginning with the chosen SIW width, a better performing microstrip-to-SIW transition, and stronger focus on impedance matching between sub-sections of the BM would most likely go a long way towards improving insertion loss, which should help with the antenna gain seen in OTA measurements.

Evaluating the OTA performance was a very difficult aspect of the presented work. The developed solution could not be beat in terms of cost and customization capability, but the physical manipulation of the VNA cables inherent to the set-up created some variability in the results. A different approach should be explored for capturing OTA data without having to handle the cables and dealing with variations due to different angles of bending the cables. Perhaps a dome (at a constant radial distance well in the far field region) with many standard probes spaced at the desired increments of  $\theta$  and  $\phi$  would offer some measurement stability. The addition of a more dynamic cable solution, either a flexible quick disconnect for connecting to the probes rapidly or a switch to connect the many probe cables all at once would make the measurement system more reliable and procure smoother plots.

### **7.2.2: Target illumination range**

Section 2.5: discussed beam steering limitations for the 2x2 square planar array driven by the Modified BM when illuminating the target surface. An exploration of a different 4-element planar

array geometry could find a way to expand the capabilities of the presented antenna system. For instance, the planar array factor equation, presented in Chapter 2 as Eqn (2.11),

$$A_i(\theta, \phi) = \sum_{n=0}^{N-1} \sum_{m=0}^{M-1} e^{j\beta(x_{mn} \sin \theta \cos \phi + y_{mn} \sin \theta \sin \phi)} e^{j\alpha_{mn} i}, \quad (7.1)$$

is reduced by assuming a square arrangement (synchronizing  $x_{mn}$  and  $y_{mn}$ ) but also using  $\lambda_0/2$  spacing to help simplify the relationship with  $\beta=2\pi/\lambda$ . To gain deeper insight, different 4-node array geometries could be explored. A search routine could be run for the phase differentials,  $\psi_1$  and  $\psi_2$ , of BM that maximize the scanning range of  $\theta$  and  $\phi$  for each configuration and its array factor. This additional investigation could not only extend the capability of the presented work but could also enable a fully-tunable beam scanning system to be discussed next.

### 7.2.3: Beam scanning

An exciting area to consider is the concept of making the presented work dynamically tunable: to enable adjusting the beam switching angle to the intended target or even leap from beam switching to beam scanning. Specifically, the work presented in [43], regarding the periodic aperture phase shifters used in the SIW BM, directly integrated capacitors across the transverse slots to increase the range of the phase shifter. Extending this to the use of varactor diodes could create a tunable SIW phase shifter in a minimal footprint that would allow the presented system to scan the target surface according to Fig. 2-20. Further, given positive results from investigating the illumination range (discussed in the previous section), it is conceivable that the proposed 2x2 planar array system could scan the target upper half space in its entirety with just a bias voltage controlling the varactor phase shifters in the Modified Butler Matrix feed network. Such a system would be small, low cost, and very capable of improving the performance of the next generation of mm-wave communications and radar-based systems.

---

## Appendix I: De-embedding Procedure

As previously mentioned, a through-only technique [44] is chosen for this purpose. Two different through structures with  $l_1$  and  $l_2$  lengths are designed for this process. When the input and output ports are identical and the through line is symmetric about its midsection, swapping Ports 1 and 2 will not change the measured S, Z, or Y matrices. The transmission matrices of the test structures can each be decomposed into 3 different two-port networks: Port 1 connector and the connector-to-line transition section, the intrinsic device, and the combined line-to-connector transition with Port 2 connector. The transmission matrix of the generalized test structure  $l_i$  can be represented as

$$M_{l_i}^t \equiv M_{P1} M_{l_i} M_{P2} \quad (I.1)$$

where  $M_{l_i}$  represents the intrinsic through line, and  $M_{P1}$  and  $M_{P2}$  represent the line-to-connector (or connector-to-line) transition and the connector corresponding to each port.

The next step in the procedure uses this model to extract the transition and port connector discontinuity effects on the designed through lines. Taking the collected data for  $l_1$  and  $l_2$ , consider multiplying  $M_{l_2}^t$  by the inverse of  $M_{l_1}^t$

$$M_{l_2-l_1}^h \equiv M_{l_2}^t [M_{l_1}^t]^{-1} \quad (I.2)$$

$$\equiv M_{P1} M_{l_2} M_{l_1}^{-1} M_{P1}^{-1} \quad (I.3)$$

$$\equiv M_{P1} M_{l_2-l_1} M_{P1}^{-1} \quad (I.4)$$

where  $M_{l_2-l_1}^h$  is a hybrid structure  $M_{l_2}^t [M_{l_1}^t]^{-1}$  and  $M_{l_2-l_1}$  is a line of length  $l_2-l_1$ .

It is then assumed the port and transition discontinuity can be modeled solely with a lumped admittance,  $Y_L$ ,

$$M_{P1} \equiv \begin{bmatrix} 1 & 0 \\ Y_L & 1 \end{bmatrix} \quad (I.5)$$

$$M_{l_2-l_1}^h \equiv \begin{bmatrix} 1 & 0 \\ Y_L & 1 \end{bmatrix} M_{l_2-l_1} \begin{bmatrix} 1 & 0 \\ -Y_L & 1 \end{bmatrix}. \quad (I.6)$$

Under this assumption, the hybrid structure can be represented by Y parameter matrix and in a parallel combination of the intrinsic through line and port and transition discontinuity

$$Y_{l_2-l_1}^h \equiv Y_{l_2-l_1} + \begin{bmatrix} Y_L & 0 \\ 0 & -Y_L \end{bmatrix}. \quad (I.7)$$

Since the intrinsic device is symmetric, the Y parameters of the device can be isolated by connecting the hybrid structure in parallel with a port-swapped version of itself, cancelling the effects of the port feed structures

$$\text{Swap} \left( \begin{bmatrix} y_{11} & y_{12} \\ y_{21} & y_{22} \end{bmatrix} \right) \equiv \begin{bmatrix} y_{22} & y_{21} \\ y_{12} & y_{11} \end{bmatrix} \text{ and} \quad (I.8)$$

$$Y_{l_2-l_1} \equiv \frac{Y_{l_2-l_1}^h + \text{Swap}(Y)_{l_2-l_1}^h}{2}. \quad (I.9)$$

The work done to this point is focused on isolating the effect of the through line from the measurement of the intrinsic device. It is imperative, though, to extract information about the feed structures, which no longer exists in (I.9). Substituting (I.9) into (I.7) and rearranging, the lumped admittance can be found from

$$\begin{bmatrix} Y_L & 0 \\ 0 & -Y_L \end{bmatrix} \equiv \frac{Y_{l_2-l_1}^h - \text{Swap}(Y)_{l_2-l_1}^h}{2}. \quad (I.10)$$

This  $Y_L$  is then substituted into (I.5) to get  $M_{P1}$ , which is inverted to yield a reciprocal output feed structure

$$M_{P2} \equiv M_{P1}^{-1}. \quad (I.11)$$

Attention now turns to de-embedding the feed structure from the non-symmetric device, in this case the Butler Matrix prototype. The generalized transmission matrix of the Butler Matrix prototype, P, is represented as

$$M_p^t \equiv M_{P1} M_{BM} M_{P2} \quad (I.12)$$

where  $M_{BM}$  represents the Butler Matrix circuit. To isolate the transmission matrix of the Butler circuit,  $M_p^t$  is multiplied by the inverse of  $M_{P1}$  and  $M_{P2}$ ,

$$M_{P1}^{-1} M_p^t M_{P2}^{-1} \equiv M_{P1}^{-1} M_{P1} M_{BM} M_{P2} M_{P2}^{-1} \quad (I.13)$$

$$\equiv M_{BM}. \quad (I.14)$$

$M_{BM}$  can now be transformed to conventional S parameters and evaluated against design simulations without the parasitic effects introduced by the prototyping feed structures.

---

## References

- [1] P. Demestichas, A. Georgakopoulos, D. Karvounas, K. Tsagkaris, V. Stavroulaki, J. Lu, C. Xiong and J. Yao, "5G on the Horizon: Key Challenges for the Radio-Access Network," *IEEE Vehicular Technology Magazine*, vol. 8, no. 3, pp. 47-53, 2013.
- [2] S. Sun, G. R. MacCartney Jr., M. K. Samimi, S. Nie and T. S. Rappaport, "Millimeter Wave Multi-beam Antenna Combining for 5G Cellular Link Improvement in New York City," in *IEEE International Conference on Communications (ICC)*, Sydney, NSW, 2014.
- [3] J. Choi, V. Va, N. González-Prelcic, R. Daniels, C. R. Bhat and R. W. Heath Jr, "Millimeter-Wave Vehicular Communication to Support Massive Automotive Sensing," *IEEE Communications Magazine*, vol. 54, no. 12, pp. 160-167, December 2016.
- [4] S. Patole, M. Torlak, D. Wang and M. Ali, "Automotive Radar: A review of signal processing techniques," *IEEE Signal Processing Magazine*, vol. 34, no. 2, pp. 22-35, 2017.
- [5] S. Churkin and L. Anishchenko, "Millimeter-wave radar for vital signs monitoring," in *IEEE International Conference on Microwaves, Communications, Antennas and Electronic Systems (COMCAS)*, Tel Aviv, Israel, 2015.
- [6] Project Soli, "Project Soli," 2019. [Online]. Available: <https://atap.google.com/soli/>. [Accessed 2019].
- [7] R. W. Heath, N. Gonzalez-Prelcic, S. Rangan, W. Roh and A. M. Sayeed, "An Overview of Signal Processing Techniques for Millimeter Wave MIMO Systems," *IEEE Journal of Selected Topics in Signal Processing*, vol. 10, no. 3, pp. 436-453, 2016.

- [8] D. M. Sheen, D. L. McMakin and T. E. Hall, "Three-dimensional millimeter-wave imaging for concealed weapon detection," *IEEE Transactions on Microwave Theory and Techniques*, vol. 49, no. 9, pp. 1581-1592, 2001.
- [9] S. Rangan, T. S. Rappaport and E. Erkip, "Millimeter-Wave Cellular Wireless Networks: Potentials and Challenges," *Proceedings of the IEEE*, vol. 102, no. 3, pp. 366-385, March 2014.
- [10] J. G. Andrews, S. Buzzi, W. Choi, S. V. Hanly, A. Lozano, A. C. K. Soong and J. C. Zhang, "What Will 5G Be?," *IEEE Journal on Selected Areas in Communications*, vol. 32, no. 6, pp. 1065-1082, June 2014.
- [11] F. Boccardi, R. W. Heath, A. Lozano, T. L. Marzetta and P. Popovski, "Five disruptive technology directions for 5G," *IEEE Communications Magazine*, vol. 52, no. 2, pp. 74-80, February February 2014.
- [12] R. W. Heath, "Millimeter Wave for 5G: Features and Implications," Presentation, University of Texas at Austin, 2015.
- [13] K. Wu, D. Deslandes and Y. Cassivi, "The Substrate Integrated Circuits - A New Concept for High-Frequency Electronics and Optoelectronics," in *6th International Conference on Telecommunications in Modern Satellite, Cable and Broadcasting Service, 2003. TELSIKS 2003*, Nis, Yugoslavia, 2003.
- [14] W. L. Stutzman and G. A. Thiele, *Antenna Theory and Design*, Hoboken, NJ: J. Wiley & Sons, 2013.

- [15] J. C. Liberti, Jr and T. S. Rappaport, *Smart Antennas for Wireless Communications: IS-95 and Third Generation CDMA Applications*, Upper Saddle River, NJ, USA: Prentice Hall, 1999.
- [16] W. Hong, Z. H. Jiang, C. Yu, J. Zhou, P. Chen, Z. Yu, H. Zhang, B. Yang, X. Pang, M. Jiang, Y. Cheng, M. K. T. Al-Nuaimi, Y. Zhang, J. Chen and S. He, "Multibeam Antenna Technologies for 5G Wireless Communications," *IEEE Transactions on Antennas and Propagation*, vol. 65, no. 12, pp. 6231-6249, 2017.
- [17] J. Butler and R. Lowe, "Beam-Forming Matrix Simplifies Design of Electronically Scanned Antennas," *Electronic Design*, vol. 9, no. 4, pp. 170-173, 1961.
- [18] S. I. Orakwue, R. Ngah and T. A. Rahman, "A two dimensional beam scanning array antenna for 5G wireless communications," in *IEEE Wireless Communications and Networking Conference Workshops (WCNCW)*, Doha, Qatar, 2016.
- [19] M. Klemes, H. Boutayeb and F. Hyjazie, "Minimal-hardware 2-D steering of arbitrarily large circular arrays (combining axial patterns of phase-modes)," in *IEEE International Symposium on Phased Array Systems and Technology (PAST)*, Waltham, MA, USA, 2016.
- [20] A. K. Pandey, "Design of a compact high power phased array for 5G FD-MIMO system at 29 GHz," in *Asia-Pacific Microwave Conference (APMC)*, New Delhi, India, 2016.
- [21] Y. Li and K.-M. Luk, "60-GHz Dual-Polarized Two-Dimensional Switch-Beam Wideband Antenna Array of Aperture-Coupled Magneto-Electric Dipoles," *IEEE Transactions on Antennas and Propagation*, vol. 64, no. 2, pp. 554-563, 2016.

- [22] B. D. Horwath and R. Abhari, "A 60 GHz  $2 \times 2$  planar phased array with SIW modified butler matrix feed," in *IEEE International Symposium on Antennas and Propagation (APSURSI)*, Fajardo, Puerto Rico, 2016.
- [23] B. D. Horwath and R. Abhari, "Characterization of a  $4 \times 4$  substrate integrated waveguide Butler matrix at 60 GHz for two-dimensional beam steering," *International Journal of RF and Microwave Computer-Aided Engineering*, vol. 28, no. 9, pp. 1-13, 2018.
- [24] P. Baniya and K. L. Melde, "Switched-Beam Endfire Planar Array With Integrated 2-D Butler Matrix for 60 GHz Chip-to-Chip Space-Surface Wave Communications," *IEEE Antennas and Wireless Propagation Letters*, vol. 18, no. 2, pp. 236-240, 2019.
- [25] F. Shigeki, "Waveguide Line (in Japanese)". Japan Patent 06-053 711, 25 February 1994.
- [26] H. Uchimura, T. Takenoshita and M. Fujii, "Development of the "Laminated Waveguide"," *IEEE Transactions on Microwave Theory and Techniques*, vol. 46, no. 12, pp. 2438-2443, 1998.
- [27] J. R. Bray and L. Roy, "Resonant frequencies of post-wall waveguide cavities," *IEE Proceedings - Microwaves, Antennas and Propagation*, vol. 150, no. 5, pp. 365-368, 2003.
- [28] A. Suntives and R. Abhari, "Characterizations of interconnects formed in electromagnetic bandgap substrates," in *9th IEEE Workshop on Signal Propagation on Interconnects*, Garmisch-Partenkirchen, Germany, 2005.
- [29] A. Suntives and R. Abhari, "Design and characterization of the EBG waveguide-based interconnects," *IEEE Transactions on Advanced Packaging*, no. 5, pp. 163-170, May 2007.

- [30] F. Xu and K. Wu, "Guided-Wave and Leakage Characteristics of Substrate Integrated Waveguide," *IEEE Transactions of Microwave Theory and Techniques*, vol. 53, no. 1, pp. 66-73, 2005.
- [31] D. Deslandes and K. Wu, "Accurate Modeling, Wave Mechanisms, and Design Considerations of a Substrate Integrated Waveguide," *IEEE Transactions on Microwave Theory and Techniques*, vol. 54, no. 6, pp. 2516-2526, 2006.
- [32] J. E. Rayas-Sanchez and V. Gutierrez-Ayala, "A general EM-based design procedure for single-layer substrate integrated waveguide interconnects with microstrip transitions," in *2008 IEEE MTT-S International Microwave Symposium Digest*, Atlanta, GA, USA, 2008.
- [33] C. J. Chen and T. H. Chu, "Design of a 60-GHz Substrate Integrated Waveguide Butler Matrix – A Systematic Approach," *IEEE Trans. on Microwave Theory and Techniques*, vol. 58, no. 7, pp. 1724-1732, June 2010.
- [34] T. Djeraji and K. Wu, "A low-cost wideband 77-GHz planar Butler matrix in SIW technology," *IEEE Transactions on Antennas and Propagation*, vol. 60, no. 10, pp. 4949-4954, October 2012.
- [35] S. Karamzadeh, V. Rafii, M. Kartal and B. S. Virdee, "Compact and Broadband 4x4 SIW Butler Matrix with Phase and Magnitude Error Reduction," *IEEE Microwave and Wireless Components Letters*, vol. 25, no. 12, pp. 772-774, December 2015.
- [36] Z. Chen, X. Wu and F. Yang, "A compact SIW butler matrix with straight delay lines at 60 GHz," in *IEEE International Symposium on Antennas and Propagation & USNC/URSI National Radio Science Meeting*, San Diego, CA, 2017.

- [37] P. Chen, W. Hong, Z. Kuai, J. Xu, H. Wang, J. Chen, H. Tang, J. Zhou and K. Wu, "A Multibeam Antenna Based on Substrate Integrated Waveguide Technology for MIMO Wireless Communications," *IEEE Transactions on Antennas and Propagation*, vol. 57, no. 6, pp. 1813-1821, 2009.
- [38] A. A. M. Ali, N. J. G. Fonseca, F. Coccetti and H. Aubert, "Design and Implementation of Two-Layer Compact Wideband Butler Matrices in SIW Technology for Ku-Band Applications," *IEEE Transactions on Antennas and Propagation*, vol. 59, no. 2, pp. 503-512, 2011.
- [39] K. Wincza, K. Staszek, I. Slomian and S. Gruszczynski, "Scalable Multibeam Antenna Arrays Fed by Dual-Band Modified Butler Matrices," *IEEE Transactions on Antennas and Propagation*, vol. 64, no. 4, pp. 1287-1297, 2016.
- [40] D. M. Pozar, "Microstrip antenna aperture-coupled to a microstripline," *Electronic Letters*, vol. 21, no. 2, pp. 49-50, 1985.
- [41] D. Deslandes and K. Wu, "Integrated microstrip and rectangular waveguide in planar form," *IEEE Microwave and Wireless Components Letters*, vol. 11, no. 2, pp. 68-70, February 2001.
- [42] W. M. Abdel-Wahab and S. Safavi-Naeini, "Wide-Bandwidth 60-GHz Aperture-Coupled Microstrip Patch Antennas (MPAs) Fed by Substrate Integrated Waveguide (SIW)," *IEEE Antennas and Wireless Propagation Letters*, vol. 10, pp. 1003-1005, 2011.
- [43] A. Suntives, K. Payandehjoo and R. Abhari, "Design and characterization of periodically-loaded substrate integrated waveguide phase shifters," in *IEEE MTT-S International*, Anaheim, CA, 2010.

- [44] A. M. Mangan, S. P. Voinigescu, M. T. Yang and M. Tazlauanu, "De-embedding transmission line measurements for accurate modeling of IC designs," *IEEE Transactions on Electron Devices*, vol. 53, no. 2, pp. 235-241, February 2006.
- [45] G. H. Golub and C. F. Van Loan, *Matrix Computations*, 4th Edition, Baltimore, MD, USA: The Johns Hopkins University Press, 2013.
- [46] P. Wongchampa and M. Uthansakul, "Orthogonal Beamforming for Multiuser Wireless Communications: Achieving higher received signal strength and throughput than with conventional beamforming," *IEEE Antennas and Propagation Magazine*, vol. 59, no. 4, pp. 38-49, August 2017.
- [47] M. A. Antoniadou and G. V. Eleftheriades, "Compact linear lead/lag metamaterial phase shifters for broadband applications," *IEEE Antennas and Wireless Propagation Letters*, vol. 2, pp. 103-106, 2003.
- [48] D. Deslandes, "Design Equations for Tapered Microstrip-to-Substrate Integrated Waveguide Transitions," in *IEEE MTT-S International Microwave Symposium*, Anaheim, CA, USA, 2010.
- [49] Cuming Microwave, "C-RAM MMW Absorber Application Note 300-13," [Online]. Available: <https://27eidpeg8qz2z1zp81eeljy1-wpengine.netdna-ssl.com/wp-content/uploads/2014/04/AN300-13-C-RAM-MILLIMETER-WAVE.pdf>. [Accessed 19 06 2018].
- [50] D. W. Metzger, J. D. Norgard and R. M. Sega, "Near-field patterns from pyramidal horn antennas: numerical calculation and experimental verification," *IEEE Transactions on Electromagnetic Compatibility*, vol. 33, no. 3, pp. 188-196, 1991.

- [51] P. J. Van Wijnen, H. R. Claessen and E. A. Wolsheimer, "A new straightforward calibration and correction procedure for "on wafer" high frequency S-parameter measurements (45 MHz-18 GHz)," in *Bipolar Circuits and Technology Meeting*, Minneapolis, Minnesota, 1987.
- [52] W. R. Eisenstadt and Y. Eo, "S-parameter-based IC interconnect transmission line characterization," *IEEE Transactions on Components, Hybrids, and Manufacturing Technology*, vol. 15, no. 4, pp. 483-490, April 1992.